Proceedings of the ISD Workshops

HUMAN CAPITAL
NATIONAL COHESION STRATEGY

EUROPEAN UNION
EUROPEAN
SOCIAL FUND

PROCEEDINGS OF THE ISD WORKSHOPS

Faculty of Physics and Applied Computer Science
AGH University of Science and Technology
Kraków, 2013

Proceedings of the ISD Workshops

Faculty of Physics and Applied Computer Science
AGH University of Science and Technology
Kraków, 2013
ISBN: 978-83-925779-3-5

SCIENTIFIC BOARD:
Andrzej Horzela, *The Henryk Niewodniczański Institute of Nuclear Physics, Kraków, Poland*
Janusz Adamowski, *AGH University of Science and Technology, Kraków, Poland*
Renata Tokarz-Sobieraj, *Jerzy Haber Institute of Catalysis and Surface Chemistry, Kraków, Poland*

EDITORS:
Marcin Perzanowski (Editor-in-chief)
Jarosław Pawłowski
Maciej Chrobak
Jakub Moroń

COVER DESIGN: Jarosław Pawłowski
COVER PHOTO: Marcin Perzanowski

PRINTING AND BOOKBINDING: K&K reklama poligrafia, Kraków

All rights reserved. No part of this publication can be reproduced, stored, transmitted, or disseminated in any form or by any means without written permission from the Faculty of Physics and Applied Computer Science, AGH University of Science and Technology.

PREFACE

We have the pleasure of presenting the Proceedings of three Scientific Workshops, organized for the students of the Interdisciplinary PhD Studies (Polish acronym ISD). The Proceedings contain the papers prepared by the ISD students as follow-ups of their oral contributions given during the ISD Workshops. The ISD Project „Advanced Materials for Modern Technology and Future Energetics" is a common scientific and educational enterprise organized and coordinated by a consortium of three scientific institutions of Kraków: Faculty of Physics and Applied Computer Science, AGH University of Science and Technology (WFiIS AGH), being a project leader, and two partner institutions: the Henryk Niewodniczański Institute of Nuclear Physics, Polish Academy of Sciences (IFJ PAN), and the Jerzy Haber Institute of Catalysis and Surface Chemistry, Polish Academy of Sciences (IKiFP PAN). The ISD project enjoys financial support by the FP7 EU Operation Program Human Capital (POKL.04.01.01-00-434/08-02). The project is aimed at providing the students with a high-level training in physics and chemistry of advanced materials, necessary to prepare and defend their PhD theses. Sixty students were enrolled in the ISD during recruitments carried out in years 2009, 2010, and 2011. The ISD students are actively participating in research programs of the institutions engaged in the project and are preparing their PhD theses under the supervision of qualified staff members of the three institutions.

The ISD Project has been an important component for the creation of the consortium founded by five scientific institutions (WFiIS AGH, IFJ PAN, IKiFP PAN, Faculty of Physics, Astronomy and Applied Computer Science of the Jagiellonian University, and Faculty of Chemistry of the Jagiellonian University) and named the Marian Smoluchowski Kraków Research Consortium „Matter — Energy — Future". In year 2012, the Ministry of Science and Higher Education awarded the status of the National Leading Scientific Center (KNOW) for the years 2012 – 2017 to the Consortium as the only one representative of physical and chemical sciences.

Three scientific workshops organized within the ISD project reach far beyond standard teaching activities of a typical PhD program: (i) The students were offered invited lectures by top-class physicists and chemists, (ii) The students could participate in open discussions with the authorities of the institutions involved in the project, (iii) The students could contribute with oral presentations of their research and engage in discussions with the lecturers and fellows, and then they were offered the opportunity to publish their work in the Workshops Proceedings, (iv) The ISD Workshops facilitated the building of interdisciplinary scientific and social communities of young researchers across the institutional boundaries of the ISD project participants.

The first ISD Workshop took place in Zakopane, a famous Polish skiing and tourist resort in the Tatra Mountains, from 11th till 18th November 2011. Invited lectures were given by Professor Wojciech Łużny, Dean of the WFiIS AGH, Professor Paweł Olko, Deputy Director of the IFJ PAN, Professor Brigitte Bacroix, University Paris-Nord, Professor Józef Spałek, Jagiellonian University, Kraków, Professor Krzysztof Wierzbanowski, WFiIS AGH, and Professor Jacek Tarasiuk, WFiIS AGH.

The second ISD Workshop took place in Ochotnica Dolna, a village in a beautiful mountain region of Beskid Sądecki, from 10th till 16th June 2012. This time the following invited lecturers presented their talks: Professor Jörn Donges, DESY, Hamburg, Professor Laurent Chaput, University H. Poincaré, Nancy, Professor Paul Lipinski, École Nationale d'Ingénieurs, Metz, Professor Mirosław Derewiński, IKiFP PAN, Professor Józef Spałek, Jagiellonian University, Kraków, Professor Jacek Tarasiuk, Professor Janusz Toboła, and Professor Marek Woch from WFiIS AGH. Special lectures on the perspectives of the basic and applied research in physics and chemistry in their institutes were presented by Professor Małgorzata Witko, Director of the IKiFP PAN, and Professor Marek Jeżabek, Director of the IFJ PAN.

The third ISD Workshop is planned to be held in Szczyrk, one of the main tourist centers in Beskid Śląski, from 9th till 15th June 2013. We have invited 10 lecturers, among them Professor Janusz Wolny, Dean of the WFiIS AGH for the tenure 2012 – 2016 and the member of the steering board of the Consortium „Matter — Energy — Future".

As the coordinators of the ISD project we would like to express our gratitude to the authorities of our home institutions for their assistance and constant support in the realization of the project. We would like to thank all the participants for attending the workshops and preparing truly interesting talks. We also address our thanks to the ISD students, who actively participated in the organization of the Workshops – the members of the Organizing Committee: Paweł Janowski, Żaneta Kalemba-Jaje, Mateusz Marzec, Magdalena Miecznik, Jarek Pawłowski, Marcin Perzanowski, and Ola Wandzilak. Last but not least, our special thanks are due to the Editorial Committee of these Proceedings — Maciej Chrobak, Jakub Moroń, Jarek Pawłowski, and Marcin Perzanowski, whose efforts and skills lead to successful publication of the book.

Professor Andrzej Horzela — Chairman of the Organizing Committee of the ISD Scientific Workshops, Vice-director of the ISD Project
Professor Janusz Adamowski — Director of the ISD Project
Professor Renata Tokarz-Sobieraj — Vice-director of the ISD Project

Kraków, April 2013

NOTE FROM THE EDITORS

Nowadays, in the begin of the XXIst century, the main obligation of scientists is to challenge requirements of modern-day technologies and to use accumulated basic knowledge to accelerate development of novel concepts in technology, industry and life sciences. Moreover, scientists themselves need to break a stereotype of being persons who only write on blackboards long lines of terribly looking equations or mix colourful liquids in fancy vessels just to stain their lab coats. During our research done within the framework of ISD Project we have used a lot of equations and vessels, but, in order to describe our contribution to the today's knowledge, the name „applied science" is perfectly on the spot. Presenting to the readers our scientific achievements we strongly believe that they will be useful for practical applications and that our PhD theses will become a good starting point for our future work. We work in different fields: computer science, catalysis, biophysics, nanoengineering, materials science, environmental research and development of the innovative electronics and this is reflected in the book. Therefore, we are convinced that everybody will find here something interesting for him or her — that is why we invite you to get acquainted with the results of our scientific work.

Have a good reading!

Marcin Perzanowski (Editor-in-chief)
Jarosław Pawłowski
Maciej Chrobak
Jakub Moroń

LIST OF PAPERS

Theoretical and Computational Physics and Chemistry

Nuclear Methods in Materials Science and Environmental Research

Modern Electronics for Physics Experiments

Physical Chemistry, Catalysis and Biophysics

THIN FILMS AND NANOSTRUCTURES

STRUCTURAL, MAGNETIC AND ELECTRONIC PROPERTIES OF CONDENSED MATTER

THEORETICAL AND COMPUTATIONAL PHYSICS AND CHEMISTRY

Structure and transport properties of colloidal multilayers

Piotr Batys

Jerzy Haber Institute of Catalysis and Surface Chemistry Polish Academy of Sciences, Niezapominajek 8, 30-239 Kraków, Poland

Supervisor: Paweł Weroński

We present computer simulation results of the layer by layer self-assembling process of colloidal particles. We have generated the multilayer structures of spherical particles according to a generalized model of random sequential adsorption of hard spheres. We have compared surface and transport properties of several multilayers of the same average thickness, obtained by adsorption of subsequent particle layers at various surface coverage. We have discussed how the thickness and roughness of multilayer changes with the number of adsorption cycles and surface coverage of subsequent particle layers. Additionally, we have characterized the film structure in terms of the porosity distribution in the direction perpendicular to the adsorption surface. Our results suggest that all the film characteristics strongly depend on the method of its preparation and can be controlled by manipulating the single-layer surface coverage or deposition time. The results can be useful for efficient designing multilayers with desired properties.

The surface roughness is a critical parameter in various fields of science and industry, such as producing high-quality optics, optical and anti-reflective coatings, controlling surface wettability, corrosion resistance, static and dynamic properties of solid surface, and tribology.[1] Molecular dynamics studies of liquid droplets in contact with self-affine fractal surfaces indicate that the contact angle of nanodroplets depends strongly on the root-mean-square (RMS) roughness amplitude but it is nearly independent of the fractal dimension of the surface.[2] A simple method for controlling the surface roughness is the deposition (irreversible adsorption) of colloidal particles on the surface.[3,4] Recent advances in the nanotechnology have made possible the production of functional colloidal materials with controlled surface and bulk properties, such as surface-activated, magnetic, conductive, biocompatible, fluorescent, hollow, or nanoporous particles, opening a big world for novel applications of multilayers. A common experimental method for fabricating a multilayer with certain characteristics is the layer by layer (LbL) technique, used originally by Iller.[5–7] It is based on the adsorption of consecutive layers by immersing the substrate alternately in suspensions of colloidal particles (or solutions of macromolecules) with positive and negative surface charges. The structure of multilayer obtained this way depends strongly on the number of adsorption cycles, amount of particles adsorbed in each cycle, and interactions in the system.[8] Also, the procedures for the LbL assembly are relatively simple and can be automated.

One of our main tools for a better understanding of the particle deposition mechanism is computer modeling of the process. The advantage of such modeling is that in addition to the global properties of the multilayer, we can also study its local properties, which play a major role in the mass transport, especially in heterogeneous systems. Thus, computer modeling can be a powerful tool in the study of structural and kinetic aspects of deposition of macromolecules, proteins, and colloidal particles.[9–12] Among a variety of possible approaches to modeling the localized particle deposition there is a class of models based on the random sequential adsorption (RSA) algorithm, appreciated for its simplicity and efficiency.[13] We can also extend the classical RSA model for the quantitative description of particle deposition in the LbL process.[9,10]

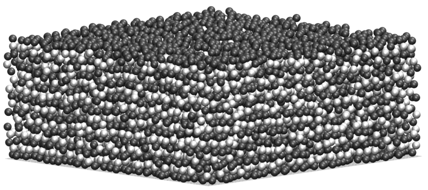

FIGURE 1: Topology of multilayer 5, obtained in Monte Carlo simulations.

We can then analyze the effect of various factors, such as the single layer surface coverage, on the resulting multilayer structure and the porosity distribution.

Multilayers of the same thickness, built from the same particles but in different ways, can vary considerably in their structures and surface properties. To see how these properties change with the single-layer surface coverage, we have simulated five multilayers at the five values of coverage: 0,10; 0,20; 0,30; 0,40; and 0,50. For each surface coverage we have chosen the total number of adsorption cycles in such a way to obtain approximately the same average multilayer thickness. In Table 1 we have collected the single-layer coverage Θ, number of cycles n, average multilayer thickness h and its standard deviation σ_h, average porosity ε_av, as well as the RMS roughness R_q of each of the five multilayers. For the sake of notation simplicity, we have normalized all dimensional parameters and variables by the particle radius, its square, or cube, to make them dimensionless.

As we can see in Table 1, the number of cycles decreases with the increase in the single-layer surface coverage. To obtain a multilayer with the average thickness of 30 particle radii, we need to adsorb 44 single layers with the coverage of 0,10 each, and only 17 layers with the coverage of 0,50. The standard deviation of the average thickness decreases dramatically with the increase in the coverage. For the multilayer 1 σ_h is about five particle radii while for the multilayer 5 the standard deviation is as small as 0,6. Multilayers generated at a higher coverage are more ordered and closer packed, as indicated by the average porosity, varying from 0,80 for the layer 1 to 0,62 for the layer 5. For the sake of illustration, in Fig. 1 we have presented the topology of the multilayer 5. It is interesting to notice that the layered nature of the structure of the multilayer formed at the high surface coverage of $\Theta = 0{,}50$ can be observed.

TABLE 1: Single-layer surface coverage, number of adsorption cycles, average thickness and its standard deviation, average porosity, and RMS roughness of simulated multilayers.

No.	Θ	n	h	σ_h	ε_av	R_q
1	0,10	44	30,0	5,0	0,80	6,2
2	0,20	25	30,4	3,6	0,78	5,0
3	0,30	20	30,4	2,0	0,74	3,6
4	0,40	18	30,2	1,0	0,68	2,4
5	0,50	17	29,8	0,6	0,62	1,6

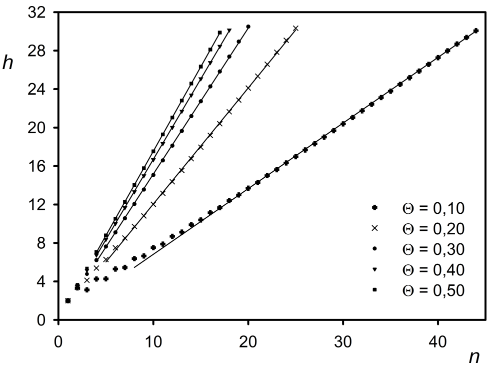

FIGURE 2: Average multilayer thickness as a function of layer number n, calculated for five values of single-layer coverage Θ. Solid lines denote linear fits.

The thickness and roughness of a thin film are important parameters that can be measured experimentally.[14,15] By means of such measurements we can experimentally verify our theoretical model. Fig. 2 presents the average thickness of multilayer as a function of the number of adsorption cycles, calculated for the five single-layer surface coverages. We can observe a direct proportionality between the thickness of each multilayer and the number of adsorbed layers, which is in a good agreement with the experimental results reported in the literature for self-assembled multilayer films of spherical particles.[14,16] The slope of these curves can be interpreted as an average thickness of a single layer of par-

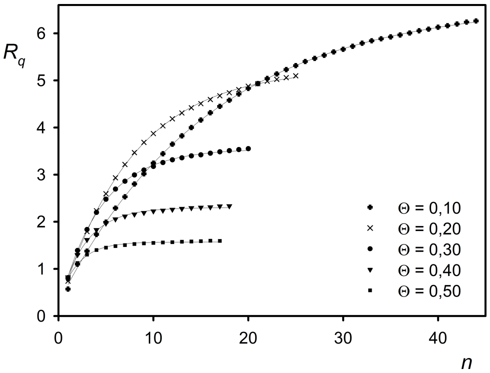

FIGURE 3: RMS roughness as a function of layer number n, calculated for five values of single-layer coverage Θ. Solid lines denote exponential fits.

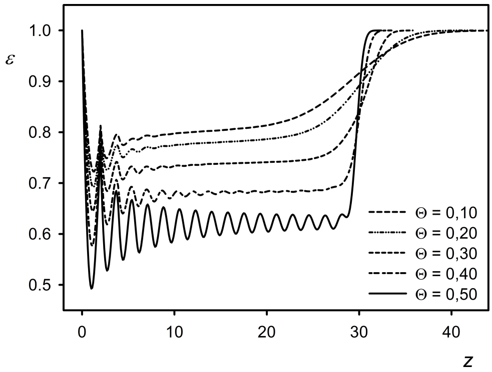

FIGURE 4: Porosity as a function of distance from adsorption surface calculated for five values of single-layer coverage Θ.

ticles adsorbed in the LbL process. It is interesting to notice that in the process of LbL assembly of hard, spherical, monodisperse particles the average single monolayer thickness cannot exceed the asymptotic value 1,868. In practice the slope m is even more limited because in real systems the single-layer coverage $\Theta < 1$. For instance, we have found that slope for the multilayer 5 at $\Theta = 0{,}50$ equals 1,7558. It is worth to mention that this value exceeds the thickness of the single layer in a hexagonally packed multilayer film, which is equal 1,73.

In Fig. 3 we present the RMS surface roughness as a function of the number n of adsorbed layers for the obtained multilayers. For each of them, the RMS roughness increases to an asymptotic value, in agreement with the experimental results.[14] We have found that the variation of the rougness can be described with a reasonable accuracy by a simple exponential relationship. A comparison of our theoretical results with those reported by Lee et al.[14] suggests that the theoretical RMS roughness calculated for $n = 20$ and $\Theta = 0,30$ is larger by about 50% than the experimental value obtained using the AFM method. This difference may result from a limited penetration depth of AFM tip.

The results presented in Fig. 3 indicate the ability of producing multilayers of the same roughness using different experimental protocols, to obtain various porosity, thickness, or other parameters. Thus, for instance, to obtain the roughness of about 3,5 we can adsorb either eight, eleven, or eighteen single layers with the coverage, respectively, 0,20; 0,10; or 0,30. In terms of the adsorption cycle number, using the coverage 0,20 is therefore the most effective way to produce a multilayer of the roughness 3,5. On the other hand, a comparison of the entire particle population of the 8-layer, 11-layer, and 18-layer suggests that the amount of consumed particles increases with Θ. Therefore, in terms of the particle volume, the experimental protocol efficiency decreases with the single layer coverage, making the use of $\Theta = 0{,}10$ the most efficient way to produce a multilayer of the same roughness.

The results presented in Fig. 4 gives us information about the variation of porosity and multilayer structure. As we see in Fig. 4, two effects at two different spatial scales can be observed in the systems. The first effect is the local short-range structure ordering manifested by decaying oscillations of the porosity. The second long-range variation of the function is more apparent for multilayers formed at a lower coverage. As we can notice in Fig. 4, the periodicity of the oscillations is roughly equal to the particle diameter, with a slight tendency to decrease with the single-layer coverage. The initial oscillation amplitude and decay rate depend stronger on the single-layer surface coverage: the initial amplitude decreases and the decay rate grows with the decrease in coverage. This is reflective of decreasing spatial correlations between the particles of subsequent layers and of decay of surface-induced layered structure with the decrease in Θ. The first minimum represents the particles of the first layer, adsorbed directly on the homogeneous adsorption surface at the well-defined distance $z = 1$. Particles of the next layer i, however, can adsorb on other type particles at a varying distance from the adsorption surface. The mean value of this distance has to be smaller than $2i - 1$. Its standard deviation, which is a measure of the surface-induced ordering, increases with the decrease in single-layer coverage, when a larger fraction of adsorbing particles can penetrate deeper into the multilayer. Therefore, the oscillations decay faster in multilayers formed at a lower coverage.

Our results suggest that the multilayer thickness is proportional to the number of adsorbed layers. The RMS roughness strongly depends on the method of multilayer preparation. It increases asymptotically with the number of adsorption cycles. The asymptotic value of roughness increases with the decrease of surface coverage. The linear character of the function $h(n)$, as well as the convergence of the function $R_\mathrm{q}(n)$ to its asymptotic limit are in a good agreement with experimental results. The obtained results allow for a better understanding of the structure and surface properties of colloidal multilayers obtained with LbL method. In particular, these results suggest that the determination of multilayer averaged parameters, such as the average thickness or porosity, might be insufficient to fully understand the behavior of the system. They may also be useful for developing catalysts and adsorbents with a precisely defined and highly developed surface. The generalized RSA simulation scheme applied in this work has proved to be an efficient tool for modeling of the formation of self-assembling particle films produced in LbL processes.

⋆ ⋆ ⋆

[1] Y. Y. Yan, N. Gao, W. Barthlott, *Adv. Colloid Interface Sci.* **169**, 80 (2011).

[2] C. Yang, U. Tartaglino, B. N. J. Persson, *Phys. Rev. Lett.* **97**, 116103 (2006).

[3] M. Ulmeanu, M. Zamfirescu, R. Medianu, *Colloids Surf. A* **338**, 87 (2009).

[4] P. M. Hansson, A. Swerin, J. Schoelkopf, P. A. C. Gane, E. Thormann, *Langmuir* **28**, 8026 (2012).

[5] R. K. Iller, *J. Colloid Interface Sci.* **21**, 569 (1966).

[6] G. Decher, *Science* **277**, 1232 (1997).

[7] K. Ariga, J. P. Hill, Q. Ji, *Phys. Chem. Chem. Phys.* **9**, 2319 (2007).

[8] P. Batys, P. Weroński, *J. Chem. Phys.* **137**, 214706 (2012)

[9] Z. Adamczyk, P. Weroński, J. Barbasz, M. Kolasińska, *Appl. Surf. Sci.* **253**, 5776 (2007).

[10] Z. Adamczyk, P. Weroński, J. Barbasz, *J. Colloid Interface Sci.* **317**, 1 (2008).

[11] G. Tarjus, P. Schaaf, J. Talbot, *J. Chem. Phys.* **93**, 8352 (1990).

[12] P. Weroński, *Adv. Colloid Interface Sci.* **118**, 1 (2005).

[13] E. L. Hinrichsen, J. Feder, T. Jossang, *J. Stat. Phys.* **44**, 793 (1986).

[14] D. Lee, M. F. Rubner, R. E. Cohen, *Nano Lett.* **6**, 2305 (2006).

[15] H. Shimomura, Z. Gemici, R. E. Cohen, M. F. Rubner, *ACS Appl. Mater. Interfaces* **2**, 813 (2010).

[16] M. Brust, D. Bethell, C. J. Kiely, D. J. Schiffrin, *Langmuir* **14**, 5425 (1998).

Calculations of the electrical resistivity of the monoatomic metallic layer

Artur Działo

Faculty of Physics and Applied Computer Science, AGH University of Science and Technology, Mickiewicza 30, 30-059 Kraków, Poland

Supervisor: Antoni Paja

In this paper we present new formula which describes the change of electrical resistivity with temperature of a mono-atomic metallic layer. We compared our results and those given by the Bloch-Grüneisen formula for bulk metals. According to our theory the calculated resistivity is significantly lower than this for a bulk material.

In recent decades nanotechnology has contributed largely in various fields including electronics, material science, chemistry and biology. There is no doubt that conductivity (or resistivity) of bulk metallic materials should in apparent way differ from that of materials downsized to nanoscale. That is why transport properties of charge and spin in such systems have been the field of interests for many scientists. First semiclassical approach to this problem was proposed by Fuchs[1] and Sondheimer[2] who explained the increase of resistivity with decrease of film thickness. Quantum size effects in thin metallic films with perfect surfaces were considered by Sandomirskii.[3] Later work by Ashcroft and Trivedi[4] extended the problem by including discreteness of the energy levels, effects of impurity potentials and surface roughness.

In this article we include the influence of the temperature on electronic transport properties by considering a single mono-atomic metallic layer through which a two-dimensional electron gas is moving. Charge motion is disturbed by interactions with crystal thermal lattice vibrations, i.e. phonons. Our model presented here is strictly two-dimensional therefore we replace Fermi/Debye sphere with Fermi/Debye circle so that every electron/phonon wave vector lies in a plane within the circle. For this reason we do not use additional symbols for k, q, etc. but we keep in mind that our system is two-dimensional.

The variational expression for the electrical resistivity given by Ziman[7] is:

$$\rho_L = \frac{\frac{1}{k_\mathrm{B}T}\iiint\{\phi_k - \phi_{k'}\}^2 \mathcal{P}_{k,q}^{k'}\, d\vec{k}\; d\vec{k}'\; d\vec{q}}{\left|\int e\vec{v}_k\phi_k \frac{\partial f_k^0}{\partial \mathcal{E}_k} d\vec{k}\right|^2}\ , \quad (1)$$

where $\vec{k}, \vec{k}'$ — electron wave vectors before and after scattering, respectively, $\vec{q}$ — phonon wave vector, k_B — the Boltzmann constant, T — temperature, ϕ_k — deviation from equilibrium of the electron distribution function, $\mathcal{P}_{k,q}^{k'}$ — transition probability from the state $\vec{k}$ to the state $\vec{k}'$ due to electron-phonon interaction, e — electron charge, $\vec{v}_k$ — electron group velocity, f_k^0 — electron distribution function, ε_k — electron energy.

We assume that the phonon system is in thermal equilibrium so that for phonon distribution function $\phi_q = 0$. Choice of the ϕ_k function is not crucial and for our calculation we shall use the standard trial function

$$\phi_k = \vec{k}\cdot\vec{u}\ , \quad (2)$$

where $\vec{u}$ — unit vector in the direction of external field.

The denominator is then given by:

$$\left|\int e\vec{v}_k\phi_k \frac{\partial f_k^0}{\partial \mathcal{E}_k} d\vec{k}\right|^2 = \left(\frac{ek_\mathrm{F}\varsigma}{4\pi^2\hbar}\right)^2 , \quad (3)$$

where k_F — Fermi radius, ς — Fermi circle circumference.

Much more effort must be made to calculate the numerator. Because calculations are complex we shall walk trough them step by step.

The transition probability due to electron-phonon interaction is

$$\mathcal{P}^{k'}_{k,q} = \left(\frac{\pi}{mN_{\mathrm{A}}\omega}\right)\delta_{g,k'-k-q}|\mathcal{F}_{q,p}(\vec{k},\vec{k}')|^2 \times$$
$$\times \mathcal{O}(\varepsilon_k + \hbar\omega - \varepsilon_{k'})n^0_q f^0_k(1-f^0_{k'}) \ , \quad (4)$$

where m — ion mass, N_{A} — number of unit cells per unit area, n^0_q — phonon occupation number, $\vec{g}$ — reciprocal lattice vector, p — polarization of the phonon, $\hbar\omega$ — is the phonon energy and $\mathcal{O}$ is Landau symbol.
For longitudinal phonons we find the $\mathcal{F}_{q,p}(k,k')$ function to be

$$\mathcal{F}_{q,p}(\vec{k},\vec{k}') = \vec{e}_{q,p}\cdot(\vec{k}'-\vec{k})\cdot\ell(|\vec{k}'-\vec{k}|) \ , \quad (5)$$

where $\vec{e}_{q,p}$ is the polarization vector of the phonon and $\ell(K)$ is a quantity which has the dimension of energy and depends on the magnitude of the scattering vector

$$\vec{K} = \vec{k}' - \vec{k} \ . \quad (6)$$

Putting all this together we can write down the variational integral

$$\frac{\pi}{k_{\mathrm{B}}TmN_{\mathrm{A}}\omega}\iiint(\vec{K}\cdot\vec{u})^2(\vec{K}\cdot\vec{e})^2 \times$$
$$\times \ell^2(K)f^0_k(1-f^0_{k'})n^0_q\mathcal{O}(\varepsilon_k+\hbar\omega-\varepsilon_{k'}) \times$$
$$\times \delta_{g,k'-k-q}d\vec{k}\ d\vec{k}'\ d\vec{q} \ . \quad (7)$$

Using the same simplifying method as Ziman[7] we obtain the following equation for electrical resistivity

$$\rho_{\mathrm{L}} = \frac{2\hbar\pi}{e^2mN_{\mathrm{A}}k_{\mathrm{B}}T}\ \frac{1}{{k_{\mathrm{F}}}^2\varsigma^2} \times$$
$$\times \iint \frac{(\vec{K}\cdot\vec{u})^2(\vec{K}\cdot\vec{e})^2\ell^2(K)}{(1-e^{-\hbar\omega/k_{\mathrm{B}}T})(e^{\hbar\omega/k_{\mathrm{B}}T}-1)}\ \frac{d\varsigma}{v}\ \frac{d\varsigma'}{v'} \ . \quad (8)$$

Following Ziman[7] we assume that N-processes are the only scattering processes taking place. For this processes the polarisation vector $\vec{e}$ is parallel to $\vec{q}$, which then equals $\vec{K}$. We can write that

$$(\vec{K}\cdot\vec{e})^2 = K^2 = q^2 \ , \quad (9)$$

and thanks to system symmetry

$$(\vec{K}\cdot\vec{u})^2 = \frac{1}{2}K^2 = \frac{1}{2}q^2 \ , \quad (10)$$

we calculate the resistivity ρ_{L} given by the Eq. (8) changing the variables in the first integral over $d\varsigma$ to $k_{\mathrm{F}}d\phi$ where ϕ is the angle between $\vec{k}$ and $\vec{k}'$ vectors and doing the integral over $d\varsigma'$ which is immediate and equals to ς

$$\rho_{\mathrm{L}} = \frac{\pi\hbar}{e^2mN_{\mathrm{A}}k_{\mathrm{B}}T}\ \frac{1}{{k_{\mathrm{F}}}^2{v^2}_{\mathrm{F}}}\ \frac{1}{\varsigma} \times$$
$$\times \int \frac{q^4\ \ell^2(q)\ k_{\mathrm{F}}d\phi}{(1-e^{-\hbar\omega/k_{\mathrm{B}}T})(e^{\hbar\omega/k_{\mathrm{B}}T}-1)} \ . \quad (11)$$

To accomplish the calculations, all we need is to find $k_{\mathrm{F}}d\phi$ expressed by the scattering vector q. This can be done by using the law of cosines in the form:

$$q^2 = k'^2 + k^2 - 2k'k\cos\phi \quad \Longrightarrow$$
$$\Longrightarrow \quad q\ dq = {k_{\mathrm{F}}}^2\sin\phi d\phi$$
$$q^2 = k'^2 + k^2 - 2k'k\cos\phi \quad \Longrightarrow$$
$$\Longrightarrow \quad \cos\phi = 1 - \frac{q^2}{2{k_{\mathrm{F}}}^2} \ . \quad (12)$$

Finally the equation describing the resistivity of an ideal two dimensional metallic system is:

$$\rho_{\mathrm{L}} = \frac{\hbar}{2e^2mN_{\mathrm{A}}k_{\mathrm{B}}T{k_{\mathrm{F}}}^4{v^2}_{\mathrm{F}}} \times$$
$$\times \int_0^D \frac{1}{\sqrt{1-\left(1-\frac{q^2}{2{k_{\mathrm{F}}}^2}\right)^2}} \times$$
$$\times \frac{q^5\ell^2(q)dq}{\left(1-e^{-\hbar\omega/k_{\mathrm{B}}T}\right)\left(e^{\hbar\omega/k_{\mathrm{B}}T}-1\right)} \ , \quad (13)$$

where D — is the Debye radius in two dimensions, $\ell(q) = n/N(\varepsilon_{\mathrm{F}})$ where $N(\varepsilon_{\mathrm{F}})$ — density of electron levels at the Fermi surface and $\omega = \omega(q)$.
For comparison, below we write the Bloch-Grüneisen formula for the electrical resistivity

which we mentioned in introduction

$$\rho_{\mathrm{L}} = \frac{3\pi\hbar}{4e^2 mNk_{\mathrm{B}}Tk_{\mathrm{F}}{}^4 v^2{}_{\mathrm{F}}} \times$$

$$\times \int_0^D \frac{q^5 \ell^2(q)dq}{\left(1 - e^{-\hbar\omega/k_{\mathrm{B}}T}\right)\left(e^{\hbar\omega/k_{\mathrm{B}}T} - 1\right)} \;, \tag{14}$$

where N is the number of unit cells per unit volume.
There is another matter which should be thoroughly considered. The real phonon dispersion relation, $\omega(q)$, is not linear and the actual form of this dispersion relation is

$$\omega(q) = \omega_0 \sin\left(\frac{qa}{2}\right) \;, \tag{15}$$

where ω_0 — characteristic frequency, a — the lattice constant.
However the Eq. (15) gives too large values of the sound velocity. Therefore we do not use the real dispersion relation but we assume the linear one

$$\omega(q) = \frac{k_{\mathrm{B}}\theta}{\hbar D}\, q \;, \tag{16}$$

where θ is the Debye temperature. This formula gives the sound velocity close to the experimental values.

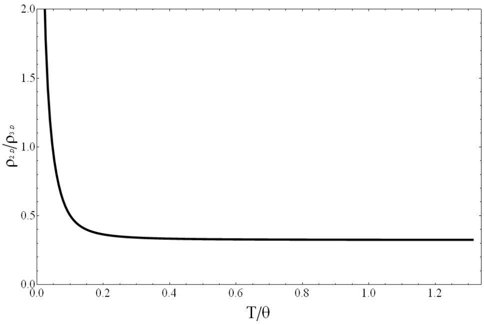

FIGURE 1: The relative resistivity $\rho_{2\mathrm{D}}/\rho_{3\mathrm{D}}$ (symbols explained in the text) vs. reduced temperature T/θ where θ is the Debye temperature.

We carried out the calculations of the resistivity in the range of temperature from $T = 0{,}04\ \theta$ to $T = 1{,}4\ \theta$, where θ is the Debye temperature (the numerical results of the investigated quantities did not significantly change for higher temperatures). We calculated the ratio of the 2D resistivity $\rho_{2\mathrm{D}}$ to the 3D resistivity $\rho_{3\mathrm{D}}$, given by the Bloch-Grüneisen formula in order to show the influence of dimensionality on the resistivity. We used the linear dispersion relation in both cases. The result is shown in Fig. 1. Of course the two-dimensional resistivity and three-dimensional one have different units. To make the ratio dimensionless we need to multiply two-dimensional resistivity by the lattice constant a. We can see that in a wide range of temperatures the resistivity of a mono-layer is about 0,3 of that of the bulk sample. It can be explained in a simple way: the charge carriers in 2D space have less final states to scatter thus the current is less damped. However, for very low temperatures we obtained the unexpected result: below $T = 0{,}2\ \theta$ the 2D resistivity rises up and becomes greater than 3D one below $0{,}05\ \theta$. It can be explained in this way: for very low temperatures the exponent $\hbar\omega/k_{\mathrm{B}}T$ is large and we can approximate the part of the function under the integral in Eqs. (13) and (14) which is dependent on temperature by $\exp(-\hbar\omega/k_{\mathrm{B}}T)$. On the other hand, this factor is equal to $\exp(-\theta q/TD)$. It resembles the well-known fact that at low temperatures the phonons of small q's give main contribution to electron scattering. This contribution is essentially greater in our 2D model because of the square root expression in the denominator.

We have investigated the influence of temperature on the electrical resistivity of a two-dimensional metallic layer. The electrical resistivity of such system is smaller than the resistivity of a bulk material in a wide range of temperatures and exceeds the bulk resistivity at very low temperatures. Both effects can be explained by the fact of low dimensionality of the considered sample. Our model is strictly two-dimensional and is difficult for experimental verification however it can be used for a semi-quantitative analysis of the samples strongly reduced in one dimension. Therefore our next goal is to investigate how the resistivity changes with temperature for film thickness greater than one atomic layer.

This work has been partly supported by the EU Human Capital Operation Program, Polish Project No. POKL.04.01.01-00-434/08-02. It was also partially supported by the Polish Ministry of Science and Higher Education and its grants for Scientific Research.

⋆ ⋆ ⋆

[1] K. Fuchs, *Math. Proc. Cambridge* **34**, 100 (1938).

[2] E. H. Sondheimer, *Adv. Phys.* **1**, 1 (1952).

[3] V. B. Sandomirskii, *J. Exp. Theor. Phys.* **52**, 158 (1967).

[4] N. W. Ashcroft, Nandini Trivedi, *Phys. Rev. B* **38**, 17 (1988).

[5] F. Bloch, *Z. Phys.* **58**, 555 (1929).

[6] F. Bloch, *Z. Phys.* **59**, 208 (1930).

[7] J. M. Ziman, Electrons and Phonons, (Oxford at the Clarendon Press, 1960).

Description of the mechanical properties of bone based on the models of composite materials

Krzysztof Janc

Faculty of Physics and Applied Computer Science, AGH University of Science and Technology, Mickiewicza 30, 30-059 Kraków, Poland

Supervisors: Jacek Tarasiuk†, Paul Lipinski‡
† AGH University of Science and Technology, Kraków, Poland
‡ Ecole Nationale d'Ingénieurs de Metz, Metz Cedex, France

This work presents the use of models averaging the mechanical properties of composite materials with ellipsoidal inclusions in order to model the elastic properties of cancellous bone tissue. In this approach, to calculate, an incremental model is used and the bone is treated as a composite material where the bone matrix is assumed as ellipsoidal inclusions. Then, using genetic algorithms one searches for an appropriate distribution of inclusions for which the effective mechanical properties are as consistent as possible with the results obtained by FEM.

Let the volume V being Representative Volume Element (RVE), [1,2] which was separated from a particular material, consist of N ellipsoidal inclusions, which we will denote by a superscript I from 1 to N. Let each of the inclusions have the volume labeled V^I and tensor c^I defining its mechanical properties. In such case the rest of the volume will be the matrix, labeled with the index 0, so the volume of the matrix will be denoted as V^0 , and its mechanical properties by c^0 . With so defined conditions we can determine the values of the strain of inclusions ε^I in the function of local strain [2,3] $\varepsilon(x)$

$$\varepsilon(x) = \frac{1}{V^I}\int_{V^I} \varepsilon(x) dV \ . \tag{1}$$

$\varepsilon(x)$ according to Eshelby's solution [4] is equal:

$$\begin{aligned}\varepsilon(x) =& E^{\mathrm{r}} - \\ & - \sum_{J=0}^{N} \int_V \mathit{\Gamma}(x-x')dV' : \Delta c^J : \varepsilon^J \ ,\end{aligned} \tag{2}$$

where $\mathit{\Gamma}(x-x')$ is so-called modified Green tensor. Substituting from (1) to the expression (2) we obtain:

$$\begin{aligned}\varepsilon(x) = & E^{\mathrm{r}} - \\ - & \int_{V^I}\int_{V^J} \mathit{\Gamma}(x-x')dVdV : \Delta c^J : \varepsilon^J \ .\end{aligned} \tag{3}$$

Now we can define so-called interaction tensor, which has the following form

$$T^{IJ} = \int_{V^I}\int_{V^J} \mathit{\Gamma}(x-x')dVdV \ . \tag{4}$$

This tensor describes the mutual interaction between inclusions. Returning to the expression (3) describing the strain of the inlcusion ε^I, we can now write is as follows:

$$\varepsilon(x) = E^{\mathrm{r}} - \sum_{J=0}^{N} T^{IJ} : \Delta c^J : \varepsilon^J \ . \tag{5}$$

Basing on the Eq. (3) we substitute instead of the strain of the inclusions ε^I and ε^J the expressions $a^I\!:\!E^{\mathrm{r}}$ and $a^J\!:\!E^{\mathrm{r}}$ and we obtain:

$$a^I : E^{\mathrm{r}} = E^{\mathrm{r}} - \sum_{J=0}^{N} T^{IJ} : \Delta c^J : a^J : E^{\mathrm{r}} \ , \tag{6}$$

after removing E^r from the equation and extracting from the sum $\sum_{J=0}^{N} T^{IJ} : \Delta c^J : a^J$ fragment of the equation with a^I we obtain:

$$\begin{aligned} a^I = & \left(\mathbf{I} - T^{II} : \Delta c^I\right)^{-1} : \\ & : \left(\mathbf{I} - \sum_{J=0, J\neq I}^{N} T^{IJ} : \Delta c^J : a^J\right)\end{aligned} \tag{7}$$

for the final determination of the value of the tensor a^I we use the following incremental formula. As the initial values of the tensors a^I

one can assume $(a^I)=\left(\mathbf{I}-T^{II}:\Delta c^I\right)^{-1}$

$$(a^I)_{i+1}=\left(\mathbf{I}-T^{II}:\Delta c^I\right)^{-1}: \\ :\left(\mathbf{I}-\sum_{J=0,J\neq I}^{N}T^{IJ}:\Delta c^J:(a^J)_i\right) . \tag{8}$$

A difficulty in the final determining the solution is the impossibility of calculating tensors T^{0I} and T^{I0} because the matrix is not an ellipsoidal inclusion. If we assume as a reference medium the mechanical properties of the matrices:

$$C^r=c^0\rightarrow\Delta c^0=c^0-C^r=0\ , \tag{9}$$

we will obtain Mori-Tanaka model. Accepting the above assumption, the value of the strain of inclusion ε^I according to the Eq. (5) takes the form

$$\varepsilon(x)=E^0-\sum_{J=1}^{N}T^{IJ}:\Delta c^J:\varepsilon^J\ , \tag{10}$$

where $I=1,\ldots,N$ and E^0 is the strain of homogenous RVE with properties of the matrix. In such a form the expression does not depend on tensor T^{I0}, because the element $T^{I0}:\Delta c^0:\varepsilon^0$ is equal zero. We are not able to calculate the value of the tensor T^{0I}, that is why we accepted indexing starting from 1. To determine effective mechanical properties of the composite material according to the formula (11) we need to know all the values of the tensor A^I

$$C^{\text{eff}}=\frac{1}{V}\int_V c(x):A(x)dV\ , \tag{11}$$

and because of this according to the relation $A(x)=a(x):\langle a\rangle^{-1}$ also all the values of tensors a^I. Because the relation (8) enables us to calculate directly the values of tensor a^0, we have to refer to the definition of tensor $a(x)$ (5) and assume that $E^0\cong\varepsilon^0$:

$$\varepsilon^0=a^0:E^r=a^0:E^0\rightarrow a^0=\mathbf{I}\ . \tag{12}$$

Defining the volume fraction of the inclusion I as $f^I=V^I/V$ where V^I the volume of the inclusion, V is the volume RVE, we can now write the value for the tensor averaged by $\langle a\rangle$ volume in the form of

$$\langle a\rangle=\frac{1}{V}\int_V a(x)dV=\sum_{J=0}^{N}f^Ia^I \tag{13}$$

according to the definition the value of the tensor A^0 is equal $A^0=a^0:\langle a\rangle^{-1}=\langle a\rangle^{-1}$ on the basis of the above equation the value of the localization tensor A^I can be expressed as follows

$$A^I=a^I:\langle a\rangle^{-1}=a^I:A^0\ . \tag{14}$$

Now knowing all the values of tensors A^I we can calculate the averaged mechanical properties of the inhomogenous material. Finally the formula for effective properties C^{GMT} according to the formula (11) has the form

$$C^{\text{GMT}}=\left\langle c^I:A^I\right\rangle=\left(\sum_{I=0}^{N}f^Ic^I:a^I\right):A^0\ . \tag{15}$$

Quite a serious problem of the presented models is the fact that they were built on on the assumption that the inclusions are immersed in the infinite medium, and in reality RVE have limited dimensions. To get a more accurate solution for the larger fraction, the incremental model has been proposed, which involves dividing the volume of the inclusions into smaller parts and slowly places them in a matrix (see Fig. 1). In every step we calculate the average value of such material and we take the next step as a template. Value of the fraction of the laced inclusions is not constant, the following steps need to add a little more inclusion fraction, due to the fact that in the step s we need to get the material which is equal to the fraction of inclusions $s\Delta f$ but one has to remember that the put inclusions of the volume Δf_s we decrease the fraction of the matrix which has the inclusion fraction inside it $(s–1)\Delta f$ from the previous step. The formula for the value of inclusion fraction J which has to fit in the step s is equal:

$$\Delta f_s^J=\frac{\Delta f}{1-1\,(s-1)\,\Delta f}\frac{f^J}{f}=r_sf^J \tag{16}$$

for the convenience in the Eq. (16) coefficient r_s was introduced, which says what part of

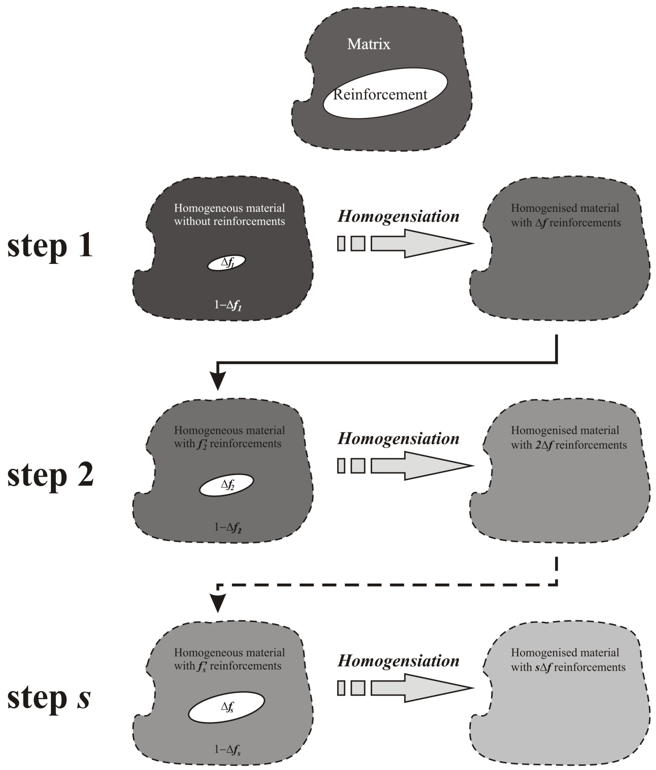

FIGURE 1: Construction of a homogeneous material using the Incremental Scheme idea.

fraction has to be inserted in step s. Coefficient r_s can be expressed in more friendly form:

$$r_s = \frac{1}{S - (s-1)\left(1 - f^0\right)} \ . \tag{17}$$

From the above equation it results that the first value r_s for the first step is equal $1/S$ and for the last one $1/\left(1 + f^0\left(S-1\right)\right)$. Finally the value of effective properties in the step s describes the following equation

$$C^{IS}_{s+1} = C^{IS}_{s} + r_s \sum_{I=0}^{N} f^I \mathit{\Delta} c^I_s : A^I_s \ . \tag{18}$$

The aim of this work is to verify whether with the presented model we can with quite good approximation model the mechanical properties of bone. In this approach as the elastic properties of the matrix are assumed the elastic properties of the bone (trabeculae), and as the inclusion – the void (the zero tensor). Another approximation is the assumption of isotropic properties of the matrix. Now the task comes to finding such parameters of the model so that it reflects the reality as good as possible. The model was compared with the results obtained using the finite element method, for two reasons: it is extremely difficult to determine fairly good and unambiguous mechanical properties using traditional mechanical measurements.

During tests, a cube with the dimensions 10 x 10 x 10 mm has been scanned with the computed microtomograph, then from the obtained numerical data a smaller fragment has been cut out 3 x 3 x 3 mm. basing on these data a secondary tetragonal grid of the FEM was generated. In the calculations we assumed that the Young's modulus of the matrix is equal 1000 MPa, and the Poisson's ratio is equal 0,3. Through a series of independent tests 3 Young's moduli, 3 shear moduli and 3 Poisson's ratios were determined. In addition, the porosity of the bone was calculated, too. Now we need to find the sizes, the volume fraction and mutual location of the ellipsoidal

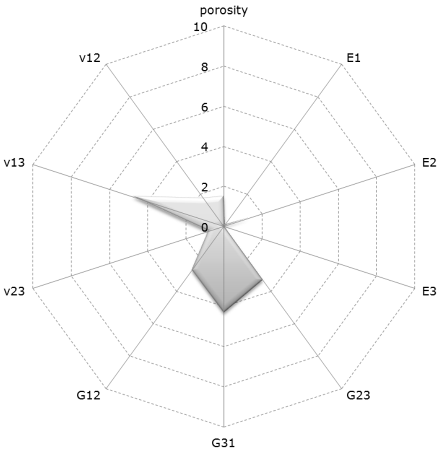

FIGURE 2: Distribution of the error depending on the parameters

inclusions, for which the results determined from the model averaging the properties, and porosity, were most similar to those obtained in FEM. We have assumed for four ellipsoids that we already get very good results. Since the model has many unknown input parameters, to determine them we used the genetic algorithm. Genetic algorithms belong to the group of non-deterministic algorithms, what means that for the same input parameters we obtain different suboptimal results, so the algorithm was run repeatedly. Ultimately, the smaller average error was obtained between the results from FEM, and from the model it was like $2 - 3$ percent. The Fig. 2 shows how the distribution of the error depending on the parameters was adjusted (for one of the runs of the algorithm) and Fig. 3 shows how look orientation ellipsoids inside matrix. Ultimately we managed to prove that, using the presented model, we are able to model the mechanical properties of bone with quite good approximation.

This work has been supported by the EU Human Capital Operation Program, Polish Project No. POKL.04.01.01-00-434/08-02.

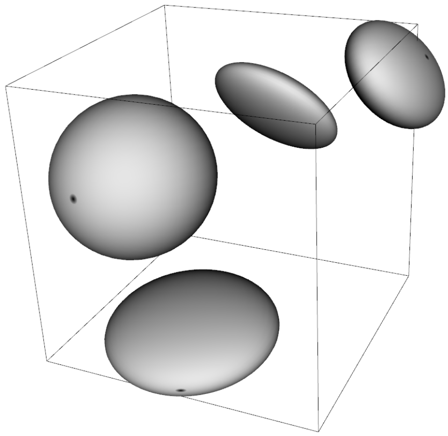

FIGURE 3: Matrix with ellipsoidal inclusions

⋆ ⋆ ⋆

[1] R. Hill, *J. Mech. Phys. Solids.* **16**, 357 (1963).

[2] T. Mura, Micromechanics of Defects in Solids (Martinus Nijhoff Publishers, The Hague, The Netherlands, 1987).

[3] D. Gross, T. Seelig, Fracture Mechanics with an Introduction to Micromechanics (Springer, Berlin, 2006).

[4] J. D. Eshelby, The determination of the elastic field of an ellipsoidal inclusion, and related problems, *Proceedings of the Royal Society of London*, 376 – 396 (1957).

[5] J. B. Aidun, T. G. Trucano C. S. Lo, R. M. Fye, Representative Volume Size: A Comparison of Statistical Continuum Mechanics and Statistical Physicis, *Sandia National Laboratories Report* (1999).

Electron transport properties calculation in alloys with Boltzmann approach.

Kamil Kutorasiński

Faculty of Physics and Applied Computer Science, AGH University of Science and Technology, Mickiewicza 30, 30-059 Kraków, Poland

Supervisor: Janusz Toboła

This work reports how using DFT based band structure calculations the temperature dependent electron transport properties can be determined. The Korringa-Kohn-Rostoker (KKR) method with coherent potential approximation (CPA) method is applied to calculate real and imaginary part of energy. The electronic structure combined with Boltzmann approach allow to calculate transport coefficients such as electrical conductivity, Seebeck coefficient and electronic thermal conductivity. Application of this methodology is presented for example of very promising thermoelectric semiconductor, doped $Mg_2Si_{1-x}Sn_x$. All electron transport quantities calculated in function of temperature and carrier concentration are compared with experimental data and satisfying agreement is found.

One of the best and most consistent theory of charge and heat transport in solid state is based on Boltzmann transport equation. Assuming that electron described, by wave package, behaves classically (semiclassical approximation) and using relaxation time approximation,[1–3] formulas for transport coefficients can be derived in consistent way in tensor form:

$$\begin{aligned} \boldsymbol{\sigma}_e &= \mathscr{L}^{(0)}, \\ \boldsymbol{S} &= -\frac{1}{eT}\frac{\mathscr{L}^{(1)}}{\mathscr{L}^{(0)}}, \\ \boldsymbol{\kappa_e} &= \frac{\mathscr{L}^{(2)}}{e^2T} - \frac{\mathscr{L}^{(1)}\mathscr{L}^{(1)}}{e^2T\mathscr{L}^{(0)}}, \end{aligned} \tag{1}$$

where

$$\mathscr{L}^{(\alpha)} = \int d\mathscr{E}\left(-\frac{\partial f}{\partial \mathscr{E}}\right)(\mathscr{E}-\mu)^{\alpha}\boldsymbol{\sigma}(\mathscr{E}). \tag{2}$$

The $\boldsymbol{\sigma}(\mathscr{E})$ is called transport function and is the key quantity of calculation

$$\begin{aligned} \boldsymbol{\sigma}(\mathscr{E}) =& e^2\sum_n\int\frac{d\mathbf{k}}{4\pi^3}\tau_n(\mathbf{k}) \\ & \mathbf{v}_n(\mathbf{k})\otimes\mathbf{v}_n(\mathbf{k})\delta(\mathscr{E}-\mathscr{E}_n(\mathbf{k})), \end{aligned} \tag{3}$$

where $\mathbf{v}_n(\mathbf{k}) = 1/\hbar\nabla_k\mathscr{E}_n(\mathbf{k})$. Upper formula, after changing integration from volume to iso-energetic surface owing to formula

$$\int d\mathbf{k}\delta(\mathscr{E}-\mathscr{E}(\mathbf{k})) = \int_{S(\mathscr{E})}\frac{dS}{|\nabla_k\mathscr{E}_n(\mathbf{k})|} \tag{4}$$

and after taking into account that structure is three-dimension and regular (then Kronecker product $|\mathbf{v}\otimes\mathbf{v}| = 1/3\ \mathbf{v}^2$), can be write in more simple way

$$\sigma(\mathscr{E}) = \frac{e^2}{\hbar}\sum_n\int_{S_n(\mathscr{E})}\frac{dS}{4\pi^3}\tau(S_n(\mathscr{E}))|\mathbf{v}(S_n(\mathscr{E}))|. \tag{5}$$

Iso-energetic surface for $\mathscr{E} = \mathscr{E}_{\mathrm{F}}$ defines Fermi surface $S_n(\mathscr{E}_{\mathrm{F}})$.

Excluding life time of electron τ all needed information to obtain transport function is included in band structure $\mathscr{E}_n(\mathbf{k})$. Generally τ contains information of many scattering mechanisms e.g. scattering on acoustic and optical phonons, vacancies and charge impurities.[4–6] Accounting for all these phenomena into calculation is mostly impossible and models with some approximations have to be made. In this work three approximations for $\tau(\mathbf{k})$ were used:

1. Constant life time: $\tau_n(\mathbf{k}) = \tau_0$ most simple and common. τ_0 is taken as parameter.

2. Constant free path: $\tau_n(\mathbf{k}) = |\mathbf{v}_n(\mathbf{k})|/\lambda_0$. λ_0 is taken as parameter.
3. Constant life time with included disorder scattering: $\tau_n(\mathbf{k}) = (\tau_{\mathrm{CPA}}(\mathbf{k})^{-1} + \tau_0^{-1})^{-1}$ τ_0 is also treated as parameter.

Thanks to CPA[7,8] calculation scattering connected to chemical disorder (on position (0,0,0) see Fig. 1) can be included due to determination of the imaginary part of energy $\tau_{\mathrm{CPA}}(\mathbf{k}) = \hbar/\operatorname{Im}\mathscr{E}(\mathbf{k})$.

Important element of calculation is also a number of electrons in a system. This information is actually comprised in the chemical potential.

$$n + n_\mathrm{d} = \int d\mathscr{E} g(\mathscr{E}) \frac{1}{1 + e^{\frac{\mathscr{E}-\mu(T,n_\mathrm{d})}{k_\mathrm{B}T}}}, \qquad (6)$$

where $g(\mathscr{E})$ is the density of state (DOS) function

$$g(\mathscr{E}) = \int_{S(\mathscr{E})} \frac{dS}{4\pi^3} \frac{1}{|\nabla_k \mathscr{E}_n(\mathbf{k})|}. \qquad (7)$$

Concentration n_d is an additional concentration corresponding to small extra number of doped electrons (rigid-band model[9]).

The above-mentioned method was used to calculate transport coefficient of $Mg_2Si_{1-x}Sn_x$ for $x = 0{,}5$; 0,6 and 0,7 focusing on $x = 0{,}6$. Mg_2(Si-Sn) alloys are one of the best thermoelectric material widely investigated these days.[10–12] Doping in these series of compounds is realized mostly by Sb and Bi. It has face-centered cubic structure (space group $Fm\bar{3}m$) with Si or Sn atoms at position $(0, 0, 0)$ and Mg atom at position $(1/4, 1/4, 1/4)$ (see Fig. 1).

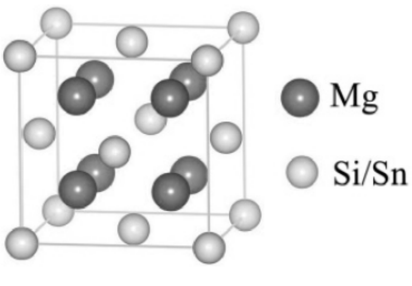

FIGURE 1: Crystal structure of Mg_2(Si-Sn) alloy.

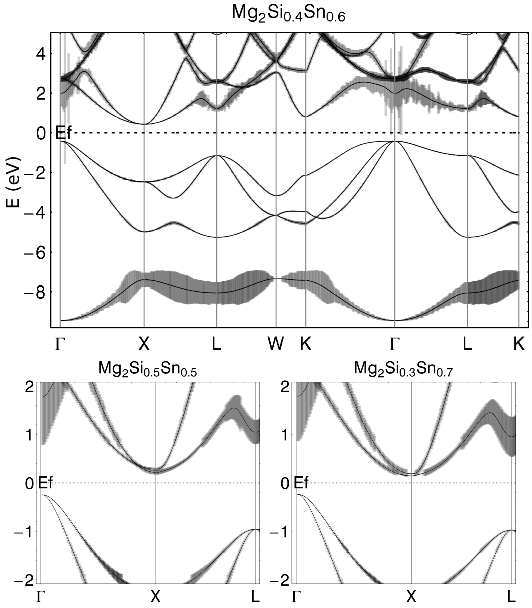

FIGURE 2: Band structure of $Mg_2Si_{0,4}Sn_{0,6}$ (up) in all energy window and direction. At bottom zoom at X point in Sn 50% and 70% compound.

Fig. 2 shows band structure of the $x = 0{,}6$ composition. Spread of band are proportional (extended 100 times) to imaginary part of energy and inversely related to electron's life time on specified bands. Indirect gap is equal

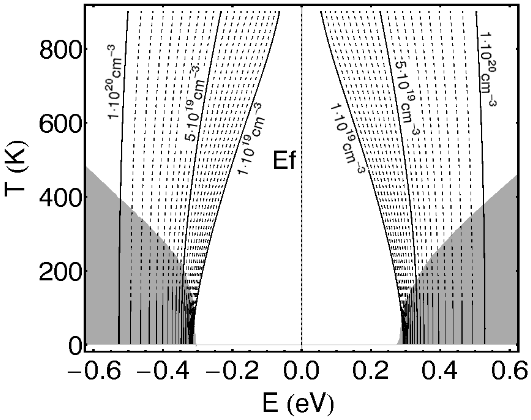

FIGURE 3: Chemical potential in function of temperature (*y*-*x* plot) for different p and n type carrier concentration. On background corresponding DOS i arbitrary units. Solid line marked 3 labelled concentration and the dashed line one with intermediate value of concentration.

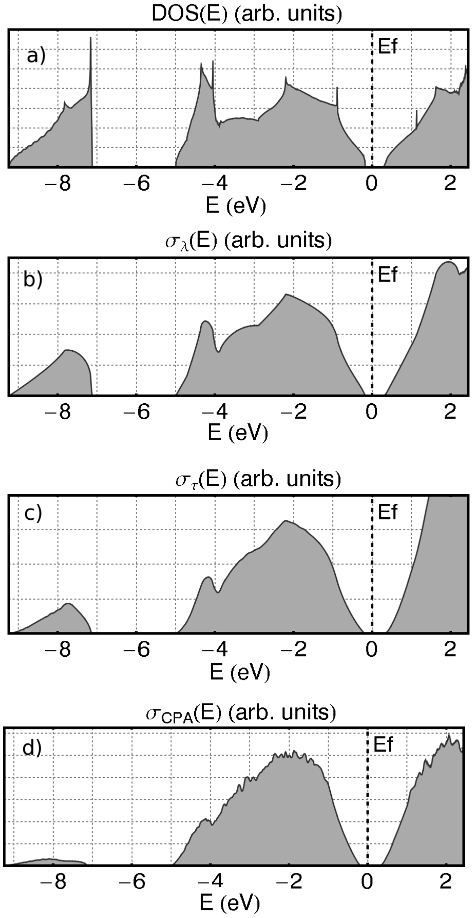

FIGURE 4: DOS (a) and three transport function (b-d) of $Mg_2Si_{0,4}Sn_{0,6}$.

$E_g = 0{,}65$ eV. At X-point two conduction bands degenerate (converge each other) when $x \sim 0{,}6$. Lower or higher amount of Sn removes the band degeneration and an energy split between the bands are as large as 67 meV ($x = 0{,}5$) and 44 meV ($x = 0{,}7$), respectively.

Chemical potential in function of temperature seen in Fig. 3 shows regular behavior. While temperature rises chemical potential moves to the center of energy gap (Fermi energy). It is worth to notice that integration in Eq. (6) is numerically hard to compute at low temperature ($T < 30$ K) and without applying highly accurate algorithm it may yield wrong values.

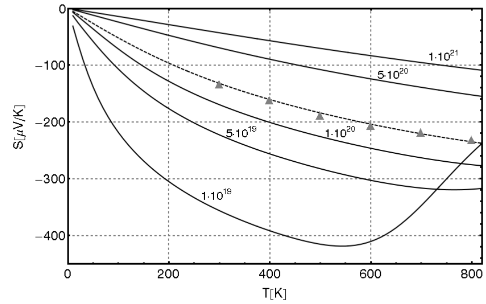

FIGURE 5: Seebeck coefficient of $Mg_2Si_{0,4}Sn_{0,6}$ in function of temperature for five different carrier concentrations (in cm^{-3}). Results for $n = 1{,}7 \cdot 10^{20}$ cm^{-3} are shown by a dashed line. Points represent experimental data measured on the sample with the same concentration.

Transport function and density of states calculated from band structure of $Mg_2Si_{0,4}Sn_{0,6}$ is shown in Fig. 4. In Fig. 4d parameter $\tau_0 = 20$ fs was used. Transport function in Figs. 4a – c are calculated with different approximations ($\tau =$ const., $\lambda =$ const., $\mu =$ const. and CPA). All these functions were obtained in resolution of 3,2 meV.

The calculated Seebeck coefficient with constant relaxation time approximation (Fig. 5) shows very good agreement with experiment.[12] Constant free path tends to underestimate Seebeck coefficient (not shown in this work). On other hand, including scattering on chemical disorder (lifetime from CPA approximation) does not alter noticeably Seebeck coefficient. Seebeck coefficient in Fig. 5 shows typical behaviour, i.e.

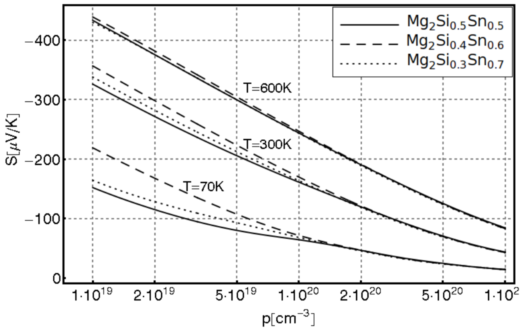

FIGURE 6: Seebeck coefficient of $Mg_2Si_{0,4}Sn_{0,6}$ in function of carrier concentration (in cm^{-3}) for 3 different temperature and 3 different Sn amount.

when temperature increases thermopower (in absolute value) also increases. At low concentration an exception from this behaviour is caused by influence of finite value of energy gap. Noteworthy, at low concentration and high temperature thermal excitation activates also carrier lying below the gap and the value of S decreases.

The Seebeck coefficient in function of concentration is presented in Fig. 6. It is seen that among all presented contents, $Mg_2Si_{0,4}Sn_{0,6}$ reaches the highest thermopower (in absolute value). This characteristic feature is seen mostly in low concentration and high temperature and results from the presence of band degeneracy at X-point. When Sn content is 50% and 70%, the band splitting between conduction bands substantially lowers the S value. The splitting is smaller in $Mg_2Si_{0,3}Sn_{0,7}$ then in $Mg_2Si_{0,5}Sn_{0,5}$ compound what confirms the feature. At higher concentration Fermi energy goes to higher energy and the influence of the splitting becomes hardly visible and results in similar thermopower values.

This work was supported by the EU Human Capital Operation Program, Polish Project No. POKL.04.01.01-00-434/08-02.

⋆ ⋆ ⋆

[1] N. W. Ashcroft, N. D. Mermin, Solid State Physics (Saunders, 1976).

[2] L. Chaput, P. Pécheur, J. Tobola, H. Scherrer, *Phys. Rev. B* **72**, 085126 (2005).

[3] J. M. Zimman, Principles of the Theory of Solids (Cambridge University Press, New York, 1964).

[4] Yu. I. Ravich, B. A. Efimov, V. I. Tamarchenko, *Phys. Status Solidi B* **41**, 11 (1971).

[5] Yu. I. Ravich, B. A. Efimov, I. A. Smirnov, Semiconducting Lead Chalcogenides (Plenum, New York, 1970).

[6] M. P. Singh, C. M. Bhandari, *Pramana J. Phys.* **62**, 1309 (2004).

[7] J. S. Faulkner, G. M. Stocks, *Phys. Rev. B* **21**, 3222 (1980).

[8] S. Kaprzyk, A. Bansil, *Phys. Rev. B* **26**, 367 (1982).

[9] G. Goran, *Phys. Kondens. Mater.* **14**, 101-104 (1972).

[10] W. Liu, Q. Zhang, *J. Electron. Mater.*, **40**, 1062 (2011).

[11] V. K. Zaitsev, K. J. Fedorov, *Phys. Rev. B* **74**, 045207 (2006).

[12] W. Liu, X. Tan, K. Yin, H. Liu, X. Tang, J. Shi, Q. Zhang, C. Uher, *Phys. Rev. Lett.* **108**, 166601 (2012).

Theoretical description of physicochemical properties of modified CuHPA: influence of Cu^{2+} position in Keggin anion

Piotr Niemiec

Jerzy Haber Institute of Catalysis and Surface Chemistry, Polish Academy of Sciences, Niezapominajek 8, 30-239 Krakow, Poland

Supervisor: Renata Tokarz-Sobieraj

Heteropolyacids (HPAs) systems exhibit a wide range of molecular sizes, compositions and architectures. Modification of those parameters leads to creation of a structure having diverse chemical and catalytic properties. In this paper, the theoretical description of electronic structure of heteropolyacids modified by copper ion (CuHPA) has been presented. The results showed that the Cu^{2+} cation introduced into the Keggin anion into the position of the central ion or addenda atom, influence the acid-base properties of the active centers present in the system. Modification of the structure leads also to the changes of redox properties of these systems.

Heteropolyacids belong to a group of compounds which due to their acid-base and redox properties are used in many catalytic processes, both homogeneous and heterogeneous.[1] The broad spectrum of reactions catalyzed by heteropolyacids is associated with specific properties of the studied system: structure mobility, thermal stability, solubility in organic and inorganic solvents, as well as simple recovery and recycling. HPAs catalysts are currently used in several industrial processes including selective oxidation, hydration of olefins, polymerisation of tetrahydrofuran.[2] All HPAs are complex protons that incorporate polyoxometalate anions having metal-oxygen octahedral as the basic structural units. The structure of HPA allows many different modifications of primary (change of the central ion, change of the type/number of the addenda atom(s)), secondary (change of the type and number of compensating cations) and tertiary (immobilization on various supports) structures providing an opportunity to tailor their catalytic properties.

The most frequently used heteropolyacids (HPA) in catalysis are Keggin type dodecaheteropolyacids[3] represented by the general formula $A_nXM_{12}O_{40}$. The central position of Keggin's anion occupies the fourth-coordinated central ion (X), which with four oxygen atoms, creates internal tetrahedron XO_4^{n-}. Tetrahedron is surrounded by twelve edge- and corner-sharing metal-oxygen octahedra MO_6. The octahedral are arranged in four M_3O_{13} groups.

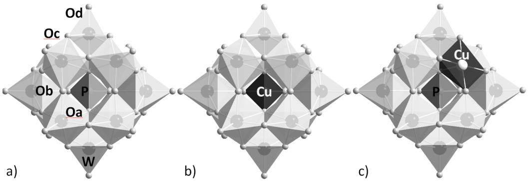

FIGURE 1: Geometric structure of Keggin polyanion: a) $PW_{12}O_{40}^{3-}$, b) $CuW_{12}O_{40}^{6-}$, c) $PW_{11}CuO_{39}^{5-}$.

In this paper, tungsten heteropolyacids, modified by copper ions, in which Cu^{2+} cation was introduced in the position of central ion $CuW_{12}O_{40}^{6-}$ (CuW) or in the position of one addenda atom $PW_{11}CuO_{39}^{5-}$ (PWCu) are presented (see Fig. 1b and 1c respectively). As a reference system typical Keggin's anion $PW_{12}O_{40}^{3-}$ (PW), with P atom in 40 position of central ion and W addenda atoms was used (see Fig. 1a).

Electronic structure of modified CuHPA were carried out within the DFT approach with cluster model, using Turbomole code.[4] Electron exchange and correlation have been

TABLE 1: Charges from Mulliken Population analysis, Wiberg Bond Indices and the energy of frontier orbitals [eV].

	$PW_{12}O_{40}^{3-}$	$CuW_{12}O_{40}^{6-}$	$PW_{11}CuO_{39}^{5-}$
	Charges (Mulliken population)		
P/Cu; W; Cu	1,14; 1,68; –	1,82; 1,63; –	1,12; 1,64; 0,46
Oa	−0,70	−1,15	−0,70 (−0,65)[a]
Ob	−0,69	−0,69	−0,70 (−0,51)[a]
Oc	−0,63	−0,63	−0,66 (−0,50)[a]
Od	−0,48	−0,58	−0,57
	Wiberg Bond Indices		
P/Cu−Oa−W; P−Oa−Cu	1,14/0,11; –	0,04/0,29; –	–; 1,21/0,11
W−Ob−W; W−Ob−Cu	0,81/0,81; –	1,15/1,15; –	0,79/0,79; 1,35/0,45
W−Oc−W; W−Oc−Cu	0,86/0,86; –	0,60/0,60; –	0,84/0,84; 1,38/0,44
W=Od	1,87	1,85	1,80
	Energy of frontier orbitals [eV]		
HOMO/LUMO	−6,89/ −4,33	−4,62/ −4,43	−5,61/ −4,58

[a]centers directly coordinated with Cu^{2+}.

described by gradient corrected functional using the revised Perdew-Burke approach[5] combined with TZVP basis sets.[6] Optimized geometries, densities of states, Mulliken population analyses,[7] bond orders[8] as well as the character and energy of boundary orbitals were determined. The solvation effect was taken into account within COSMO approximation (COnductorlike Screening MOdel).[4]

In the Keggin's anion both: oxygen and metallic centers are presented. There are four types of oxygen atoms: four oxygen atoms of the central tetrahedron (Oa), twelve oxygen atoms that bridge two addenda atoms not sharing a central oxygen atom (Ob), twelve oxygen atoms that bridge two addenda atoms sharing the same central oxygen atom (Oc) and twelve terminal oxygen atoms (Od) associated with a single addenda atom.

The acid-base properties of the active centers were estimated by charge analysis. Table 1 summarizes charges on active centers obtained from Mulliken population analysis. The results of the population analysis show that atomic charges on oxygen atoms (Oa–c) and metal (W, Cu) centers are far from the formal oxidation states indicating mixed ionic covalent nature of the metal-oxygen bonds in Keggin anion. Results of calculations show that Cu^{2+} ion introduced into the Keggin's anion has different charge, depending on the position which it occupies in the structure. As a tetra-coordinated central ion, the charge on Cu^{2+} ion equals 1,82 and is substantially higher than charge on P (equal 1,14) in the reference system. In the position of addenda atom, surrounded by five oxygen ions, the charge of Cu^{2+} is much lower, and equals 0,46. As a central ion Cu^{2+} influences only closely localized oxygen atoms, Oa, which charge, in comparison with the reference system PW, increases about 0,45. The charge on bridging oxygens Ob,c and on addenda atoms (W) stays nearly unchanged. Results of calculations for modified HPA in which one addenda atom was substituted by Cu, show that atom influences the nucleophilic character mostly of bridging oxygen atoms coordinated to introduced element. Results of population analysis show decrease of acidic character of oxygen atoms coordinated with Cu (values for the charges can be found in parentheses in Table 1). In both modified systems, CuW and PWCu, a slight increase in nucleophilic character of oxygen atoms, Od, (singly-coordinated with metal center) is observed.

The parameter which allows to describe the the ionic-covalent character of the bonds is the bond order. Results of Wiberg anal-

TABLE 2: Compositions of frontier orbitlas [%].

	$PW_{12}O_{40}^{3-}$		$CuW_{12}O_{40}^{6-}$		$PW_{11}CuO_{39}^{5-}$	
	HOMO	LUMO	HOMO	LUMO	HOMO	LUMO
P/Cu	0	0	**59,37**	**54,93**	0,03	0,01
Oa	0,01	0,01	**27,00**	**30,51**	0,39	0,10
W; Cu	0,84	**74,72**	2,95; –	3,32; –	**6,65**; **36,68**	**9,78**; **54,18**
Ob	**47,26**	**11,92**	0,99	1,13	**20,15**	**13,32**
Oc	**50,88**	**13,22**	6,59	7,46	**27,84**	**17,33**
Od	1,01	0,13	3,10	2,65	8,26	5,28

ysis (shown in Table 1) suggest that introducing copper into the central ion position causes differentiation of the bridging oxygen-addenda atom bonds. Bond order of oxygen atoms connecting triads increases (bond order W – Ob – W equals 1,15) in result of decreasing of bond orders within the triads (bond order W – Oc – W equals 0,60). The character of interactions between internal tetrahedron and the rest of an Keggin anion also changes. In the reference system PW, strong, single bond P – Oa (bond order 1,14) and weak interaction Oa – W (bond order 0,11) can be observed. When Cu ion is introduced into the position of the central ion, copper ion does not interact with surrounding oxygen atoms Oa, nevertheless, the bond order of these oxygen atoms with the rest of the ion (defined through Oa – W interaction) is the highest from all of the investigated systems and equals 0,29. Influence of copper, in the position of addenda atoms, on P – Oa and W – O – W bonds presented in PWCu system is negligible. At the same time, strong differentiation of W – Ob, c – Cu bonds can be noticed. The Wiberg bond indices suggests the strong covalent W – Ob, c bond (bond order equals 1,35 for W – Ob and 1,38 for W – Oc) and weak interaction Ob, c – Cu (bond order close to 0,45).

Total and partial density of states enables additional analysis of active centers. Density of states obtained from the theoretical calculations for the PW, CuW, PWCu systems respectively, are shown in Fig. 2a – c. In the reference system (PW) whole area of valence band is dominated by the 2*p*-orbitals of bridging (Ob,c) oxygen atoms with small amount of 5*d* tungsten orbitals, in the central part of the band. The contribution of central ion orbitals, in the bands near the Fermi level, is negligible. On the other hand, the conduction band exhibits metallic character and follows mainly from 5*d* orbitals of addenda atoms (W) with small amount of oxygen 2*p*-orbitals (mainly, bridging Ob,c oxygen atoms). The change of P for Cu atom in the position of central ion in the CuW system results in emergence of additional peaks between valence and conduction band. These peaks are dominated mainly by 3*d* Cu orbitals with addition of 2*p*-orbitals of terminal, Oa, oxygen atoms. The character of the main valence and conduction band stays almost the same as the character of bands in the reference PW system. Similar changes (in the form of emergence of additional bands consisting of Cu orbitals) can be observed in

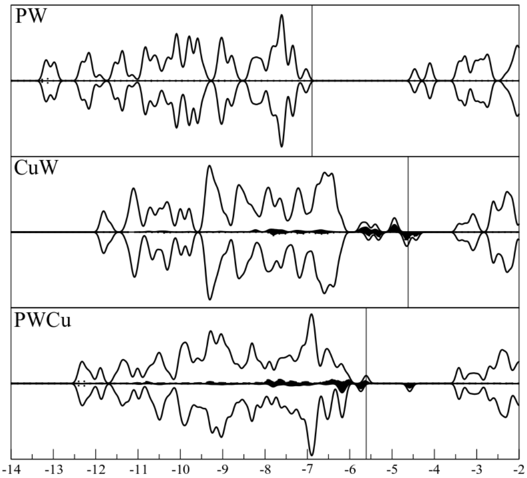

FIGURE 2: Total and atom density of states spectra for a) $PW_{12}O_{40}^{3-}$, b) $CuW_{12}O_{40}^{6-}$, c) $PW_{11}CuO_{39}^{5-}$ systems.

the density of states in PWCu system, where Cu was introduced in the position of addenda atom. The gap between the main part of valence and conduction band (disregarding additional peaks connected with cooper cation) are almost identical in all studied systems and equal 2,6.

Detailed analysis of frontier orbitals (demonstrated in Table 2 as proportional composition) shows that in PW system the character of frontier orbitals agree with the character of main part of valence and conduction bands. HOMO orbital is dominated by $2p$-orbitals of bridging oxygen atoms, while LUMO orbital consists of $5d$ orbitals of tungsten atoms with the small admixture of $2p$-orbitals of bridging oxygen atoms Ob,c. In the CuW system, where copper takes the position of central ion, both HOMO and LUMO orbitals (localized in additional peaks, which appeared between the valence and conduction band) consist of Cu $3d$-orbitals with addition of $2p$-orbitals of internal, Oa, oxygen atoms. Orbitals coming from substituted copper ions appear also as main components of frontier orbitals in PWCu system, where copper substituted one addenda atom. In that system, both HOMO and LUMO orbitals are characterized by copper orbitals with small admixture of bridging Ob,c atoms.

The influence of Cu ion on the energy of frontier orbitals is represented in the last row in Table 1, where those energies are presented. Energy values are calculated for the solvent systems, where water was used as a solvent ($\epsilon = 80$). Values of collected energies show that introducing Cu into the system influences the energy of HOMO orbitals, which increases in order: PW($-6{,}89$) < PWCu($-5{,}61$) < CuW($-4{,}62$). Smaller changes can be observed in LUMO energy orbital, which presents only slight decrease (0,10 – 0,25 eV) in systems modified with Cu^{2+}.

The results of calculations for modified CuHPA show that changes in chemical composition lead to the changes in physicochemical properties of the studied system. The results of population analysis for CuW show that only properties of internal oxygen sites that are bonded to the central ion and addenda atoms depend on chemical character of Cu^{2+} localized in position of the central ion. The results of calculations for PWCu system, where one addenda atom was substituted, show that chemical character of introduced atom influences the nucleophilic character mostly of bridging oxygen atoms coordinated with the introduced element. Spectra of density of states indicates that, in all modified systems, the valence band close to the Fermi level is dominated by orbitals of bridging oxygen centers, whereas the conduction band follows mainly from the introduced addenda metal. Introducing of Cu^{2+} ions into Keggin anion results in new peaks between the balance and conduction band that is characterized by copper ion. The analysis of character of frontier orbitals and spectrum of density of states suggests that in CuHPA modified system the reduction process will occur with participation of copper ion.

⋆ ⋆ ⋆

[1] N. Mizuno, M. Misono, *Chem. Rev.* **98**, 199 (1998).

[2] I. V. Kozhevnikov, *Innovations in Pharm. Technol.* 96 (2003).

[3] J. F. Keggin, *Proc. Roy. Soc. A.* **144**, 75 (1934).

[4] Forschungszentrum Karlsruhe GmbH — Turbomole GmbH saf, Turbomole V6.3 2011 adoUoKa, (2011).

[5] J. P. Perdew, K. Burke, M. Ernzerhof, *Phys. Rev. Lett.* **77**, 3865 (1996).

[6] A. Schaefer, H. Horn, R. Ahlrichs, *J. Chem. Phys.* **97**, 2571 (1992).

[7] R. S. Mulliken, *J. Chem. Phys.* **23**, 1833 (1955).

[8] I. Mayer, *Chem. Phys. Lett.* **97**, 270 (1983).

Negative trion emission spectrum in stacked quantum dots: external electric field and valence band mixing

Wojciech Julian Pasek

Faculty of Physics and Applied Computer Science, AGH University of Science and Technology, Mickiewicza 30, 30-059 Kraków, Poland

Supervisor: Bartłomiej Szafran

We study the negatively charged exciton trion in stacked quantum dots by configuration interaction method. We discuss the trion recombination spectrum in external electric field (F) and look for the effects of the valence band mixing leading to the antibonding hole ground-state formation in the quantum dot molecule. We find that the antibonding hole ground-state produces a distinct modification of the trion emission for strongly coupled dots inverting the intensities of recombination line in the principal avoided crossing appearing in the spectrum within the range of low F. The exciton and trion emission spectra are distinctly different for weak interdot tunnel coupling. The dissociation of the negative trion ground state appears as a two-stage process with a characteristic shape of the recombination line as observed experimentally.

Wave functions of valence band hole states confined in quantum dots are of mainly heavy-hole band-like nature in the low-energy part of the spectrum. Although the light-hole band contribution is weak, it is[1] crucial when considering double quantum dots, where it causes hole ground state to be an antibonding one. The purpose of the present paper is to determine the impact of the antibonding hole ground-state formation for the emission spectrum of the negatively charged exciton trion. We investigate an extent to which the PL spectra of the trion are affected by the antibonding nature of the hole ground state. We use the Luttinger-Kohn Hamiltonian (KL) and generalize the study to excited states in both the initial and the final states of the trion recombination.

We consider below both neutral and singly charged negative excitonic complexes. We use the following Hamiltonian for the exciton consisting of an electron in the conduction band and a hole in the valence band

$$\hat{H}_{\mathrm{exc}} = \hat{H}_{\mathrm{e}}\mathbf{I} + \hat{H}_{\mathrm{h}} + \hat{H}^{\mathrm{int}}_{\mathrm{eh}} + \hat{H}^{F}_{\mathrm{exc}} \ , \qquad (1)$$

where $\mathbf{I}$ is the identity matrix of the KL subband space. For the negative trion formed by two electrons and a hole the operator

$$\begin{aligned}\hat{H}_{\mathrm{trion}} &= \hat{H}_{\mathrm{e}_1}\mathbf{I} + \hat{H}_{\mathrm{e}_2}\mathbf{I} + \hat{H}_{\mathrm{h}} + \\ &+\hat{H}^{\mathrm{int}}_{\mathrm{e}_1\mathrm{h}} + \hat{H}^{\mathrm{int}}_{\mathrm{e}_2\mathrm{h}} + \hat{H}^{\mathrm{int}}_{\mathrm{e}_1\mathrm{e}_2} + \hat{H}^{F}_{\mathrm{trion}} \end{aligned} \qquad (2)$$

is used, where $\hat{H}_{\mathrm{e}}$ represents the one-particle Hamiltonian for an electron. $\hat{H}_{\mathrm{h}}$ stands for the one-particle Hamiltonian of the hole. $\hat{H}^{\mathrm{int}}_{\alpha\beta} = \pm\mathbf{I}/\epsilon r_{\alpha\beta}$ is the Coulomb interaction for a pair of particles (α, β) (all formulae are written in atomic units). $\hat{H}^{F}_{\mathrm{exc}} = \mathrm{e}(z_{\mathrm{h}} - z_{\mathrm{e}})F\mathbf{I}$ and $\hat{H}^{F}_{\mathrm{trion}} = \mathrm{e}(z_{\mathrm{h}} - z_{\mathrm{e}_1} - z_{\mathrm{e}_2})F\mathbf{I}$ are the external electric field Hamiltonians as the field is externally applied along the z axis (F is the field strength) for the exciton and trion, respectively.

We work in the effective mass approximation and envelope ansatz. The kinetic energy of an electron in a non-degenerate conduction band is given by $\hat{T}_{\mathrm{e}} = -\nabla^2_{\mathrm{e}}/2m^*_{\mathrm{e}}$. The kinetic energy for the hole in the valence band is calculated using the axial approximation of the 4-band KL (Kohn-Luttinger) Hamiltonian[2] accounting for the light and heavy hole bands that are degenerate at the top of the valence band.

We model the confinement potential of the pair of vertically stacked InGaAs quantum dots by a double rectangular quantum well along the z axis. We take for simplicity an infinite quantum well for the confinement in the direction perpendicular to the growth direction. The dot is assumed circularly symmetric. After adding the potential energy terms $\hat{U}_{\rm e}$ and $\hat{U}_{\rm h}$, the one-particle Hamiltonians are

$$\hat{H}_\alpha = \hat{T}_\alpha + \hat{U}_\alpha \ , \tag{3}$$

where $\alpha \in \{{\rm e},{\rm h}\}$. In the variational basis for the trion we use the single-electron eigenfunctions in form

$$\Psi^{\rm e}_j(\vec{r}_{\rm e}) = \exp\left(il\phi\right) J_l\left(\frac{\kappa_{kl}\rho}{R}\right) Z_{\rm n}(z). \tag{4}$$

J_l is a Bessel function of the first kind and κ_{kl} is the k-th zero of that function. The hole eigenfunctions are 4-component spinors with total angular momentum defined and equal $\left(l_{\rm h}+\frac{3}{2}\right)\hbar$.

We compare the results of the KL modeling including the heavy-light hole mixing with the results obtained for separate bands approximation. The calculations for separate bands are performed for a diagonal Hamiltonian $(\hat{T}^{\rm d}_{\rm h})_{1,1}=(\hat{T}^{\rm d}_{\rm h})_{4,4}=\frac{1}{2}(\gamma_1+\gamma_2)(\hat{p}_\perp^2+\hat{p}_z^2)+V_h^{\rm pot}(\vec{r}_{\rm h})$, $(\hat{T}^{\rm d}_{\rm h})_{2,2}=(\hat{T}^{d}_{\rm h})_{3,3}=\frac{1}{2}(\gamma_1-\gamma_2)(\hat{p}_\perp^2+\hat{p}_z^2)+V_{\rm h}^{\rm pot}(\vec{r}_{\rm h})$ (in the same base space as the KL Hamiltonian), with corresponding eigenfunctions

$$\psi^{HH}_{k,l,n}(\vec{r}_{\rm h}) = \exp(il\phi)J_l\left(\frac{\kappa_{kl}\rho}{R}\right) Z^{HH}_n(z) \tag{5}$$

$$\psi^{LH}_{k,l,n}(\vec{r}_{\rm h}) = \exp(il\phi)J_l\left(\frac{\kappa_{kl}\rho}{R}\right) Z^{LH}_n(z) \tag{6}$$

that are used for construction of the trion basis.

In the calculations we assume dielectric constant $\epsilon = 12{,}9$ and all the other material parameters were taken from the work of Vurgaftman et al.[3] using nonzero bowing parameters when appropriate. The dots that were considered here are circular with radius R = 10 nm.[1] The heights of the dots are assumed 2,0 nm (bottom dot) and 2,1 nm (top dot). In this paper the degenerated top of GaAs valence band and the bottom of the GaAs conduction band are assumed as reference energy levels, for the hole and the electron respectively.

In this work the radiative recombination probability of interband excitonic transitions is calculated using the envelope approximation to Fermi golden rule.

The energy spectra and recombination probabilities of an asymmetric quantum dot molecule (QDM) with strong tunnel coupling (barrier width D = 4,1 nm) are shown on Fig. 1. The results obtained with the KL Hamiltonian — where the hole in the ground-state occupies the antibonding orbital are shown in Fig. 1a. The results with the diagonal Hamiltonian — where the hole ground state is bonding — are displayed in Fig. 1b. The width of the lines is set proportional to the calculated recombination probability.

The considered final states correspond to bonding and antibonding electron orbital when the interdot tunnel coupling is present (low F) and to the lowest-energy states of the electron localized in a single dot for the electric field strong enough to remove the tunnel coupling.

For a schematic description of the particle localization corresponding to the initial and final states of the electron-hole recombination table-like diagrams were added to Fig. 1. The capital letter (E or H) indicates that charge density of one particle is nearly completely localized in a dot. The minuscule (e or h) indicates that small part of charge density of a particle penetrates to a dot as an effect of tunneling coupling. The upper row stands for the top dot and the lower one for the bottom dot. An asterisk indicates angular (in-plane) electron excitation.

In both Fig. 1a and Fig. 1b there are pronounced anticrossings in the central part of the figure between $F = 0$ and $F = 20$ kV/cm. The anticrossing pattern near $F = 0$ is very similar for both the exciton and the trion. Individual spectra are shifted in energy and electric field and have slightly different slopes and intensities but have common characteristic elements (minima, maxima and large anticrossing patterns). The centra of these anticrossings occur when the electric field compensates for the asymmetry of the confinement potential. In the present results the energy of the ground-state exciton recombination line is maximal for $F \simeq 10$ kV/cm. For

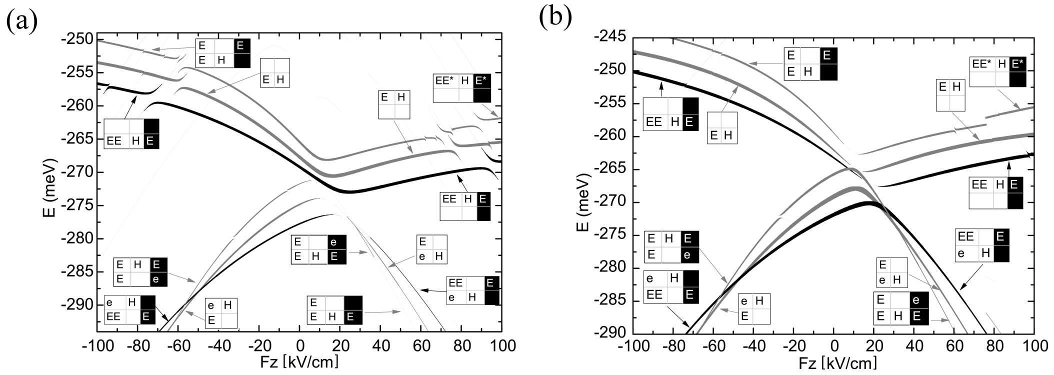

FIGURE 1: Energy spectrum and recombination probabilities (marked as line width) for negative trion and exciton versus electric field intensity parallel to z axis. The case of asymmetric dots with barrier width $D = 4{,}1$ nm. (a) for KL Hamiltonian; (b) for unmixed *HH* and *LH* bands Hamiltonian. Light gray color indicates the exciton recombination, black is for trion recombination to electron ground state, dark gray color — to first excited state. Particle localization diagrams are described in text.

$F = 0$ the hole density is shifted toward the larger dot in a larger extent than the electron. This is because the interdot tunnel coupling (stronger for the electron) compensates for the asymmetry of the potential. For $F > 0$ the hole (electron) is shifted to the bottom (top) dot, hence the maximum of the recombination energy occurs at the positive side of the origin.

For the recombination of the trion to the electron ground-state (black line) a stronger electric field is needed to align both electrons with the hole than in the exciton case producing the center of the avoided crossing. For the other trion line (blue curve) a weaker field is needed. For $F = 0$ the lowest-energy trion (black curve) has the ground-state trion in the initial state, while the lowest line with the excited electron in its final state has a highly excited initial trion state. The electron in the excited final state has a nearly odd parity wave function which needs to agree in spatial symmetry with the initial trion state in order to produce a non-zero recombination probability.

For the KL Hamiltonian the lowest (second-lowest) bright state of each kind has a minimum (maximum) of recombination probability near the resonance anticrossing about 10 − 20 kV/cm. For the separate-band approximation the intensities of recombination lines are just opposite. The minimal recombination probability from the ground state is an effect of the antibonding hole ground state character obtained when calculated using KL Hamiltonian. The recombination probability depends on the „overlap" of the electron and hole wave functions. In the low-energy states of strongly coupled dots the electron orbitals have bonding character with zero angular momentum. For $D = 4{,}1$ nm the dominant heavy hole component in the ground-state have zero spatial angular momentum but its wave function is nearly antisymmetric in the growth direction. The light hole contributions correspond then to non-zero spatial angular momenta hence the small value of the „overlap" for both the exciton and the trion g-nd state.

The case of asymmetric dots with weak tunnel coupling is shown in Fig. 2. The differences between the results of KL theory and separate bands approximation is reduced to a varied width of minor anticrossings in the spectra. However one finds now a big difference in the form of recombination lines between the exciton and the trion lines. The exciton line has only one major anticrossing resulting from electron tunneling from the top to the bottom dot. For $F = 0$ both the trion and the final electron ground states are local-

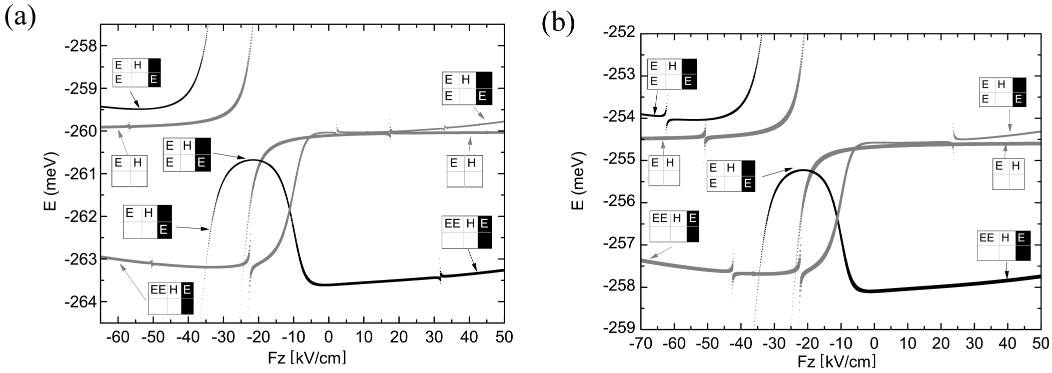

FIGURE 2: Same as Fig. 1 only for interdot barrier of 10,1 nm.

ized in the top dot (see black curve in Fig. 2). The most remarkable feature of all the spectra is the significant increase in „black" line energy in the region near -25 kV/cm. As can be seen on the diagrams this phenomenon is connected with trion dissociation — one of the electrons moves to bottom dot leaving the other one and the hole in the top dot (steep slope from -5 to -20 kV/cm). This takes place simultaneously with the tunneling of the final electron to the bottom dot. The energy of the „black" trion line for $F \in (-25; -20)$ kV/cm (about -261 meV for KL — see Fig. 2a) is nearly equal to the energy of exciton line outside the main anticrossing (see the light gray curve for $F > -10$ kV/cm, and $F < -40$ kV/cm). This is because the dissociated trion system (an electron-hole pair in one dot and the second electron in the other dot) is similar to exciton one. The small difference in energies is due to resultant marginal interdot Coulomb interaction energy. As the electric field intensity becomes more negative, the second electron tunnels to the bottom dot and the trion becomes completely torn. This process manifests itself as another steep drop of the recombination line that is accompanied by vanishing recombination probability due to the separation of the carriers. The PL features of the ground-state trion recombination with respect to the exciton that are presented in Fig. 2 exactly reproduce the qualitative features observed in the Fig. 1b of reference[6] (mind the inverted orientation of F). The „dark gray" trion line that is given in Fig. 2 coincides with the exciton line at the positive F and crosses the ground-state trion line at the stage of the removal of the first electron from the dot occupied by the hole.

In conclusion, we have found that inversion of the hole ground-state chirality affects mainly the recombination probabilities. The effect makes the trion ground-state optically inactive at $F = 0$ in favor of the first excited state. We demonstrated that the trion PL spectrum is for strongly coupled dots very similar to the exciton one. For weaker coupling the trion spectra differ significantly from the exciton spectra and the effects of the antibonding hole ground-state are negligible.

⋆ ⋆ ⋆

[1] J. I. Climente, M. Korkusiński, G. Goldoni, P. Hawrylak, *Phys. Rev. B* **78**, 115323 (2008).

[2] S. L. Chuang, Physics of Photonic Devices, 2nd ed. (Wiley, New York, 2009).

[3] I. Vurgaftman, J. R. Meyer, L. R. Ram-Mohan, *J. Appl. Phys.* **89**, 5815 (2001).

[4] M. Stopa, C. M. Marcus, *Nano Lett.* **8**, 1778 (2008).

[5] V. Jovanov, S. Kapfinger, G. Abstreiter, J. J. Finley, arXiv:1110.3709v1.

[6] H. J. Krenner, E. C. Clark, T. Nakaoka, M. Bichler, C. Scheurer, G. Abstreiter, J. J. Finley, *Phys. Rev. Lett.* **97**, 076403 (2006).

Manipulation of single electron spin in a quantum dot without magnetic field

Jarosław Pawłowski

Faculty of Physics and Applied Computer Science, AGH University of Science and Technology, Mickiewicza 30, 30-059 Kraków, Poland

Supervisor: Stanisław Bednarek

In this work we propose the construction of nanodevice performing spin rotations of an electron confined in an electrostatic quantum dot without use of magnetic field. Sinusoidally varying voltage applied in different phase to four gates, causes that the electron moves along a two-dimensional closed path. The spin-orbit interaction, present in the structure, induces spin rotations. For properly adjusted ac signal duration, one can perform the logical NOT operation or the Hadamard quantum gate on the electron spin. We perform a simulation of a time evolution of the nanodevice.

Due to the long coherence time, the single electron spin confined in an electrostatic quantum dot may be used as a quantum bit carrier.[1,2] Presently, a strong theoretical and experimental research effort has been made toward the implementation of quantum logical operations on the electron spin. In first nanodevices[3–6] constructed for this purpose manipulation of electron spins required an external microwave, which induces coherent transitions (Rabi oscillations) between energy levels split by magnetic field. Recently, electron spin manipulations are managed without using a microwave. Spin rotations are mediated by the spin-orbit interaction,[7,8] but the authors do not avoid the use of an external magnetic field.

In theoretical works[9–11] it has been shown that to perform the operation on the electron spin without magnetic field, it is necessary to force the electron to move on a two-dimensional closed curve. In work[11] a construction of such nanodevice was proposed and simulation of time evolution accomplished. Spin rotations are performed by the electron movement along the two-dimensional closed path, which is determined by quantum wires, induced under metal electrodes placed on a surface of a semiconductor structure which contains a quantum well.[12] In nanodevices proposed in work[11] the electron passes only one round and must travel under electrode a few μm distance. The electron binding energy in the induced quantum wire is relatively small (about 2 meV) so this method is sensitive to disturbance and proposed nanodevices may be, with the current technology, too difficult to construct.

In this letter we show that the spin rotations without magnetic field can be also performed in electrostatic quantum dots whose structure and size are presently easy to achieve, like these used in experimental works.[3–8]

We propose a nanodevice based on a planar heterostructure AlGaAs/GaAs/AlGaAs, which is similar to that considered in work.[12] It contains a 15 nm wide quantum well sandwiched between two barriers each 40 nm thick. The structure is separated from the strongly doped substrate by an undoped buffer layer 50 nm thick. Four metal gates are deposited on top of the upper barrier. Their layout and sizes used in computations are shown in Fig. 1. A constant voltage V_0 is applied between the gates and the substrate. The constant voltage is modulated by an sinusoidally varying voltage applied to each of the four gates with phase $\pi/2$ between them:

$$V_j = V_0 + V_1 \sin\left(\omega t + \frac{j\pi}{2}\right), \qquad (1)$$

where j labels the gate number, varying from 1 to 4. The voltages applied between the gates and the substrate form a confinement potential in GaAs layer, whose minimum moves along a closed path in a plane parallel to the heterostructure layers. As a result, the electron confined within is moving along the same trajectory. The value of ω is arbitrary, however it must be small enough to preserve adiabaticity of the confinement potential variation.

The simulations assume the system of coordinates with the y axis oriented parallelly to the growth direction and the x and z axes aligned in the plane of the quantum well. The electron motion in the y direction is frozen and free to move in the x and z directions within the quantum well. We write its wave function, taking into account the spin, as a two-row column matrix (spinor):

$$\Psi(x,z,t) = \begin{pmatrix} \varphi_\uparrow(x,z,t) \\ \varphi_\downarrow(x,z,t) \end{pmatrix}, \tag{2}$$

where upwards (downwards) arrow describes the amplitude of the eigenstate of the spin oriented parallel (antiparallel) to the z axis. The state function depends on two spatial coordinates and time. The Hamiltonian for the electron in this representation we write as a square matrix

$$\hat{H} = \begin{pmatrix} \hat{H}_0 & 0 \\ 0 & \hat{H}_0 \end{pmatrix} + \hat{H}_{\mathrm{SO}}. \tag{3}$$

The first term contains the electron kinetic energy and the potential energy in the electrostatic field:

$$\hat{H}_0(x,z,t) = -\frac{\hbar^2}{2m}\left(\frac{\partial^2}{\partial x^2} + \frac{\partial^2}{\partial z^2}\right) - e\phi(x,y_0,z,t), \tag{4}$$

where $\phi\,(x,y_0,z,t)$ is the electrostatic potential in the quantum well with center in y_0. The potential comes from the voltages applied to the gates and the charges induced on them. The second term of the Hamiltonian (3) introduces the spin-orbit coupling. We assume for simplicity that due to the symmetry of the the quantum well the Rashba spin-orbit coupling term is negligibly small and only the Dresselhaus term is present in the structure. Then

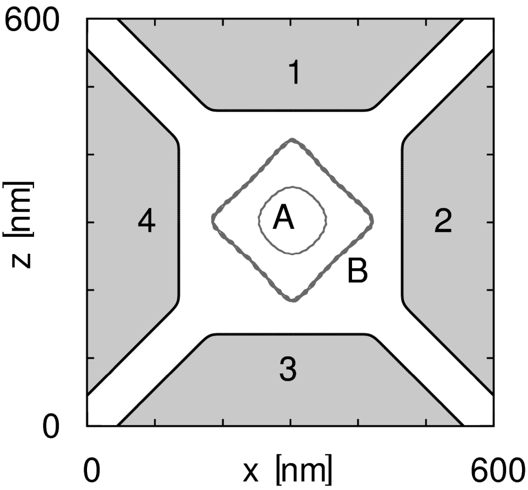

FIGURE 1: Gate configuration (grey color). Dark grey solid lines show the electron trajectory.

$$\hat{H}_{\mathrm{SO}} = \frac{\hbar k_{\mathrm{so}}}{m}\left(\hat{p}_x\hat{\sigma}_x - \hat{p}_z\hat{\sigma}_z\right), \tag{5}$$

where $\hat{\sigma}_x$ and $\hat{\sigma}_z$ are the Pauli matrices, and the characteristic wavevector k_{so} depends on the quantum well thickness d, electron band mass m, and bulk coupling constant γ: $k_{\mathrm{so}} = m/\hbar^2\,(\pi/d)^2\,\gamma$.

We perform a simulation of a time evolution of the nanodevice. We solve iteratively the time-dependent Schroedinger equation with the Hamiltonian (3) for the single electron confined in the nanostructure. The electrostatic potential $\phi\,(x,y_0,z,t)$ in expression (4) is evaluated in a three-dimensional region containing the entire nanodevice by solving the Poisson's equation. Due to the alternating voltage applied to the gates and a moving electron wavepacket the potential must be evaluated in every time step. In such a way, changes in the confinement potential in the quantum dot are taken into account. Details of the method can be found in work.[12]

Fig. 1 shows proposed layout of the gates deposited on the nanostructure. The electron trajectories (shown in figure) are calculated as the expectation value of the position vector components. Simulations were carried out

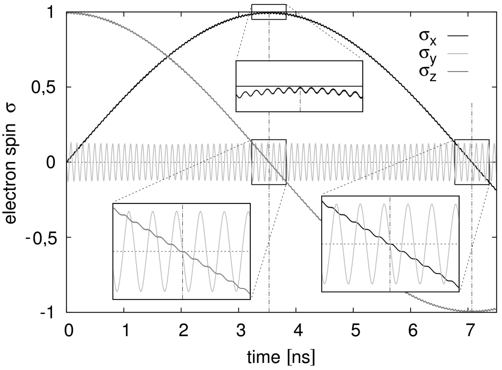

FIGURE 2: The time evolution of the expectation values of the Pauli matrices $\langle\sigma_x\rangle$, $\langle\sigma_y\rangle$ and $\langle\sigma_z\rangle$ for the A trajectory from Fig. 1 denoted by black, light grey and dark grey lines respectively.

as follows. For the initial condition the ground state wave function with the spin parallel to the z axis was formed. For this purpose the appropriate voltages, according to the expression (1) with the substitution $t = 0$, were applied between the substrate and the electrodes. To find the ground state wave function of the electron we use the imaginary time evolution method, with simultaneous solving Poisson's equation in each iteration. Thus the electron wave function and distribution of the confinement potential at the ground state is obtained. Then we launched iterations of the time-dependent Schroedinger equation. In the calculations we adopted GaAs material parameters with the electron effective mass $m = 0{,}067\, m_0$, the dielectric constant $\varepsilon = 12{,}5$, and the spin-orbit characteristic wave vector $k_{\mathrm{so}} = 0{,}0013$ nm^{-1}, which corresponds to quantum well thickness about 14 nm in GaAs.

The trajectory A has been evaluated for the constant voltage component in (1) $V_0 = -80{,}0$ mV and the alternating voltage amplitude $V_1 = 16{,}0$ mV. When the alternating voltage amplitude V_1 is small compared to the constant component V_0, we obtain trajectories resembling a circle.

The time evolution of the expectation values of the Pauli matrices $\langle\sigma_x\rangle$, $\langle\sigma_y\rangle$ and $\langle\sigma_z\rangle$ is shown in Fig. 2 by black, light grey and dark grey lines respectively. At the initial moment the x and y spin components are equal to 0. For the z component: $\langle\sigma_z\rangle = 0{,}985$ is slightly smaller than 1. In the ground state the spin is not well defined because of the spin-orbit interaction. During each cycle of motion along the trajectory a small value of $\langle\sigma_y\rangle$ emerges at cost of $\langle\sigma_z\rangle$, then disappears and transforms into $\langle\sigma_x\rangle$.

We can enlarge a size of the trajectory at higher alternating amplitude. The trajectory B from Fig. 1 is obtained for $V_0 = -80{,}0$ mV and $V_1 = 29{,}7$ mV. Its shape is changed and is approaching to a rectangle. The spin components are shown in Fig. 3. Increases and reductions of the spin components are arranged in a characteristic stepped curves. After eight cycles the z component of the spin completely disappears and the spin is parallel to the x axis — we obtain the Hadamard gate operation. After a further eight cycles $\langle\sigma_x\rangle$ is again near zero and $\langle\sigma_z\rangle$ is close to -1. We obtain the logical NOT gate operation. A number of required cycles depends on the trajectory size and is controlled by a ratio between the constant and alternating voltage components applied to the gates. To obtain values of $\langle\sigma_x\rangle$ ($\langle\sigma_z\rangle$) at the final moments as close to 1 (-1) for the Hadamard (NOT) gate, the moment of zeroing of the corresponding components $\langle\sigma_z\rangle$ ($\langle\sigma_x\rangle$) and $\langle\sigma_y\rangle$ should be fit together. The curves shown in Figs. 2 and 3 demonstrate that an increase of the alternating voltage amplitude enlarges the trajectory and simultaneously shortens the gate time.

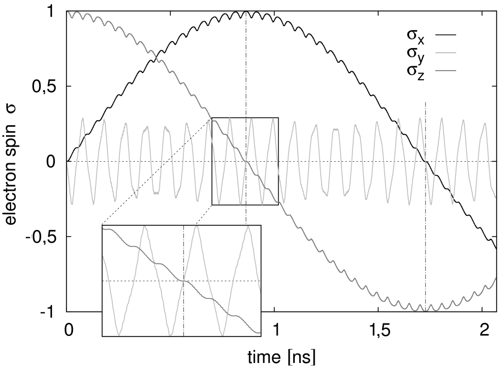

FIGURE 3: Same as Fig. 2, but for the B trajectory from Fig. 1.

The time can also be reduced by increasing the frequency of the alternating voltage, but not arbitrarily. The frequency increasing can lead to loss of adiabaticity of the process. In two presented simulations we assumed the frequency $\nu = 9{,}5$ GHz.

In this letter we have proposed the design and simulated working of the nanodevice, which can perform operations on the electron spin without use of an external magnetic field. The simulation was carried out by iterative solving of the time-dependent Schroedinger equation with the electrostatic confinement potential calculated in every time step. For the nanodevice dimensions corresponding to these currently built we obtain the NOT operation time about 2 ns.

This work has been supported by the Grant number N N202 128337 from the Ministry of Science and Higher Education. J. P. has also been partly supported by the EU Human Capital Operation Program, Polish Project No. POKL.04.01.01-00-434/08-02.

⋆ ⋆ ⋆

[1] D. Awschalom, D. Loss, N. Samarth, Semiconductor Spintronics and Quantum Computation (Springer Verlag, 2002).

[2] R. Hanson, L. P. Kouwenhoven, J. R. Petta, S. Tarucha, L. M. K. Vandersypen, *Rev. Mod. Phys.* **79**, 1217 (2007).

[3] J. M. Elzerman, R. Hanson, L. H. Willems van Beveren, B. Witkamp, L. M. K. Vandersypen, L. P. Kouwenhoven, *Nature* **430**, 431 (2004).

[4] T. Meunier, I. T. Vink, L. H. Willems van Beveren, F. H. L. Koppens, H. P. Tranitz, W. Wegscheider, L. P. Kouwenhoven, L. M. K. Vandersypen, *Phys. Rev. B* **74**, 195303 (2006).

[5] J. R. Petta, A. C. Johnson, J. M. Taylor, E. A. Laird, A. Yacoby, M. D. Lukin, C. M. Marcus, M. P. Hanson, A. C. Gossard, *Science* **309**, 2180 (2005).

[6] F. H. L. Koppens, C. Buizert, K. J. Tielrooij, I. T. Vink, K. C. Nowack, T. Meunier, L. P. Kouwenhoven, L. M. K. Vandersypen, *Nature* **442**, 766 (2006).

[7] K. C. Nowack, F. H. L. Koppens, Y. V. Nazarov, L. M. K. Vandersypen, *Science* **318**, 1430 (2007).

[8] S. Nadj-Perge, S. M. Frolov, E. P. A. M. Bakkers, L. P. Kouwenhoven, *Nature* **468**, 1084 (2010).

[9] P. San-Jose, B. Scharfenberger, G. Schöon, A. Shnirman, G. Zarand, *Phys. Rev. B* **77**, 045305 (2008).

[10] S. Prabhakar, J. Raynolds, A. Inomata, R. Melnik, *Phys. Rev. B* **82**, 195306 (2010).

[11] S. Bednarek, B. Szafran, *Phys. Rev. Lett.* **101**, 216805 (2008).

[12] S. Bednarek, B. Szafran, R. J. Dudek, K. Lis, *Phys. Rev. Lett.* **100**, 126805 (2008).

The methodology of investigation the particle statistics effect in X-rays diffraction

Piotr Ramza

Faculty of Physics and Applied Computer Science, AGH University of Science and Technology, Mickiewicza 30, 30-059 Kraków, Poland

Supervisor: Andrzej Zięba

The particle statistics effect concerns X-rays diffraction on powder crystallite samples. This effect is manifested by extra-appearing fluctuations of intensity of diffracted beam due to finite number of diffracting grains of crystal. Because of this reason, the uncertainty of measured number of registered photons per single observation seems to be larger than well known „counting statistics" refers only to uncorrelated Poisson fluctuations. The particle statistics effect could be used to estimate specimen's grains sizes also.

X-rays diffraction is an important analytical technique used in various areas of science. For example, it allows the phase content of powder specimen to be determined. In this method, the reflection of X-rays occurs only for a small fraction of crystallites of the powder sample for which the Bragg condition is met. The detector signal is a weighted sum of the contributions of crystallites. They are randomly oriented, so the number of „diffracting" crystallites is finite. When the sample is gradually inclined at a small angle ω or φ (while the position of the X-ray source and detector remains fixed) certain crystallites cut out to reflect the X-rays, while others start to diffract the radiation. This leads to variation in the detected intensity of signal N_i (number of registered photons per single observation) as a function of the angles ω or φ. This effect is called the „particle statistics" and it leads to growing up the uncertainty of measured intensity of diffracted beam.

The first theoretical investigation of particle statistics has been done by Aleksander[1] and De Wolff,[2,3] and there was no many significant works in this matter up to present. Due to this theory one should estimate at first the effective number of irradiated grains of crystal N_{eff} and then the number of diffracting grains N_{diff} (how many grains fulfill the Bragg condition and diffract). This consideration allows to write the formula which describe the relative standard deviation of intensity of diffracted reflection like

$$\sigma_{\mathrm{r}} = 2R\sqrt{\frac{\pi\mu}{3Shw_{\mathrm{eff}}m_{\mathrm{hkl}}}}d^{\frac{3}{2}}, \qquad (1)$$

when d — average crystallites size, m — average linear absorption coefficient of the specimen, S — irradiated area of sample, w_{eff} — effective extension of the beam due to Soller slit, h — the arithmetic mean of divergence and receiving slit's height, m_{hkl} — multiplicity factor of reflection under investigation and R — distance source-goniometer axis and goniometer axis-receiving slit.

The successive measurements of intensity are autocorrelated numbers because the same crystallite contributes to the whole signal for a few successive values of the angles. This fact allows the statistical aspects of measured data to be described with the mathematical formalism of autocorrelated data, what have been done first time in this work. Especially the estimator of standard deviation $S_{\mathrm{a}}(x)$ which was derived in assumption of non-zero and positive correlation between numbers in statistical sample was used. This formalism was investigated by authors earlier.[4] The estimator $S_{\mathrm{a}}(x)$ used to calculate the relative standard deviation of measured intensity of diffracted beam has a following formula

$$S_{\mathrm{a}}(\bar{x}) = \sqrt{\frac{\sum\limits_{i=1}^{n}(x_i - \bar{x})^2}{n\left(\hat{n}_{\mathrm{eff}} - 1\right)}},$$

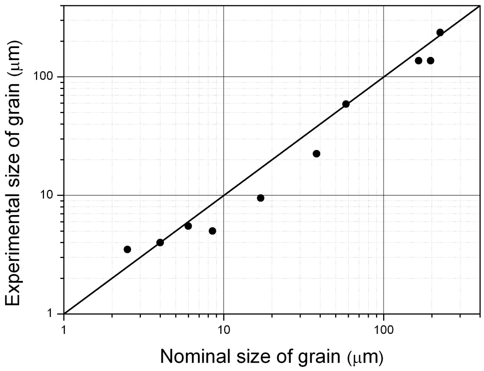

FIGURE 1: Comparison of nominal and real size of grains. The line shows identity. Measured was done for synthetic diamond powders. Points mean the most probability size of grain in sample.

$$\hat{n}_{\text{eff}} = \frac{n}{1+2\sum\limits_{k=1}^{n_c}\left(1-\frac{k}{n}\right)r_k}, \tag{2}$$

when $\hat{n}_{\text{eff}}$ — effective number of observation, n — number of all elements of autocorrelation function, r — following element of autocorrelation function and n_c — truncation limit of summing.

In X-rays diffraction the samples of synthetic diamond were used. It was necessary to check their real size of grains and compare it to the nominal one. This experiment has been done with the use of the laser grains size analyzer. This technology uses the single grain diffraction of laser beam to estimate the grain size. The advantage of this method is that one can see an all distribution of grains sizes which are consisted in measured sample, on the contrary to other methods. The grain size distribution function received by this method could help us to calculate the volume weighted mean size of grains. As we can see on Fig. 1 there is a good correspondence between nominal and real sizes.

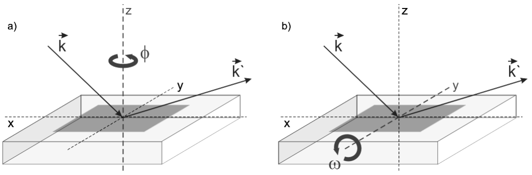

FIGURE 2: Two ways of observation the particle statistics effect in laboratory: rotating (a) and rocking (b) the sample in diffractometer.

The diffraction experiment was made with X'Pert-Pro, powder diffractometer in Brag-Brentano geometry. There were two ways of measuring data to observe the powder statistic effect. At first the sample was gradually inclined at a small angle ω (in few degrees) while the position of the X-ray source and detector was fixed. In the second way the sample was rotating around the vertical axis z (φ angle was changing). Both measurements were done for (111) reflection, because of its high relative intensity, to maximally eliminate the calculate statistics effect.

The comparison of results of those two methods is shown in Fig. 3 and in Table 1. It is convenient to compare the relative standard deviation, because the magnitude of absolute variations depends on crystallites size and it makes this quantity difficult to show.

This work contains some new elements in investigation of particle statistics effect. At first, real grains sizes were verified with the use of new method which had never earlier been applied in works concerning this matter. At second, there were compared two methods of observation the particle statistics effect, which had been proposed in literature (first time it was done on modern diffractometer). Except of minimal differences in results, we can say, that there is no disparity between those methods (in uncertainty of measuring limit). At third, there was a pioneer use of au-

TABLE 1: The relative standard deviations received for few samples with different grains sizes and calculated with $S_a(x)$ estimator.

Grains size	10 μm	50 μm	60 μm	230 μm
$S_a(x)_{\text{relative}}$ for scan ω	0,10	0,28	0,41	0,52
$S_a(x)_{\text{relative}}$ for scan φ	0,09	0,24	0,43	0,51

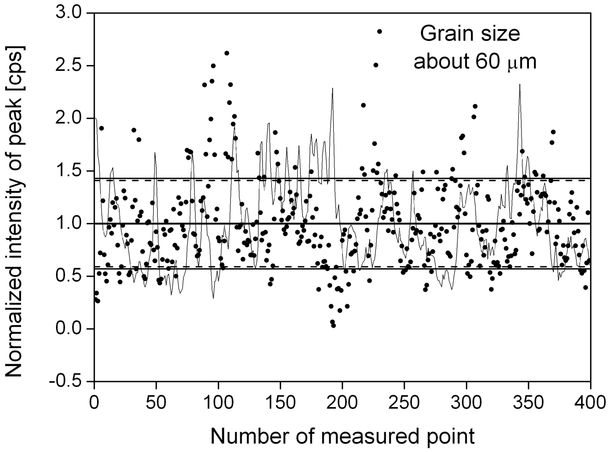

FIGURE 3: Intensity of selected Bragg reflection of synthetic diamond as a function of the inclination angle ω and φ. Horizontal lines show relative standard deviation calculated with $S_{\mathrm{a}}(x)$ estimator. Solid line and horizontal solid line mean experiment with rocking sample (scan ω). Points and horizontal dashed line mean experiment with rotating sample (scan φ). The range of ω is ±2° and 360° for φ angle.

tocorrelated statistical formalism to describe the appearing of the particles statistic effect. It could be done, because the following values of the function of beam intensity due to angle ω (or φ), are non-zero and positive mode correlated.

⋆ ⋆ ⋆

[1] L. Alexander, P. K. Harold, E. Kummer, *J. Appl. Phys.* **19**, 742 (1948).

[2] P. M. De Wolff, J. M. Tayor, W. Parish, *J. Appl. Phys* **30**, 63 (1959).

[3] P. M. De Wolff, *Appl. Sci. Res. Sect. B* **7**, 102 (1958).

[4] A. Zieba, P. Ramza, *Metrol. Meas. Syst.* **18**, 529 (2011).

Implementation of polycrystalline deformation model into finite elements method code

Marcin Wroński

Faculty of Physics and Applied Computer Science, AGH University of Science and Technology, Mickiewicza 30, 30-059 Kraków, Poland

Supervisors: Krzysztof Wierzbanowski†, Brigitte Bacroix‡
† AGH University of Science and Technology, Kraków, Poland
‡ Université Paris 13, 99 av. J. B. Clément, 93430 Villetaneuse, France

The main goal of this work was to include the crystallographic deformation model of polycrystalline material to the Finite Elements Method (FEM) with. The LW model was selected to be coupled with FEM, and therefore the FEM+LW calculation tool was obtained. In order to check this software, the uniaxial tensile test along x_3 direction was simulated and applied to the initial material with a random texture. The FEM+LW model enables the study of heterogeneous deformation process taking into account its crystallographic nature. The FEM+LW software can be used to simulate other deformation processes with complex geometry, like deep drawing, extrusion or stamping.

The implementation of a crystallographic model into FEM code is an important issue for the description of anisotropic behavior of metals during industrial processing. LW crystallographic model[1] was selected, because it is quick and relatively simple in its formulation. It was implemented into ABAQUS/Explicit FEM code using subroutine VUMAT[2] and, consequently, the FEM+LW model was created .

A representative polycrystalline model sample, with appropriate number of grains, is attached to each Gauss integration point. Calculation in ABAQUS are carried out incrementally. The complete macroscopic solution is obtained by dividing the deformation process into thousands of smaller increments. The calculation sequence in VUMAT subroutine (where LW model is implemented), in each Gauss point progresses as follows:

- at the beginning of each calculation step the ABAQUS program transfers to the VUMAT procedure a total strain increment $\Delta E_{i,j}$ to be attained in this step (it is calculated basing on a stress state from the end of the preceding step and is called $\Sigma^{\mathrm{Old}}_{i,j}$ in the present step),
- LW model performs the imposed deformation $\Delta E_{i,j}$ and calculates a new resulting stress state, $\Sigma^{\mathrm{New}}_{i,j}$, which is transferred to ABAQUS (it will become $\Sigma^{\mathrm{Old}}_{i,j}$ at the beginning of the next step). The logical scheme of these operations is shown in Fig. 1.

Let us summarize. The input parameters for VUMAT subroutine (with LW model included) are:

- $\Sigma^{\mathrm{Old}}_{i,j}$ — stress old (stress state from the end of the previous ABAQUS increment),
- $\Delta E_{i,j}$ — strain increment tensor,
- state variables – external variables defined by the user (in our case they are: lattice orientations of grains, critical shear stresses, τ_c, for all slip systems in all grains, grain deformations, etc.). After a calculation step performed by VUMAT we have to return the new stress value, $\Sigma^{\mathrm{New}}_{i,j}$, and new state variables (new lattice orientations, new critical shear stresses for slip, new grain deformations, etc.). The ABAQUS increments are repeated until the final deformation of the material is attained.

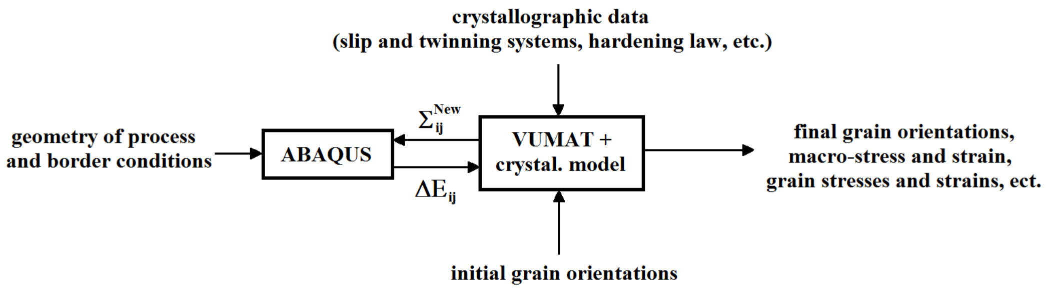

FIGURE 1: Scheme of interaction of LW model (included in VUMAT subroutine) with ABAQUS program.

In order to check the correctness of the FEM+LW model the tensile deformation of α-brass with random initial texture was considered (Fig. 2). The deformation of 40% was imposed along x_3 axis. One FEM element was used, which contained a polycrystalline sample of 500 grains with random initial lattice orientations. An important check of correct FEM calculations (in explicit version) is a low value of kinetic energy compared with internal energy (the kinetic energy should not exceed typically 10% of the internal energy during the process [2]). Our result confirms a very good proportion: the internal energy is about 10^6 times higher than the kinetic one (Fig. 3).

The tensile fcc textures predicted by FEM+LW algorithm and solely by LW model are compared with experimental texture for α-brass in Fig. 4. We observe a good agreement: two principal components of experimental textures, i.e., <111> and <100> fiber orientations, appear in the LW and FEM+LW predicted textures.

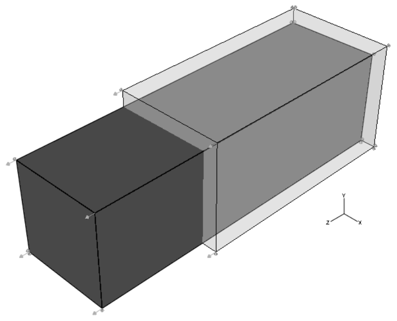

FIGURE 2: Geometry of uniaxial tensile test.

The main conclusions are:

- the calculation tool basing on FEM and taking into account the crystallographic nature of polycrystaline materials was created (FEM+LW model),
- the correctness of the FEM+LW model was checked considering the example of uniaxial deformation test; one FEM element was used and it contained a polycrystalline sample with 500 grains,
- the created calculation tool can be used to study deformation processes with more complicated geometries. [3]

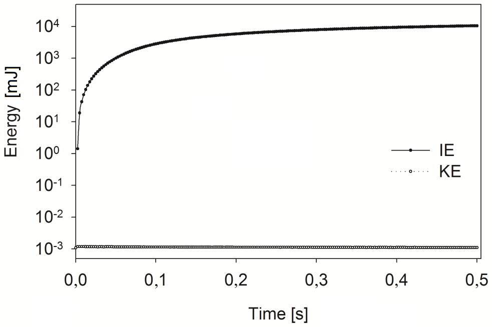

FIGURE 3: Variation of internal and kinetic energy vs. calculation time (proportional to deformation). The total simulation time was 0,5 s.

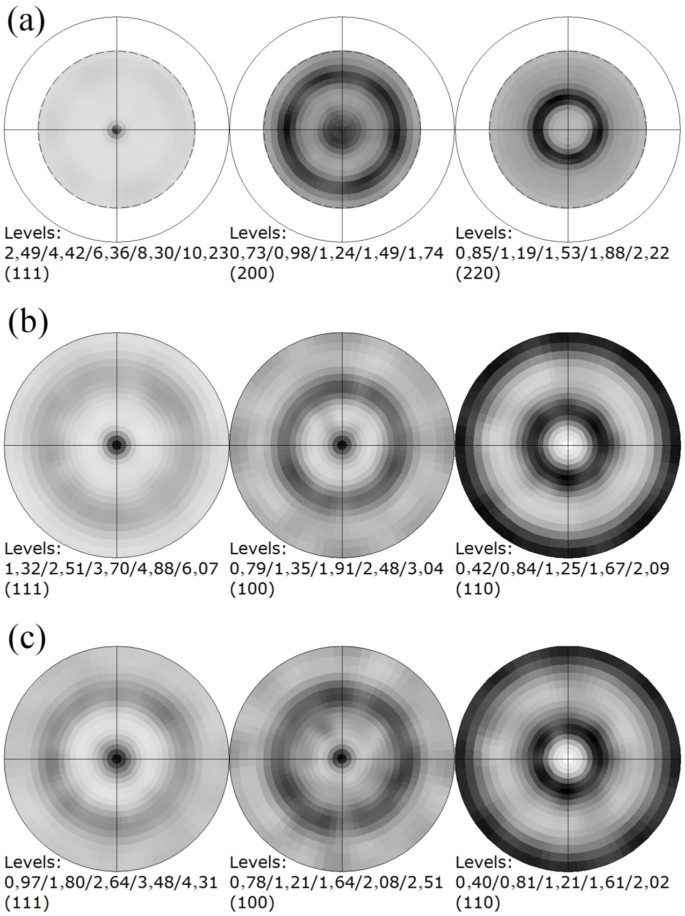

FIGURE 4: Experimental and predicted tensile textures of α-brass: (a) experimental tensile test texture of α-brass, (b) tensile texture predicted by LW model only, (c) tensile texture predicted by FEM+LW model.

⋆ ⋆ ⋆

The support of the Polish National Centre for Science (NCN), by the grant: DEC-2011/01/B/ST8/07394, is acknowledged.

[1] K. Wierzbanowski, J. Jura, W. G. Haije, R. B. Helmholdt, *Cryst. Res. Technol.* **27**, 513 (1992).

[2] Abaqus V6.10. Analysis users manual (Providence, RI, USA: Abaqus Inc., 2010).

[3] S. Wroński, K. Wierzbanowski, B. Bacroix, M. Wróbel, E. Rauch, F. Montheillet, M. Wroński, *Arch. Metall. Mater.* **54**, 89 (2009).

Hund's rule induced spin-triplet superconductivity coexisting with magnetic ordering in the degenerate band Hubbard model

Michał Zegrodnik

Faculty of Physics and Applied Computer Science, AGH University of Science and Technology, Mickiewicza 30, 30-059 Kraków, Poland

Supervisor: Józef Spałek

The Hartree-Fock approximation combined with the Bardeen-Cooper-Schrieffer (BCS) method is applied for the degenerate band Hubbard model to analyze the coexistence of spin-triplet superconductivity with ferromagnetism and antiferromagnetism. In the presented approach the Hund's rule exchange term is responsible for both pairing mechanism and magnetic ordering. The proper phase diagrams are presented and the influence of the intersite hybridization on the stability of considered phases is discussed. Additionally, the calculated temperature dependences of superconducting gaps and magnetic moment are shown.

It is believed that Sr_2RuO_4,[1] UGe_2,[2], and URhGe[3] are the candidates for the spin-triplet superconductors. The last two are particularly interesting as the paired state appears inside the ferromagnetic phase. It has been suggested by a proper qualitative analysis[4–6] that the intra-atomic Hund's rule can lead to the coexisting superconducting and magnetically ordered phases. In this letter we further discuss the idea of real-space spin-triplet pairing in the regime of weakly correlated particles and include both inter-band hybridization and corresponding Coulomb interactions. We think that this relatively simple approach is relevant to the mentioned at the beginning ferromagnetic superconductors because of the following reasons. Even though the effective exchange (Weiss-type) field acts only on the spin degrees of freedom, it is important in determining the second critical field of ferromagnetic superconductor in the so-called Pauli limit,[7–9] as the orbital effects in the Cooper-pair breaking process are then negligible. The appearance of a stable coexistent ferromagnetic-superconducting phase means, that either Pauli limiting situation critical field has not been reached in the case of spin-singlet pairing or else, the pairing has the spin-triplet nature, without the component with spin $S^z = 0$, and then the Pauli limit is not operative.

We begin with the extended orbitally degenerate Hubbard Hamiltonian which has the following form

$$\begin{aligned}\hat{H} = &\sum_{ij(i\neq j)ll'\sigma} t_{ij}^{ll'} a_{il\sigma}^{\dagger} a_{jl'\sigma} + U\sum_{il}\hat{n}_{il\uparrow}\hat{n}_{il\downarrow}\\ &+ (U'+J)\sum_{i}\hat{n}_{i1}\hat{n}_{i2}\\ &- J\sum_{ill'(l\neq l')}\Big(\hat{\mathbf{S}}_{il}\cdot\hat{\mathbf{S}}_{il'} + \frac{3}{4}\hat{n}_{il}\hat{n}_{il'}\Big),\end{aligned} \tag{1}$$

where $l=1,2$ label the orbitals. The first term describes electron hopping between atomic sites i and j. For $l \neq l'$ this term corresponds to inter-site, inter-orbital hybridization. Next two terms describe the Coulomb repulsion between electrons on the same atomic site. As one can see the third term contains the contribution that originates from the exchange interaction (J). The last term expresses the (Hund's rule) ferromagnetic exchange and is going to be regarded as responsible for the spin-triplet pairing mechanism. It can be expressed in terms of the spin-triplet pairing operators

$$\hat{A}_{i,m}^{\dagger} \equiv \begin{cases} a_{i1\uparrow}^{\dagger}a_{i2\uparrow}^{\dagger} & m=1,\\ a_{i1\downarrow}^{\dagger}a_{i2\downarrow}^{\dagger} & m=-1,\\ \frac{1}{\sqrt{2}}(a_{i1\uparrow}^{\dagger}a_{i2\downarrow}^{\dagger} + a_{i1\downarrow}^{\dagger}a_{i2\uparrow}^{\dagger}) & m=0.\end{cases} \tag{2}$$

The results presented here have been carried out for the case of square lattice with nonzero hopping t between nearest neighbors only. As we are considering the doubly degenerate band model, we make a simplifying assumption that the hybridization matrix element $\epsilon_{\mathbf{k}12} = \beta_{\mathrm{h}}\epsilon_{\mathbf{k}}$, where $\beta_{\mathrm{h}} \in [0,1]$ is the parameter, which specifies the hybridization strength. After applying the Hartree-Fock approximation to (1) and performing the transformation to the reciprocal space, one gets the following mean-field parameters in the resulting Hamiltonian

$$\begin{aligned} \Delta_{\pm 1} &\equiv -\frac{(J-U')}{WN}\sum_{\mathbf{k}}\langle \hat{A}_{\mathbf{k},\pm 1}\rangle, \\ \Delta_0 &\equiv -\frac{(J-U')}{\sqrt{2}WN}\sum_{\mathbf{k}}\langle \hat{A}_{\mathbf{k},0}\rangle, \end{aligned} \tag{3}$$

$$S_l^z \equiv \frac{1}{2N}\sum_{\mathbf{k}}\big(\langle \hat{n}_{\mathbf{k}l\uparrow}\rangle - \langle \hat{n}_{\mathbf{k}l\downarrow}\rangle\big), \tag{4}$$

where N is the number of atomic sites and W is the bare band width. The Δ_m parameters have the interpretation of spin-triplet superconducting gaps, while S_l^z is the expectation value of the magnetic moment per site, per band. Because the considered bands are equivalent the magnetic moment fulfills the relation $S_1^z = S_2^z \equiv S^z$. Mean field parameters (3) and (4) are used to define the following phases

- normal state (**NS**): $\Delta_{\pm 1} = 0$, $S^z = 0$,
- pure superconducting phase type A (**A**): $\Delta_{\pm 1} \equiv \Delta \neq 0$, $S^z = 0$,
- pure saturated ferromagnetic phase (**SFM**): $\Delta_{\pm 1} = 0$, $S^z = S^z_{\mathrm{max}} \neq 0$,
- pure nonsaturated ferromagnetic phase (**FM**): $\Delta_{\pm 1} = 0$, $0 < S^z < S^z_{\mathrm{max}}$,
- saturated ferromagnetic phase coexistent with superconductivity of type A1 (**A1+SFM**): $\Delta_1 \neq 0$, $\Delta_{-1} = 0$, $S^z = S^z_{\mathrm{max}} \neq 0$,
- nonsaturated ferromagnetic phase coexistent with superconductivity of type A1 (**A1+FM**): $\Delta_1 \neq 0$, $\Delta_{-1} = 0$, $0 < S^z < S^z_{\mathrm{max}}$.

One could also consider the so called superconducting phase of type B for which $\Delta_0 = \Delta_{\pm 1} \neq 0$. However this phase never coexists with magnetic ordering. Moreover in the absence of magnetic ordering the A phase has always lower free energy than the B phase. Therefore the superconducting B phase is absent in the following discussion.

In the case of antiferromagnetic ordering one has to divide the system into two interpenetrating sublattices A and B. The average staggered magnetic moment of electrons on each of the $N/2$ sublattice A sites is equal, $\langle S_i^z\rangle = \langle S_A^z\rangle$, whereas on the remaining $N/2$ sublattice B sites we have $\langle S_i^z\rangle = \langle S_B^z\rangle \equiv -\langle S_A^z\rangle$. Following this division one has to introduce the sublattice gap parameters $\Delta_{\pm 1A}$ and $\Delta_{\pm 1B}$ which are defined analogically as (3) but with regard to each of the sublattices separately. The sublattice gap parameters fulfill the relations

$$\begin{aligned} \Delta_{+1A} = \Delta_{-1B} \equiv \Delta_+ \ , \\ \Delta_{-1A} = \Delta_{+1B} \equiv \Delta_- \ . \end{aligned} \tag{5}$$

The considered here antiferromagnetically ordered phases are defined as follows

- pure antiferromagnetic phase (**AF**): $\Delta_{\pm 1A(B)} = 0$, $S^z_s \neq 0$,
- coexistent superconducting and antiferromagnetic phase (**SC+AF**): $\Delta_{\pm 1A(B)} \neq 0$, $S^z_{\mathrm{s}} \neq 0$,

where the S^z_{s} is the so-called staggered magnetic moment. By using the Bogolubov-Nambu-de Gennes scheme one can diagonalize the Hartree-Fock Hamiltonian and construct the set of self consistent equations for all the mean field parameters and chemical potential. For given values of the microscopic parameters U, U', J, β_{h}, n, the set of self-consistent equations has several solutions that correspond to different phases. The free energy can be evaluated for each of the solutions and the one that corresponds to the lowest free energy is regarded as the stable phase.

The numerical calculations have been carried out for $U'{=}U{-}2J$, which is usual for $3d$ electrons. For $U'{>}J$ the interorbital Coulomb repulsion suppresses the pairing mechanism, so the necessary condition for the spin-triplet paired phases to appear in our model is $U < 3J$. It represents a rather stringent condition as usually for $3d$ metals we have $U \sim 3J$. This may explain why only in few compounds the coexistent superconducting and ferromagnetic phase has been indeed observed.

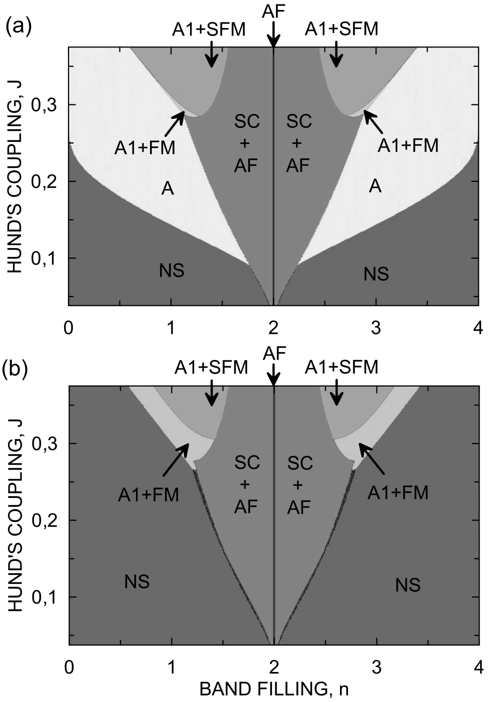

Figure 1: Phase diagrams in (n, J) space for $k_B T/W = 10^{-4}$; $\beta_h = 0{,}0$ (a) and $\beta_h = 0{,}11$ (b).

In Fig. 1 we present the phase diagrams in (n, J) space for two different values of the β_h parameter. It can be seen that they contain regions of stability of pure spin-triplet superconducting phase as well as superconducting phase coexisting with either ferromagnetism or antiferromagnetism. The appearance of the AF state for half filling ($n = 2$) corresponds to the fact that the bare Fermi-surface topology has a rectangular structure with $Q{=}(\pi, \pi)$ nesting. The symmetry of the phase diagrams with respect to half-filled band situation is a manifestation of the particle-hole symmetry, since the bare density of states is symmetric with respect to the middle point of the band. One can see from the presented diagrams that the influence of hybridization is significant quantitatively when it comes to the superconducting phase A, as for $\beta_h{=}0{,}11$ the region of stability of this phase has disappeared completely from the diagram mainly in favor of the NS phase. Moreover due to hybridization the region of stability of the A1+SFM phase narrows down in favor of the A1+FM phase. Antiferromagnetically ordered phase is not affected much by the rise of the β_h parameter. The diagram in (n, T) space (Fig. 2) shows how the critical temperature corresponding to A and SC+AF phases depends on the band filling.

The temperature dependences of the gap parameters and staggered magnetic moment in the SC+AF phase for selected values of n and J are shown in Fig. 3. It is clearly seen from the plots that while the temperature is being raised the system undergoes two phase transitions. The first one is the transition from SC+AF to AF, when the superconducting gaps Δ_+ and Δ_- close in the critical temperature T_S. The second one is the transition from AF to NS, when the staggered structure of the system is destroyed in the Néel temperature T_N. With the increase of the hybridization strength the critical temperature T_S decreases slightly, while the Néel temperature increases. The transition temperature ratio $T_N/T_S \approx 10$. In Fig. 4 we show similar plots but for the case of superconductivity coexisting with ferromagnetism. Analogously as in the case of SC+AF, the system undergoes two phase transitions. The influence of hy-

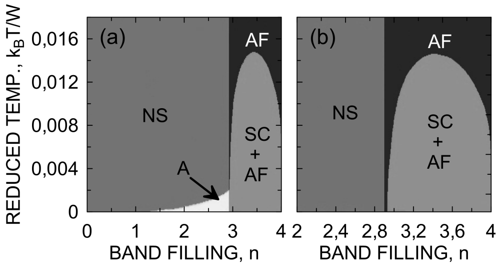

Figure 2: Phase diagrams in (n, T) space for $J{=}0{,}175$; $\beta_h{=}0{,}0$ (a) and $\beta_h{=}0{,}11$ (b).

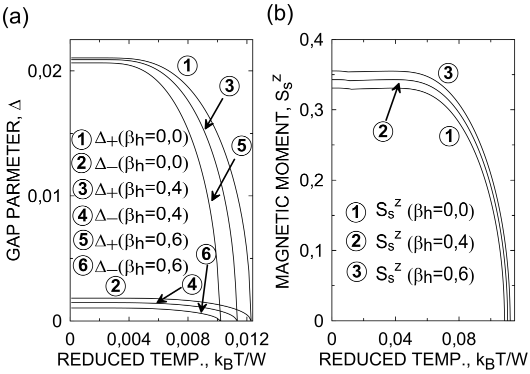

FIGURE 3: The temperature dependences of superconducting gaps (a) and magnetic moment (b) corresponding to the SC+AF phase for $n = 1{,}9$; $J = 0{,}175$.

bridization on the temperature dependences is also similar as in the case of SC+AF phase. This time the transition temperature ratio $T_C/T_S \approx 5$.

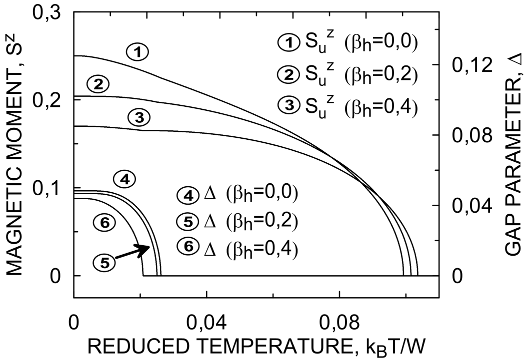

FIGURE 4: The temperature dependences of the superconducting gap and magnetic moment corresponding to A1+FM phase for $n = 1{,}0$; $J = 0{,}31625$.

In this letter we have carried out the Hartree-Fock analysis of the hybridized degenerate band Hubbard model with both spin-triplet pairing and magnetism induced by the Hund's rule. We have determined the regions of stability of the pure paired phase as well as paired phase coexisting with magnetic ordering. We have discussed the effect of hybridization which reduces significantly the stability regime of the A phase as well as decreases the critical temperature of all the superconducting phases considered. The influence of hybridization on the region of stability of SC+AF phase is not significant. It should be mentioned that the easiness with which the superconducting phase is accommodated within the antiferromagnetic phase is the result of the fact that the SC gaps have a intraatomic origin and the corresponding spins have then the tendency to be parallel. Therefore the spins do not disturb largely the staggered structure, which is of interatomic character.

M. Z. has been partly supported by the EU Human Capital Operation Program, Polish Project No. POKL.04.01.01-00-434/08-02. J. S. acknowledges the financial support from the Foundation for Polish Science (FNP) within project TEAM.

⋆ ⋆ ⋆

[1] Y. Maeno, H. Hashimoto, K. Yoshida, S. Nishizaki, T. Fujita, J, G. Bednorz, F. Lichtenberg, *Nature* **372**, 532 (1994).
[2] S. S. Saxena, P. Agarwal, K. Ahilan, F. M. Grosche, R. K. W. Haselwimmer, M. J. Steiner, E. Pugh, I. R. Walker, S. R. Julian, P. Monthoux, G. G. Lonzarich, A. Huxley, I. Sheikin, D. Braithwaite, J. Flouquet, *Nature* **406**, 587 (2000)
[3] N. Tateiwa, T. C. Kobayashi, K. Hanazono, K. Amaya, Y. Haga, R. Settai, Y. Onuki, *J. Phys.: Condens. Matter* **13**, 117 (2001).
[4] K. Klejnberg, J. Spałek, *J. Phys.: Condens. Matter* **11**, 6553 (1999).
[5] J. Spałek, *Phys. Rev.* B **63**, 104513 (2001).
[6] J. Spałek, P. Wróbel, W. Wójcik, *Physica C* **387**, 1 (2003).
[7] A. M. Clogston, *Phys. Rev. Lett.* **9**, 266 (1962).
[8] L. W. Gruenberg, L. Gunther, *Phys. Rev. Lett.* **16**, 996 (1966).
[9] K. Maki, T. Tsuento, *Prog. Theor. Phys.* **31**, 945 (1964).

Thermoelectric and magnetic properties of Mn-doped Mg_2Si studied from the electronic structure calculations

Piotr Zwoleński

Faculty of Physics and Applied Computer Science, AGH University of Science and Technology, Mickiewicza 30, 30-059 Kraków, Poland

Supervisor: Janusz Toboła

Analysis of the electronic structure of Mg_2Si compound obtained from the fully self-consistent Korringa-Kohn-Rostoker method with the coherent potential approximation (KKR-CPA) is presented, focusing on its thermoelectric properties. We also consider Mn dopant for which Mg lattice site was found to be preferred from the formation energy calculation. Mn impurity in Mg_2Si exhibits a strong polarisation of DOS resulting in large magnetic moment c.a. 4 μ_B, which suggests a magnetic semiconducting-like state as an energy gap is preserved at the Fermi level. A type of charge conduction upon Mn doping is discussed detecting the E_F position with respect to conduction/valence band. Furthermore, thermopower was estimated from the simplified Mott's formula and the rigid band model was employed to mimic doping.

The phenomena in solids in which temperature gradient $\vec{\nabla}T$ is converted into electric voltage U (or electric current if the circuit is closed) is called Seebeck effect $\vec{E}=S\vec{\nabla}T$ and its magnitude is expressed by the Seebeck coefficient S (thermopower), which is characteristic for a material and depends on temperature.[1] The efficiency of thermoelectric phenomena is usually defined by the figure of merit:

$$Z = \frac{S^2\sigma}{\kappa} , \qquad (1)$$

where S is the Seebeck coefficient, σ is an electrical conductivity and κ is a thermal conductivity.[2] The Z factor (in K^{-1}) is usually multiplied by temperature T to obtain dimensionless value that allows to easily compare different thermoelectric materials. The more efficient thermoelectric material is, the higher ZT possesses, therefore it should exhibit both high thermopower and electrical conductivity, while thermal conductivity should be as low as possible. Because of competition among those properties, balance must be achieved which strongly limits the effectiveness of thermoelectric effects.

Quantum electrodynamics calculations based on Density Functional Theory (DFT) equations belong to well-established theoretical tools that permit investigations of electronic structure of crystals. One of the DFT technique, namely Korringa-Kohn-Rostoker method (KKR), was applied to study electronic structure and selected physical properties of Mg_2Si compound. On the whole, DFT based calculations offer many possibilities in condensed matter physics as for example total energy of a compound to analyse its formation energy (see below) in the ground state[3] (T=0 K) and to investigate its crystal stability. Electronic structure itself contains important information responsible for electronic transport properties such as electron's velocity and life-time or energy gap. Besides, electronic densities of states (DOS) are useful to estimate thermopower of investigated compound. In the case of investigations of magnetism, spin-polarised calculations allowed to study local magnetic moments on individual crystallographic sites as well as total magnetic moment per unit cell, assuming magnetic structure type.

Mg_2Si is the lighter member of Mg_2X (X = Si, Ge, Sn) compounds, a promising family of thermoelectric materials due to low volume density and non toxic element containment.[4] Their optimal working temperature range is expected from 500 to 900 K.[2] X is IV A group element in the periodic table of elements and it was observed that semiconducting properties decrease with increasing atomic number (Mg_2Pb is a metal). Mg_2X materials form crystals of anti-fluoride structure that belongs to $Fm\bar{3}m$ space group (no. 225). X atoms occupy face centred cubic lattice ($4a$, Wyckoff's positions) and Mg atoms are located in tetrahedral holes ($8c$). Experimental crystal structure data was used to perform *ab initio* calculations. Alloying and doping allow to beneficially modify properties of these compounds. Hence, one should focus on searching suitable dopants (n- or p-type) and alloy compositions that may increase thermoelectrical effectiveness. However, we should also bear in mind that many dopants may appear unstable just after chemical synthesis or may also decompose after annealing. However in principle thermodynamic phenomena are not accounted for the formation energy analysis.

Electronic structure of ordered Mg_2Si compound was computed using the KKR method based on the Green function Multiple Scattering Theory.[5,6] Chemical disorder (alloying or doping) modifies translational symmetry of crystals and generally introduces randomness to the lattice sites. In order to recover crystal symmetry the coherent potential approximation (CPA) was incorporated to the KKR method allowing to compute electronic structure in disordered systems. The crystal potential of the muffin tin form was constructed using the local density approximation (LDA), with von Barth and Hedin parametrization for the exchange correlation part. Experimental values of lattice constants[4] were applied in calculations. Fig. 1 presents calculated spin-polarised electronic DOS of $Mg_2Si_{0,99}Mn_{0,01}$. We see that there is an energy gap in the vicinity of E_F. Doping with Mn shifts the Fermi level into the valence band therefore the Mn impurity (on the Si site) behaves as p-type dopant. The computed energy differences between energy bands at standard high-symmetry points in the first Brillouin Zone of fcc Mg_2X are collected in the Table 1.

As mentioned already, electronic DOS $n(E)$ contains useful information on thermopower of investigated compound. Indeed, the Seebeck coefficient that depends on DOS can be obtained from the simplified Mott's formula:[7]

$$\frac{S(T)}{T} = -\frac{\pi^2}{3}\frac{k_B^2}{e}\left[\frac{d\ln n}{dE}\right]_{E=E_F}, \qquad (2)$$

where k_B is the Boltzmann constant, $e > 0$ is electrical charge. This formula is valid under assumption that mobility of electrical charge carriers is constant. Hereafter, such approach allows only to determine linear term of thermopower (generally, $S(T) = AT + BT^3 + \ldots$). The Figs. 2 and 3 show estimated thermopower of Mg_2Si assuming that bands are not affected by electronic states of dopant (rigid band approximation). It is valid when the crystal potential of impurity is close to that of substituted element (e.g. Sb and Sn).

Dopants have an influence on crystal stability of doped product that could be character-

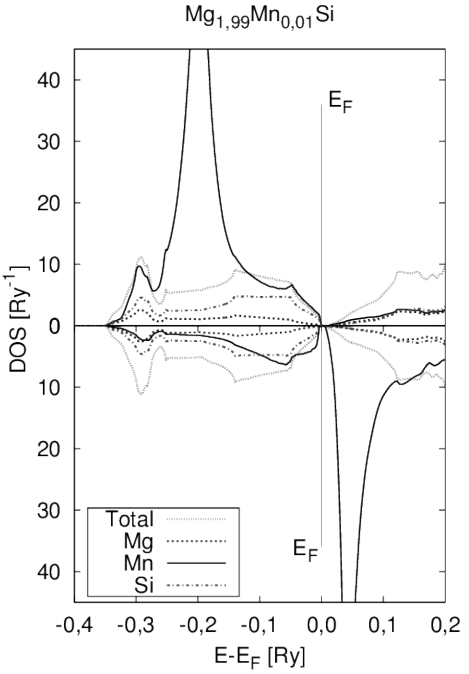

FIGURE 1: Calculated spin-polarized DOS of $Mg_{1,99}Mn_{0,01}Si$. Top graph is for spin-up electrons, bottom one for spin-down electrons.

TABLE 1: Lattice constants a and calculated energy gaps E_g of Mg_2X compounds.

Compound	a [Å]	$E_g(X-\varGamma)$ [eV]	$E_g(K-\varGamma)$ [eV]	$E_g(X-L)$ [eV]
Mg_2Si	6,3380	0,16	0,71	0,80
Mg_2Ge	6,3849	0,18	0,77	0,85
Mg_2Sn	6,7650	—	0,34	0,57

ized by formation energy E_{form}. Two substitutions are considered: dopant can be located on Mg or Si site, accounting for possible chemical reaction of magnesium silicide synthesis from elements

$$2\text{Mg} + \text{Si} = \text{Mg}_2\text{Si}$$

defines formation energy of this compound

$$E^{\text{Mg}_2\text{Si}}_{\text{form}} = E(\text{Mg}_2\text{Si}) - 2E(\text{Mg}) - E(\text{Si}).$$

Chemical potentials for magnesium and silicon have limited variation range:

$$\mu(\text{Mg}) \leq E(\text{Mg}),\ \ \mu(\text{Si}) \leq E(\text{Si}),$$

$$2\mu(\text{Mg}) + \mu(\text{Si}) = E(\text{Mg}_2\text{Si}).$$

Each E in the aforementioned equations represents total energy of crystal (bulk) systems (i.e. fcc Si, hcp Mg and Mg_2Si) as calculated from the KKR-CPA computations. This leads to two border cases, which bounds the possible ranges of Mg and Si chemical potential variation:[3]

Mg-rich limit :
$\mu(\text{Mg}) = E(\text{Mg})$,
$\mu(\text{Si}) = E(\text{Mg}_2\text{Si}) - 2E(\text{Mg})$.
Si-rich limit :
$\mu(\text{Si}) = E(\text{Si})$,
$\mu(\text{Mg}) = 0{,}5(E(\text{Mg}_2\text{Si}) - E(\text{Si}))$.

Two possible locations of dopant in Mg_2Si are assumed — on Mg or Si lattice, e.g. for manganese:

$$(2-x)\text{Mg} + \text{Si} + x\text{Mn} = \text{Mg}_{2-x}\text{Mn}_x\text{Si},$$

and

$$2\text{Mg} + (1-x)\text{Si} + x\text{Mn} = \text{Mg}_2\text{Si}_{1-x}\text{Mn}_x.$$

Formation energy for these reactions is defined as follows:

$$\begin{aligned} E^{\text{Mg}}_{\text{form}} &= E(\text{Mg}_{2-x}\text{Mn}_x\text{Si}) - (2-x)\mu(\text{Mg}) \\ &\quad -\mu(\text{Si}) - xE(\text{Mn}), \\ E^{\text{Si}}_{\text{form}} &= E(\text{Mg}_2\text{Si}_{1-x}\text{Mn}_x) - 2\mu(\text{Mg}) \\ &\quad -(1-x)\mu(\text{Si}) - xE(\text{Mn}). \end{aligned}$$

Negative sign of formation energy in principle imply stability of doped compound, but in finite temperatures it is required to take lattice vibrations into account (neglected here).[8] Formation energy can be helpful in dopant site preference determination in the ground state. Impurity locates on the site where formation energy of system is lower than on the other site in both limits. Mg-site is preferred in the case of 1% dilution of Mn in Mg_2Si in the ground state.

Negative formation energy in principle leads to compound stability in the ground state. At temperatures above ($T = 0$ K), it is demanded to take into account crystal lattice vibrations, through entropy factor, which is difficult to obtain in disordered systems. However the lattice vibrations in ($T > 0$ K) will stabilize structure, at least for some con-

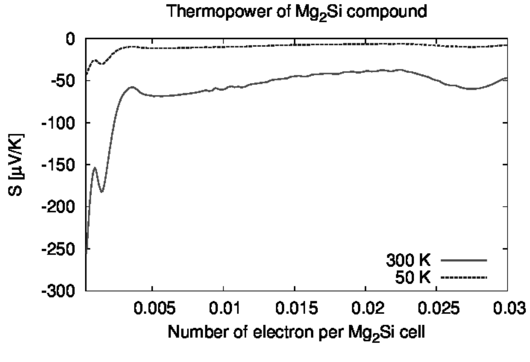

FIGURE 2: Calculated thermopower of n-type Mg_2Si compound as a function of concentration of donated electrons.

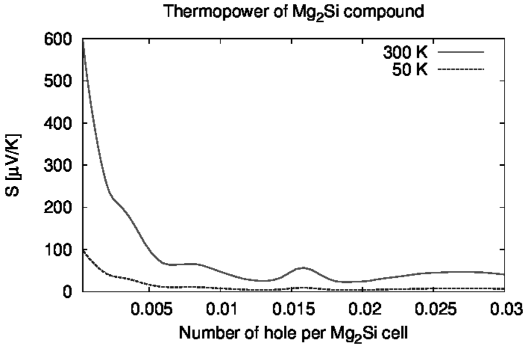

FIGURE 3: Calculated thermopower of p-type Mg_2Si compound as a function of concentration of holes from acceptor dopant.

centrations x. It is important to mention that determination of the site preference is very sensitive to dopant crystallographic structure type and require very accurate total energy calculations with very high convergence, up to 5 decimal places.

The research on the magnetic dopants of magnesium silicide at this stage is only theoretical. To our knowledge, there was no experiments conducted to verify magnetic properties of manganese doped Mg_2Si. The 1% transition metal Mn impurity, diluted in Mg_2Si exhibit a large spin-polarization of d-states. Magnetic behaviour is rather diluted magnetic semiconducting than half-metallic ferromagnetic. Calculated magnetic moments of Mn-doped Mg_2Si are 3,9 μ_{B}/f.u. on the Mg-site and 3,3 μ_{B}/f.u. on the Si-site. The case of Mn on the Mg-site is interesting from the point of view of thermoelectric power enhancement (low DOS for spin-up electrons and high DOS value change at once favours large Seebeck coefficient according to the Mott's formula). At higher concentrations the Fermi level crosses valence and conduction bands for both spin orientations of electrons.

I would like to thank my supervisor Prof. Janusz Toboła and Prof. Stanisław Kaprzyk for providing Fortran packages (RKKR005 and RCPA005) for *ab initio* electronic structure calculations. This work was supported by the EU Human Capital Operation Program, Polish Project No. POKL.04.01.01-00-434/08-02.

⋆ ⋆ ⋆

[1] M. Rowe, Thermoelectrics Handbook, Chap. 1. (CRC, Boca Raton, FL, 2006).

[2] K. Mars, H. Ihou-Mouko, G. Pont, J. Tobola, H. Scherrer, *J. Elect. Mater.* **38**, 1360 (2009).

[3] J. Tani and H. Kido, *Intermetallics* **16**, 418 (2008).

[4] V. Zaitsev, M. Fedorov, I. Eremin, E. Gurieva, Thermoelectrics Handbook: Macro to Nano-Structured Materials, Chap. 29 (CRC press, New York, 2005).

[5] A. Bansil, S. Kaprzyk, P. E. Mijnarends, J. Tobola, *Phys. Rev. B* **60**, 13396 (1999).

[6] T. Stopa, S. Kaprzyk, J. Tobola, *J. Phys. Condens. Mat.* **16**, 4921 (2004).

[7] N. Mott, *Adv. Phys. 13, 325 (1964)*, *Phil. Mag.* **26**, 1249 (1972).

[8] J. Tani, H. Kido, *Comp. Mater. Sci.* **42**, 531 (2008).

[9] G. Nolas, D. Wang M. Beekman, *Phys. Rev. B* **76**, 235204 (2007).

[10] V. K. Zaitsev, M. I. Fedorov, E. A. Guriewa, I. S. Eremin, P. P. Konstantinov, A. Y. Samunin, M. V. Vedernikov, *Phys. Rev. B* **74**, 0452071 (2006).

NUCLEAR METHODS IN MATERIALS SCIENCE AND ENVIRONMENTAL RESEARCH

A „front-flush” mode implementation in the GC system with a μ-ECD detector in high-quality measurements of atmospheric N_2O mixing ratios

Michał Gałkowski

Faculty of Physics and Applied Computer Science, AGH University of Science and Technology, Mickiewicza 30, 30-059 Kraków, Poland

Supervisor: Kazimierz Różański

The nitrous oxide (N_2O), both ozone-depleting and powerful greenhouse gas, has been gaining attention of scientists and policy makers for some years now. New gas analysers based on laser spectrometry have only recently been introduced to measure atmospheric concentrations of N_2O. However, their wider usage in trace gas monitoring is hampered by their high costs. Therefore, a majority of high-quality measurements of atmospheric N_2O mixing ratios is still performed using gas chromatography (GC) technique. This is especially true for the monitoring networks conducting quasi-continuous measurements of N_2O.

Nowadays, nitrous oxide (N_2O) is the third most important greenhouse gas and the first most important ozone-depleting substance in the Earth's atmosphere. The global warming potential (GWP) of N_2O calculated over 100-year time interval is approximately 310 times larger than that of carbon dioxide.[1] Although the ozone-depleting potential (ODP) of this gas is equal only ca. 0,017 of that calculated for CFC-11, the overall impact of N_2O on the ozone layer is two times higher than that of CFC-11.[2] For the past 150 years the atmospheric concentrations of N_2O had been steadily increasing, with growing and still not fully understood impact on the environment.

The ice-core data demonstrate that atmospheric concentrations of nitrous oxide oscillated between 200 ppb during glacial periods and 270 ppb during interglacials.[3] During the last four thousand years, the N_2O mixing ratios fluctuated around 270 ppb, which means that the sources and sinks of this gas were approximately in balance. Since mid of the XIX century the atmospheric concentrations of N_2O started to rise, reaching ca 324 ppb in 2011.[4] The rate of this growth was not constant; it increased from ca. 0,15 ppb yr^{-1} between 1900 and 1955, to the value of approximately 1.0 ppb yr^{-1} during the period 2005 – 2011.[4] This growing presence of N_2O in the atmosphere is attributed to human activity.

Nitrous oxide emissions are reported, along with other greenhouse gases, in the framework of Kyoto Protocol (of which Poland is an Annex I party). Currently, there is a lack of high-quality information about variability of N_2O in the atmosphere over Central Europe across diverse spatial and temporal scales, as well as about typical levels of emissions of this gas from natural ecosystems and anthropogenic sources in the region.

In order to quantify both atmospheric loads and fluxes of N_2O, an ability to measure its mixing ratios with a high precision has to be established. Here we present the modification of an Agilent 6890N GC system equipped with a μ-ECD (Electron Capture Detector) that allows the user to measure the N_2O concentrations at relatively high precision.

In conventional analysis with the use of μ-ECD, the air is flushed through the analytical column and passes on to the detector. Due to the physicochemical attributes of the column filling (HaysepQ, 80/100 mesh in the described system), O_2 molecules have the lowest retention times, while N_2O follows closely behind. However, the detector is still influenced by the oxygen molecules, which results in a N_2O peak being generated on a downward

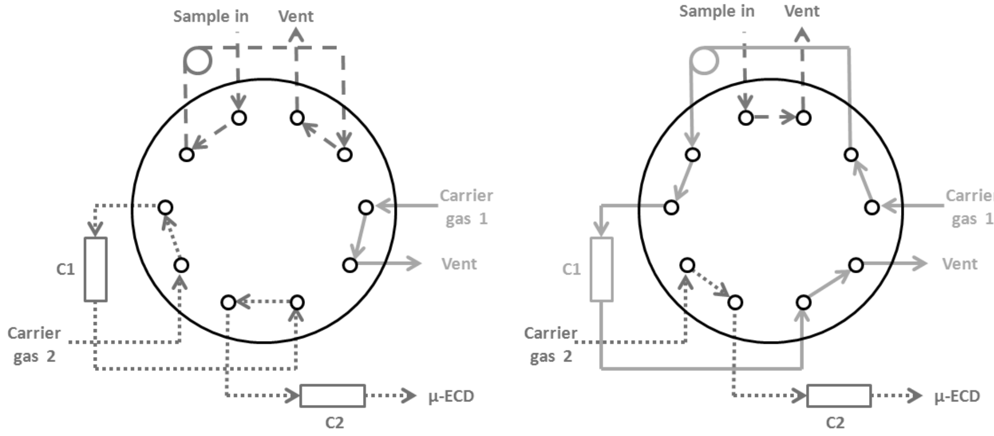

FIGURE 1: Layout of the „front-flush" GC system. Positions: A (left) — sampling, B (right) — injection.

slope of the O_2 peak on a chromatogram. By allowing the preceding O_2 peak to be vented before it enters the detector after the 10-port valve is switched to B position (see Fig. 1), the internal stability of the μ-ECD is maintained which assures better linearity of the detector and better stability of the instrument thus ensuring better overall precision of the analysis.

To test the performance of the GC system after the modifications, a large volume air sample (ca. 50 litres in aluminium cylinder) was repeatedly analysed (around 60 times). The air sample chosen for the test contained known concentrations of N_2O (350,5 ppb). The concentration of N_2O in the analysed sample was calculated using the following formula:

$$c_{\text{measured}}(i) = \frac{2c_{\text{known}}A_{\text{i}}}{[A_{\text{i-1}} + A_{\text{i+1}}]}\ , \tag{1}$$

where: $c_{\text{measured}}(i)$ is the i^{th} measured value, c_{known} is the assigned N_2O mixing ratio of of the analysed large-volume sample, A_{i} is the chromatograph peak area of the i^{th} measurement.

Fig. 2 presents the deviation of individual measurements from the mean value, as well as their distribution. For further analysis, we

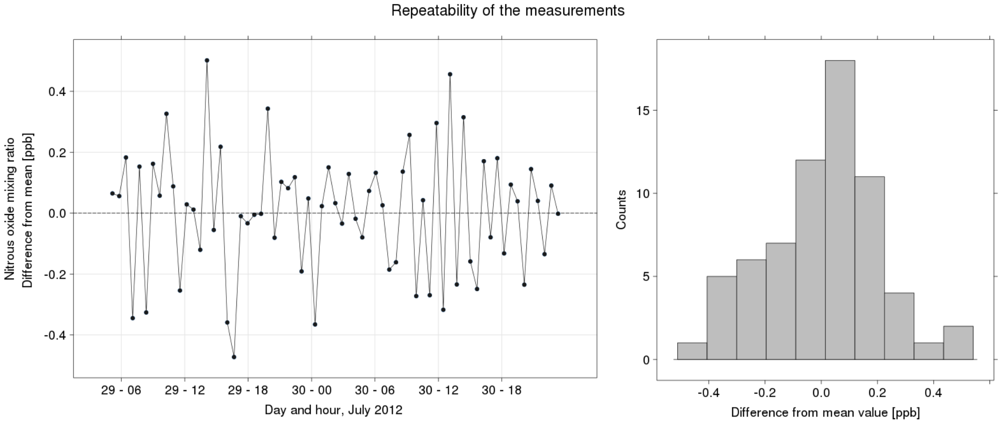

FIGURE 2: Results of the repeatability test. Left: results from the air tank measurements. Right: distribution of the results.

assume that there is no significant correlation between individual measurements. Based on a Shapiro-Wilk statistical test for normality of the distribution ($W = 0{,}984$, $p = 0{,}562$), we assume that the distribution of the measured values is normal. Thus, we can use the standard deviation of the distribution as an estimator of the single measurement uncertainty, which yields 0,20 ppb. This value is very close to the precision reported for more sophisticated analytical systems used currently in monitoring of atmospheric N_2O mixing ratios.[5]

Fig. 2 also shows that variations of individual measurements are larger during the daytime hours, which could indicate a feedback loop between the external measurement conditions such as temperature in the laboratory, power supply, etc., generally more stable during the night hours, and the measurement performance. A detailed study of the reasons behind apparent deterioration of measurement precision during daytime may lead to improvement of the overall performance of the analytical system and further reduction of the standard uncertainty, possibly even below 0,1 ppb.

One of main disadvantages of the front-flush mode is the long analysis time. Configuration of the inlet system forces all the gases with the retention times longer than O_2 to be flushed through the detector. In some cases, e.g. when analysing samples of soil gases, relatively large amounts of substances with high affinity to the column filling material generate late peaks that need to be flushed before the next analysis can be performed. In worst case this could last above 1 hour. However, typical duration of single analysis of atmospheric samples is in the order of 15 minutes.

Summarizing, the front-flush mode provides the opportunity to measure ambient concentrations of nitrous oxide with the precision recommended for state-of-the-art monitoring of greenhouse gas, without significant investments in the analytical infrastructure. The obtained precision (0,2 ppb) is only 2 times lower than that reported for the state-of-the-art laser spectrometers and comparable with more sophisticated GC systems. The front-flush mode applied to measurements of atmospheric N_2O mixing ratios may be particularly useful at those monitoring sites where high measurement frequency is not crucial.

⋆ ⋆ ⋆

1. P. Forster, V. Ramaswamy, P. Artaxo, Climate Change 2007: The Physical Science Basis. Contribution of Working Group I to the Fourth Assessment Report of the Intergovermental Panel on Climate Change (Cambridge University Press, Cambridge and New York, 2007).
2. A. R. Ravishankara, J. S. Daniel, R. W. Portmann, *Science* **326**, 123 (2009).
3. J. Flückiger, T. Blunier, B. Stauffer, J. Chappellaz, R. Spahni, K. Kawamura, J. Schwander, T. F. Stocker, D. Dahl-Jensen, *Global Biogeochem. Cy.* **18**, GB1020 (2004),
4. NOAA Earth Systems Research Laboratory, Nitrous Oxide Combined Data Set website (2012), http://www.esrl.noaa.gov/gmd/hats/combined/N_2O.html.
5. A. T. Vermeulen, A. Hensen, M. E. Popa, W. C. M. van den Bulk, P. A. C. Jongejan, *Atmos. Meas. Tech. Discuss.* **3**, 4169 (2010).

High-dose effects in the LiF:Mg,Cu,P (MCP-N) thermoluminescent detectors

Wojciech Gieszczyk

The Henryk Niewodniczański Institute of Nuclear Physics Polish Academy of Sciences, Radzikowskiego 152, 31-342 Kraków, Poland

Supervisor: Paweł Bilski

High-sensitive thermoluminescent (TL) detectors, LiF:Mg,Cu,P (MCP-N), have been investigated, with respect to their high-temperature emission, observed after doses up to hundreds of kGy. Emission spectra and TL glow curves were measured up to 550° C. Two ranges of emission were distinguished and denoted as the main (220 – 450 nm) and the long wavelength (450 – 800 nm) emission. The long wavelength emission was observed at the doses of 4 kGy and higher, indicating that such an amount of energy, deposited in the detector volume, makes additional recombination centers active. At the „B" peak temperature range (above 400° C) an average wavelength of emitted light was identical, as for the main TL glow peak, at low doses. It seems that high-dose, high-temperature emission of MCP-N occurs along the same recombination path, as the emission below 1 kGy. We suggested, that appearance of the „B" peak may be an effect of some clustering processes induced by the high density of radiation creating all kinds of defects. Then, the high-temperature emission from MCP-N may result from disintegration of such clusters, accompanied by the cascade detrapping processes.

LiF-based thermoluminescent detectors (TLDs), LiF:Mg,Cu,P (MCP-N), are widely used in the dosimetry of ionizing radiation. Their main advantages are small dimensions (typically 4,5 x 0,9 mm) combined with tissue equivalent composition (Z_{eff} = 8,4). This high-sensitive material can be used to measure doses of ionizing radiation from micrograys up to the saturation of response, which occurs around 1 kGy. Over this dose range the response of MCP-N does not exhibit supralinearity and the shape of the main dosimetric peak, located around 220°C (at $\beta = 2°\text{C}\,\text{s}^{-1}$), remains practically unchanged (see Fig. 1). Also the previous measurements of MCP-N emission spectra[1] showed that the spectrum does not undergo any changes, up to the saturation level, showing a narrow peak with a maximum around 360 nm. Recently it was found that, using MCP-N TL detectors, doses even higher than 1 MGy can be evaluated, when relevant procedures are applied.[2]

High-temperature structure of the MCP-N TL glow curves was many times described after irradiations with very high doses of γ-rays,[2,3] thermal neutrons,[4] protons,[5] and electrons.[6] These works indicate, that the shape of the glow curve of MCP-N TL detectors, after irradiation above 1 kGy, undergoes a complete alteration (see Fig. 1). Decrease of the amplitude of the main dosimetric peak is observed, with simultaneous growth of the peaks located between 250 – 400°C,

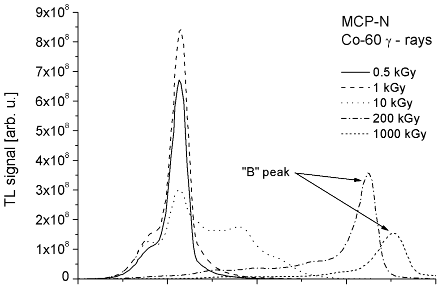

FIGURE 1: Non-normalized TL glow curves of LiF:Mg,Cu,P TL detectors, irradiated with Co-60 γ-rays doses of 0,5; 1; 10; 200 and 1000 kGy.

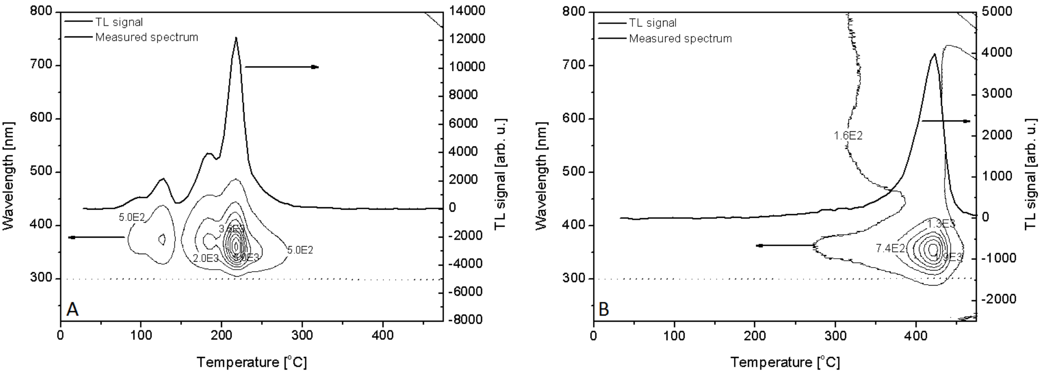

FIGURE 2: Contour plots of LiF:Mg,Cu,P emission spectra after irradiation with Co-60 γ-rays doses of 1 kGy (left panel) and 284 kGy (right panel). Corresponding TL glow curves obtained by summation over a whole wavelength range are also presented. Dotted lines indicate the level of 300 nm.

which are not visible below 1 kGy. This high-temperature structure undergoes further alterations after doses of 50 kGy and higher, when a new peak, at temperatures exceeding 400°C, becomes visible. This high-temperature TL glow peak was denoted as the „B" peak.[2] The mechanism of its formation remains still not explained. Moreover, previous papers[7] gave the evidence, that the behavior of this new TL peak, with increasing doses, is inconsistent to existing simple models of TL phenomenon.[8,9]

To get better understanding of the processes creating the high-temperature structure of the MCP-N TL glow curves, the measurements of high-dose, high-temperature emission spectra were performed. Detectors were irradiated with Co-60 γ-rays doses up to 284 kGy, at the Delft University of Technology, Delft, the Netherlands. The wavelength resolved readouts were performed using Ocean Optics QE65000 spectrometer combined with the Riso TL/OSL-DA-15A/B manual TLD reader, with a temperature resolution of 5°C. Heating was realized up to 550°C, at the constant heating rate, $\beta = 2°\mathrm{C\,s^{-1}}$. The TL emission spectra were recorded in a range of 220 – 800 nm. All measured spectra have been numerically corrected to the system response. For the authors knowledge, the present work constitutes the first attempt to determine the TL emission spectra of MCP-N TL detectors at the high temperature range.

Fig. 2 presents some examples of the contour plots of MCP-N emission spectra, measured for doses of 1 and 284 kGy. Corresponding TL glow curves, obtained by summation over the whole wavelength range, are also presented. Two ranges of emission can easily be distinguished, one, denoted as the main (short wavelength) emission and the second one, denoted as the long wavelength emission, ranging from 220 to 450 nm and from 450 to 800 nm, respectively. It is clearly visible that for the lowest doses only the short wavelength emission is present. Its maximum, for the dose of 1 kGy, is located around 350 nm and no significant changes are observed in this region with increasing dose. Only a slight shift of the whole spectrum occurs, about 10 – 20 nm towards shorter wavelength, similarly as described by Harris and Jackson, 1970[10] and Fairchild et al., 1978[11] for LiF:Mg,Ti. The long wavelength emission appears after doses of 4 kGy and higher, analogously as measured by Mandowska et al.[1] These results show that not all, available recombination centers, are always active. Some of them become activated on exposure to high density of ionizing radiation. Appearance of this additional emission band, with a maximum around 560 nm, is associated with the growth of the high-temperature TL peaks

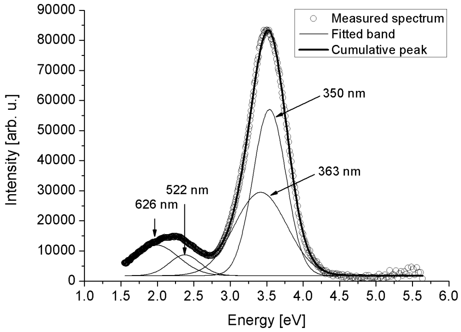

FIGURE 3: Deconvolution into single gaussian shape bands, performed in the energy domain, for the spectrum measured at the dose of 64 kGy.

on the TL glow-curve. All recorded data indicate that positions of the maxima of the high-temperature TL peaks correspond to the maximum of the long wavelength emission.

Deconvolution into single gaussian shape bands, performed in the energy domain, shows the following structure. The main emission consists of two components, located around 350 and 385 nm.[12,13] At lower doses both bands are markedly visible. At higher doses the band of 350 nm becomes dominant. The long wavelength emission can be fitted with at least two bands, located around 530 and 630 nm, but more complex structures are also possible. In the intermediate dose range intensities of the long wavelength bands are comparable. At higher doses the band of 630 nm is dominant. Gaussian deconvolution performed for the spectrum measured at the dose of 64 kGy is presented in the Fig. 3. Parameters of the fitted bands remain in a general agreement with previous measurements.[1]

Interesting behavior was observed at the temperature range of the „B" peak. In the Fig. 4, TL glow curves (full symbols) and data showing an average wavelength of the TL light (open symbols), emitted at given temperatures, are compared. The typical wavelength range of emission of MCP-N, for doses below 1 kGy, is 300 – 500 nm, with maximum around 360 nm (see Fig. 4(left panel)). The sharp growth of this curve, for temperatures above 350°C, visible also for the dose of 284 kGy (Fig. 4(right panel)), is just a high-temperature background. For doses >100 kGy, at low temperatures, the long wavelength emission is dominant in the MCP-N emission spectrum. It shifts the average wavelength of emitted light towards longer wavelengths (see Fig. 4(right panel). It is remarkable that at the temperature range of the „B" peak, an average wavelength of emitted light is practically the same, as for the main dosimetric peak, at low doses. It seems that the high-dose, high-temperature emission of MCP-N occurs along the same recombination path, as the emission below 1 kGy. A small difference results from different contributions of the long wavelength emission to the total spectrum, in case of the dose of 1 kGy and doses above 100 kGy. As a main result of this work we consider finding that the „B" peak's light emission is nearly the same as the main dosimetric peak's, at low doses. However, the process that shifts the high-dose, low-temperature emission of MCP-N towards longer wavelengths remains not explained.

In summary, the high-temperature emission spectra of MCP-N TL detectors, irradiated with doses up to hundreds of kGy, were measured up to 550°C. For doses exceeding 4 kGy a new, relatively weak, long wavelength emission was observed. Appearance of this additional emission indicates that some other recombination centers become active. The main emission band can be fitted with two gaussian shape peaks, located around 350 and 385 nm. At higher doses the first one is dominant. The long wavelength emission, located around 530 and 630 nm, was only observed at higher temperatures ($T>250$°C). Positions of the fitted bands do not change with increasing dose. Results of deconvolution remain in a general agreement with previous measurements.[1] At the temperature range of the „B" peak, an average wavelength of the emitted TL light is practically the same, as for the main dosimetric peak, at low doses, what suggests that high-dose, high-temperature emission of MCP-N occurs along the same recombination path as the emission below the saturation level.

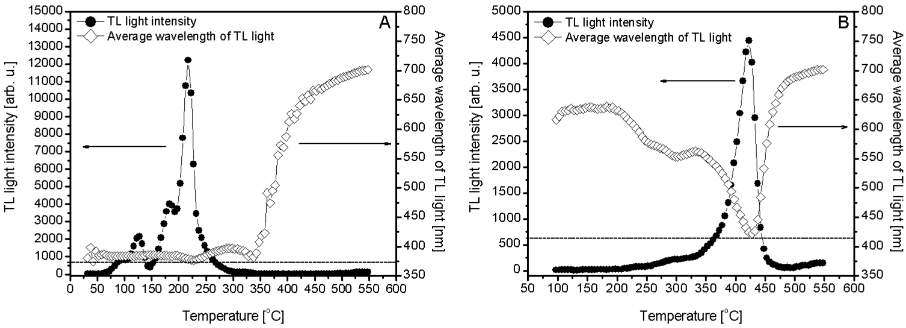

FIGURE 4: Comparison of the TL glow curves with data presenting an average wavelength of the TL light, emitted at given temperatures, for the doses of 1 kGy (left panel) and 284 kGy (right panel).

For an explanation of the observed changes in the glow curves and emission spectra one needs more knowledge about the nature of the trapping and recombination centers, which cannot be derived from the present data. The observations described in this paper suggest, that during the irradiation with doses above 1 kGy both new trappings and recombination centers are involved. It is speculated that some clustering processes will taken place.[14] The high temperature TL peak „B" may be then the result of disintegration of these clusters, accompanied by the cascade detrapping. Enlarging of the clusters with increasing dose may explain the shift of the „B" peak position towards higher temperatures, because in such a case the greater amount of the energy is needed to disintegrate them. However, the recombination of the detrapped charge producing the „B" peak takes place at an already existing luminescent centers, since its wavelength is the same as for the emission of the main peak.

Work performed within the strategic research project „Technologies supporting the development of safe nuclear power" financed by the National Centre for Research and Development (NCBiR). Research Task „Research and development of techniques for the controlled thermonuclear fusion", Contract No. SP/J/2/143234/11.

⋆ ⋆ ⋆

[1] E. Mandowska, P. Bilski, B. Obryk, A. Mandowski, P. Olko, J. Kim, *Radiat. Meas.* **45**, 579 (2010).

[2] B. Obryk, P. Bilski, M. Budzanowski, M. Fuerstner, M. Glaser, C. Ilgner, P. Olko, A. Pajor, Z. Stuglik, *IEEE Trans. Nucl. Sci.* **56**, 3759 (2009).

[3] P. Bilski, B. Obryk, P. Olko, E. Mandowska, A. Mandowski, J. L. Kim, *Radiat. Meas.* **43**, 315 (2008).

[4] B. Obryk, M. Glaser, I. Mandić, P. Bilski, P. Olko, A. Sas-Bieniarz, *Radiat. Meas.* **46** 1882 (2011).

[5] B. Obryk, P. Bilski, M. Glaser, M. Fuerstner, M. Budzanowski, P. Olko, A. Pajor, *Radiat. Meas.* **45**, 643 (2010).

[6] P. Bilski, B. Obryk, Z. Stuglik, *Radiat. Meas.* **45**, 576 (2010).

[7] B. Obryk, 2010. Ph. D. Thesis, (Institute of Nuclear Physics PAN, Krakow).

[8] A. J. J. Bos, *Radiat. Meas.* **41**, S45 (2007).

[9] S. W. S. McKeever, Thermoluminescence of solids (Cambridge University Press, Cambridge, 1985).

[10] A. M. Harris, J. H. Jackson, *J. Phys.* **3**, 624 (1970).

[11] R. G. Fairchild, P. L. Mattern, K. Lengweiler, P. W. Levy, *J. Appl. Phys.* **49**(8), 4512 (1978).

[12] K. Meijvogel, A. J. J. Bos, *Radiat. Meas.* **24**, 239 (1995).

[13] K. Meijvogel, A. J. J. Bos, P. Bilski, P. Olko, *Radiat. Meas.* **24**, 411 (1995).

[14] A. Mandowski, *Radiat. Meas.* **43**, 167 (2008).

Krypton-85 and radioxenon isotopes sampling and detection

Paweł Janowski

The Henryk Niewodniczański Institute of Nuclear Physics Polish Academy of Sciences, Radzikowskiego 152, 31-342 Kraków, Poland

Supervisor: Jerzy Wojciech Mietelski

Design, development and test of a method of sampling and measurement of krypton-85 and capturing of radioxenons are described. Sampling at ambient temperature on a charcoal trap and its results in gamma ray spectrometry measurements is discussed. The first capturing efficiency at the level of ca 5 % was achieved and is going to be improved further.

Radioisotopes of krypton and xenon are short-living radionuclides and do not occur in nature.[1] They are released to the environment first of all by normally operated nuclear power plant or during nuclear tests. Besides, they also appear in increased amounts near sites of manufacturing spent nuclear fuel and radiopharmaceutical industry (for example ^{133}Xe or $^{81\mathrm{m}}$Kr being used in lungs diagnostic). These noble gases are emitted to the atmosphere even in cases of underground nuclear explosions, when other radioactive substances may not be released over the ground.

Because of this monitoring of short-living radioisotopes of xenon in the atmospheric air is a good system for detecting undeclared nuclear activities (including conducting nuclear weapon tests) against the Comprehensive Test Ban Treaty (CTBT). Therefore, the CTBT Organization (CTBTO) in 1999 has formed an informal group of experts, the developers of radioactive xenon measurement systems. The group was named International Noble Gas Experiment (INGE) and it objectives were to develop and test systems of detecting radioactive isotopes of xenon. All four of presented systems meet the requirements and have been approved for commercial production.

Krypton was omitted in this part of International Monitoring System (IMS) which aims in detecting undeclared nuclear activities all over the world using stations measuring radionuclides of noble gases. It is because of its relatively long half-life of its most important isotope, Kr-85 (10,7 years); already existing background of Kr-85 in the atmosphere is too large to detect small differences in its level. Krypton-85 is simply still accumulated in the air. Other radioisotopes of krypton are too short-living for being used in qualitative measurements; their half-times are shorter than 5 h so they cannot be detect at large distances from the source.

Regarding planned development of polish nuclear industry (i.e. building first nuclear power plants) it is very required to measure continuously the level of radioactive noble gases in the atmospheric air.

Created sampling system consists of 3 main parts. The first stage is a commercially available automatic dust sampling station, HVS-30 (produced by polish manufacturer), used for forcing the air movement, removing dust particles and measuring the flow rate and total volume of air transferred. The minimum flow rate is 25 m^3 h^{-1} and this value is used in this project as the lowest possible. Gas outlet and further hosing diameter is 5 cm. The second stage is own design and construct water vapor remover. Made of plexiglass hollow tube with the inner diameter of 14 cm and length of 40 cm with two also acrylic covers with inlet and outlet of the air it contains ca. 5 dm^3 of granulated absorber (silica gel). Steel nets at both ends prevents the dryer from spilling.

The last, third stage is for absorb noble gases, krypton and xenon. When maintaining continuous capture and measurement in front of gamma detector it is aluminum Marinelli beaker filled with ca. 700 cm^3 of activated carbon. When capturing in the low tempera-

TABLE 1: Physical properties of Kr-85 and selected radioisotopes of xenon. T is half-life; X — energies and (intensities) of emitted quantum of Roentgen radiation; g — energies and (intensities) of emitted quantum of gamma radiation; b — energies and (intensities) of emitted beta radiation; IC — energies and (intensities) of emitted electrons of internal conversion.

Nuclide	^{85}Kr	^{131m}Xe	^{133}Xe	^{133m}Xe	^{135}Xe
T	10,7 y	11,9 d	5,24 d	2,19 d	9,1 h
X	13 keV	30,4 keV (54 %)	31,6 keV (48,9 %)	30,4 keV (56,3 %)	31,6 keV (5,2 %)
g	514 keV (0,43 %)	164 keV (2 %)	81 keV (37 %)	233 keV (10 %)	250 keV (90 %)
b	687 keV (99,57 %)	—	346 keV (100 %)	—	910 keV (100 %)
IC	—	129 keV (61 %)	45 keV (54 %)	199 keV (63 %)	214 keV (5,7 %)

ture own constructed system is used; four aluminium tubes of ca 2,5 cm diameter with activated carbon with steel nets covers are submerged in liquid nitrogen. Because of the flow attenuation they are connected 2 in series and these two series parallel. After collecting sample the carbon can be broadcast into a container of known geometry for use in gamma detection.

Measurements are performed with HPGe detector with beryllium window which provides the lower limit of gamma ray energy detection of ca. 30 keV. For detection of krypton-85 it is used directly (514 keV gamma line) and for xenon it will work in a tandem with a scintillation detector in a coincidence mode using coincidence beta-gamma lines of each isotope of xenon.

After sampling for over 24 hours, which corresponds to 600 m^3 of air pumped through the silica gel dryer and activated charcoal trap, several gamma-ray measurements were performed. Better results in gamma spectra were achieved when measuring silica gel rather than activated charcoal, therefore series of time-delayed spectra was gained for the dryer. 514 keV line was analyzed by mathematical deconvolution of Gaussian peaks: annihilation line 511 keV and line of interest.

Results are presented on Fig. 1. The lower values of the second and next measurements than the first one may be explained by partial desorption of absorbed krypton. Assuming actual concentration of activity of this radionuclide in the air as 1 mBq m^{-3} [2] the efficiency of absorption may be estimated, it is 5% (ratio of activity of Kr-85 absorbed to the total activity of this radionuclide in pumped air). These results are insufficient, especially regarding small ratio of areas of Kr-85 peak at 514 keV and background peak at 511 keV.

Next tests will include use of liquid nitrogen for cooling the trap to increase the amount of noble gases absorbed in the activated charcoal and thus improve the determination of its activity concentration in the atmospheric air.

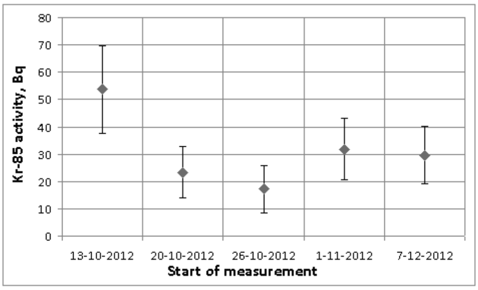

FIGURE 1: Time dependence of activity of Kr-85 absorbed in silica gel trap.

⋆ ⋆ ⋆

[1] P. Janowski, *Postępy Techniki Jądrowej* **57**, 9 (2012).

[2] J. Bieringer, C. Schlosser, H. Sartorius, S. Schmid, *Appl. Radiat. Isotopes* **67**, 672 (2009).

Numerical modeling of hydrological aspects in landfill safety for radioactive wastes disposal in Różan (NE Poland)

Magdalena Miecznik

The Henryk Niewodniczański Institute of Nuclear Physics Polish Academy of Sciences, Radzikowskiego 152, 31-342 Kraków, Poland

Supervisor: Wojciech Jerzy Mietelski

The paper is a discussion about numerical modeling problems related to the geological structure of the National Radioactive Wastes Landfill area in Różan (90 km from Warsaw — NE), which is the Ph. D. „Study on the geological materials sorption of long-lived radioactive isotopes Tc-99, Sr-90, Cs-137 in model systems with the use of short-lived isotopes, Tc-95m, Sr-85, Cs-134” case study. Conceptual, mathematical and numerical models has been discussed here for the study geological structure.

The National Radioactive Wastes Landfill in Różan is located in the vicinity of arable land and grassland, about 800 meters west of the Narew river. Geologically Różan is located on an extensive geomorphological form called glacial Krzyżew plateau. Krzyżew plateau consists mainly sands of water-gacial accumulation rising to a height of about 115 – 120 meters above the sea level. On the basis of the material collected during the geological work, from two cores 7 and 8 m deep, made in the vicinity of KSOP, it was found a Pleistocene cover separates into 3 basic types of layers. These layers can be distinguished in terms of the structural features and deposition mechanism into:

- fine, light yellow sand, yellow-rust sand, water-glacial;
- fine light yellow sand mixed with gravel, gravel, water-glacial;
- boulder clay, sandy rust colored, glacial.[1]

Based on study area geomorphological structure a conceptual model has been outlined. It covers an area of 780 meters from the National Radioactive Wastes Landfill in Różan to the Narew River bed and from 0 to 32 m below the surface (approximate Narew river bed depth). The modeled area has been divided into layers according to the range of different geological deposits, adequate for the present geological layers in the taken cores. Since the purpose of the model is to determine the rate of migration of contaminants from the surface to the water table, constructed model is two-dimensional. Initial condition for the system is the lack of any contamination in the model. Then, contamination will appear pointwise in the model surface layer, and will be subjected to diffusion in each direction according to the gravity and the concentration difference. The most important information resulting from the model calculations is the depth and rate of contamination infiltration throughout successive geological deposits. Because of that model was divided into a grid of 50×78 size, where the first two vertical meters are reproduced with an accuracy of 0,1 m, and then every 1 m up to 32 m below the surface, while in the horizontal direction nodes are present every 10 m. The grid density is one of the accuracy conditions, but also affects the computation time, that is why it is necessary to compromise between these two aspects of the model. From the mathematical point of view studied processes can be described by two equations: the transportation Eq. (1) and Darcy's law (2).

$$\frac{\partial C}{\partial t} - \nabla \cdot (D \nabla C) + \\ + \nabla \cdot (\vec{a} C) + S = 0 \ , \tag{1}$$

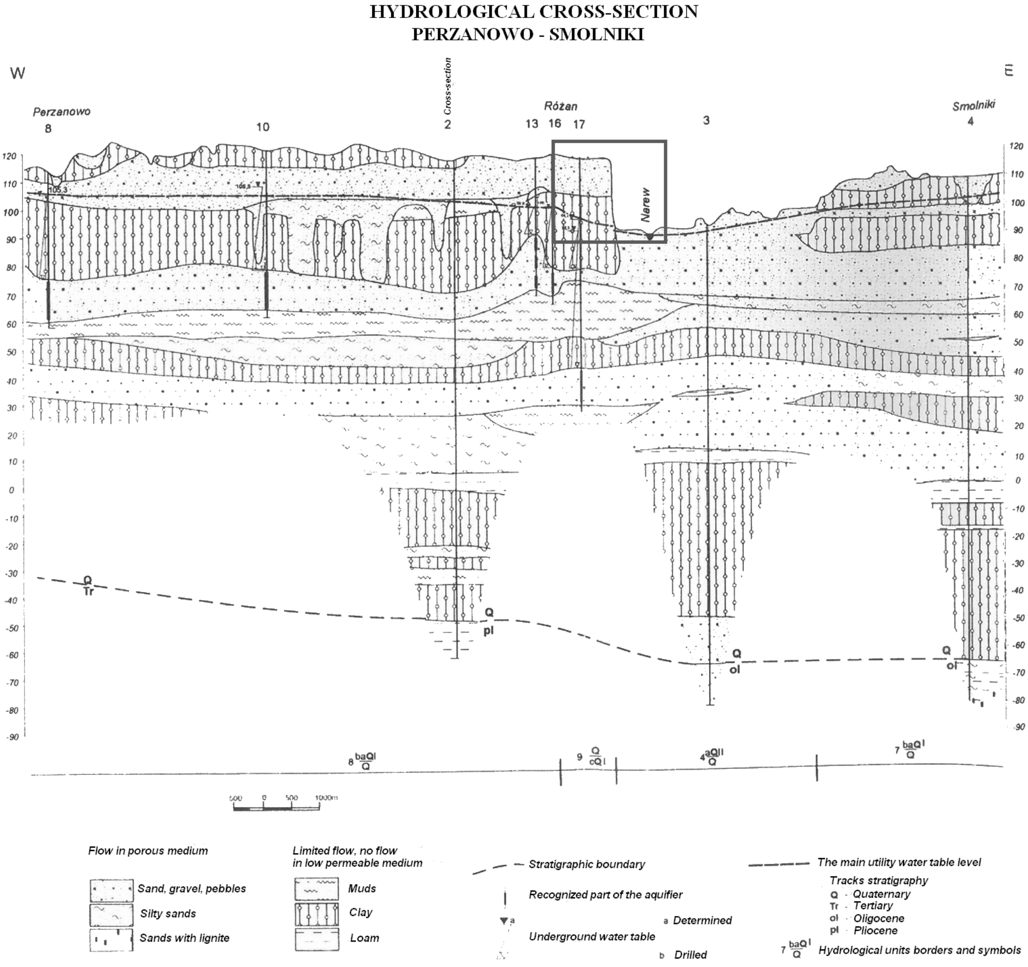

FIGURE 1: Hydrological cross-section. Perzanowo-Smolniki [2] (edited by M. Miecznik).

$$-\frac{K}{\mu}\nabla\left(P-\rho\vec{g}\vec{y}\right)=\vec{a}\ . \qquad (2)$$

The transportation equation says that the concentration change in time is due to the substances diffusion, advection and the sources presence (S). Darcy's equation says that the advection velocity comes from the pressure difference. Advection velocity calculated from Darcy's law can be used in the transportation equation. Constants appearing in the Darcy's equation are permeability K, the kinetic viscosity of the fluid μ and gravitational acceleration $\vec{g}$. In the transportation equation, there is one constant, diffusion constant, which includes information about sorption properties of the system. Since the searched information in the model is the spread of the contamination throughout the whole modeled area, the edges of the model are not imposed by any fixed boundary conditions (Dirichlet-type boundary conditions), but there have been used Neumann boundary conditions allowing for the contamination inflow and outflow.

The advantage of the numerical solution of partial differential and ordinary differential equations systems over algebraic methods is the fact that it is always possible. On the other hand, a numerical solution is an approximate solution, possible after previous discretization of the research area, and the result is obtained for each grid node. As was mentioned above, the denser grid the more accurate computing solution, but the longer computing time. For a limited class of problems, there are analytical solutions possible, and even if this requires the number of assumptions adoption, it is very valuable to do such calculations for verification the numerical method. There are three groups of methods used for the numerical solution of differential equations:

- finite differences method,
- finite element method,
- finite volume method.

To solve the problem presented in the introduction the simplest of these methods has been used, the finite differences method. It involves the conversion of differential equations into difference equations, which means replaceing the differential operations by subtraction operations. The main advantage of this method is its simplicity and its main drawback is a limit to the geometry of the area resulting from the discretization. In the opposite to the two other mentioned methods rectangular or rectangles are required in 2D or 3D case respectively in discretized area. Since the modeled area is not complicated in terms of geometry, finite difference method is sufficient to describe the studied phenomena. Another factor beside the grid density affecting the accuracy of the calculation is the approximate precision and resulting from it the truncation error. The easiest way to demonstrate the problem is to expand in a Taylor series the function value in the environment of a given point. The truncation error is the smaller, the more factors will be taken into account in the Taylor expansion. A reasonable compromise between accuracy and computation time is necessary here. The inaccuracy of the calculations can also be minimized by the conditions imposed to the model, i.e. the calculation loop is interrupted only when the differential value of the function at the point in the current and the previous step is not greater than that from the condition. Another problem that has to be discussed during the numerical model construction is the choice of the calculation scheme and the calculations stability associated with it. In general it can be distinguish between the explicit and the implicit calculation schemes. In the case of explicit scheme, function value at a given point in time $k+1$ is calculated for the spatial derivative from the value at this point and the neighboring points in time k. In the case of implicit scheme function value at a given point in time $k+1$ is calculated in the case of the spatial derivative from the value at neighboring points in time $k+1$, which requires solving the system of equations. The explicit scheme is computationally simpler method, however, to ensure the stability of the method the stability condition have to be assumed, for example, in the case of parabolic problems: two times the time step must be less than or equal to the square of the spatial step. The stability of the numerical solution means here, computational error does not increase in subsequent time steps. In the case of calculations that are the research subject the implicit scheme was used. It should be noted also that there is a unconditionally stable Crank-Nicholson pattern that require more complex calculations, however, in the case of the study does not improve the calculation results. Furthermore, in addition to the stability there are associated concepts of convergence and coherence for each finite difference scheme. The convergence refers to whether the solution obtained by a particular method coincides with the exact solution, and compliance tells whether the difference operator well represents the exact differential operator.[3]

The model constructed for the pollution transport calculation issues in the area of about 30 m below the surface to 800 m long in the neighborhood of the National Radioactive Waste Landfill in Różan is based on the transportation equation and Darcy's equation. In the model the area geometry was incorporated (lowering of the land surface according to the Narew riverbed approach) and the presence of different geological layers identified on the basis of geological cores taken. The Neumann boundary conditions were used in the model. The calculation method used to solve the Ph. D. thesis problems is the finite difference method with implicit calculation scheme. It is planned to calibrate the model with the data obtained after completion the laboratory experiment. The other, still unresolved issue of discussed model is the calculations time length. Calculating the one second of the model currently takes more than 20 seconds. To solve this problem it is necessary to optimized the computing code for example by using an iterative methods rather than analytical solving the system of equations resulting from the use of implicit computational scheme, better use of multi-core computer by entering the corresponding function in the computing code, and other minor improvements.

⋆ ⋆ ⋆

[1] T. Kozioł, Ekspertyza geologiczna określająca osady plejstoceńskie w sąsiedztwie składowiska odpadów promieniotwórczych w Różanie, woj. mazowieckie (Pracownia Badań Geologicznych Kraków, 2011).

[2] R. Janica, Objaśnienia do mapy hydrogeologicznej Polski w skali 1:50 000. Arkusz Różan (372) (Polgeol S.A., Państwowy Instytut Geologiczny, Warszawa, 2002).

[3] A. Trykozko, Modelowanie komputerowe w ochronie środowiska, Interdyscyplinarne Centrum Modelowania Matematycznego i Komputerowego (2012), http://www.icm.edu.pl/~aniat/modele.

Development of a dosimetry system based on alanine detectors for patients undergoing proton radiotherapy at IFJ PAN in Kraków

Gabriela Mierzwińska

The Henryk Niewodniczański Institute of Nuclear Physics Polish Academy of Sciences, Radzikowskiego 152, 31-342 Kraków, Poland

Supervisors: Michael P. R. Waligórski, Barbara Michalec

The aim of the project is to develop a system able to measure cumulatively the dose received by a patient undergoing proton radiotherapy at the Institute of Nuclear Physics of the Polish Academy of Sciences (IFJ PAN) in Krakow. This system will serve as an element of the Quality Assurance (QA) procedure of proton radiotherapy. The radiation detector is based on L-α-alanine in which stable radiation-induced free radicals are produced and can be measured using electron paramagnetic resonance (EPR) over the dose range 1 – 10^3 Gy. EPR readout of the exposed alanine dosimeter does not destroy its signal, therefore the dose received by the patient in successive radiotherapy sessions (fractions) can be accumulated in the same detector and documented for QA purposes. The chemical composition of alanine is inherently tissue-equivalent with respect to gamma-ray and proton irradiation. Properties have been initially verified of some commercially available alanine detectors exposed to Co-60 gamma-rays and proton beams over a range of proton energies, namely: dose range, linearity, sensitivity-relative to Co-60, dose-rate effects, signal stability and repeatability of readout. These commercially available alanine detectors will now be tested more systematically. We are also investigating techniques of in-house manufacture of such detectors. The developed cumulative dosimetry system based on alanine detectors will serve in routine QA dosimetry of patients undergoing proton radiotherapy at the IFJ PAN.

At the Henryk Niewodniczański Institute of Nuclear Physics of the Polish Academy of Sciences (IFJ PAN) in Krakow a proton radiotherapy facility has been developed to treat ocular melanoma patients. So far, 15 patients of the Clinic of Ophthalmology and Ophthalmological Oncology of the University Hospital in Kraków have been treated. A beam of 60 MeV protons of ca. 28 mm range in water is accelerated by the AIC-144 cyclotron at IFJ PAN.[1] A new 230 MeV IBA Proteus C-235 cyclotron, where the proton ranges in water exceed 200 mm, has recently been installed at the IFJ PAN. Following the installation and commissioning of a rotating gantry and a pencil beam scanning system, after 2015 this new facility will be able to treat all sites in cancer patients.

Novel dosimetry systems able to accurately measure proton beam doses applied in clinical proton radiotherapy are being investigated at IFJ PAN. Free-radical alanine dosimetry has been introduced some 40 years ago as a cheap and reliable method for dose estimation in many industrial and medical applications.[2,3] Due to linearity of its dose response over a dose range of at least 5 – 500 Gy, covering therapeutic doses delivered to cancer patients, alanine dosimetry may be applied in Quality Assurance (QA) of proton radiotherapy. In a typical ocular radiotherapy procedure, the patient receives a total dose to the tumour of 60 Gy, delivered in a sequence of four 15 Gy exposure sessions (fractions). For other sites, the typical cumulated dose is about 60 Gy, delivered in up to thirty 2-Gy fractions.

In the crystalline structure of the L-α-alanine amino acid (CH_3–$CH(NH_2)$–COOH), ionizing radiation generates a variety of free radicals.[4] The dominant stable free radical is formed by deamination of L-α-alanine (CH_3–$^\bullet$CH–COOH). The number of stable free radicals can be measured via electron paramagnetic resonance (EPR) using a sensitive EPR spectrometer, such as the X-band Bruker ESP 300 EPR spectrometer available at IFJ PAN. The alanine EPR spectrum has a rather complex structure consisting of five lines (Fig. 1). Under suitable measurement conditions the concentration of radiation-produced free radicals rises linearly with dose deposited in the alanine detector. According to ISO International Standard WD 15566[5] the amplitude of the central line (Fig. 1) represents the concentration of free radicals and the signal (response) of the alanine dosimeter.

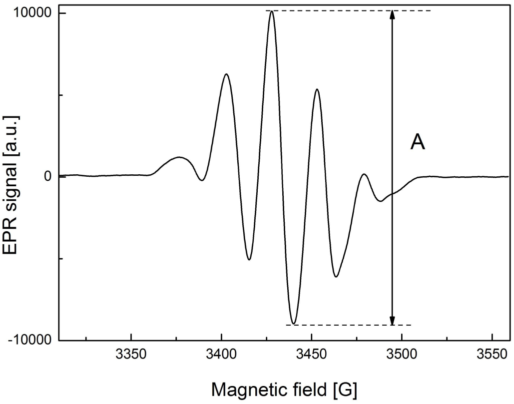

FIGURE 1: The EPR spectrum of irradiated alanine. The amplitude of the central line (A) — the detector signal — is a measure of dose absorbed in the alanine detector.

Alanine dosimeters consist of pure alanine powder mixed with a suitable binder and are available commercially in the form of pellets, rods or foils. Binders are typically cellulose, paraffin, silicone, polyethylene, polystyrene or polyvidone (or other polymers), which do not show any EPR signal over the alanine signal range and protect the hygroscopic alanine powder against ambient humidity. Alanine detectors tested so far at IFJ PAN were rods of 4,9 mm diameter and 10,5 mm height (containing 95% alanine and 5% of polyethylene, by weight, produced by A. Wieser), pellets of 4,8 mm diameter and 3,0 [mm] thickness (96% alanine and 4% polyethylene, produced by Gamma Service), and 250 μm thick foils of 4,9 mm diameter (30% alanine, 70% polyethylene[6]). The sensitivity of the alanine detector depends on its alanine concentration. Due to their low alanine content, alanine foils show a distinct signal only above c. 150 Gy, however their low thickness makes them suitable for measurements of relative effectiveness in proton beams (see below). Tests of rod and pellet alanine detectors showed them to have sufficient sensitivity for purposes of radiotherapy.

While, as shown in Fig. 1, the EPR spectrum values are given in arbitrary units, in principle alanine may also be used as an absolute dosimeter. In practice, a reference calibration curve is obtained by exposing the detector to a range of doses well-determined by ionization chamber dosimetry. In Fig. 2 calibration curves are shown of the rod alanine detectors exposed to Co-60 gamma-rays and to 60 MeV protons, over the dose range 1 – 70 Gy. Within the uncertainty of regression fits, both calibration curves overlap, indicating that in these conditions the efficiency of alanine after 60 MeV proton irradiation, relative to that after Co-60 gamma-rays is 1,0. The examined dose range (1 – 70 Gy) covers the range of doses applied in proton radiotherapy.

The relative effectiveness of alanine is defined as the ratio of amplitudes of the EPR signal after exposure to a dose of the tested radiation, and after exposure to the same dose of reference radiation (typically, Co-60 gamma-rays). Measurements of relative effectiveness, e.g. after proton irradiations, are usually carried out using thin detectors, so that the proton energy is well defined over the detector volume. The relative effectiveness of alanine after proton irradiation which is 1,0 for 60 MeV protons (see above and Fig. 2) is known to decrease as the proton energy decreases.[7] Results of measurements of relative

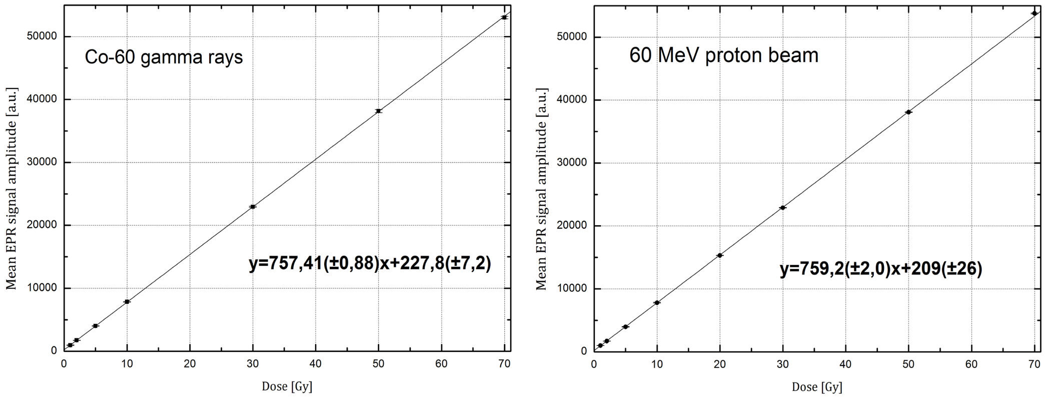

FIGURE 2: Measured and least-square-fitted calibration curves of rod-type alanine detectors (see text) after doses of Co-60 gamma rays and of 60 MeV protons. Error bars are contained within the plotted data points.

effectiveness of alanine as a function of proton energy using the foil detectors, are shown in Fig. 3.[8] In these measurements foils were positioned at different depths in a pristine 60 MeV proton beam, including the Bragg peak region. In this manner, measurements could be made for protons at different energies, as the energy of protons in the beam gradually decreases with increasing depth. In order to achieve good quality and reproducibility of EPR spectra, the foil detectors were exposed to doses of 250 Gy. Measurement uncertainties (shown as error bars in Fig. 3) included those of EPR signal measurements, nominal dose delivery, long term spectrometer performance and detector mass normalization. The results generally agree with those measured and estimated theoretically by other authors.[8]

An initial attempt was made to verify the dose rate dependence of alanine detectors. For this purpose 14 alanine rod detectors were irradiated in the 60 MeV proton beam at four different dose rate values: 0,16; 0,29; 0,38, and 0,49 Gy/s. Each dosimeter was exposed to a dose of 15 Gy which is typically delivered to the ophthalmic tumour in one proton therapy session (fraction). Results of these measurements (five independent measurement for each detector, at least three detectors exposed at each dose rate value) are shown in Fig. 4. Data points were normalized to the mean value of all measurements (here, error bars represent the uncertainty of EPR readouts only). No dependence between detector response and proton beam dose rate was observed within measurement uncertainties. Further investigations concerning dose-rate dependence of alanine detectors are under way.

At IFJ PAN we are developing our own techniques for manufacturing alanine detectors. In our first attempt, we are investigating the mechanical properties of stable alanine detectors with microcrystalline cellulose as a binder. The aim is to achieve optimum properties of the detector: good mechanical stability and dimensions adapted to our EPR

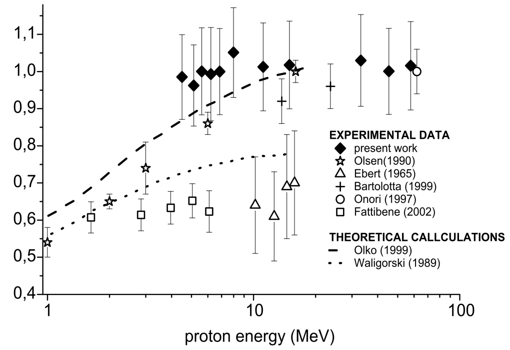

FIGURE 3: Relative effectiveness of alanine film detectors (see text) after proton irradiation versus proton energy.[8]

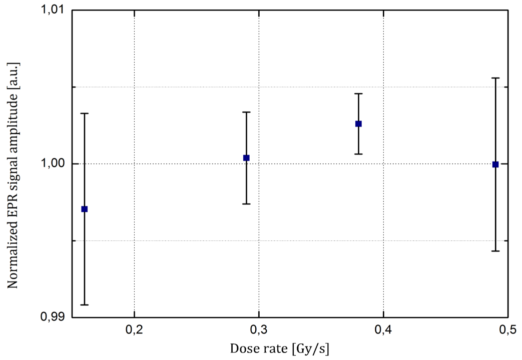

FIGURE 4: Estimation of dose-rate dependence for alanine rod detectors exposed in a 60 MeV proton beam. Data are normalized to the mean value of results obtained at the four dose rates. Error bars represent the uncertainty of EPR readouts only.

spectrometer and optimum alanine-to-binder concentration ratio, in order to achieve good sensitivity and maintain the mechanical stability of the dosimeter. The properties of our in-house produced detectors will be then compared with those of commercial detectors in a series of measurements in Co-60 and proton beams at IFJ PAN. Measurements will be performed in the radiation field and outside the beam. At the final stage of this work, a protocol for alanine dosimetry of proton beams will be developed. The developed alanine dosimetry system will then be applied at the IFJ PAN proton radiotherapy facilities for documenting cumulatively doses applied to tumour volumes of patients undergoing proton radiotherapy, as a part of the Quality Assurance procedure in proton radiotherapy of cancer patients at the IFJ PAN.

This work is partly supported by the research project „EPR/alanine dosimetry for radiotherapeutic ion beams", carried out within the PARENT — BRIDGE Program, supported by the Polish Science Foundation, and co-financed by EU structural funds under Action 1.2 „Strengthening the human resources potential of science" of the Innovative Economy Operational Program 2007 – 2013.

The contribution of Dr. Barbara Michalec and of Ms. Iwona Ogłodek in designing, performing and analysing the results of some of the measurements presented here is gratefully acknowledged.

⋆ ⋆ ⋆

[1] J. Swakoń, P. Olko, D. Adamczyk, T. Cywicka-Jakiel, J. Dabrowska, B. Dulny, L. Grzanka, T. Horwacik, T. Kajdrowicz, B. Michalec, T. Nowak, M. Ptaszkiewicz, U. Sowa, L. Stolarczyk, M. P. R. Waligorski, *Radiat Meas* **45**, 1469 (2010).

[2] W. W. Bradshaw, D. G. Cadena, G. W. Crawford, H. A. W. Spetzler, *Radiat Res* **17**, 11 (1962).

[3] W. l. McLaughlin, *Radiat Prot Dosim* **47**, 255 (1993).

[4] E. Malinen, E. A. Hult, E. O. Holea, E. Sagstuena, *Radiat Res* **159**, 149 (2003).

[5] International Standard ISO/WD 15566.1, Practice for use of the alanine-EPR dosimetry system, International Organization for Standarization (1998).

[6] I. Janovsky, In: High-Dose Dosimetry for Radiation Processing: Proc. Int. Symp. High-Dose Dosimetry for Radiation Processing, (Vienna. IAEA-SM-314/47, 173 1990).

[7] P. Olko, *Radiat Protect Dosim* **84**, 63 (1999).

[8] B. Michalec, G. Mierzwińska, U. Sowa, M. Ptaszkiewicz, T. Nowak, J. Swakoń, *Nukleonika* **57**, 503 (2012).

Retrospective dose assessment in a radiation mass casualty by optically stimulated luminescence with the use of mobile phones

Anna Piaskowska

The Henryk Niewodniczański Institute of Nuclear Physics Polish Academy of Sciences, Radzikowskiego 152, 31-342 Kraków, Poland

Supervisor: Barbara Marczewska

Present time, because of increasing demand for ionizing radiation in industry and health service, the risk of a mass radiological accident is also increasing. It requires the development of appropriate dosimetric tools, which can be used to implement procedures for emergency response. Up to now, in retrospective and also accidental dosimetry, building materials and chemicals, which give luminescence signals were used to assess the doses. However, previous researches with new materials present in personal electronic objects, enabled the assessment of individual doses, which are absorbed during radiological accident. These electronic objects are close to the human body and are very popular. Luminescence properties of these materials have to be investigated in order to create a procedure which works properly in crisis situation. The first results in which the mobile phone was irradiated showed that dose could be recovered with satisfactory precision.

Wide use of ionizing radiation in health service (hospitals, oncology centers), but also in the industry (metallurgical facilities, manufacturing facility) requires the development of dosimetry methods which could be used to carry out routine inspection for persons who are occupationally exposed to radiation during different application. Also, it requires the research for new materials for dose measurements in recessionary condition. Wherever the ionizing radiation is being used, there is a risk of radiological accident. Beyond the peaceful usage of radiation, it is also possible to use it for military purposes, such as wars or terrorists attacks. In both cases there exists the range of activities, which have to be accomplished immediately after the occurrence of mass radiological accident. These activities are estimating dose absorbed by the human who does not have individual dosimeter; population selection in terms of the amount of the received ionizing radiation dose and also minimizing destructive or lethal effects of radiation. Until now, optically stimulated luminescence (OSL) was being applied in retrospective dosimetry to dating and determination of exposure in accidental situation by using objects found in the place of accident (for example porcelain and chemicals). However, the usage of these objects to assess the dose which was absorbed by people, has important drawback — it will never be accurate dose assessment for human. The situation could change, if for estimation individual dose personal electronic objects were used for example electronic devices like mobile phones, music players, memory sticks.[1] Development of a method for measurement of retrospective dose using personal objects allow to create procedures for radiological accident and also contribute to improvement of radiation safety.

The aim of this project is to investigate dosimetric properties of electronic components devices like mobile phones, which could be useful during radiological accident to estimation dose. The first part of this work was dedicated to investigate the properties of luminescence signal from electronic components such as reproducibility and dose-response. Next part was destined to dose assessment of individuals potentially exposed to ionizing after simulation of a radiological accident. Implementation of the results will be last step for the emergency plan and the management system for civil service.

The experiments were carried out with the use of parts of electronic devices which were removed from a mobile phone. The circuit board of a mobile phone contains different electronic components, but investigation was performed for resistors because of the structure these electronic components which are made in technology SMD (Surface Mounted Devices). The resistors are composed of ceramic substrates contain approximately 97% Al_2O_3 and 3% SiO_2,[2] which is covered by resistive layer. This substrate of alumina rich ceramic is sensitive to ionizing radiation. Al_2O_3:C is a well known type of material, which is used in production of OSL (optically stimulated luminescence) detectors routinely used in radiation protection systems in many countries.[3] The atomic composition of the detector material is expressed by the average effective atomic number (Z_{eff}).[4] The average effective atomic number of Al_2O_3 is approximately 10,2 and it is relatively high compared with soft tissue ($Z_{eff} = 7{,}4$),[5] but in spite of it makes the resistors potential, attractive material to be dosimeter. The luminescence properties of resistors were investigated by optically stimulated luminescence method (OSL). Production of OSL signal is caused by defects in the structure of material. Ionizing radiation causes that charges are captured by trapping centers. In the laboratory conditions, the trapped electrons are released by providing appropriate amount of energy in the form of light. The next step is a recombination of charges to recombination centers (centers of luminescence). The recombination process can be accompanied by the emission of light, which is the luminescent signal.[6] The number of trapped electrons in the defects is proportional to the amount of absorbed dose of the material. The light yield is then recorded as a function of time in a decay curve.

The resistors (dimensions 1×0,5×0,35 mm) were used to investigate the overall OSL luminescence properties of resistors such as dose response and reproducibility. The number of resistors per one sample equals 10, because of small dimension of resistors.

Resistors were removed from circuit board of mobile phone by scalpel during trials to recover dose from simulation accident. These resistors were removed under dark room conditions, because of the fact that stimulation wavelength light (460 nm) is very close to day light. The microscope was also necessary because of small dimension of resistors.

During this measurements, the number of resistors is the same like above.

OSL measurements were performed on RISOE TL/OSL reader. The resistors were excited with blue diodes, which emit light with wavelength of 460 nm. RISOE TL/OSL reader is equipped with optical filters (Hoya U-340). The samples were stimulated and read with continuous-wave OSL mode (the stimulation light intensity is constant during measurements). For part of measurements, resistors were irradiated with a 90Sr/90Y beta source placed in RISOE TL/OSL using the dose rate of 0,081 Gy/s. The mobile phone was irradiated with a source of high-energy photons ^{137}Cs for simulation of accident irradiation. This source is placed in the Laboratory for Calibration of Radiation Protection Instruments at the Institute of Nuclear Physics Polish Academy of Sciences.

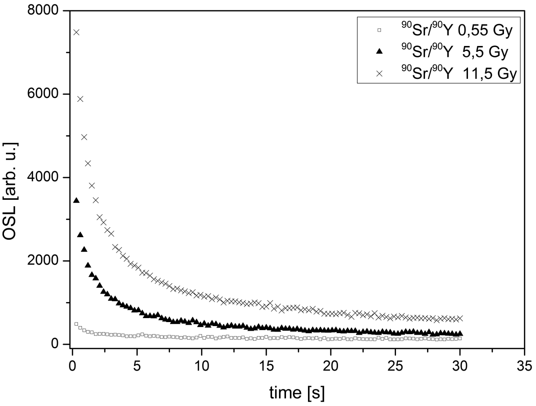

FIGURE 1: OSL decay curves from surface-mount resistors irradiated with 0,55 Gy; 5,5 Gy; 11,5 Gy 90Sr/90Y source, respectively.

Important point of these researches is measuring of OSL dosimetric properties of resistors such as their response to dose and reproducibility.

Fig. 1 shows a shape of OSL curves to a given dose of 0,55 Gy; 5,5 Gy; 11,5 Gy irradiated with 90Sr/90Y source. Dose dependance of OSL signal was investigated for doses from 0,5 to 12 Gy. The resistors were irradiated with 90Sr/90Y source inbuilt in RISOE TL/OSL reader and after that measured in this reader (Fig. 2). The data points are fitted by a linear function of form (1):

$$y = ax + b. \tag{1}$$

It allows to construct linear function of dose for single sample. It is useful for building calibration curve during measurements of doses from radiological accidents.

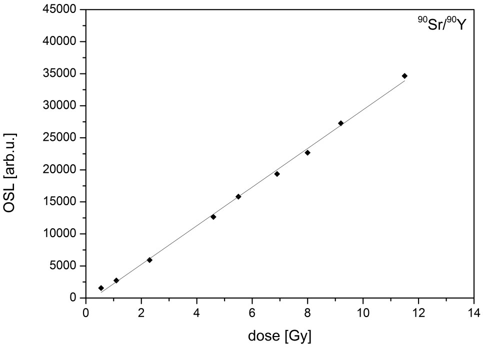

FIGURE 2: Dose response of resistors irradiated in the dose range from 0,55 Gy to 11,5 Gy (calibration curve).

Reproducibility tests of resistors for various samples are shown in Fig. 3. Resistors were irradiated with 90Sr/90Y source with a dose of 0,6 Gy and measured. It was repeated in 10 cycles. It seems that OSL signal remains with less than 15% of initial sensivity during several irradiation and measurement cycles.

The main measurements were just a trial to recover dose from the simulated radiological accident using Nokia mobile phone.

The investigated mobile phone was irradiated with a dose of 1 Gy. Measurements were taken two times, using the two delay time between irradiation and OSL measurement of the „accidental" dose. The first trial to recover dose was carried out 2 days after irradiation and the second 6 days after irradiation. Between these two trials mobile phone was placed in a black bag to avoid signal loss which could be caused by exposure to a day light. After removing resistors from mobile phone and putting their into reader, resistors were read in order to recover dose and next the same resistors were irradiated with calibration dose of 5 Gy.

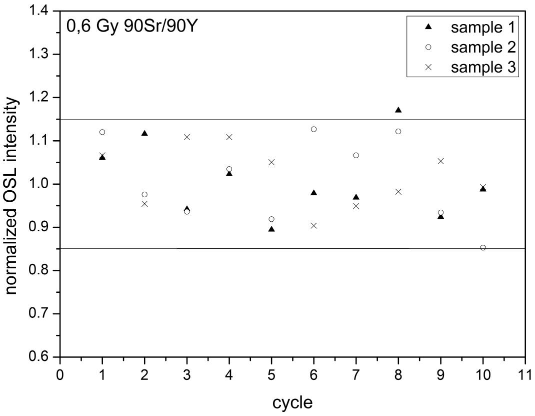

FIGURE 3: Reproducibility test for 3 sample. Each sample consisted of 10 small resistors. All samles were coming from one circuit board of the mobile phone.

Unfortunately, the electronic components, especially the resistors, have a strong instability in time.[2,5] Their signal after irradiation is lost very fast. The highest degree of fading rate is during the first minutes and hours after irradiation. The decay is given by the function of (2):

$$y = a \ln(x) + b, \tag{2}$$

where x — time [s] and a, b are fitting parameters.

OSL signal has to be corrected for fading according to delay time between irradiation and OSL measurement.

In resistors, absorbed dose was 0,84±0,11 Gy and 0,92±0,12 Gy, respectively obtained after 2 and 6 days. The fading is a serious problem for dosimetry of electronic components. The decay of luminescence signal can

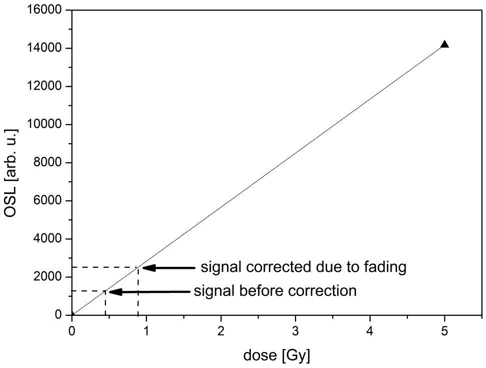

FIGURE 4: Dose for the first trial including uncorrected and corrected signal with fading factors.

lead to errors in dose estimation. The results of dose recovery tests are shown in Fig. 4.

It is possible to divide OSL curve for small parts connected with decay time. For each component of OSL curve, the value of dose could be calculated in delay time function. These components are very interesting for estimating dose, especially the first 6 seconds of measurements (Fig. 5). For this interval the value of estimation dose does not change. This area is called plateau and these measurements are called plateau test.[7] For this interval luminescence signal originates from deep energy traps, accurately stable at ambient temperature. With this interpretation of results, value of dose can be obtained for this range of plateau.

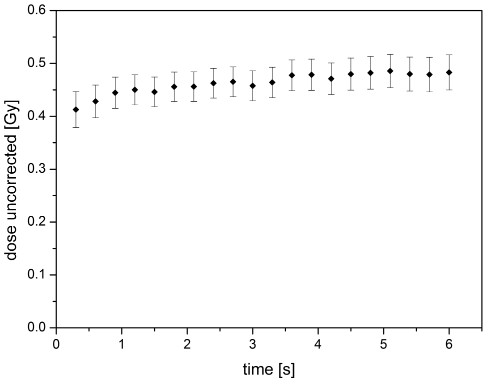

FIGURE 5: Plateau test for uncorrected dose measured by using resistors from irradiated mobile phone.

This investigation presents a great possibility of use resistors for dose assessment after radiological accident. The results of investigated properties of resistors show linear dose response which is useful for obtaining calibration curve during measurements of „accident" dose, good reproducibility better than 15% variation of initial sensivity and dose recovery with uncertainties at 13%. It is necessary to remember that the signal stability is a critical point for estimation dose.

Common electronic devices, such as mobile phones, music players, memory sticks etc. are very useful for dosimetry purposes. In emergency situations, like nuclear accidents it could be very easy to collect them from potential victims and measure them to recover the dose absorbed by the owners.

Although losing of signal is large, the dose recovery with well-rounded precision is still possible. Personal electronic objects seem to be promising for this application.

⋆ ⋆ ⋆

[1] E. L. Inrig, D. I. Godfrey-Smith, S. Khanna, *Radiat. Meas.* **43**, 726 (2008).

[2] E. L. Inrig, D. I. Godfrey-Smith, C. L. Larsson, *Radiat. Meas.* **45**, 608 (2010).

[3] L. Boetter-Jensen, S. W. S McKeever, A. G. Wintle, Optically Stimulated Luminescence Dosimetry, 1st edition (Elsevier Science, 2003).

[4] P. Olko, Habilitation thesis, Microdosimetric modelling of physical and biological detectors, (report no 1914/D, Kraków, 2002).

[5] D. Ekendahl, L. Judas, *Radiat. Prot. Dosim* **150**, 134 (2012).

[6] C. Woda, C. Bassinet, F. Trompier, E. Bortolin, S. D. Monaca, P. Fattibene, *Ann Ist Super Sanita* **3**, 297 (2009).

[7] A. Bluszcz, Datowanie luminescencyjne osadów czwartorzedowych — teoria, ograniczenia, problemy interpretacyjne, 7th edition (Wydawnictwo Politechniki Śląskiej, Gliwice, 2000).

Determination of the relative TL efficiency of LiF: Mg,Ti and LiF: Mg,Cu,P detectors to protons

Michał Sądel

The Henryk Niewodniczański Institute of Nuclear Physics Polish Academy of Sciences, Radzikowskiego 152, 31-342 Kraków, Poland

Supervisor: Paweł Bliski

Thermoluminescent detectors are frequently used in dose measurements e.g. cosmic radiation in space, and proton radiotherapy beams. In both this fields precise dosimetry is crucial issue. The relative thermoluminescent efficiency for the most widely applied detectors of LiF to protons are not straightforward. On the one hand, available date concerning efficiency to light ions exceed unity, sometimes more than 30%. For the other hand, there are reports showing that efficiency is close to unity or even lower. The reason of this effects may be different, e.g. influence of experimental conditions, or variability of TLD properties. So that to resolve this problem, using 60 MeV protons beam from cyclotron AIC-144 in IFJ PAN in Kraków, efficiency of LiF:Mg,Ti (MTS) detectors over last 20 years was measured. In consequence, all values of the relative TL efficiency exceed unity, with average of 1,09 and dispersion below 4%. For the next experiment, for LiF:Mg, Ti and LiF:Mg,Cu,P detectors dependence of the relative efficiency was measured. The results for LiF:Mg,Ti, showing efficiency of 1,20 at about 20 MeV. Whereas, for LiF:Mg, Cu, P the relative efficiency is of 0,96 at 56 MeV, to 0,61 at 11 MeV.

The relative thermoluminescent efficiency is a ratio of the emitted light intensity per unit dose, to the same quantity for the reference gamma radiation (Cs-137). The relative TL efficiency for LiF:Mg, Ti, detectors, depends on ionization density. For weakly ionizing radiation (photons) it is assumed to be equal to unity. For strongly ionizing radiation, efficiency usually decreases.[1] The problem with efficiency is of high importance, as it significantly affects crucial thing of application, which is radiotherapy with protons beams, where TL detectors are a primary method of measurement doses. For the most widely applied LiF:Mg, Ti, TL detectors the relative efficiency to light ions relative to gamma-rays, may visibly exceed unity even more than 30%.[2–4] On the other hand, many others reports shows the efficiency close to unity or even lower.[5–8] The reasons for this may be various. One of them is variability of TLD properties. In order to resolve this problem, an experiment at the Institute of Nuclear Physics (IFJ) in Krakow, using the 60 MeV proton beam of the AIC-144 cyclotron was started. The aim of measuring was comparison of the relative TL efficiency to protons for many of TLDs groups produced over a long period of time at the IFJ.

Experiment has been realized at the Proton Eye Radiotherapy Facility at the IFJ.[9] Using AIC-144 isochronous cyclotron, protons were accelerated with nominal energy of 60 MeV. The proton beam range was controlled by a PMMA range shifter. During irradiation proton dosimetry was carried out by a PTW 23343 Markus ionization chambers coupled with a PMMA moderator of variable thickness. The actual energy at the position of TLD exposures was 58,7 MeV. The main part of experiment were realized using the most widely applied LiF:Mg,Ti thermoluminescent detectors in form of sintered pellets with typical dimensions 4,5 × 0,9 mm and density 2,5 g/cm^{-3}. Two versions of TLDs with different isotopic Li composition were used: MTS-

TABLE 1: Comparison of the relative TL efficiency of LiF:Mg,Ti (MTS-N) and LiF:Mg,Ti (MTS-7) TLDs from different production batches for 58,7 MeV proton beam.

	MTS-N			MTS-7	
Batch	Relative TL efficiency		Batch	Relative TL efficiency	
	Peak area	Peak height		Peak area	Peak height
1992	1,13±0,02	1,06±0,02	1994	1,06±0,03	1,09±0,03
1994	1,10±0,02	1,08±0,02	1996	1,08±0,03	1,05±0,04
1997	1,10±0,01	1,05±0,02	1999	1,08±0,03	1,11±0,03
2000	1,11±0,02	1,05±0,02	2002	1,07±0,03	1,09±0,01
2003	1,07±0,02	1,09±0,02	2005	1,07±0,02	1,06±0,04
2006	1,07±0,02	1,07±0,02	2008	1,07±0,03	1,09±0,02
2010	1,09±0,03	1,08±0,02	2010	1,07±0,03	1,08±0,02
2012	1,08±0,03	1,11±0,03	2012	1,11±0,02	1,12±0,04

N (natural Li) and MTS-7 (Li-7 enriched). In total, 16 batches of TLDs produced between 1992 and 2012 was investigated.

In a second part of experiment the dependence of the relative TL efficiency on proton energy was measured. Special miniature TLDs with diameter 3,2 mm and thickness 0,3 mm were manufactured. Measurement was realized with two types of TLDs; LiF:Mg, Cu, P (MCP-N) and LiF:Mg, Ti (MTS-N). Before each experiment TLDs were specially prepared. For MTS, the annealing conditions were 400°C/1h + 100°C/2 h: for MCP 240°C/10 min. TLDs were readout using manual TL reader Harshaw Series 3500. Before readout, detectors were preheated at a temperature of 100°C for 10 min. TL glow-curves were registered with heating up to temperature 320°C (MTS-7, MTS-N) or 265°C in case of MCP, at a heating rate of 5°C s^{-1}. Calibrations of TLDs were performed by irradiating a group of TLDs from each batch with 100 mGy dose of ^{137}Cs gamma rays at the secondary standard calibration laboratory at IFJ. To minimize any spread of sensitivity between TLDs pellets of one group, individual response factors for each detector were determined. Table 1 contain values of the relative TL efficiency for LiF:Mg, Ti organized in sixteen batches measured for 58,7 MeV proton beam. Standard methods of glow-curve analysis: Region-of-Interest approach (ROI), i.e. integration of a glow-curve over the main peak area and the height of the main peak were used.

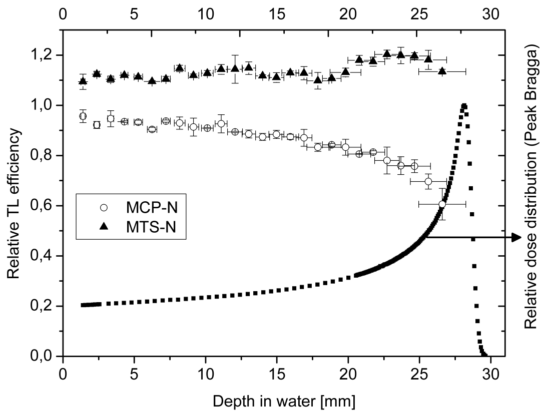

FIGURE 1: Dependence of the relative TL efficiency of LiF:Mg, Ti (MTS-N) and LiF:Mg, Cu, P (MCP-N) on relative dose distribution in water. Measurement were realized with special prepared TLDs with thicknesses 0,3 mm.

The main conclusion is that all values of the relative TL efficiency significantly exceed unity, with the average value around 1,09 for MTS-N, and 1,08 for MTS-7. What is more, all data points lay within 4% around the mean value. In a second experiment, the dependence of the relative TL efficiency on proton energy was measured. Results are presented in Fig. 1 and Table 2. The energy and LET for a given depth in water were calculated using SRIM code.[10] For MTS-N detectors, relative TL efficiency is more or

Table 2: Dependence of the relative TL efficiency of MTS-N and MCP-N detectors (main peak area) on proton energy.

Depth in water [mm]	Energy [MeV]	LET H_2O [keV/μm]	Relative TL Efficiency	
			MTS-N	MCP-N
1,40	55,7	1,16	1,09±0,03	0,96±0,01
2,37	54,6	1,18	1,12±0,01	0,92±0,01
3,34	53,5	1,2	1,10±0,01	0,95±0,01
4,31	52,3	1,22	1,12±0,01	0,94±0,02
5,28	51,1	1,24	1,11±0,01	0,93±0,04
6,24	49,9	1,26	1,09±0,01	0,90±0,01
7,21	48,7	1,29	1,10±0,01	0,94±0,02
8,18	47,4	1,32	1,15±0,01	0,93±0,01
9,15	46,1	1,35	1,12±0,01	0,91±0,02
10,12	44,8	1,38	1,13±0,02	0,91±0,01
11,09	43,4	1,41	1,14±0,06	0,93±0,01
12,06	42	1,45	1,14±0,03	0,89±0,01
13,03	40,6	1,49	1,15±0,01	0,89±0,03
14	39,2	1,54	1,12±0,02	0,87±0,01
14,96	37,7	1,58	1,11±0,01	0,88±0,01
15,93	36,1	1,64	1,13±0,03	0,87±0,05
16,9	34,5	1,7	1,13±0,03	0,87±0,03
17,87	32,8	1,77	1,10±0,01	0,83±0,03
18,84	31	1,85	1,11±0,02	0,84±0,02
19,81	29,2	1,95	1,13±0,02	0,83±0,02
20,78	27,2	2,06	1,18±0,02	0,81±0,03
21,75	25,2	2,2	1,18±0,02	0,81±0,01
22,72	22,9	2,37	1,17±0,03	0,78±0,05
23,68	20,6	2,59	1,20±0,04	0,76±0,05
24,65	17,9	2,9	1,20±0,01	0,76±0,03
25,62	14,8	3,38	1,18±0,04	0,69±0,03
26,59	11,2	4,26	1,14±0,01	0,61±0,06

less constant at the level 1,10-1,15 for energies above 30 MeV. Similar value 1,13 was obtain for MTS-N for 43 MeV energy protons.[4] During decreases energy of protons, the efficiency increases, reaching maximum of 1,20 for 20 MeV. Available date concerning such values.[3] There are also empirical models which predicted efficiency even close to 2 for LiF:Mg,Ti.[11] For lower energy, the efficiency starts to decline, what is argue with the known behavior of LiF:Mg,Ti for high-LET radiation.[12,13] In case of MCP-N detectors, it is clearly visible, that during decreasing proton energy the efficiency decreases, what is in agreement with the general trend of the dependence of LiF:Mg,Cu,P efficiency on ionization density.[13] For LiF:Mg,Ti all values of the relative TL efficiency significantly exceed unity.

TLDs organized in sixteen LiF:Mg,Ti batches revealed a significant low dispersion of the relative TL efficiency, as all measured values were found to be within 4% around the average. However, the dependence of the relative efficiency on proton energy revealed that for LiF:Mg,Ti this relationship possess a maximum of 1,20 at about 20 MeV. For LiF:Mg,Cu,P the relative efficiency decreases with decreasing proton energy, what is an effect of the well-known low efficiency of this material to densely ionizing radiation.

⋆ ⋆ ⋆

[1] P. Bilski, *Nucl. Instrum. Meth.* **251**, 121 (2006).

[2] W. Schoener, N. Vana, M. Fugger, *Radiat. Prot. Dosim.* **85**, 263 (1999).

[3] P. Schmidt, J. Fellinger, J. Henniger. K. Hübner, *Kernenergie* **29**, 339 (1986).

[4] P. Schmidt, J. Fellinger, K. Hübner, *Radiat. Prot. Dosim.* **33**, 171 (1990).

[5] P. Fattibene, A. Calicchia, F. d'Errico, E. De Angelis, C. Egger, S. Onori, *Radiat. Prot. Dosim.* **66**, 305 (1996).

[6] T. Loncol, J. M. Denis, S. Vynckier, P. Scalliet, P. Bilski, M. Budzanowski, M. Waligorski, P. Olko, *Radiat. Prot. Dosim.* **84**, 179 (1999).

[7] G. Massillon-JL, I. Gamboa-deBuen, M. E. Brandan, *J. Phys. D: Appl. Phys.* **40**, 2584 (2007).

[8] S. Vatnitsky, D. Miller, J. Siebers, M. Moyers, *Med. Phys.* **22**, 469 (1996).

[9] J. Swakon, P. Olko, D. Adamczyk, *Radiat. Meas.* **45**, 1469 (2010).

[10] J. F. Ziegler, J. D. Ziegler, J. P. Biersack, *Nucl. Instrum. Meth. B*, **268**, 1818 (2010).

[11] M. P. R. Waligorski, R. Katz, *Nucl. Instrum. Meth.* **175**, 48 (1980).

[12] T. Berger, M. Hajek, *Radiat. Meas.* **43**, 146 (2008).

[13] P. Bilski, M. Puchalska, *Radiat.Meas.* **45**, 1495 (2010).

Remarks about source contribution in positron spectroscopy

Krzysztof Siemek

The Henryk Niewodniczański Institute of Nuclear Physics Polish Academy of Sciences, Radzikowskiego 152, 31-342 Kraków, Poland

Supervisor: Jerzy Dryzek

We analyze influence of the backscatter coefficient and multiple scattering effect in the commonly ^{22}Na *and* ^{68}Ge/^{68}Ga *positron sources on the source fraction in the positron lifetime spectra. A simple theoretical model is presented. The calculated intensities of the positron source is compared with the measured values. The good agreement was achieved. Additionally the positron implantation profiles obtained within this model is compared with GEANT4 simulations profiles and measured experimentally.*

Positron annihilation techniques are widely used in material research.[1,2] They let to i.a. obtain information about the electronic structure and atomic-scale defects. In this techniques the Doppler broadening of annihilation line, positron lifetime and angular correlation of annihilation radiation are measured. These methods as a source of the positrons employee β^+ radioisotopes mainly ^{22}Na and ^{68}Ge/^{68}Ga. Emitted positrons from radionuclides before implantation to the sample pass through the source. The analysis of results in all of these methods requires consideration of the corrections resulting from the construction of the positrons source.

Commonly used radioisotopes β^+ are usually in the form of chemical compounds, especially their salts such as ^{22}NaCl and ^{68}GeCl/^{68}GaCl. The salt in the form of their solutions is placed on the thin 7 μm kapton films and evaporated forming $1-2$ micrometer crystals. To isolate the radionuclide from the environment kapton foils are sealed together at the edges. Thus prepared positron source prevent contamination of the sample by the radionuclide and enables its reuse. Preparation of such a source is unique; hence each of them has its individual features.

Radioisotopes emit positrons isotropically and with some energy distribution determined by the Fermi distribution. Different values of their energies give specific positron implantation profile with a total range which for metals is typically a few hundreds of micrometers and is associated with absorption in the material. Measurements using a given source is done by placing the source between two identical samples. The positron after leaving the nuclei can annihilate in the source. However, most of the positrons reaching the surface of the source-sample border and penetrate the sample or are scattered backwards. Backscattered positrons traverse the source again, until it encounters the next border between the source and the sample. There, they can penetrate into the sample or undergo backscatter again. As a result, a positron emitted from the nuclei of the radionuclide can repeatedly pass the source, as shown in Fig. 1, and this significant influences on the measurement. Certainly, during the traverse in the source positrons can annihilate which is reflected in the measured spectra. In the positron lifetime measurement, the component associated with annihilation in the source is usually fitted numerically and its value ranges from several to dozens of percent. However, the numerical fitting gives poor results when the positron lifetime of the material is similar to that in kapton polyimide, which is in the range $360-460$ ps.[3–5] For the measurement of the Doppler broadening of annihilation line the effect of the source often is not taken into account, and the results are meaningful only within series of measurements carried out on the same apparatus and using the same source. The purpose of this paper is to present the method for calculating

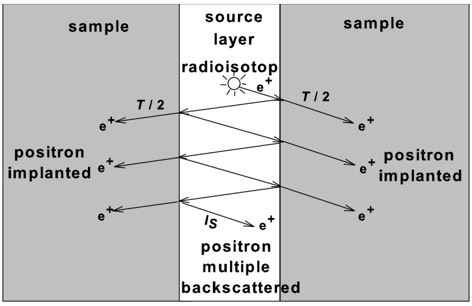

FIGURE 1: Schematic representation of the multiple scattering model for the sandwich geometry sample-source-sample. The figure shows also the fraction of positrons implanted to sample T and absorbed by the source I_S described in the text.

corrections of the contribution of positrons annihilated in the source and determine the implantation profiles in a symmetrical structure sample-source-sample. The results will be confronted with the experimental measurements.

If the examined sample is located in a sandwich geometry, Fig. 1, the total fraction of positrons implanted to the samples and absorbed by the source can be determined as the sum of the geometric series due to the multi backscattered effect, which gives:

$$T = \sum_{i=0}^{\infty} (1-R) I_m\left(\frac{d}{2}\right) (R I_m(d))^i = \frac{(1-R) I_m\left(\frac{d}{2}\right)}{1-R I_m(d)}, \qquad (1)$$

$$I_s = 1 - T, \qquad (2)$$

where d is the thickness of the source layer, R means the backscatter coefficient, which is the probability of positrons backscattering from the border of the source, and $I_m(z)$ is the positrons implantation profile on the depth z away from the source. Considering the positrons contribution transmitted by the collimated, heterogenic positron beam in the homogeneous, uniform medium, taking into account the geometry of the measuring Saoucha[6] determined $I_m(z)$ function as:

$$I_m(z) = e^{-\alpha_+ z} + \alpha_+ z E_i(-\alpha_+ z), \qquad (3)$$

where $E_i(-x) = -\int ds \exp(-s)/s$ is rapidly convergent exponential integral, z is distance from the source of positrons, α^+ is the linear absorption coefficient of the sample material. α^+ depends on both the energy E_{max}, which is the end-point energy of the positrons emitted during β^+ decay of the radionuclide, as well as the density ρ and the average atomic number Z of the material. On the basis of measurements carried out radionuclides ^{22}Na and ^{68}Ge/^{68}Ga, Dryzek and Singleton[7] proposed the generalized absorption coefficient formula:

$$\alpha^+ = \frac{12{,}6 Z^{0{,}17}}{E_{max}^{1{,}28}} \rho \qquad [\mathrm{cm}^{-1}], \qquad (4)$$

Number of backscattered positrons rise with increasing atomic number Z of the material to which the positrons are implanted. Backscatter phenomenon has been investigated by many authors.[8–10] MacKenzie et al.[8] the best fit of coefficient R to the experimental Doppler broadening of annihilation line measurements carried out ^{22}Na and ^{68}Ge/^{68}Ga radionuclides in all ranges of the atomic numbers obtained for:

$$R = 0{,}342 \log_{10} Z - 0{,}146. \qquad (5)$$

In this paper authors also propose an alternative exponential formula that fits better to results for small and large values of Z, but overestimate the values of R in the range $30 < Z < 70$:

$$R = 0{,}52\left(1 - e^{-0{,}045 Z}\right). \qquad (6)$$

Arifov et al.[9] proposed for the collimated, nonmonoenergetic positrons emitted from the ^{22}Na isotope another empirical formula:

$$R = (0{,}0577 \pm 0{,}0058) Z^{(0{,}4724 \pm 0{,}0249)}. \qquad (7)$$

Based on the known values of the coefficients of positrons scattering it can also be possible to determine the positrons implantation profile in a sample, which is differential of total positron contribution on the z depth from the source $dI(z)/dz$. Function $I(z)$ can be evaluated as in Eq. (8), where d is the thickness of source.

$$I(z)=\begin{cases} Te^{-\alpha_{+}z}, & z>|d| \\ \frac{1}{2}I_{\mathrm{m}}\left(\frac{z}{2}\right)+(1-T)\left(\frac{1}{2}I_{\mathrm{m}}\left(\frac{d}{2}+z\right)\frac{1}{2}I_{\mathrm{m}}\left(\frac{d}{2}-z\right)\right), & z<|d| \end{cases} \tag{8}$$

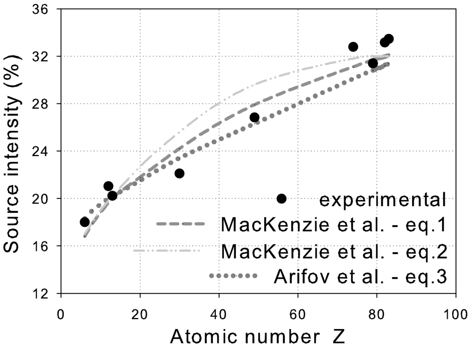

FIGURE 2: The fraction of positrons annihilated in the source in dependence on the atomic number Z of measured material. The dotted curves represent the best fit of the Eq. (2) for different backscatter coefficient described by Eqs. (5), (6), (7).

The fraction of positrons which annihilate in the source was determined as follows. The measurements for various materials with different Z were performed using a fast-fast positron lifetime spectrometer with the timing resolution (FWHM) of about 260 ps. As a positron source ^{22}Na isotope closed in the 7 μm thick kapton foil envelop was used. The positron lifetime spectrum was measured during 24 hrs to obtain more than 2×10^6 counts in the spectrum. The deconvolution of the spectra was performed using the LT program.[11] Positrons were implanted into bulk materials of graphite, Mg, Al, Zn, In, W, Au, Pb, Bi. For pure elements positrons lifetimes are well known from experiments[5] and theoretical models.[12,13] They depend on the material to which positrons are implanted and for the metals are usually in the range of 90 to 250 ps.[14] From the measurements for these materials obtained lifetimes were consistent with reported values of other authors.

Fig. 2 shows the percentage fraction of positrons annihilated in the source depending on the atomic number of the sample material. As expected, the fraction of the positrons which annihilate in the source increases with increasing atomic number of the sample sandwiched the source was observed. The Eq. (2) was fitted to the points, where the only adjustable parameter was the thickness d of the source, while R coefficients were alternately described by Eqs. (5), (6), (7). Dependency received from fitting are marked by dotted lines in Fig. 2. The best ones was obtained with the formula developed by McKenzie et al. — Eq. (5). The adjusted thicknesses d were equal 58 μm; 62,5 μm; 74 μm; respectively for Eqs. (5), (6), (7). The thicknesses of source were near 3 – 4 times greater than the thickness of the kapton foils, what was influenced mainly by seal material, which won't account in calculations, and also several micrometers layer of crystalline salt ^{22}NaCl, which has definitely different absorption coefficient than Kapton.

In this case, the thickness d only responds for generalized way of replacing complicated nature of source to simple problem of one homogeneous layer. Based on the presented

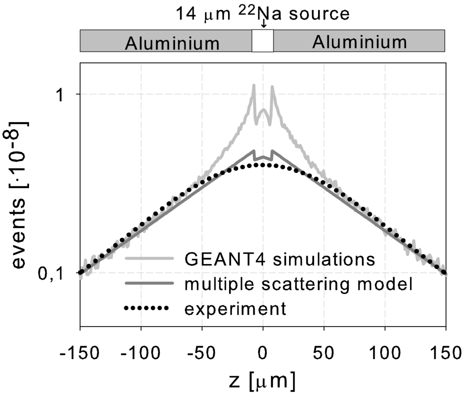

FIGURE 3: The positron implantation profiles measured for the sandwich: Al-source-Al in dependence on the distance from the source z. Black, dark gray and dotted gray line correspond to profile obtained from experiment, multiple scattering model and GEANT4 simulations, respectively.

model the number of positrons using Eq. (8) reaching a given depth z away from source can be determined. For comparison, the profile like this can also be generated using Monte Carlo simulation using the code e.g. of GEANT4.[15] Both evaluated profiles and experimental results measured by DSIP methods[16] for the Al-source-Al structure is shown in Fig. 3.

Calculated profiles predict the exponential dependence of the implantation profile for depths greater than 100 μm and remain in full compliance with the experimental data in this range. However, within the source, the profile obtained from multiple scattering model better reproduce the experimental results. In conclusion, the presented model enables evaluation of the contribution of the source for a variety of homogeneous materials. It also allows to calculate the positron implantation profiles which are consistent with experiment. It is worth noting that the proposed simplified calculations (Eq. (8)) lets us to obtain results that are substantial consistent with the results obtained with long-duration method such as Monte Carlo (GEANT4) simulations.

⋆ ⋆ ⋆

[1] P. Hautojärvi, Positrons in Solids, Topics in Current Physics No. 12 (Springer Verlag, 1979).

[2] M. J. Puska, R. M. Nieminen, *Rev. Mod. Phys.* **66**, 841 (1994).

[3] T. E. M. Staab, B. Somieski, R. Krause-Rehberg, *Nucl. Instrum. Meth. A* **381**, 141 (1996).

[4] N. Djourelov, M. Misheva, *J. Phys.-Condens. Mat.* **8**, 2081 (1996).

[5] H. Weisberg, S. Berko, *Phys. Rev.* **154**, 249 (1967).

[6] A. Soucha, *J. Appl. Phys.* **85**, 1802 (1999).

[7] J. Dryzek, D. Singleton, *Nucl. Instrum. Meth. B* **252**, 197 (2006).

[8] I. K. MacKenzie, C. W. Shulte, T. Jackman, J. L. Campbell, *Phys. Rev. A* **7**, 153 (1973).

[9] P. U. Arifov, A. R. Grupper, H. Alimkulov, *Mater. Sci. Forum*, 699 (1982).

[10] J. Dryzek, E. Dryzek, *Phys. Lett A* **320**, 238 (2003)

[11] J. Kansy, *J. Nucl. Instr. and Meth. in Phys. Res. A* **374**, 235 (1996).

[12] J. M. Campillo Robles, E. Ogando, F. Plazaola, *J. Phys.-Condens. Mat.* **19**, 176222 (2007).

[13] A. Rubaszek, Z. Szotek, W.M. Temmerman, *Phys. Rev. B* **58**, 11285 (1998).

[14] S. McGuire, D. J. Keeble, *J. Appl. Phys.* **100**, 103504 (2006).

[15] GEANT4, http://cern.ch/geant4, (available on 07.02.2013)

[16] J. Dryzek, *Acta Phys. Pol. A* **107**, 598 (2005).

Optically and thermally stimulated luminescence of lithium aluminate

Anna Twardak

The Henryk Niewodniczański Institute of Nuclear Physics Polish Academy of Sciences, Radzikowskiego 152, 31-342 Kraków, Poland

Supervisor: Paweł Bilski

Preliminary studies of optically and thermally stimulated luminescence properties of polycrystalline lithium aluminate growth by Czochralski and Micro-Pulling-Down methods were presented. Thermoluminescent glow curves and optically stimulated luminescent decay curves after alpha and beta exposures were shown. Achieved results of samples sensitivities were compared to commercially applied dosimeters. Moreover initial measurement of fading was conducted.

Thermally (TL) and optically stimulated luminescence (OSL) are one of the most widespread methods of passive dosimetry and find applications in variety of radiation measurements.[1,2] Although there are many known luminescent materials there is still a need to search of new materials and methods based on OSL and TL techniques which can be used in individual and accidental dosimetry. Lithium aluminate ($LiAlO_2$) is one of new materials considered as a luminescent material.[3] In particular, the use of this material as an OSL detector can bring benefits in comparison to commercially used Al_2O_3:C. In particular, lithium aluminate has lower effective atomic number than aluminum oxide, which resulting in lower photon energy dependence and it is also better tissue equivalent. Moreover adhibition of Li-6 enables application in neutron dosimetry. Recently, two methods of crystal growth of lithium aluminate was demonstrated by groups of Chou (Czochralski method) and Pejchal (Micro-Pulling-Down method).[4,5] The purpose of this study is to describe and examine the basic TL and OSL properties of lithium aluminate.

Samples under study were prepared using two different crystal growth techniques: the Czochralski method, available at The Korea Atomic Energy Research Institute (KAERI) in Daejeon and the Micro-Pulling-Down method with an induction furnace and iridium crucible, available at Institute of Nuclear Physics (INP) in Cracow.

The melted materials were turned into the powder form, from which samples of about 20 mg were used in the measurements. All OSL and TL results were normalized to the sample mass. For comparison purposes, a powdered sample of aluminum oxide (Al_2O_3:C) produced by Landauer, current standard OSL material, was used.

The measurements were realized using the Risø TL/OSL DA-20 reader. Thermoluminescence was measured up to 400°C at the rate of $5°\mathrm{C\,s^{-1}}$. OSL was measured under continuous wave stimulation using blue light. The reader was equipped in its standard filter U-340, what enables measurement of luminescence in the range 300 – 400 nm. Irradiations were performed exploiting the alpha and beta sources built in the reader. The investigated samples were thermally annealed by heating up to 450°C in the DA-20 reader, followed by subsequent irradiations with beta (Sr-90/Y-90) or alpha (Am-241) particles and OSL measurements under continuous wave blue light stimulation (CW-OSL).

It is interesting to note that some of the $LiAlO_2$ samples, including the KAERI material, show an increase of the OSL signal in the first second of the stimulation, before the subsequent exponential decay. Such behavior was however observed only for beta irradiated samples. Such a shape of the OSL decay curve may indicates the participation of shallow traps in optically stimulated luminescence process. In general, there is an apparent dif-

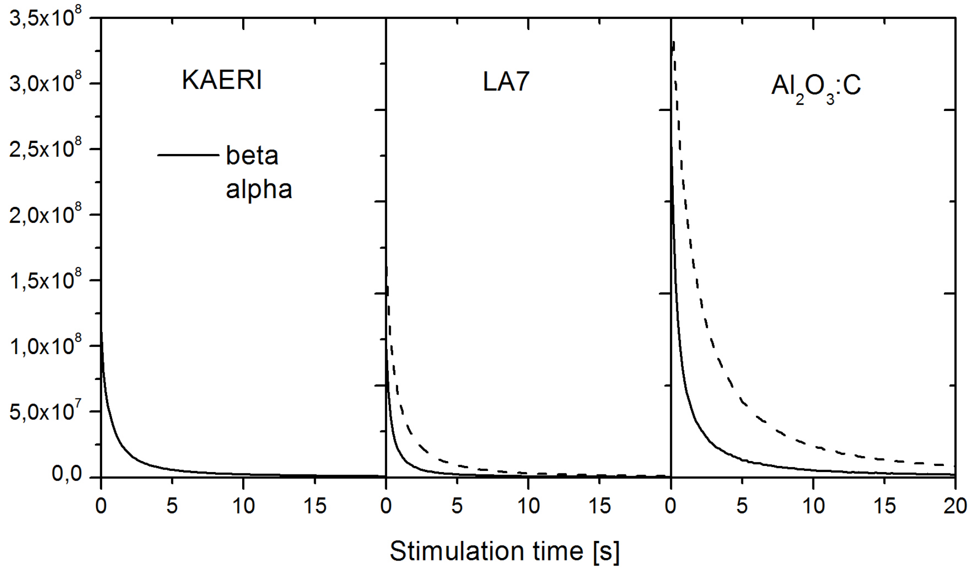

Figure 1: Comparison of CW-OSL decay curves after beta and alpha irradiations for the selected samples.

ference in the decay pattern following alpha and beta exposure, what is illustrated in the Fig. 1. The decay of alpha irradiated samples was found to be faster in all cases.

The OSL sensitivity of the tested samples is presented in the Table 1 with respect to the Al_2O_3:C material. The total signal of the KAERI sample after beta exposure was found to exceed that of Al_2O_3:C. Other samples show approximately between 25% and 60% of the Al_2O_3:C signal. It should be however mentioned that the spectral sensitivity of the used configuration of the DA-20 reader is not optimum for Al_2O_3:C, which emits light in the blue region, while for lithium aluminate most of the emission is located below 400 nm.

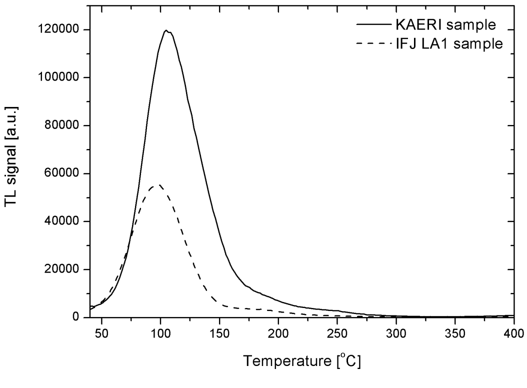

Figure 2: Examples of TL glow curves measured for KAERI and IFJ $LiAlO_2$ samples following beta irradiation.

In the Fig. 2 the examples of the thermoluminescent glow curves are presented. The temperature at which the main peak is located is rather low: in the range 100 – 110°C, which may result in significant fading of the sample's signal. There are no significant differences between glow curves shape following beta and alpha exposures.

A Table 2 summarizes the TL response of the studied samples. The response is low, reaching only a few percent of the Al_2O_3:C signal, unlike it is in case of OSL. This effect is also illustrated by the data presented ratio between OSL and TL signals. For $LiAlO_2$ samples this ratio varies between 35 and 123,9 while for Al_2O_3:C it amounts only to about 2. This means that in lithium aluminate optical stimulation is much more effective in producing intensive luminescence than thermal stimulation, while for aluminum oxide the difference between both modes is much smaller.

As mentioned before the position of the TL peak at relatively low temperature may suggest possibility of the thermal instability

TABLE 1: CW-OSL response after alpha and beta irradiation, with respect to the Al_2O_3:C.

	Beta		**Alpha**	
Sample	Total OSL signal*	Fast component of the OSL signal**	Total OSL signal*	Fast component of the OSL signal**
LA-1	0,58	0,63	0,59	0,67
LA-2	0,41	0,47	0,30	0,34
LA-3	0,33	0,41	0,33	0,37
LA-6	0,25	0,34	0,24	0,29
LA-7	0,30	0,39	0,34	0,39
LA-8	0,31	0,38	0,31	0,35
KAERI	1,10	0,83	0,61	0,63
Al_2O_3:C	1,00	1,00	1,00	1,00

* integral over 40 s, ** integral over first 4 s.

of the stored signal (fading). For that reason an experiment aimed on studying such effects was undertaken using the KAERI prepared sample of lithium aluminate. The OSL measurements were realized after various times after exposure, ranging from 0,5 h to 24 h. The total OSL signal in dependence on the storage time is presented in the Fig. 3. It is apparent that indeed the OSL signal decreases with the storage time and after 24 hours and 8% loss of the signal is observed. This effect will be studied in longer periods of time and it must be one of the main properties subjected to optimization, as the fading might be a significant shortcoming of the developed material. The evolution of the decay curves with the storage time is illustrated in the Fig. 3.

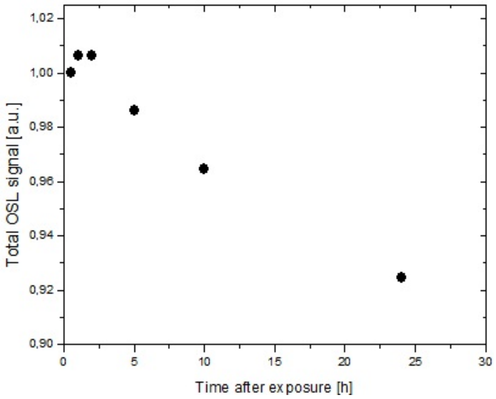

FIGURE 3: Fading of the total OSL signal of the KAERI sample after beta exposure.

TABLE 2: TL response after beta and alpha irradiation.

	Beta			**Alpha**		
Sample	Total TL signal*	Peak height*	Ratio OSL/TL	Total TL signal*	Peak height*	Ratio OSL/TL
LA-1	0,029	0,032	43,9	0,014	0,0003	64,1
LA-2	0,012	0,014	75,1	0,007	0,0002	67,3
LA-3	0,011	0,009	67,8	0,008	0,0001	60,3
LA-6	0,010	0,009	54,6	0,010	0,0002	34,1
LA-7	0,005	0,005	123,9	0,007	0,0001	75,5
LA-8	0,008	0,008	86,2	0,010	0,0002	47,5
KAERI	0,067	0,072	35,5	0,021	0,0006	43,2
Al_2O_3:C	1,00	1,00	2,2	1,00	1,00	1,5

* relatively to Al_2O_3:C.

To summarize the $LiAlO_2$ samples prepared at KAERI and at IFJ were investigated, with respect to their OSL and TL response after beta and alpha exposure. The most important outcome is that the sensitivity of the KAERI samples under blue light stimulation is comparable with that of Al_2O_3:C, current standard OSL material. This is a very promising result, even keeping in mind that the spectral sensitivity of the used DA-20 reader is not optimum for Al_2O_3:C. Also OSL response of the polycrystalline $LiAlO_2$ samples prepared at IFJ was found to be on the similar level. A potential disadvantage of the studied samples is observed fading. This will be an important factor in the planned optimization of the preparation techniques. Taking into account many important factors of the crystal growth, which might be subjected to optimization, like temperature, gas atmosphere, dopants, as well as possible post-growth thermal treatment, one may expect a possibility of considerable improvement of the material properties. Furthermore investigations of other dosimetric properties, including response to neutrons, are foreseen.

⋆ ⋆ ⋆

[1] E. G. Yukihara, S. W. S. McKeever, Optically Stimulated Luminescence: Fundamentals and Applications, 1st edition (A John Wiley and Sons, Ltd., Chichester, 2011).

[2] R. Chen, S. W. S. McKeever, Theory of Thermoluminescence and Related Phenomena (World Scientific Publishing Co. Pte. Ltd., Singapore, 1997).

[3] J. I. Lee, A. S. Pradhan, J. L. Kim, I. Chang, B. H. Kim, K. S. Chung, *Radiat. Meas.* **47**, 837 (2012).

[4] M. M. C. Chou, P. C. Tsao, H. C. Huang, *J. Cryst. Growth* **292**, 542 (2006).

[5] J. Pejchal, Y. Fujimoto, V. Chani, T. Yanagida, A. Yoshikawa, M. Nikl, A. Beitlerova, *J. Cryst. Growth* **360**, 127 (2011).

Application of medium-energy proton beam from AIC-144 cyclotron for the trace elements determination in biological reference materials and human thyroids

Anna Wójcik

The Henryk Niewodniczański Institute of Nuclear Physics Polish Academy of Sciences, Radzikowskiego 152, 31-342 Kraków, Poland

Supervisor: Jerzy Wojciech Mietelski

Activation analysis is a well known analytical technique which provides both qualitative and quantitative analysis of major, minor and trace elements in a given matrix, without or with chemical separation. Activation by charged particles like protons is by no means restricted to the low atomic number elements, although after appropriate optimization procedures, proton activation analysis can be highly effective in simultaneous quantitative determination of medium-heavy trace elements in biological samples. AIC-144 cyclotron at the Institute of Nuclear Physics Polish Academy of Sciences can accelerate proton up to the energy of 60 MeV while the beam intensity does not exceed 50 nA (which is suitable for the radiotherapy of eye melanoma). Since 2010 we have studied several types of biological samples trying to check whether a proton beam with such intensity and energy can be used in activation analysis. As a result the elements which are possible to be determined under the above-mentioned experimental conditions have been selected. The sources of possible interferences were also identified.

ICP MS (Inductively Coupled Plasma Mass Spectrometry), ICP AES (Inductively Coupled Plasma Atomic Emission Spectrometry), ICP OES (Inductively Coupled Plasma Optical Emission Spectrometry), AAS (Atomic Absorption Spectrometry), AFS (Atomic Fluorescence Spectrometry) and XRF (X-ray Fluorescence Spectrometry) are nowadays very useful tools in environmental, biological, and geological samples analysis. These methods have almost completely superseded the activation techniques of qualitative and quantitative trace elements determination. It does not mean that they are better in terms of obtained detection limits and the accuracy of results. The problem with such nuclear analytical techniques like activation analysis is the necessity for a research centre to posses the appropriate radiation source and high exploitation costs related to it, which comprises a kind of inconvenience. Most of the cyclotrons existing in the world today are dedicated to the isotope production or hadron therapy for cancer treatment. No one considers today the use of proton beam for other purposes like activation analysis although it seems that this topic is not exhaustible. The only activation technique which is still expanded is the neutron activation analysis. Meanwhile, proton (charged particle) activation analysis (CPAA) could often complement the studies conducted using neutron activation analysis (NAA), although it has predominant applications in the determination of light elements, which are inaccessible to NAA. After the appropriate optimization procedures, proton activation analysis can be highly effective in simultaneous quantitative determination of medium-heavy trace elements in biological samples. So far, the papers published on CPAA of biological materials have shown the results of studies in which the applied proton energy was less than 32 MeV (usually it varied from 12 to 31 MeV), with the beam intensities up to 500 nA.[1] There is no point in looking for the data from activations using higher energy proton beams because it simply does not exist.

TABLE 1: Precision of iodine determination in biological reference material BCR 279.

Sample ID	Iodine concentration [μg/g]	Reference [μg/g]
1	162±15	—
2	155±18	—
3	157±21	—
4	159±13	—
5	160±23	—
6	154±20	—
Mean	157,8±3,1	158±4

After modernization, which took place in 2004, the AIC-144 isochronous cyclotron at the Henryk Niewodniczański Institut of Nuclear Physics Polish Academy of Sciences was adopted to the medical application such as radiotherapy of eye melanoma. This means that the only obtained protons' energy now is 60 MeV, while the beam intensity does not exceed 50 nA. Such conditions were suitable for cancer treatment but not for commercial scale radioisotope productions. A question has arisen whether a proton beam with such intensity and energy could be used for other applications like quantitative and qualitative analysis of different kind of materials, and if so, what elements could be determinate. To answer this question, four biological reference materials issued by National Institute of Standards and Technology, USA (NIST), Institute for Reference Materials and Measurements, Belgium (IRMM), and Institute of Nuclear Chemistry and Technology, Poland (INCT), have been examined and elements which are possible to be determined under afore-mentioned experimental conditions have been selected. The procedure for sample preparation was described elsewhere.[2,3] All employed reagents of analytical grade, which were used as working standard solutions, were purchased from Sigma-Aldrich.

A rotating sample holder was designed to irradiate many samples simultaneously and uniformly. Each sample was sealed separately into a polypropylene vial to avoid the cross contamination of samples. Al foils (^{27}Al(p,x)^{24}Na reaction) were used to monitor the current of the external proton beam[4] and to compare it with the current of the internal beam.

A preliminary analysis was undertaken to identify the possible channel reactions leading to the production of radionuclides. It was shown that 60 MeV of the incident protons corresponds to the high yield of ^{123}Xe production (^{127}I(n,5p)^{123}Xe reaction) and therefore 158,97 keV gamma-ray from ^{123}I

$$^{123}\mathrm{Xe} \xrightarrow{\beta^+} {}^{123}\mathrm{I}\ ,\ \ T_{1/2} = 13{,}27\ \mathrm{h}$$

can be used for the ^{127}I detection. It is known that human body contains 15 − 20 mg of iodine with 70 − 80% being located in the thyroid gland and iodine forms an indispensable part of thyroid hormones, i.e., thyroxine (T4) and 3,5,3'-triiodothyronine (T3).[5] Since the number of methods available for iodine determination, which are appropriate for use in biological materials analysis, is highly limited, we decided to check if the proton activation analysis would work for iodine determination in human thyroid samples (when the opportunity occurs other elements were also analyzed). In order to establish the precision of the method, the iodine was determined in six 0,25 g samples of BCR 279. The results are shown in Table 1. IRMM BCR 279 (Sea lettuce) was the only standard for the analysis of iodine in biological materials (158±4 μg/g).[6] It was chosen because no other commercially available reference materials with relatively low concentration of iron in comparison to iodine were available. It occurred that the 158,97 keV gamma-ray from ^{123}I tends to be overlapped with 159,377 keV from ^{47}Sc ($T_{1/2}$ = 3,35 d). In case of biological materials this overlapping cannot be negligible because of the high concentration of copper. It is not easy to correct or reduce the interference from ^{47}Sc. One could use the ion-exchange chromatography based on the application of Dowex 50 W X 4 (100-200 mesh) resin, but the simplest way is to perform the measurement after several hours of the cooling period when the ^{123}Xe decayed to ^{123}I and ^{47}Sc has not managed yet to decay in significantly high amount. As it was shown, the obtained results were in good agreement with reference values. Iodine content in 25 analyzed human thyroid samples varied from 0,050±0,033 mg/g to 7,89±0,85 mg/g. The mean value amounted to 1,24±1,80 (S. D.) mg/g.

It is concluded that the proposed method seems to be useful for trace iodine concentration determination because of its simplicity and relatively good sensitivity. Further studies should be undertaken to extend this method for iodine determination to urine, blood and serum samples. This could be only done if irradiate previously liofilized biological material to eliminate the influence of ^{7}Be (which is produced via ^{16}O(p, spall)^{7}Be spallation reactions) on the high Compton continuum when using gamma-ray spectrometry.

⋆ ⋆ ⋆

[1] D. De Bartolo, M. C. Cantone, A. Giussani, *Appl. Radiat. Isotop.* **7**, 49(1998).

[2] A. K. Wójcik, P. Zagrodzki, J. W. Mietelski, B. Wąs, *J. Radioanal. Chem.* **2**, 291 (2012).

[3] A. K. Wójcik, J. W. Mietelski, *Proceedings on 5th International Interdisciplinary Technical Conference of Young Scientists*, p. 145 (Poznań, 2012).

[4] IAEA Report, IAEA-TECDOC-1211 — Charged particle cross-section database for medical radioisotope production: diagnostic radioisotopes and monitor reactions. Final report of a co-ordinated research project (IAEA, Vienna, 2001).

[5] J. Kučera, Z. Řanda, L. Soukal, *J. Radioanal. Chem.* **1**, 249 (2001).

[6] B. Griepink, M. Mubtau, The certification of the contents (mass fractions) of arsenic, cadmium, copper, lead, selenium and zinc in a sea lettuce (Ulva lactuca) CRM N°279 (Office for Official Publications of the European Communities, Luxemburg, 1987).

MODERN ELECTRONICS FOR PHYSICS EXPERIMENTS

A two-dimensional radiotherapy proton beam imaging system based on a scintillator and a CCD camera — preliminary results

Marzena Boberek

The Henryk Niewodniczański Institute of Nuclear Physics Polish Academy of Sciences, Radzikowskiego 152, 31-342 Kraków, Poland

Supervisor: Michael P. R. Waligórski

In the process of preparing a proton beam for radiotherapy, quality control (QC) of the beam parameters of pristine and spread-out proton beams is necessary. Among the controlled parameters are: transverse profiles of proton beam emittance, uniformity of dose and extent of lateral penumbra across the beam cross-section at different beam depths (ranges), and dose and distal fall of along the beam range, for pristine and spread-out radiotherapy beams. So far, such measurements are performed by scanning a semiconductor diode along and across the beam, a laborious and time-consuming process. To facilitate and speed-up this process, a beam imaging system is under development at IFJ PAN, comprised of a beam-imaging scintillator, a high-resolution CCD camera, and a data acquisition system with dedicated image processing software. Results of preliminary tests of a prototype of this beam imaging system are reported.

Ocular proton therapy is currently being performed at IFJ PAN using 60 MeV protons from the AIC-144 isochronous cyclotron.[1] To cover the volume of the melanoma tumour in the eye, passive spreading system of the proton beam is used, whereby an individually designed absorber of variable thickness, is applied. The absorber allows the narrow Bragg peak of the proton beam to be converted to a broader spread-out Bragg peak (SOBP), effectively as a superposition of suitably range-displaced and intensity-matched Bragg peaks, achieving uniform dose distribution along the range of the SOBP. Additionally, the proton beam is individually collimated for each patient. Prior to patient exposure, the passively formed and collimated proton beam has to undergo a strict Quality Control (QC) procedure to verify the correctness of uniformity of dose and extent of lateral penumbra across the beam cross-section at different beam depths (ranges), and uniformity of dose and distal fall of along the beam range, against the therapy planning calculations. Presently, such measurements are being performed by scanning a semiconductor diode along and across the beam, a laborious and time-consuming process.

In 2013 a new IBA-Proteus C-235 cyclotron recently installed at IFJ PAN will begin operation, with a 230 MeV proton beam dedicated to cancer therapy and basic nuclear physics research. In 2014 a rotating beam line (Gantry) and a scanning beam head will be added to this facility, enabling this new beam to be used for treating all locations in the cancer patient from any direction. The spot scanning beam technique available at IFJ PAN from 2015 onwards, allows three-dimensional conformation of the dose to the target volume, replacing the passive Bragg peak spreading technique.

Clinical application of passive beam scattering or of scanned proton pencil beam techniques in radiotherapy requires that precise localization and repeatability of the physical parameters of the beam be verified In particular, accurate measurements of the dose distribution along the beam range (the percent dose-depth — PDD) and across the beam axis (the dose profiles) at different beam depths are essential. Such measurements are part of

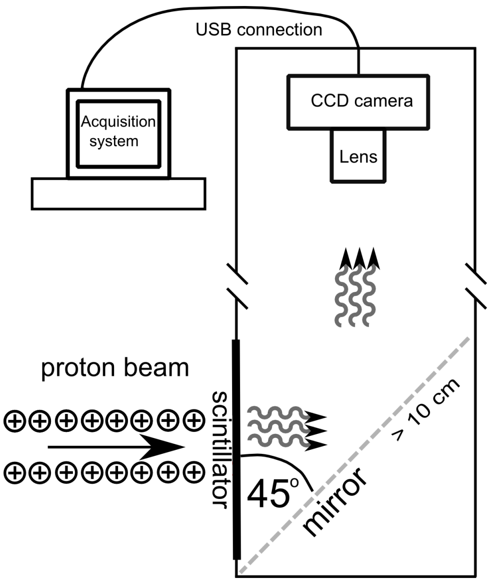

FIGURE 1: Layout of the beam scanning system under development.

the QA (Quality Assurance) system in radiotherapy, to enable precise and repeatable delivery of the beam dose to the tumour volume. To fulfil this requirement and to speed up the beam quality control procedure, a new system for proton beam spatial fluency imaging is under development.

Our prototype system consists of a Gd_2O_2S:Tb (Gadolinium Sulphate Oxide doped with Terbium) scintillator[2] to efficiently convert the passage of protons of the beam through the scintillator to visible light pulses, and of a sensitive ATIK 383 CCD camera of high spatial resolution (3362x2504 pixels), able to record the 550 nm light emitted by the proton- irradiated scintillator. The overall scheme of the system is presented in Fig. 1. Modern CCD cameras offer high resolution imaging in visible-light wavelength range with a greyscale level of up to 16 bits. To avoid radiation damage to the CCD camera sensor from protons in the beam, the camera is positioned perpendicularly to the beam axis and light from the scintillator is reflected by a 45-degree glass mirror. Hence, correct performance of the optical system to view the scintillator surface by the CCD camera is also an important feature of the device. The ATIK 383 CCD camera is a digital output camera, whereby the digital signal is transmitted via an USB interface to the data acquisition system where data can be analyzed with LabVIEW software. The acquired images undergo detailed analysis in order to extract the physical and geometrical parameters of the beam. Prototype in-house developed software for image analysis is being developed in MATLAB programming environment. The specific functions and algorithms are then moved to NI LabVIEW environment. The general aim of the PhD project is to develop a stand-alone system using LabVIEW, to acquire beam images and to determine the physical and geometrical parameters of the beam by executing one software command.

The most important elements of the beam imaging system are the CCD camera and the scintillating screen. The requirements which the scintillator should fulfil to be applied in constructed system, are:[3,4]

- the scintillation spectrum and CCD sensor spectral sensitivity should be matched (350 – 550 nm);
- the scintillator should be as thin as possible (no thicker than 2 mm) so as not to markedly affect the range of the proton beam;

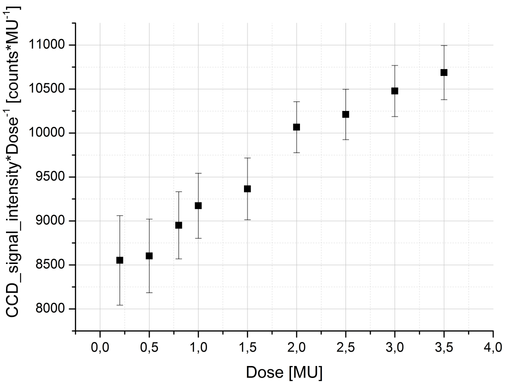

FIGURE 2: Average intensity of light from the Gd_2O_2S:Tb scintillator (recorded with CCD sensor) per dose (MU) as a function of absorbed dose. The available CCD signal intensity range is 0 – 65536.

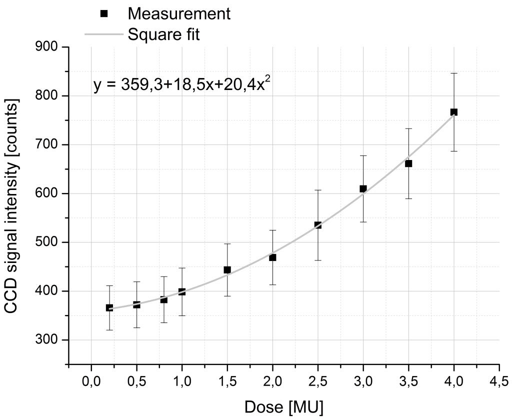

FIGURE 3: Background level as a function of absorbed dose. The available CCD signal intensity range is 0 – 65536.

- high scintillation efficiency is necessary, to gather an image of sufficient intensity over a reasonably short exposure time;
- scintillation efficiency should be a linear function of ionizing particle energy, enabling proton energy fluence distributions to be measured.

In the prototype system a Gd_2O_2S:Tb scintillator was used. Preliminary measurements of this scintillator allowed us to evaluate its applicability in the system under development. In Fig. 2 the intensity of light form the scintillator per dose, measured in Monitor Units (MU), is presented as a function of the dose. Each value is calculated as the most probable pixel readout value (i.e. the argument of the maximum of best-fitted Gaussian to the histogram of pixel values over the Region Of Interest — ROI). Each point represents light intensity per dose unit, the dose being measured by the Monitor Ionization Chamber. It is readily seen from Fig. 2 that the increase of scintillating light intensity per dose is not constant with increasing dose. This is an undesired property of Gd_2O_2S:Tb as it implies that light intensity recorded by the CCD camera is not proportional to the deposited beam dose, so it cannot be applied in measurements of the energy parameters of the beam. Moreover, as shown in Fig. 3, the background level of the Gd_2O_2S:Tb screen changes dynamically. This level varies with the dose absorbed in the scintillator, expressed as the dose. While the background level should be a linear function of the dose, a second-order function best fits the measured data. This entails an unwanted apparent increase of the measured dose, as the abnormally high background (light intensity induced by the dose deposited in the scintillator) would contribute to dose measurement.[5,6] This nonlinearity makes reliable measurements over the Bragg peak or the spread-out Bragg peak impossible. Thus, the Gd_2O_2S:Tb scintillator examined so far, will not meet the requirements of the system under development. It is necessary to investigate other types of scintillators to find the one most suitable. Among candidates to be considered are: Thallium doped caesium iodide (CsI:Tl), calcium tungsten-based intensifying screens (type PERLUX Universal, models: 28868UH, 28868UV, UH060478, UV 060478), rare earth-doped intensifying screens (type PERLUX, models: 752213, 851260) or plastic scintillators (type BC404 and BC408).

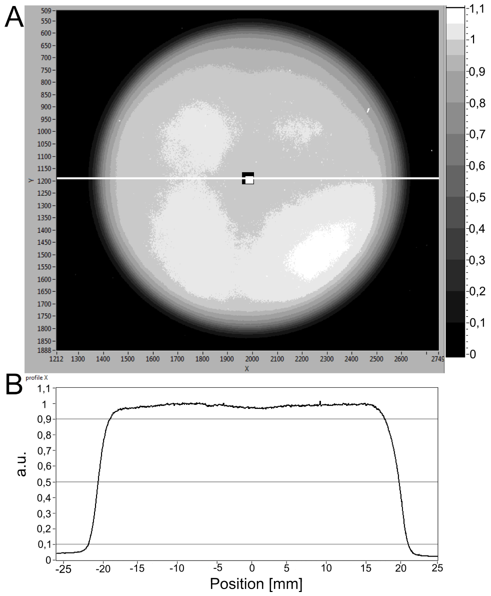

FIGURE 4: 2-dimensional spatial fluence distribution of the 60 MeV proton beam recorded with the new system under development (A), and a profile extracted from this distribution (B).

The beam imaging system under development will allow on-line control of the spatial stability of the beam. It is expected that beam parameters will be calculated more rapidly (i.e. within up to 10 seconds, against the present 4 minutes) and acquired more efficiently. In Fig. 4 an example is shown of the 2-dimensional beam fluence distribution recorded with the new system, using the Gd_2O_2S:Tb scintillator. Lateral profiles over any beam intersection plane (such as the one presented in figure 4) can be drawn from such images. In the current ocular treatment facility the space and energy parameters of the proton beam are measured with a silicone diode and by ionization chambers. These devices provide only the 1-dimensional fluence distribution in a single measurement cycle. Fig. 5 presents a current 1-dimensional measurement of the spatial distribution of proton beam fluence recorded with a semiconductor diode. The X and Y profiles are measured with a the diode and the depth dose distribution over the Bragg peak — with a Marcus Ionization Chamber.

The presented beam imaging system under development enables 2D spatial distribution of the 60 MeV proton beam allows the 2-D image of proton beam intensity to be determined within about 10 seconds. The CCD camera-based recording, accompanied by dedicated software provides high resolution imaging of the scintillating events. This is expected to result in high precision real-time dose measurements within the dose estimation procedure prior to patient treatment. Better quality of spatial fluence imaging is an important element of the Quality Assurance System, through which the highest medical standards are maintained by precise evaluation of the physical characteristics of the radiotherapy proton beam.

The contribution of Dr. Jan Swakoń in developing the design of the instrument and of Marta Ptaszkiewicz and Liliana Stolarczyk in performing some of the reported measurements, are gratefully acknowledged.

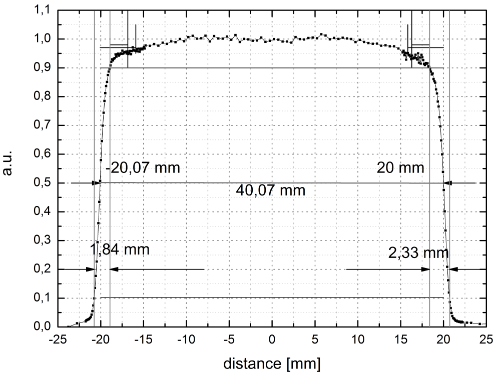

FIGURE 5: Spatial distribution of proton beam fluence measured with a silicon diode.

⋆ ⋆ ⋆

[1] B. Michalec, J. Swakoń, U. Sowa, M. Ptaszkiewicz, T. Cywicka-Jakiel, P. Olko, *Appl. Radiat. Isotopes* **68**, 738 (2010).

[2] E. I. Gorokhova, V. A. Demidenko, S. B. Mikhrin, P. A. Rodnyi, C. W. E. van Eijk, *IEEE T. Nucl. Sci.* **52**, 3129 (2005).

[3] G. A. P. Cirrone, G. Cuttone, D. Giove, P. A. Lojacono, R. Messina, A. Piemonte, *IEEE* **3**, 1752 (2004).

[4] G. A. P. Cirrone, S. Coco, G. Cuttone, C. De Martinis, D. Giove, P. A. Lojacono, M. Mauri, R. Messina, *IEEE* **51**, 1401(2004) .

[5] J. W. Kwon, H. J. Ryu, W. H. Ha, J. K. Lee, *J. Korean Phys. Soc.* **48**, 759 (2006).

[6] D. W. Kim, Y. K. Lim, J. Shin, S. Ahn, D. Shin, M. Yoon, S. B. Lee, *J. Korean Phys. Soc.* **55**, 702 (2009).

[7] J. Swakoń, P. Olko, D. Adamczyk, T. Cywicka-Jakiel, J. Dabrowska, B. Dulny, L. Grzanka, T. Horwacik, T. Kajdrowicz, B. Michalec, T. Nowak, M. Ptaszkiewicz, U. Sowa, L. Stolarczyk, M. P. R. Waligórski, *Radiat Meas.* **45**, 1469 (2010).

Data transmission and clock generation in advanced readout systems

Mirosław Firlej

Faculty of Physics and Applied Computer Science, AGH University of Science and Technology, Mickiewicza 30, 30-059 Kraków, Poland

Supervisor: Marek Idzik

Advanced readout systems need to transmit a lot of information to data center. It's not possible without advanced data transmission and data serialization circuits. Multichannel readout systems, with multichannel analog to digital converters (ADC) produce hundreds megabytes of data needed to be send in real time. Parallel transmission requires a huge amount of wires, which are not feasible in high energy physics experiments. Data serialization and transmission circuits are necessary to convert parallel data from multiple channels to serial data and send it using single wire or optical fiber. Integrated digital serialization systems require high-frequency clocks, generated by frequency multiplication circuits based on Phase Locked Loops.

Typical multichannel readout system is presented on Fig. 1. Signal generated in radiation sensors goes to charge preamplifier, which produces at its output a voltage signal in response to a current input signal coming from the sensor.[1] The amplitude of this signal is proportional to input charge. After the shaping, signal goes to Analog to Digital Converter (ADC), which converts it to digital representation. Number of ADC bits determines precision of analog to digital conversion and the width of parallel large amount of data need to be read in multi-channel system on the parallel bus. For example the readout system for LHCb experiment, 128 channels with 6-bit ADC, produce 768 bits of data per one sample. The output bus in this system should have 768 wires (without any serialization). In practice it is not possible to use large number of connections between analog to digital converters and data processing systems and transmitters, so each readout channel includes it's own serialization circuit (1st serialization level). For 6-bit ADC (for LHCb) each channel produces serial output signal with bitrate 240 Mbit s^{-1} — 6 times faster than sampling frequency, which is equal to 40 MHz. Serial data from 128 channels go to next level serializators, which give 4 serial data links with faster data rate (optical fiber). In principle number of channels connected to one serializer depends on readout system architecture and maximum output frequency obtained by serial data transmitter. In realistic readout systems often it is not possible to transmit all data generated in channels. Zero suppression circuit is necessary to reduce data transmission rate. In LHCb experiment output data rate was estimated to four links 320 Mbit s^{-1} each.

Fig. 2 shows principle of data serialization.[2] Parallel input data goes from 10-bit analog to digital converter, sampled with frequency f_s. For multiplication by 10 a phase locked loop (PLL) is used. The PLL output is used to clock the counter and multiplexer inside the serializer. Every rising edge of sample clock produces 10 bits of new data. During one sample clock period all 10 bits should be sent, so one bit lasts 1/10 of this time.

Phase locked loop[3] block diagram is shown in Fig. 3. Input reference signal (f_{in}) goes directly to the phase frequency detector (PFD). Second PFD input is connected to frequency divider, which divides output signal frequency by 10. Phase frequency detector compares frequencies and phases of reference and divided output signal. When two PFD input signals have the same frequency and the time shift between them is equal Δt, the phase

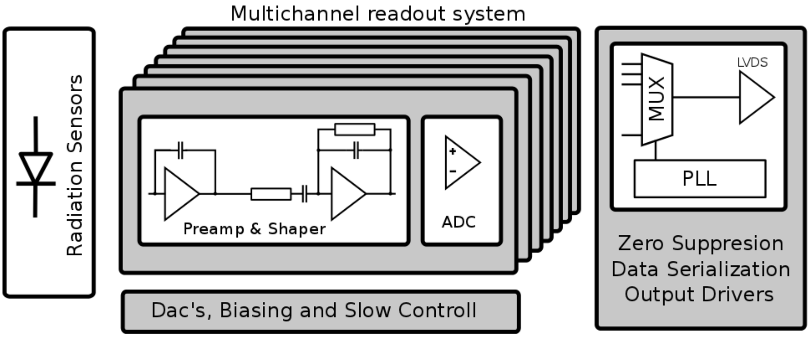

FIGURE 1: Typical multichannel readout system.

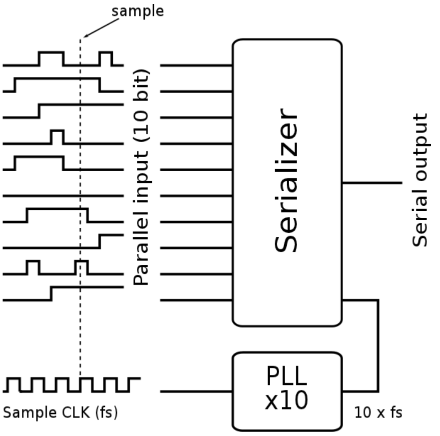

FIGURE 2: Data serialization principle.

shift is given by

$$\Delta\phi = \frac{\Delta t}{T} \cdot 2\pi \ [rad] \ , \tag{1}$$

where Δt is delay between signals and T — input signals period.

Phase and frequency detector produces two output signals (U and D), which control charge pump current pulses. When $\Delta\phi$ is positive, signal U is active and low-pass filter is charging. When $\Delta\phi$ is negative low-pass filter is discharging. In result average value of charge pump current is given by Eq. 2 where K_{PD} is the phase and frequency detector gain.

$$I_{\mathrm{CP}} = \frac{I_{\mathrm{P}}}{2\pi} \cdot \Delta\phi = K_{\mathrm{PD}} \cdot \Delta\phi \ , \tag{2}$$

$$\Delta\phi = K_{\mathrm{PD}} \cdot (\phi_{\mathrm{REF}} - \phi_{\mathrm{CLK}}) \ , \tag{3}$$

where ϕ_{REF} is input signal phase and ϕ_{CLK} — output signal phase.

In simple implementation a RC circuit is used as low-pass filter and voltage controlled oscillator (VCO) has linear transfer function. The output VCO frequency linearly depends on low-pass filter voltage (V_{cn}) with gain K_{V}. For simplicity lets set the division factor in feedback loop equal to 1. Transfer function is given by

$$H(s) = \frac{\phi_{\mathrm{CLK}}}{\phi_{\mathrm{REF}}} = \frac{\frac{I_{\mathrm{CP}} K_{\mathrm{V}}}{2\pi s}\left(\frac{1}{sC} + R\right)}{1 + \frac{I_{\mathrm{CP}} K_{\mathrm{V}}}{2\pi s}\left(\frac{1}{sC} + R\right)} \ . \tag{4}$$

According to new variables

$$\omega_{\mathrm{n}} = \sqrt{\frac{I_{\mathrm{CP}} K_{\mathrm{V}}}{2\pi C}}, \qquad \xi = \frac{1}{2} \cdot \omega_{\mathrm{n}} RC \ , \tag{5}$$

output signal phase is given by

$$\phi_{\mathrm{CLK}}(s) = \frac{\omega_{\mathrm{n}}^2 + 2\xi\omega_{\mathrm{n}} \cdot s}{s^2 + 2\xi\omega_{\mathrm{n}} \cdot s + \omega_{\mathrm{n}}^2} \cdot \frac{\phi_{\mathrm{i}}}{s} \ , \tag{6}$$

where ϕ_{i} is amplitude of phase jump.

Transforming this function to time domain gives equation similar to

$$\phi_{\mathrm{CLK}}(t) = \phi_{\mathrm{i}} + \phi_{\mathrm{i}} \cdot e^{-At} \cdot \cos(Bt + C) \ , \tag{7}$$

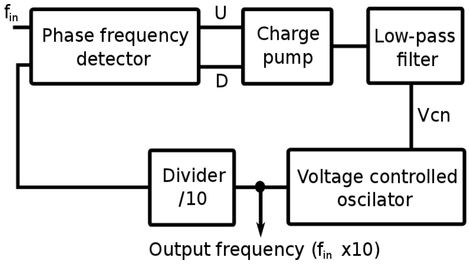

FIGURE 3: Phase locked loop block diagram.

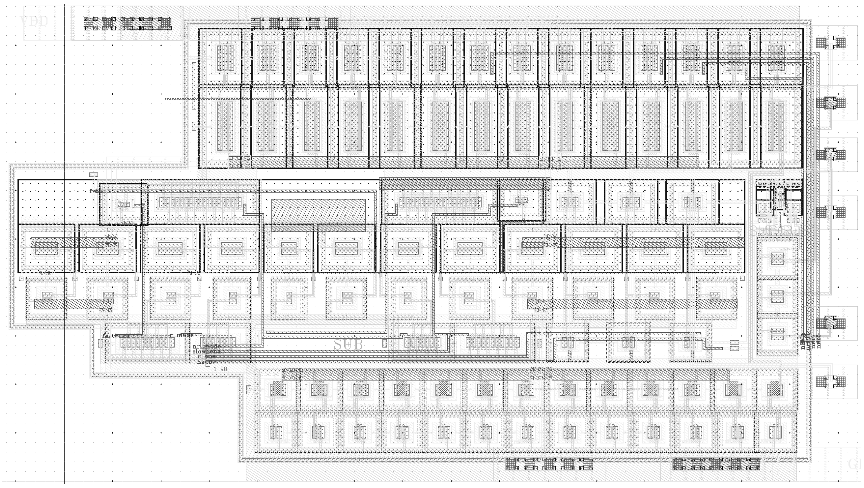

FIGURE 4: Voltage controlled oscillator layout in IBM 130 nm technology.

where A, B and C are constant values. A small phase jump at input gives oscillation damped by e^{-At}. After PLL synchronization the ϕ_{CLK} is equal to ϕ_{REF}, the low-pass filter voltage is constant and also the output signal frequency is constant.

Phase locked loop prototype was design in IBM 130 nm technology and submitted in february 2012. This design obtained in simulation low power consumption around 0,2 mW at frequency 500 MHz and works correctly in output frequency range from 60 MHz to 520 MHz. Implemented of switched divider (by 8 or by 10) makes this design suitable for data serialization from 8-bit or 10-bit ADC. Fig. 5 shows transient simulation results at VCO input of PLL prototype. After power on the voltage controlled oscillator starts with random frequency. The low-pass filter Vcn voltage is changing until the phase of divided output signal is equal to the phase of reference signal. In result VCO oscillates at 8 or 10 (depends on divider) times higher frequency than reference signal.

Second PLL prototype, submitted in May 2012 has very wide output frequency range (8 MHz – 3 GHz) and very low power consumption around 1 mW at 3 GHz. Main advantages of this design are automatically adjustable VCO modes, and increased number of feedback loop division factors (6, 8, 10 or 16). The main application of second phase locked loop prototype is data serialization in 6-bit ADC, designed for LHCb experiment. After simulations the layout was manually drawn in IBM 130 nm technology. Fig. 4 shows the layout of voltage controlled oscillator used in second PLL prototype. In the end of design process also post-layout simulations were done using parastatic components extracted from layout.

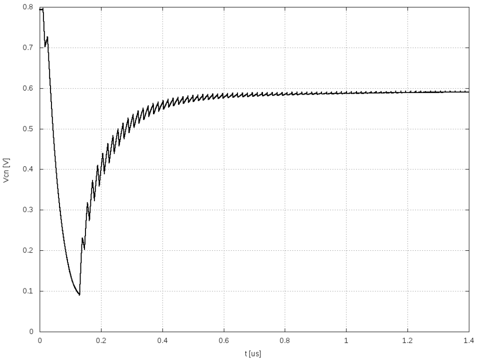

FIGURE 5: PLL simulation results — synchronization.

⋆ ⋆ ⋆

[1] K. Korbel, Układy elektroniki Front-End, (Uczelniane Wydawnictwa Naukowo-Dydaktyczne, 2000).

[2] G. Cervelli, *IEEE T. Nucl. Sci.* **51**, 836 (2004).

[3] D. Abramovitch, *P. Amer. Contr. Conf.* **1**, 1 (2002).

Development of front-end electronics for silicon strip detectors

Jakub Moroń

Faculty of Physics and Applied Computer Science, AGH University of Science and Technology, Mickiewicza 30, 30-059 Kraków, Poland

Supervisor: Marek Idzik

Development of detectors for high energy physics experiments causes continuous increase in the requirements for readout electronics. The designs of two prototype front-end electronics ASICs for detector readout are presented. Switched gain with simple CR−RC shaping front-end electronics for luminocity detector (LumiCal) at the International Linear Collider (ILC) design is discussed in detail. Challenges on pulse shaping for Large Hadron Collider beauty (LHCb) experiment upgrade with the proposed solution are presented.

Future high energy physics experiments such as Large Hadron Collider beauty (LHCb) or the International Linear Collider (ILC) will contain multilayer strip detectors. The main task of tracking system at LHCb is to provide efficient reconstruction of charged particle tracks, while the luminocity detector at ILC should both reconstructs the track and measure the deposited energy. The Silicon Tracker at LHCb experiment at Large Hadron Collider (LHC) comprises two detectors — the Trigger Tracker (TT) and the Inner Tracker (IT). Both TT and IT are built of silicon detectors divided into strips with pitch around 200 μm. The TT is composed of the few 150 cm wide and 130 cm high planar tracking stations, which are located upstream of the LHCb dipole magnet, while the IT is composed of three large planar tracking stations about 120 cm wide and 40 cm high and is located downstream of the magnet. In total the whole Silicon Tracer contains above 270 000 channels[1] and can reproduce the position of particle with resolution better than 0,05 mm. Luminocity detector (LumiCal) at ILC is composed of 30 interleaved layers of active silicon detector and passive wolfram absorbers. The active layer covering the whole azimutal angle is divided into 24 azimutal sectors, each of them comprises 96 radial pads of 300 μm thick silicon sensor. The whole system contains about 140 000 channels.[2]

Large amount of detector channels in both experiments requires a new approach to readout electronics design, specially to fullfill the restrictions on power consumption and occupied area. The whole channel readout electronics, comprising both analog and digital circuits, should be integrated in a multichannel readout system ASIC as shown in Fig. 1. The digital part contains Analog to Digital Converters (ADCs) and the digital data processing, such as zeros suppression, transmission protocol encapsulation and parallel to serial conversion (serialization). Prototypes of 10-bit (for ILC) and 6-bit (for LHCb) ADCs were already designed and fabricated). The analog part of readout — front-end electronics contains a preamplifier and a pulse shaping circuit (shaper). This work presents the design of ASICs prototype of the front-end electronics for both LHCb and ILC experiments.

Two front-end circuits were designed corresponding to different requirements in both experiments as shown in Table 1. Both designs comprise charge sensitive preamplifier[3] with slightly different feedback circuit. The front-end for LumiCal detector should work in two modes (calibration and physics) to cover the whole input dynamic range. In the calibration mode it should be able to measure signals as small as 2 fC, corresponding to low end of Landau distribution for minimum ion-

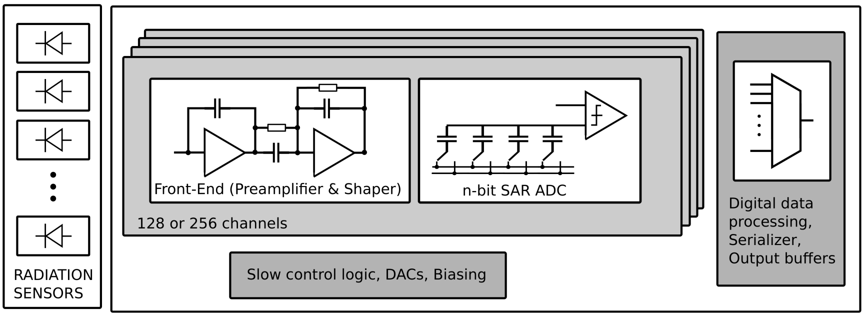

FIGURE 1: Architecture of multichannel detector readout chip.

TABLE 1: Readout chip requirement for LumiCal and IT/TT detectors.

	ILC	LHCb	
Variable	LumiCal	IT	TT
Load capacitance per channel [pF]	5 – 50	5 – 35	35 – 49
Dynamic range [fC]	2 – 10 000	2 – 10	2 – 10
Peaking Time [ns]	50	25	25
Signal polarity	positive	negative	positive/negative
Pulse shape	CR−RC	CR−RC^n	CR−RC^n
Maximum ENC [e$^-$]	1250 at 30 pF	1000 at 10 pF	1000 at 10 pF
ADC resolution [bits]	10	6	6

izing particle (MIP) in 300 μm thick silicon. In the calibration mode the equivalent noise charge (ENC) of at most 0,2 fC — for typical detector capacitance 30 pF — should be obtained in order to achieve the signal to noise ratio (SNR) above 10. The preamplifier feedback time constant was optimized to achieve lowest possible noise[4] and is equal to 400 ns. In the physics mode electromagnetic showers in detector results in high energy depositions which can produce up to 10 pC charge at the preamplifier input. The preamplifier output dynamic range is limited by technology (IBM 130 nm) power supply voltage to about 300 mV. The output amplitude V_{preamp} in function of input charge Q_{in} can be approximated as

$$V_{\mathrm{preamp}} \approx \frac{Q_{\mathrm{in}}}{C_{\mathrm{feed}}} \ , \tag{1}$$

where C_{feed} is the preamplifier feedback capacitance. Due to the limitation in ASIC area and parasitic couplings the feedback capacitance C_{feed} was set to 20 pF which results in charge dynamic range about 6 pC, slightly less than the specified maximum charge 10 pC. To simplify shaper design the feedback time constant is the same in physics and calibration mode one.

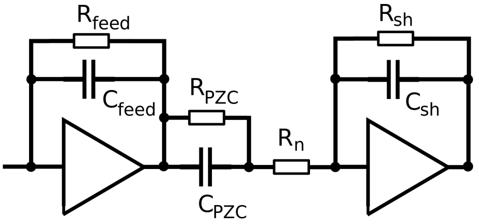

FIGURE 2: Front-end for LumiCal architecture.

The next stage of front-end electronics is pole-zero cancellation circuit (PZC) shown in Fig 2. Assuming preamplifier feedback time constant $\tau_{\mathrm{feed}} = R_{\mathrm{feed}}C_{\mathrm{feed}}$ and time constant of pole-zero cancellation $\tau_{\mathrm{PZC}} = R_{\mathrm{PZC}}C_{\mathrm{PZC}}$ the transfer function of preamplifier and PZC circuit is given by[3]

$$\frac{U_{\mathrm{out}}(s)}{I_{\mathrm{in}}(s)} = \frac{1}{C_{\mathrm{feed}}} \frac{s + \frac{1}{\tau_{\mathrm{PZC}}}}{s + \frac{1}{\tau_{\mathrm{feed}}}} \ . \tag{2}$$

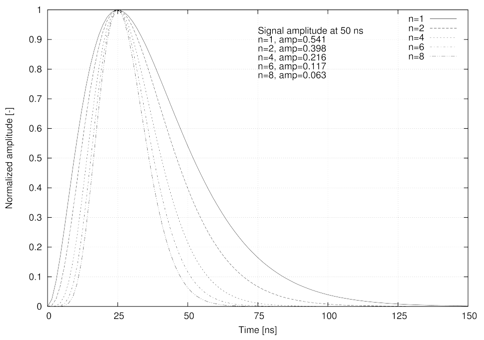

FIGURE 3: Normalized nuclear pulse shape at different shaping order CR−RC^n.

As seen from Eq. 2 the condition $\tau_{\mathrm{feed}} = \tau_{\mathrm{PZC}}$ is required to cancel the amplifier pool. If this equality is hold, the current gain of preamplifier with PZC circuit is given by ratio

$$k_{\mathrm{I}} = \frac{I_{\mathrm{out}}(s)}{I_{\mathrm{in}}(s)} = \frac{C_{\mathrm{PZC}}}{C_{\mathrm{feed}}} = \frac{R_{\mathrm{feed}}}{R_{\mathrm{pzc}}} \ . \qquad (3)$$

For LumiCal design in calibration mode the current gain is set to $k_{\mathrm{I}} = 40$, which gives C_{PZC} equal to 20 pF, while in physics mode the current gain is set to one.

It is well known[4] that CR−RC^2 pulse shaping is usually used to reduce equivalent noise charge of front-end electronics. For LumiCal readout simplest CR−RC pulse shape was chosen in order to allow efficient digital signal processing (DSP).[5] Analog pulses formed by CR−RC shaper are digitalized by internal ADC (as shown in readout chip architecture, Fig. 1) and represented as time-discrete sequence of digital samples. The samples can be filtered in digital domain using one of digital filters architecture such as Finite Impulse Response (FIR) — non recursive linear filter.[6] The result of FIR filter is weighted average (called convolution) of N digital samples v_{k}

$$s_{\mathrm{k}} = \sum_{i=0}^{N-1} w_i v_{\mathrm{k-1}} \ , \qquad (4)$$

where s_{k} is the output sample and w_i represent samples weight. It is also possible to perform inverse processing called deconvolution which allows to reproduce input signal from filtered output s_{k}. The deconvoluted pulse allows to obtain precise information about time and charge deposited by ionizing particle in detector. The number N of samples (and also samples weights w_i) required by deconvolution algorithm depends on shaping filter order. Higher order filter require more samples N and more calculations to obtain deconvolution which results in higher power consumption. The deconvolution computational complexity can be easily reduced using the simplest CR−RC shaping.

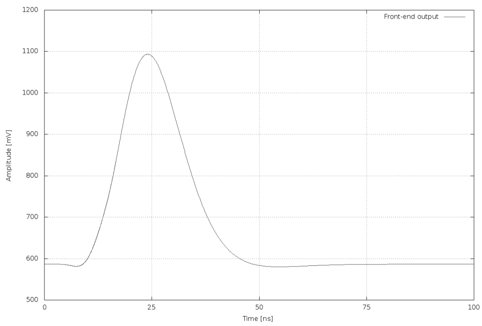

FIGURE 4: LHCb front-end output pulse for 12 fC (3 MIPs) input charge.

The complete front-end chain for LumiCal detector is presented in Fig. 2. The CR−RC shaping is obtained using single amplifier with two pole transfer function formed by feedback circuit (C_{sh} and R_{sh}) and PZC circuit combined with input resistance R_{n}. Using Eq. (2) and assuming that $\tau_{\mathrm{feed}} = \tau_{\mathrm{PZC}}$ the whole front-end transfer function can be represented as

$$\frac{U_{\mathrm{out}}(s)}{I_{\mathrm{in}}(s)} = \frac{1}{C_{\mathrm{feed}} R_{\mathrm{n}} C_{\mathrm{sh}}} \times \frac{1}{s + \frac{1}{C_{\mathrm{sh}} R_{\mathrm{sh}}}} \times \qquad (5)$$
$$\times \frac{1}{s + \frac{1}{C_{\mathrm{PZC}}(R_{\mathrm{PZC}} || R_{\mathrm{n}})}} \ ,$$

where

$$T_{\mathrm{peak}} = \tau_{\mathrm{sh}} = C_{\mathrm{sh}} R_{\mathrm{sh}} = \frac{C_{\mathrm{PZC}} R_{\mathrm{PZC}} R_{\mathrm{n}}}{R_{\mathrm{PZC}} + R_{\mathrm{n}}} \ , \qquad (6)$$

is needed to obtain the CR−RC shaping.

Unlike the LumiCal preamplifier, only one gain mode is needed for LHCb experiment readout to cover the whole input dynamic range (Table 1). The preamplifier feedback time constant was set to 60 ns with small 100 fF C_{feed}, in order to obtain high gain, and large 600 kΩ resistor R_{feed} with negligible parasitics effects. Such configuration gives output dynamic range about 30 fC. Pole-zero cancellation circuit similarly as it was designed according to the Eq. (2) shown previously for LumiCal detector. Pseudo-gaussian pulse shaping designed for LHCb prototype (described later) determines the PZC capacitance value and gives current gain $k_{\mathrm{I}} \approx 18{,}7$.

Pulse shaping for LHCb experiment is more complicated. The main goal is to achieve signal level below 5% of pulse amplitude at time equal $2T_{\mathrm{peak}} = 50$ ns. Fig. 3 shows the normalized pulse shape in function of $\mathrm{CR}{-}\mathrm{RC}^n$ order. Even as high shaping order as $\mathrm{CR}{-}\mathrm{RC}^8$ is not enough to meet the mentioned above shape requirement, since at 50 ns the signal is still above 6,3% of maximum amplitude. Obtaining the 10-th order pulse shaping using typical (Sallen-Key) filter topology requires a chain of at least 5 stages of shapers and oversteps the limitation in power consumption and occupied ASIC area. The solution to this problem was proposed by Nowlin[7] and Ohkawa[8]. Adding the complex poles ans zeroes to the filter transfer function allows to obtain the pseudo-gaussian pulse shape using lower filter order n than the $\mathrm{CR}{-}\mathrm{RC}^n$ one. The transfer function $H(s)$, when the number of poles is odd is given by formula:[8]

$$H(s) = \frac{A_0 \prod_{i=1}^{k} \left(A_i^2 + W_i^2\right)}{(\sigma s + A_0) \prod_{i=1}^{k} \left[(\sigma s + A_i)^2 + W_i^2\right]} , \quad (7)$$

and when is even by

$$H(s) = \frac{\prod_{i=1}^{k} \left(A_i^2 + W_i^2\right)}{\prod_{i=1}^{k} \left[(\sigma s + A_i)^2 + W_i^2\right]} , \quad (8)$$

where A_0 is the real pole, A_i and W_i are the real and imaginary parts of the complex pole pair, k is the number of complex pole pairs and $\sigma = 1{,}0844\tau$ where τ if filter time constant. Since the transfer function given by formulas (7) and (8) is to complicated for analytical analysis, numerical computation was used to determinate real and complex poles and zeroes for this design. Pulse shape obtained from simulation of the LHCb front-end is shown on Fig. 4. Pulse amplitude is equal 507,4 mV for 12 fC (3 MIPs) input charge. Peaking time for 5 pF detector capacitance is about 24 ns. Some overshoot observed at the pulse end is negligible since its amplitude is only 6,4 mV (1,26% of pulse amplitude) below the base line. Signal level at 50 ns is about 0,61% of pulse amplitude. Simulation results shows that all requirements for the LHCb front-end pulse shape are met.

Both front-end prototypes, for LumiCal detector and LHCb experiment, were send for fabrication in february 2013. Measurements results and complete ASICs performance test are expected in the first half of the year 2013.

⋆ ⋆ ⋆

[1] M. Needham, D. Volyanskyy, *LHCb note* **2006-032**, 1 (2006).

[2] H. Abramowicz, K. Afanaciev, S. Denisov, R. Dollan, D. Drachenberg, V. Drugakov, I. Emeliantchik, S. Erin, R. Ingbir, S. Kananov, A. Kowal, E. Kouznetsova, R. Kwee, W. Lange, A. Levy, W. Lohmann, J. Lukasik, M. Luz, D. Miller, I. Minashvili, U. Nauenberg, B. Pawlik, N. Rusakovich, A. Rybin, N. Shumeiko, A. Stahl, L. Suszycki, K. Suzdalev, V. Vrba, W. Wierba, J. Zachorowski, F. Zyazyulya, *IEEE T. Nucl. Sci.* **51**, 2983 (2004).

[3] K. Korbel, Układy elektroniki Front-End (Uczelniane Wydawnictwa Naukowo-Dydaktyczne, 2000).

[4] W. M. C. Sansen, Z. Y. Chang *IEEE T. Circuits Syst.* **37**, 1375 (1990).

[5] S. Gadomski, G. Hall, T. Høgh, P. Jalocha, E. Nygård, P. Weilhammer, *Nucl. Instrum. Meth. A* **320**, 217 (1992).

[6] R. G. . Lyons, Understanding Digital Signal Processing (Prentice Hall 2010).

[7] C. H. Nowlin, *IEEE T. Nucl. Sci.* **17**, 226 (1970).

[8] S. Ohkawa, M. Yoshizawa, K. Husimi, *Nucl. Instrum. Methods* **138**, 85 (1976).

Front-end electronics design in submicron CMOS technologies

Dominik Przyborowski

Faculty of Physics and Applied Computer Science, AGH University of Science and Technology, Mickiewicza 30, 30-059 Kraków, Poland

Supervisor: Marek Idzik

A brief description of the front-end electronics for the silicon sensors that must fulfill very strict requirements given by the modern HEP experiments is presented. The letter contains a comparison of two popular deep-submicron CMOS technologies (130 nm and 350 nm) used for IC fabrication. Special attention has been paid to the noise analysis which is a key aspect in the readout electronics design process.

Modern High Energy Physics (HEP) experiments demand very precise measurement of the particle tracks and the energy of hadronisation products. High particle flux and collision rate require high detector granularity. Strict requirements for the detector performance have great influence on the readout electronics that has to be optimised in terms of speed, silicon area, power consumption and the noise performance. A typical front-end electronics circuit is shown in Fig. 1. A current signal generated by a charged particle traversing the active volume of the detector is integrated on a feedback capacitance (C_{F}) of the charge sensitive amplifier (CSA), followed by a pulse shaper realised in a band-pass filter topology. The pulse shaper circuitry with optimised signal-to-noise ratio (SNR) forms a signal into desired shape. The overall system performance in terms of noise and speed is determined mainly by the design of the preamplifier, thus the paper focuses only on this particular building block of the front–end readout chain.

Present designs of the front-end electronics for HEP experiments are still manufactured in rather old CMOS processes (between 130 and 350 nm) due to their good analogue parameters (intrinsic gain, supply voltage, etc.) combined with low power consumption, low fabrication costs and satisfactory intrinsic radiation tolerance. Table 1 shows the comparison of transistor parameters from two popular technologies.[1,2] From Table 1 it can be observed that technology downscaling results in an increase of transistor speed and transconductance (higher transition frequency f_{t} and current gain K) but the intrinsic transistor gain and output dynamic range (due to lower power supply voltage) are significantly smaller.

A simplified schematic diagram of the CSA implemented as voltage amplifier with transimpendance feedback loop ($R_{\mathrm{F}}, C_{\mathrm{F}}$) is shown in Fig. 2. Resistor R_{F} is used as DC feedback path to discharge capacitor C_{F} and avoid CSA saturation. The amplitude of the output voltage is proportional to the input charge (Q_{in}) with the charge gain (K_{q}) inversely proportional to feedback capacitance. The signal generated by charged particles in radiation detector is small, e.g. a minimum ionisation particle (MIP) generates about 24000 electrons, while for typical X-rays (5 – 20 keV) this number is in the range of 1300 – 6000

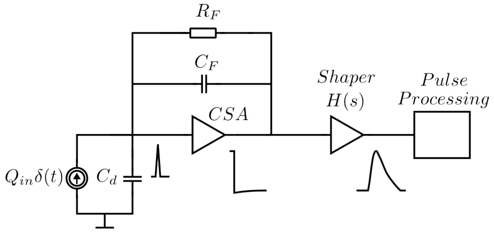

FIGURE 1: Block diagram of the front-end electronics circuitry.

Table 1: Transistor parameters in two different CMOS processes.

Parameter	350 nm	130 nm
t_{OX} [nm]	7,6	2,2
K $(\mu \cdot C_{\mathrm{OX}})$ NMOS [$\mu\mathrm{A} \cdot \mathrm{V}^{-2}$]	170	720
K $(\mu \cdot C_{\mathrm{OX}})$ PMOS [$\mu\mathrm{A} \cdot \mathrm{V}^{-2}$]	45	340
typical intrinsic gain $(g_m \cdot r_{ds})$	90	30
V_{dd} [V]	3,3	1,2 (1,5)
Peak f_{t} [GHz]	28	94

electrons, assuming the typical thickness of the silicon sensor of 300 μm. This shows the importance of the noise analysis and the CSA optimisation during the entire design process. The main noise sources are: the input transistor, the amplifier loading current source and for DC coupled detectors, its leakage current. The small signal equivalent circuit of the CSA shown in Fig. 3 containing noise sources is shown below. In the above diagram one can find two different noise sources: voltage series noise source and current parallel noise source. They are characterised with the spectral density noise of $\overline{v_{\mathrm{s}}^2}$ and $\overline{i_{\mathrm{p}}^2}$, respectively. The series noise includes: flicker noise of the input transistor, channel modulation noise of the input and the load transistors and thermal noise of the gate resistance:

$$\overline{v_{\mathrm{s}}^2} = \frac{K_{\mathrm{F}}}{WLC_{\mathrm{OX}}f} + 4k_{\mathrm{B}}T\left(R_{\mathrm{eq}} + R_{\mathrm{gate}}\right), \quad (1)$$

where K_{F} is a technology dependent flicker noise parameter, C_{OX} is a gate oxide capacitance, W and L are transistor's width and length, respectively, and R_{eq} is an equivalent resistance of channel modulation noise and is equal to:

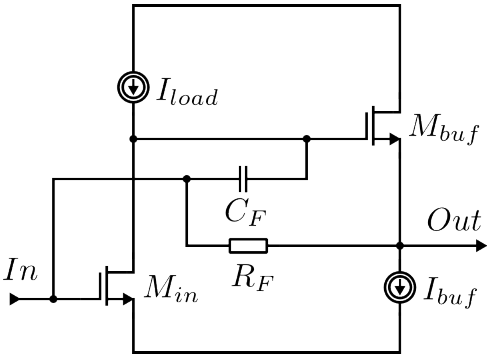

Figure 2: Simplified schematic of the CSA.

$$R_{\mathrm{eq}} = \frac{\gamma}{g_{\mathrm{m}}}. \quad (2)$$

The γ factor depends on transistor inversion level and the channel length, and it can be in the range between 0,5 (for long channel transistors operating in the weak inversion region) up to 2,5 (for short channel devices).[3] The parallel noise containing shot noise of detector (only in semiconductor ones) and thermal noise of feedback resistor is given by Eq. (3):

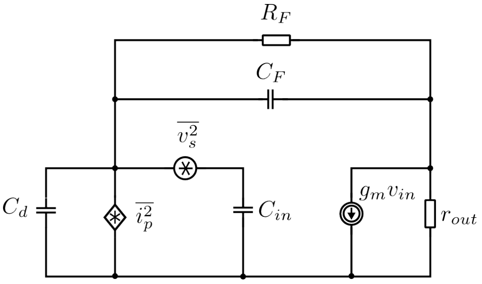

Figure 3: Small signal CSA equivalent circuit used in noise analysis.

$$\overline{i_{\mathrm{p}}^2} = 2qI_{\mathrm{leak}} + \frac{4k_{\mathrm{B}}T}{R_{\mathrm{F}}}. \quad (3)$$

The total noise power spectrum at the output of the CSA circuitry can be calculated as presented in[4]:

$$\overline{v_{\mathrm{out}}^2} = \left|\frac{C_{\mathrm{d}}+C_{\mathrm{in}}+C_{\mathrm{F}}}{C_{\mathrm{F}}}\right|^2 \cdot \overline{v_{\mathrm{s}}^2} + \left|\frac{1}{\omega C_{\mathrm{F}}}\right|^2 \cdot \overline{i_{\mathrm{p}}^2}. \quad (4)$$

In order to provide good SNR performance, a CSA is followed by the band-pass filter responsible for shaping of the output signal. The most popular and widely used are filters from the CR$-$RC^n family with transfer function given as follows:

$$H(s) = A \cdot \frac{s\tau}{(1+s\tau)^{n+1}}, \quad (5)$$

where A is a DC gain of filter and τ is its time constant. The amplitude of an output signal of a fully analogue block containing an n–order filter is following:

$$V_{\mathrm{amp}} = \frac{A}{C_{\mathrm{F}}} \cdot \frac{n^n}{n!\; e^n} \cdot Q_{\mathrm{in}} \; . \tag{6}$$

As it was mentioned before the input signal of front-end electronics is a charge collected in the detector, so the most natural units for noise analysis are electrons. For this reason a new parameter called equivalent noise charge (ENC) is defined. ENC is the charge injecting into the spectrometric chain in a form of Dirac delta that generates a pulse with the amplitude equal to the RMS value of noise. For the first order of filter (n=1) an ENC is given by formula (7): [5]

$$\mathrm{ENC} \approx \left[\overline{i_{\mathrm{p}}^2}\tau + \frac{\overline{v_{\mathrm{s}}^2}}{\tau} \cdot \left(C_{\mathrm{F}} + C_{\mathrm{d}} + C_{\mathrm{in}}\right)^2 + \frac{4K_{\mathrm{F}}}{WLC_{\mathrm{OX}}} \cdot \left(C_{\mathrm{F}} + C_{\mathrm{d}} + C_{\mathrm{in}}\right)^2 \right]^{\frac{1}{2}} \; . \tag{7}$$

The ENC is determinated by 3 components related to 3 different noise types. First is related to the current parallel noise source it does not depend on the capacitances connected to the input node of the CSA. Its influence increases with the shaper time constant. Second s related to thermal series noise. It decreases with the shaper time constant. The last component represents flicker noise of the input transistor and it is independent on the shaping time. The component related to the voltage series noise sources is multipled by the square of the total capacitance conected to the CSA input. Hence, in first approximation the realtion between ENC and detector capacitance is linear.

⋆ ⋆ ⋆

[1] Austriamicrosystems, 0,35 μm CMOS C35 Process Parameter, Revision 6 (2008).

[2] J. Kaplon, M. Noy, *IEEE T. Nucl. Sci.* **59**, 1611 (2012).

[3] B. Razavi, Design of Analog CMOS Integrated Circuits (McGraw-Hill, 2001).

[4] W. Sansen, Z. Y. Chang, *IEEE T. Circuits Syst.* **37**, 1375 (1990).

[5] K. Korbel, Układy elektroniki Front-End (Uczelniane Wydawnictwa Naukowo-Dydaktyczne, 2000).

PHYSICAL CHEMISTRY, CATALYSIS AND BIOPHYSICS

Studies on the photocatalytic degradation of the humic substances supported by chemical oxidation

Justyna Dziedzic

Jerzy Haber Institute of Catalysis and Surface Chemistry Polish Academy of Sciences, Niezapominajek 8, 30-239 Kraków, Poland

Supervisor: Piotr Warszyński

Humic substances (HS) are the example of highly problematic pollutants in water. HS represent a major fraction of natural organic matter (NOM) in ground and surface waters. What is more, they react with chlorine species producing trihalomethanes (THMs), haloacetic acids (HAAs) and other halogenated disinfection by-products (DBPs) in chlorinated waters.[1] *THMs have been known to cause cancer and other toxic effects in human beings.*[2] *For these reasons, new technologies are being developed, which would decontaminate heavy organics from water in an efficient, inexpensive and secure way. In this work the main emphasis will be put to investigate the synergistic effect between two methods: photocatalytic oxidation process on the semiconductor surface and chemical oxidation using active substances, which in turn will lead to improvement the removal efficiency of NOM from water, with efficiency greatly exceeding the performance achieved by traditional methods.*

The effectiveness of TiO_2 photocatalytic oxidation for removal of humic substances from water with the use of titanium dioxide powder (Degussa P-25) and with the addition of oxidant-sodium persulphate has been investigated. The photocatalytic removal of the model humic component (humic acid sodium salt, Aldrich) under UV irradiation was examined by monitoring changes in the absorbance measured at the wavelength of 254 nm (UV_{254}) that is widely accepted as a parameter which shows degradation rate of humic acids. It is often applied as a surrogate parameter to for the total organic carbon (TOC) — usually used coefficient to measure photodegradation of HA.[3] The photodegradation rate of HA has also been followed by the determination of Chemical Oxygen Demand (COD). The intensification of photocatalytic process through the simultaneous application of chemical oxidant (sodium persulphate) and titanium dioxide was the main part of investigations in this work.

The photodegradation experiments were performed in two quartz flat bottomed batch reactors of the volume 40 ml as shown in Fig. 1. In one of the reactors halogen lamp (150 W) was used as the artificial sunlight (ASL) source, in the other one, dedicated for ultraviolet (UV) region, the high pressure xenon arc lamp (250 W) was applied. Both lamps were used without any cut-off filters, except the layer of cooling water flowing below the bottom of the cell. The cell illumina-

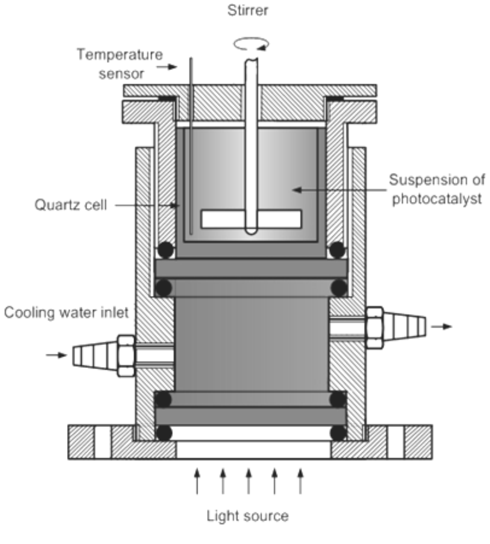

FIGURE 1: The scheme of the quartz flat bottomed photoreactor.

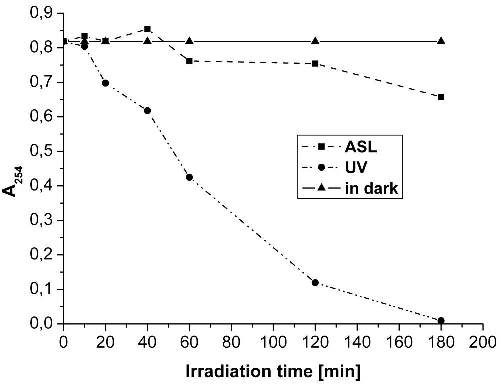

FIGURE 2: Changes of absorbance at 254 nm of HA solution under UV and ASL irradiation at the presence of TiO_2. Concentration of photocatalyst: 100 $mg\,l^{-1}$, concentration of HA: 40 $mg\,l^{-1}$.

tion was monitored by the radiometer. The radiation intensity was 68,8 $mW\,cm^{-2}$ for ASL and 48,8 $mW\,cm^{-2}$ for UV source. The photocatalyst suspension was stirred during the experiments with a mechanical stirrer at a constant rate of 300 rpm. The temperature was stabilized at $25 \pm 0{,}5$°C. Together with the sample used in the photocatalytic experiment an identical reference sample was always prepared and kept in dark during the same time period. The UV absorption of the supernatant at the wavelength of 254 nm was measured using Specord 40 (Analytic Jena) single beam spectrophotometer. COD values were determined according to the Standard Method — PN-85/C-04578.02. In preliminary studies we observed no degradation under visible light and a very low degradation rate under UV. After 9 hours of irradiation with the UV lamp only 5,3% decrease of the HA concentration (absorbance at 254 nm (A_{254})) was noticed. Since the ultraviolet light alone wasn't enough to decompose humic acid, the effect of simultaneous action of irradiation and application of photocatalyst — TiO_2 was determined. In the experiment the suspension consisting of 40 $mg\,l^{-1}$ of HA sodium salt and 100 $mg\,l^{-1}$ of TiO_2 was exposed to the ASL and UV radiation. The results are shown in Figs. 2 and 3 and compared with the blank experiment. A_{254} and the normalized COD are well correlated, which substantiate the selected spectroscopic detection method. However, for low concentrations of humic acid COD was still measurable, whereas decrease of absorbance was almost 100%. It has been known that HA is composed of at least two components, one can adsorb easily at the TiO_2 surface, the other one does not adsorb at all or adsorbs to a very limited extent. Moreover, the photodegradation reaction of such complicated compounds as HS does not probably occur in one stage, so intermediate species formed during degradation may not absorb UV light in the range near 254 nm. Therefore, it seems that non-zero COD value indicated exactly on these parts of humic substances, which do not degrade in the first step and consequently their decay is not detected by UV spectrometry.[4] Much higher efficiency was achieved when TiO_2 and sodium persulphate were used simultaneously. The experimental results showed in Fig. 4 indicate that in the presence of UV light the degradation rate of HA increases with increasing $Na_2S_2O_8$ concentration. Without photocatalyst it reaches 23,6% in concentration of 1×10^{-3} $mol\,l^{-1}$ of sodium persulphate.

But in the case that sodium persulphate and TiO_2 were used together, nearly 90% conversion was attained after 60 min of UV irradiation. It is also worth to note that after the visible light illumination c.a. 30% decrease of the A_{254} signal is observed. Hu-

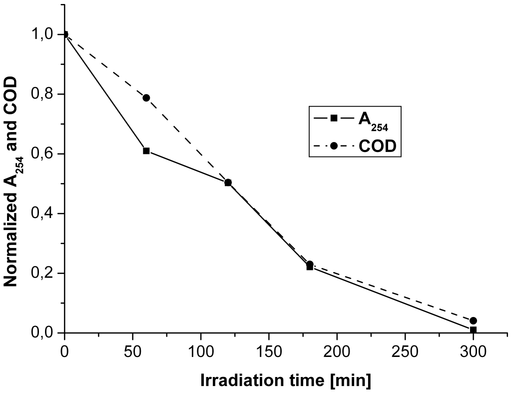

FIGURE 3: Changes of normalized absorbance at 254 nm (A_{254}) and COD values of humic acid solution under UV irradiation.

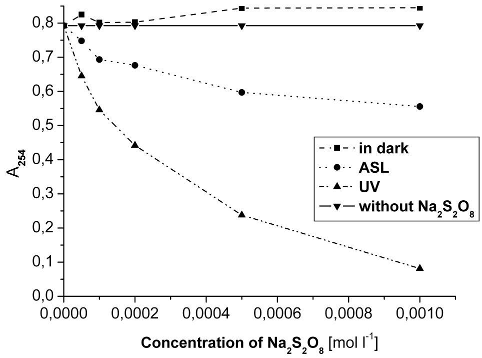

FIGURE 4: The effectiveness of the oxidation of HA by simultaneous action of UV or ASL radiation, TiO_2 and sodium persulphate. Irradiation time: 60 min, concentration of HA: 40 mg l^{-1}, concentration of TiO_2: 100 mg l^{-1}, data for experiment without $Na_2S_2O_8$: 40 mg l^{-1} HA + 100 mg l^{-1} TiO_2 in dark.

mic acid does not decompose under ASL alone. Table 1 provides the collected results of measurements of the decomposition of HA in systems: TiO_2/UV, $Na_2S_2O_8$/UV and TiO_2/$Na_2S_2O_8$/UV. These data clearly indicate on the existence of synergy between the UV light-activated TiO_2 photocatalysis and sodium persulphate oxidation of humic substances. That synergy can be observed in both spectroscopic and COD measurements, although again the COD results indicate on the uncompleted decomposition of HA in the photocatalytic process. Literature reports confirm that sodium persulphate is the suitable oxidant, which exhibits synergistic effect with photocatalytic oxidation on titanium dioxide. The reactions of persulphate ions ($S_2O_8{}^{2-}$), which are created before dissociation of persulphate salts in water and have a strong oxidation potential ($E^o = 2{,}01$ eV) with various organic and inorganic compounds have been extensively studied.[5,6] During UV irradiation very strong oxidizing species, sulphate radical anions — $SO_4{}^{\bullet -}$ are produced (the oxidation potential $E^o = 2{,}6$ eV). They may react with photogenerated electrons and with water molecules producing additionally hydroxyl radicals. $SO_4{}^{\bullet -}$ reacts with many organic compounds as an oxidant more effectively than $OH^\bullet$. The reason would be that sulphate radical anion is more selective to oxidation while $OH^\bullet$ would react quickly by hydrogen abstraction or addition.[6] Taking into account the presence in solution both sulphate and hydroxyl radicals, the efficiency improvement of organic contaminants degradation process, which was observed in our investigations, can be expected.

To summarize, these investigations demonstrated that more than 50% of humic acid may be removed from the solution simply by its adsorption on the titanium dioxide surface if the concentration of TiO_2 in suspension is high enough. 100% removal of HA can be achieved even at relatively low dosage of TiO_2 (100 mg l^{-1}) if UV illumination of the suspension is applied for sufficiently long time (at least 3 hours). Addition of oxidant to the solution containing TiO_2 suspension and dissolved humic acid greatly enhances the activity of TiO_2 in the process of decomposition of organic substances. We showed that more than 90% conversion of HA can be obtained when sodium persulphate was applied as chemical oxidant already after one hour. Therefore, the synergistic effect was observed when TiO_2 and $Na_2S_2O_8$ were used simultaneously for the removal of humic substances.

TABLE 1: The results indicating on the synergistic effect of TiO_2 and sodium persulphate in photocatalytic degradation of HA.

Composition of UV investigated solution	40 mg l^{-1} HA + 1×10^{-3} mol l^{-1} $Na_2S_2O_8$		40 mg l^{-1} HA + 100 mg l^{-1} TiO_2 Degussa		40 mg l^{-1} HA + 1×10^{-3} mol l^{-1} $Na_2S_2O_8$ + 100 mg l^{-1} TiO_2 Degussa	
Type of parameters	COD	UV	COD	UV	COD	UV
Degradation rate [%]	21,1	23,6	21,3	46,1	63,2	90,0

The work was supported by the EU Human Capital Operation Program, Polish Project No. POKL.04.01.01-00-434/08-02.

⋆ ⋆ ⋆

[1] M. Bekbolet, C. S. Uyguner, H. Selcuk, L. Rizzo, A. D. Nikolau, S. Meri, *Desalination* **176**, 155 (2005).

[2] R. Mosteo, N. Miguel, S. Martin-Muniesa, M. P. Ormad, J. L. Ovelleiro, *J. Hazard. Mater.* **172**, 661 (2009).

[3] N. Sobana, K. Selvam, M. Swaminathan, *Sep. Purif. Technol.* **62**, 648 (2008).

[4] J. Dziedzic, D. Wodka, P. Nowak, P. Warszyński, Ch. Simon, I. Kumariki, *Physicochem. Probl. Mi.* **45**, 15 (2010).

[5] O. S. Furman, A. L. Teel, R. J. Watts, *Environ. Sci. Technol.* **44**, 6423 (2010).

[6] R. E. Huie, C. L. Clifton, S. A. Kafafi, *J. Phys. Chem.* **95**, 9336 (1991).

Physicochemical and catalytic properties of modified clinoptilolite from Slovakia

Anna Dziedzicka

Jerzy Haber Institute of Catalysis and Surface Chemistry Polish Academy of Sciences, Niezapominajek 8, 30-239 Kraków, Poland

Supervisor: Bogdan Sulikowski

In this work raw and modified forms of natural clinoptilolite from Kučin (Slovakia) were used as catalysts to test their activities in the transformations of α-pinene. Raw clinoptilolite was modified to obtain a suitable catalyst with various Si/Al ratio by dealumination with hydrochloric acid of different concentrations and calcination. Catalysts were characterized by X-ray powder diffraction (XRD), Fourier transform-infrared (FT-IR), N_2 gas adsorption-desorption techniques and ^{27}Al and ^{29}Si Magic-Angle-Spinning NMR studies. Isomerization of α-pinene was chosen as a test reaction. The selectivity towards limonene and camphene formation on the dealuminated and calcinated samples was strongly preferred.

Zeolites are based on infinitely extending three-dimensional network of AlO_4 and SiO_4 tetrahedra linked to each other by sharing all of the oxygens. More than 30 zeolites occur in natural deposits, of which the most important in industry are clinoptilolite, chabazite, mordenite and erionite.[1] Clinoptilolite, which is world's most abundant zeolite, belongs to heulandite-group minerals, because of their similarity of the structure and composition. The deposits are accompanied by calcite, quartz, aragonite, thenardite, halite, mordenite, phillipsite and ferrierite. The framework of clinoptilolite is constructed of 4-4-1 secondary buildings units. The structure of crystals contains three types of channels: A (10-membered, 0,44×0,72 nm), B (8-membered, 0,41×0,47 nm), both running parallel to the crystallographic axis c and C (also 8-membered, 0,40×0,55 nm), which runs parallel to the axis a and cross-links the A and B channels.[2,3]

In this study raw clinoptilolite was modified by two different methods. First of them was dealumination. Dealumination is regarded as isomorphous substitution of the type: Al^{3+}, $M^+ \rightarrow Si^{4+}$, where M^+ is a cation compensating the negative charge of the aluminosilicate framework. The most common charge-compensating cations in clinoptilolite structure are Na^+, K^+, Mg^{2+} and Ca^{2+}. Net decrease of the framework charge and a decrease in the number of charge-balancing cations are caused by the insertion of silica. The methods of dealumination are divided into two groups depending on the way silicon is provided for the healing of framework vacancies created while aluminium is removed from tetrahedral sites. In the first group of methods no extra silicon source is added during chemical or hydrothermal process. The most commonly chemicals used in this methods are ethylenediaminetetraacetic acid (H_4EDTA) and mineral acids. The external source of silicon is provided in the second group, for example by using the silicon tetrachloride vapour or ammonium hexafluorosilicate. In this work hydrochloric acid was used in order to remove framework aluminium. Acid treatment leads to the breaking of Al−O bonds, but also may modify the silicate structure by formation of a non-crystalline Si-layer and releasing Al.[4] The zeolite was crushed and sieved to get the fraction <250 μm. After washing with distilled water clinoptilolite was dealuminated with hydrochloric acid of different concentrations at a temperature of 95°C for 4 hours. The following concentrations of HCl were used: 0,05, 0,1, 0,25, 0,5, 1,0, 2,0, 5,0, 8,0 and 11,5 M, respectively. The solid-to-liquid ratio was always kept constant 1 g of zeolite : 15 cm^3 of HCl solution. Afterwards

TABLE 1: Structural parameters calculated from N_2 adsorption analysis.

HCl concentration [M]	S [m^2 g^{-1}]	V_{mic} [cm^3 g^{-1}]	S_{mic} [m^2 g^{-1}]	A_{ext} [m^2 g^{-1}]
parent clinoptilolite	33,50	0,0032	5,5	27,94
1,0	164,71	0,0533	101,6	63,12
11,5	90,04	0,0183	35,2	54,85

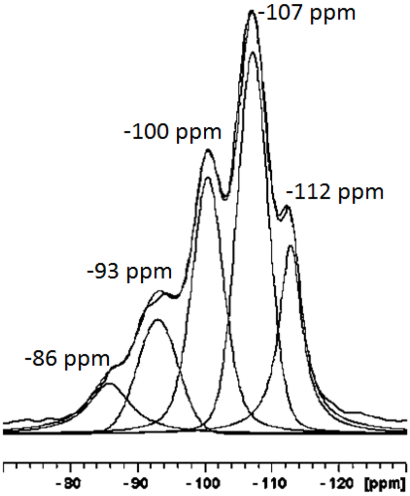

FIGURE 1: ^{29}Si MAS NMR spectra of natural clinoptilolite.

samples were washed intensively with distilled water until Cl^- free and dried at 70°C.

The second method of modification clinoptilolite was calcination. It is well known that heat treatment changes the acidity of zeolite. Brønsted and Lewis acid sites are responsible for the catalytic activity of zeolites. If hydrogen is a charge balancing cation associated with the tetrahedral aluminium, the surface acts as a proton donor and it serves as a Brønsted acid centre. Electron acceptors (Lewis centres) are formed after the zeolite is heated to a temperature higher than 550°C.[5] Clinoptilolite was crushed and washed as previously. The ammonia form of zeolite was obtained by ion exchange with aqueous 10% NH_4NO_3 solution at 80°C for 2 hours. Ion exchange was repeated three times. The solid : liquid ratio was 1 g of zeolite : 10 cm^3 of solution. The NH_4-clinoptilolite was washed and dried. Then the acid form was obtained by air calcination at temperatures 300°C or 400°C.

A quantitive evaluation of the crystallinity of the samples were determined from the intensity of XRD signals that are most affected during modification. The use of hydrochloric acid of concentration 1,0 M causes decrease of crystallinity of approximately 50%. The Al extraction results in changes in the unit cell parameters and cell volume. Partial amorphization of the zeolite is also observed as broadening of baseline in the XRD patterns of the samples dealuminated with the highly-concentrated acid. Significant dealumination process is also visible in IR spectra. The main changes are related to the band around 1062 cm^{-1} in natural clinoptilolite. It is associated with the asymmetric internal T−O stretching vibrations of the tetrahedra. Along with the dealumination process the signal shifts to 1092 cm^{-1} for sample modified with 8,0 M acid. The results of nitrogen adsorption-desorption (Table 1) measurements confirm changes in the clinotilolite structure. Increase of the specific surface area and micropore volume for samples modified with diluted HCl is observed. Low-concentrated acid solutions remove impurities from clinoptilolite channels and contribute to formation of the aluminium vacancies in the framework. A decrease in micropore volume is an evidence of the amorpization.

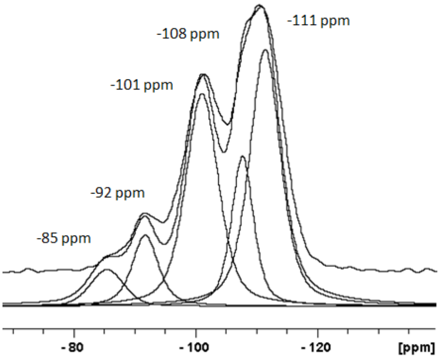

FIGURE 2: Si MAS NMR spectra of clinoptilolite modified with 5,0 M HCl.

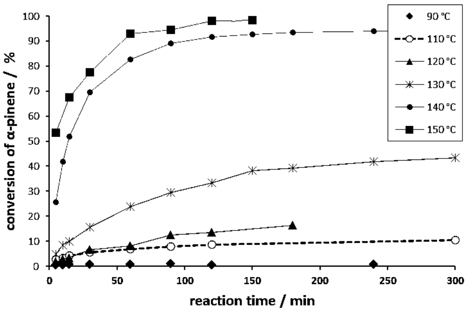

FIGURE 3: Conversion of α-pinene vs. the reaction time over unmodified natural clinoptilolite at a temperature range of 90°C (100 mg catalyst/5 ml α-pinene).

In the ^{27}Al MAS NMR spectum of natural clinoptilolite from Slovakia two signals associated with tetrahedral (55,54 ppm) and extraframewok octahedral (3,33 ppm) aluminium are observed. The amount of tetrahedral aluminium decreases while treatment with HCl. It is possible to remove one-third of tetrehedral aluminium by using 0,25 M HCl while the most concentrated (11,5 M) acid removes about 60% Al in tetrahedral sites. The amount of extraframework aluminium remains unchanged. ^{29}Si MAS NMR of unmodified clinoptilolite is shown in Fig. 1 where five resonance lines are observed. They are associated with different silicon environment in the zeolite framework. The intensity of signal at -112 ppm, which is related to Si(0Al) groupings, increases for dealuminated samples. It is shown in Fig. 2 that the intensities of other signals decrease.

The transformation of α-pinene in the liquid phase was chosen as a reaction to test catalytic activity of all the samples. It should be emphasized that the dimensions of α-pinene are $0{,}47 \times 0{,}58 \times 0{,}66$ nm, what is important from availability of zeolite channels point of view. Isomerization products are mainly monocyclic (limonene, terpinenes, terpinolenes) and tricyclic compounds (camphene, tricyclene, fenchenes, bornylene). Camphene and limonene are widely used in the industry. Camphene is used for synthesis of camphor. Both of them found an application in the cosmetic industry. A conventional catalyst for manufacturing terpenes is acid-treated TiO_2. However, the reaction rate over TiO_2 is low so tests are conducted to find high active and selective catalyst. Different catalysts have been tested for the synthesis of camphene. In the literature results of α-pinene isomerization over activated carbon, clays, heteropoly acids, sulfated zirconium oxide as well as zeolites like ZSM-5 and ZSM-12 are presented.[6,7] The influence of the catalysts amount on the reaction course and concentration of HCl used to modify parent material was also studied. Kinetic studies of the process were also carried out.

The results obtained for conversion of α-pinene over unmodified clinoptilolite at different temperatures are shown in Fig. 3. As it can be seen, the catalyst is unactive at the temperatures lower than 90°C. At higher temperatures it is possible to convert all α-pinene. Minor changes in the selectivity can be observed but the main products are always camphene and limonene. For example, selectivity to camphene is 57% and to limonene 36% after 300 min reaction at 130°C. Activation Energy E_a for reaction catalysed over the raw material was calculated from the Arrhenius plot at the beginninig of the reaction. Assuming first-order kinetics, the resulting value was 19,1 kJ mol^{-1}. It may indicate some raction diffusion limitation of the reaction.

To lower the reaction temperature, clinoptilolite must be modified. Catalytic test were performed for dealuminated and calcined

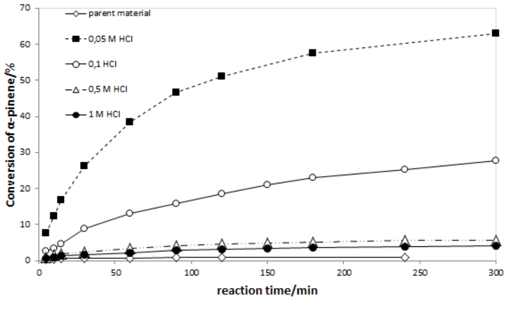

FIGURE 4: Conversion of α-pinene vs. the reaction time over the modified clinoptilolite at 90°C (100 mg catalyst/5 ml α-pinene).

TABLE 2: Initial rection constant rates.

Catalyst (concentration of HCl) [M]	Weight [mg]	Reaction temperature [°C]	Initial constant rate, k [s^{-1}]
unmodified clinoptilolite	100	120	$3{,}9\cdot10^{-5}$
	100	130	$1{,}3\cdot10^{-4}$
	100	140	$8{,}6\cdot10^{-4}$
0,05	100	90	$3{,}0\cdot10^{-4}$
	200		$1{,}0\cdot10^{-3}$
	300		$1{,}8\cdot10^{-3}$
	350		$2{,}0\cdot10^{-3}$
0,1	100	90	$8{,}0\cdot10^{-5}$
	200		$3{,}0\cdot10^{-4}$
	300		$5{,}0\cdot10^{-4}$
0,2	100	90	$4{,}0\cdot10^{-5}$
	200	90	$2{,}0\cdot10^{-4}$
0,5	200	90	$5{,}0\cdot10^{-5}$

samples. Decrease in conversion was observed for samples with low crystallinity. The best result was obtained using clinoptilolite modified with diluted (0,05 M) hydrochloric acid. Conversion of α-pinene with time at 90°C is visualized in Fig. 4. The conversion level is increased probably because of removing impurities from the sample without profound modification of the zeolite structure. Initial reaction constant rates for most interesting catalysts based on cinoptilolite were calculated. The results are presented in Table 2. A significant drop in the value is observed for the samples modified with HCl solutions of increased concentrations (100 mg catalyst, 90°C reaction temperature). It should also be noted that the initial rate determined for reaction proceeding over sample dealuminated with 0,05 M HCl is much higher than the initial rates for all temperatures reactions carried out over unmodified zeolite.

The reaction was also tested over calcined clinoptilolite. It was found that total conversion of α-pinene decrease with increase of calcination temperature. For calcination temperature 300°C conversion of α-pinene is 45%, while for 400°C it decreases to 27% (after 300 min). It is clearly due to the decrease of some amount of acid sites during calcination.

Interestingly, the already catalytic tests show a significant increase of the α-pinene conversion over the sample modified with 0,05 M HCl.

⋆ ⋆ ⋆

[1] B. Sulikowski, *Heterogen. Chem. Rev.* **3**, 203 (1996).

[2] Y. Garcia-Basabe, I. Rodriguez-Iznaga, L. C. de Menorval, P. Llewellyn, G. Maurin, D. W. Lewis, R. Binions, M. Autie, A. R. Ruiz-Salvator, *Micropor. Mesopor. Mater.* **135**, 187 (2010).

[3] M. Akgül, A. Karabakan, *Micropor. Mesopor. Mater.* **131**, 238 (2010).

[4] G. E. Christidis, D. Moraetis, E. Keheyan, L. Akhalbadashvili, N. Kekelidze, R. Gevorkyan, H. Yerisyan, H. Sargsyan, *Appl. Clay Sci.* **24**, 79 (2003).

[5] O. Akpolat, G. Gündüz, F. Ozkan, N. Beşün, *Appl. Catal. B-Gen.* **265**, 11 (2004).

[6] S. Fidik, G. Gündüz, *J. Am. Chem. Soc.* **74**, 1145 (1997).

[7] B. Gil, Ł. Mokrzycki, B. Sulikowski, Z. Olejniczak, S. Walas, *Catal. Today* **152**, 24 (2010).

Metal-organic frameworks of metals from s-block — new barium and strontium dicarboxylates

Marta Grzesiak-Nowak

Jerzy Haber Institute of Catalysis and Surface Chemistry Polish Academy of Sciences, Niezapominajek 8, 30-239 Kraków, Poland

Supervisor: Wiesław Łasocha

Metal organic frameworks (MOF) are compounds built by metal centers or metal clusters linked by organic, usually rigid, ligands. MOFs form many different structures due to diversity of used metal atoms and organic ligands. They can form layered or 3D structures, appropriate choice of metal center and bridging ligands can lead to obtain structures with tunable pore size and physical properties. Compounds with metals from second group of periodic table of elements may be model substances in crystal engineering.

Materials like MOFs bring high scientific attention nowadays. They can be porous and have large surface areas and therefore these materials may have promising practical applications, such as gas adsorbents, catalysts, gas separators, ion exchangers, luminescent or magnetic substances. Similarly to zeolites, they are crystalline and porous systems, however they are organic-inorganic hybrid compounds built by metal atoms or clusters linked through organic ligands.[1] As linkers in many compounds multi-carboxylates are present, especially multi-carboxylate derivatives of benzene, but compounds bridged by simple aliphatic carboxylates are also known.[2] Although most MOFs are transition metal compounds, some examples of systems with s-block metals can be found in the literature.[3,4]

Syntheses and investigations of barium and strontium salts of simple aliphatic dicarboxylic acids with different length of carbon chain ($C_nH_{2n}(COOH)_2$, $n=3-10$) have been performed in our group. We wanted to find structural tendencies for compounds formed by similar organic ligands and different metal centers. In our study, we have obtained two groups of MOFs compounds with dicarboxylic acid using atoms of barium and strontium as metal centers. Obtained systems form layered and three-dimensional structures.

We have tried to synthesize salts of simple dicarboxylic acids $(C_nH_{2n}(COOH)_2$ with cations of metals from first and second group of periodic table: Li, K, Mg, Ca, Sr and Ba. Among the obtained compounds, the biggest groups are salts of barium and strontium. For these syntheses in most cases oxide or carbonate of selected metal with an appropriate amount of a dicarboxylic acid were used.

To synthesize new compounds 0,005 mol of barium or strontium carbonate and 0,005 mol of appropriate dicarboxylic acid (glutaric, adipic, pimelic, suberic, azelaic or dodecanedioic acid) were dissolved in 50 ml of water. The solution was first boiled for 1 h and then filtered and left for crystallization. After 24 – 48 h, white or colorless precipitates crystallized from each solution. The precipitates were filtered off, washed with warm mixture of water and propanol (1:1), and dried in air. Some compounds were obtained through hydrothermal synthesis, when aforementioned described simple synthesis failed. The obtained compounds were investigated by single crystal or powder diffraction methods depending on the form of the samples. For some of them it was possible to determine the crystal structure and to examine their high temperature decomposition by XRPD vs. temp.

Barium salts are a group of six compounds, which crystallized in different crystal systems

TABLE 1: Crystallographic data for barium compounds.

Chemical formula	$BaC_5H_6O_4 \cdot 5H_2O$	$BaC_6H_8O_4$	$BaC_7H_{10}O_4 \cdot H_2O$
Crystal system	Orthorhombic	Triclinic	Monoclinic
Space group	*Pnma* (62)	*P*–1 (2)	*C*2/*m* (12)
a [Å]	12,152(1)	4,5948(4)	8,789(1)
b [Å]	7,354(2)	9,9469(3)	25,021(3)
c [Å]	13,293(2)	4,4595(3)	4,9357(7)
α [°]	90,0	99,486(6)	90,0
β [°]	90,0	97,037(9)	116,80(1)
γ [°]	90,0	96,840(5)	90,0
V $\left[\text{Å}^3\right]$	1187,5(2)	197,53(4)	968,8(1)
Z	4	1	4
Chemical formula	$BaC_{16}H_{26}O_8$	$BaC_{18}H_{30}O_8$	$BaC_{24}H_{42}O_8$
Crystal system	Tetragonal	Tetragonal	Tetragonal
Space group	*P*–4*b*2 (117)	*I*4/*mcm* (140)	*P*–4*b*2 (117)
a [Å]	12,0906(4)	8,565(2)	8,604(1)
b [Å]	12,0906(4)	8,565(2)	8,604(1)
c [Å]	13,0713(5)	28,718(8)	18,172(2)
α [°]	90,0	90,0	90,0
β [°]	90,0	90,0	90,0
γ [°]	90,0	90,0	90,0
V $\left[\text{Å}^3\right]$	1910,8(1)	2106,73(9)	1347,2(3)
Z	4	4	4

from triclinic to tetragonal. Compound with glutaric acid is quite unusual, because it contains five water molecules (four molecules as ligands and additional 2 water molecules with population parameter $pp = 0{,}5$ are crystallization water), whereas other salts are monohydrates or anhydrous. Moreover, coordination number of metal is 9, while in other barium compounds is 8. The salt of glutaric acid is built by isolated layers of edge shared Ba$-$O polyhedra connected by acid molecules (Fig. 1A). It is interesting, that barium glutarate obtained during our investigations is different from compound known already and described in literature.[5] The sample formed by barium and adipic acid (Fig. 1B) consist of edge-shared coordination dodecahedra bridging by adipic acid molecules and finally forms polyhedra layers linked by organic carbon chains. Compound obtained using barium carbonate and dicarboxylic acid with 7 carbon atoms in organic chain (pimelic acid) is monohydrate. Barium pimelate is built by coordination polyhedra, which shares two opposite edges and two vertices forming layers bridging by carbon chains (Fig. 1C). Three other barium salts are similar to each other. They crystallize in tetragonal crystal system and are built by isolated polyhedra layers connected by acid molecules (Fig. 1D). Additional similarity of these three compounds is that salts formed by suberic, azelaic and dodecanedioic acids are acidic. The acid molecules in barium suberate and barium azelate are randomly single deprotonated and due to significant similarities of salt with dodecanedioic acid to aforementioned compounds, we assume that it is also acidic. Despite many similarities to barium salts of suberic and dodecanedioic acids, barium azelate exhibit unusual structure. The structure consist parallel acid molecules occupying two

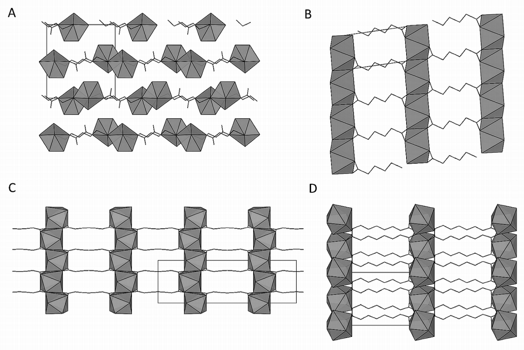

FIGURE 1: Barium dicarboxylates, view of polyhedra layers. A — barium glutarate, B — barium adipate, C — barium pimelate and D — barium suberate (salts with azelaic and dodecanedioic form analogical layers).

positions at a distance of 2,5 Å relative to each other, with population parameter 0,5.

Some tendency can be observed in presented group of compounds. Synthesized salts with shorter acids contain water molecules and compounds crystallize in systems with lower symmetry, while with extending length of carbon chain the higher symmetry and anhydrous compounds are preferable. Barium salts decompose to barium carbonate during heating in temperature above 400°C as indicate investigations of their thermal decomposition by XRPD.[6] Crystal data of each barium compound are listed in Table 1.

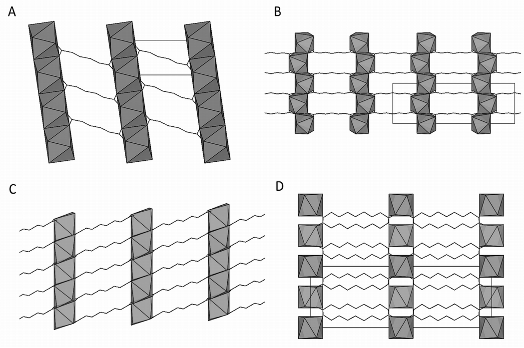

FIGURE 2: Strontium dicarboxylates, view of polyhedra layers. A — strontium adipate, B — strontium pimelate, C — strontium suberate and D — strontium azelate (salt with dodecanedioic forms analogical layers).

The group of strontium compounds consists of five salts of dicarboxylic acid with different length of C$-$C chain. They crystallize in various crystal systems, similarly to barium compounds, but the highest symmetry system in which strontium salts crystallize is orthorhombic. Strontium adipate is anhydrous salt built by layers of coordination polyhedra connected by adipic acid molecules (Fig. 2A). Each Sr$-$O$_8$ (coordination number of Sr is 8) polyhedron shares four edges with four neighboring coordination polyhedra. Salt of pimelic acid contains one water molecule, as one of 8 ligands of strontium. Coordination polyhedra shares two opposite edges and two opposite vertices forming layers of polyhedra linked by acid molecules (Fig. 2B). Compound formed by strontium and suberic acid contains polyhedra layers connected by suberic acid molecules. Polyhedra Sr$-$O$_n$ have four common edges with other coordination polyhedra and therefore layers are formed (Fig. 2C). Different situation is present in compound of azelaic acid and dodecanedioic acid, where polyhedra layers consist of isolated Sr$-$O$_n$ dodecahedra (Fig. 2D). In all strontium salts, coordination number of metal is 8. Crystal data of strontium dicarboxylates is presented in Table 2.

Strontium dicarboxylates exhibit some structural resemblance to barium compounds, especially in cases of adipic and pimelic salts. Different situation is observed for barium and strontium compounds with suberic acid. Barium suberate crystallizes in tetragonal crystal system and form acidic salt built by layers of isolated coordination Ba$-$O polyhedra, while compound of strontium is triclinic and is built by layers of edge-shared polyhedra.

In our investigations, we have synthesized and investigated 11 new dicarboxylates with barium or strontium cations. All synthesis were performed without structure directing agents. Studies of prepared compounds were carried out using single crystal or powder diffraction methods, because obtained samples crystallized as single crystal or polycrystalline specimens. For each compound crystallographic data have been collected and for

TABLE 2: Crystallographic data for strontium compounds

Chemical formula	$SrC_6H_8O_4$	$SrC_7H_{10}O_4\cdot{}\cdot H_2O$	$SrC_8H_{12}O_4$	$SrC_{18}H_{28}O_8$	$SrC_{24}H_{42}O_8$
Crystal system	Triclinic	Monoclinic	Triclinic	Orthorhombic	Orthorhombic
Space group	P–1 (2)	$C2/m$ (12)	P–1 (2)	$I222$ (23)	$Ccca$ (68)
a [Å]	4,4248(9)	8,3868(16)	6,482(2)	8,4750(2)	36,041(12)
b [Å]	9,9786(17)	24,661(4)	12,490(4)	8,8411(3)	9,371(3)
c [Å]	4,1841(8)	4,7883(12)	5,713(3)	28,0506(7)	7,931(3)
α [°]	97,957(17)	90,0	102,23(4)	90,0	90,0
β [°]	97,03(2)	114,56(2)	93,67(6)	90,0	90,0
γ [°]	97,061(16)	90,0	92,21(4)	90,0	90,0
$V\ \left[\text{Å}^3\right]$	179,74(6)	900,8(4)	450,5(2)	2101,78	2678,62
Z	2	4	2	8	4

all compounds some crystallographic tendencies have been observed. Salts of shorter acids (from 5 to 7 carbon atoms in carbon chain) form layers of coordination polyhedra sharing edges and vertices, while for compounds with acids containing from 8 to 12 carbon atoms, the tendency to form layers of isolated polyhedra is observed.[7] Obtained compounds crystallize in different crystal systems from triclinic to tetragonal for barium salts or from triclinic to orthorhombic for strontium compounds. Generally, specimens formed by shorter dicarboxylic acids prefer low symmetry systems, salts with longer acids crystallize in systems with higher symmetry. In both groups of investigated compounds, salts of pimelic acid are monohydrated, other salts are anhydrous with the exception of barium glutarate, which consist of six additional water molecules. Interesting is the observation that despite the same synthesis conditions (reactants ratio, temperature, time) salts with acids longer than suberic acid form acidic salts in which the ratio of acid molecules per one metal atom is 2:1.

The investigations of compounds built by s-block metals with dicarboxylic acids revealed some structural tendencies present in two groups of compounds. Further study will be focused on measurements of surface areas and sorption properties of obtained compounds. The obtained results of structural studies of new dicarboxylates will be useful and helpful in our further investigations of similar metal-organic frameworks built by metals with different valence.

⋆ ⋆ ⋆

[1] Ch. Janiak, J. K. Vieth, *New J. Chem.* **34**, 2366 (2010).

[2] L.A. Borkowski, Ch.L. Cahill, *Cryst. Growth Des.* **6**, 224 (2006).

[3] A. Mesbah, L. Aranda, J. Steinmetz, E. Rocca, M. François, *Solid State Sci.* **13**, 1438 (2011).

[4] K. M. Fromm, *Coordin. Chem. Rev.* **252**, 856 (2008).

[5] K. Aliouane, A. Djeghri, A. Guehria-Laidoudi, S. Da-haoui, C. Lecomte, *J. Mol. Struct.* **832**, 150 (2007).

[6] M. Grzesiak, A. Rafalska-Łasocha, W. Łasocha, *Powder Diffr.* **1**, 53 (2011).

[7] M. Grzesiak, W. Nitek, A. Rafalska-Łasocha, W. Łasocha, *Z. Kristallogr.* **9**, 629 (2012).

Studies of liposomes stability using atomic force microscopy

Iwona Habina

Faculty of Physics and Applied Computer Science, AGH University of Science and Technology, Mickiewicza 30, 30-059 Kraków, Poland

Supervisor: Květoslava Burda

Liposomes are spherical bilayer vesicles formed after dispersing phospholipids in water solution. They serve as model systems for biomembranes and have already found applications as biosensors, drug and gene carriers or other bioactive agents. Atomic force microscopy (AFM) provides us information about shapes and sizes of liposomes on nanoscale resolution as well as their stability and mechanical properties without destroying these soft structures. In this work we present studies of egg yolk phosphatidylcholine (Egg PC) liposomes deposited on a mica surface using AFM. Atomic force microscopy measurements are performed in a contact mode in air. We investigate and analyze stability of liposomes exposed to air as a function of time deposition (up to a few days). We show examples of images in which one sees adsorbed isolated liposomes and changes of their structures in time.

Phospholipids dispersed in water solutions self assembly in many kinds of structures according to the length of their hydrophobic tail and the area occupied by their hydrophilic head-group. Spherical and cylindrical micelles, inverted micelles, planar bilayers and liposomes, which are spherical bilayer vesicles can be observed.[1]

Liposomes are versatile structures: they serve as model systems of studying interactions between biomembranes and biomolecules such as proteins,[2] carotenoids,[3] pigments[4] or DNA.[1] Applying liposomes as drug delivery systems has been extensively studied in recent years.[1,5] They can be prepared for specific applications by modification of their surface through conjugation with antibodies[5] or peptides.[5] Nanoparticles loaded into liposomes have also been investigated for diagnostic and therapeutic applications.[6] Studies on nanodevices of carbon nanotubes integrated with lipid bilayers for bio-sensing[7] or drug delivery systems[8,9] have also been reported.Besides liposomes, planar bilayers deposited on substrates are investigated for potential applications such as: biosensors, biofunctionalization of inorganic solids, as well.[10]

Liposomes are prepared from natural and synthetic phospholipids using one or several kinds of lipids and other molecules such as cholesterol. According to their size they can be divided into small unilamellar vesicles (SUV) with a diameter of 20 – 100 nm, large unilamellar vesicles (LUV, 100 nm – 1 μm), giant unilamellar vesicles (GUV, 1 – 300 μm), multilamellar vesicles (MLV) which usually range from 500 nm to 10 μm and multivesicular vesicles (MVV) containing incapsulated vesicles.[1]

Sizes and shapes of liposomes are very often influenced by the type of lipids and by the detailed protocol used during their preparation. The most used techniques in laboratory practice are based on the method developed by Bangham, who first got and described liposome suspension.[11] Phospholipids are dissolved in an organic solvent, e.g. chloroform or ethanol. Then the solvent is evaporated using a nitrogen stream or vacuum and a dry lipid film is resuspended in an aqueous solution, incubated at a temperature approximately 5°C above the phase transition temperature of the highest melting temperature of lipid in the mixture and followed by vortexing. This allows us to obtain suspension of multilammelar vesicles or giant unilamellar vesicles[12] if minimal perturbations are applied in the hydratation step. Subsequently, a multivesicular suspension can be: (i) sonicated in an ultrasonic bath or using a probe sonicator,[13] (ii) extruded using a thermostable extruder with polycarbonate membranes of defined pore sizes (size of pores: from 50 nm to 400 nm)[14,15] or (iii) freeze-thawed.[16] Liposomes can also be produced by solvent injection methods,[13,17] detergent removal methods,[13] reversed phase evaporation[18] or electroformation.[19]

Properties of liposomes has been examined using wide variety of techniques. Among microscopic techniques used in liposomes investigations transmission electron microscopy (TEM) plays a significant role, allowing achieving information on the size distribution, shape and form of vesicles.[15,20] The main disadvantage of this technique is a need of fixation and staining biological samples which can damage and alter their structure. Therefore such a tool as atomic force microscopy (AFM) owing to the family of scanning probe microscopes with nanoscale resolution (lateral: below 1 nm, vertical: approximately 0,1 nm), which allows to probe samples surfaces without damage and alteration of them, is an excellent tool for fragile samples.

Atomic Force Microsopy can operate in many kinds of modes. If used in a contact mode a tip attached to a cantilever having a specified spring constant is scanning across the sample surface and is in a constant touch with the surface. Deflection of the cantilever is measured through a laser beam reflected from the back of the cantilever and focused on a position-sensitive photodiode detector. In a non-contact mode the cantilever is oscillating near the resonance frequency in the attractive regime of van der Waals force and shifts of the resonant frequency or the amplitude and the phase is influenced by the sample topography. In an intermittent contact (named also a tapping mode) the cantilever is also oscillating as in the non-contact mode but it touches the sample surface in the lower amplitude, what causes the reduction of the oscillation amplitude. Lateral forces applied to the sample are minimized in the intermittent contact mode what allows to examine fragile and soft biological materials without their damage or alteration. Moreover, samples can be investigated in air and in liquid environments as well and can be prepared easily allowing routine analysis.[22,23] Besides topographical representation of a sample surface it is possible to obtain information on physical properties of the sample including friction,[23] adhesion forces,[23] viscoelasticity,[22,24,25] etc.

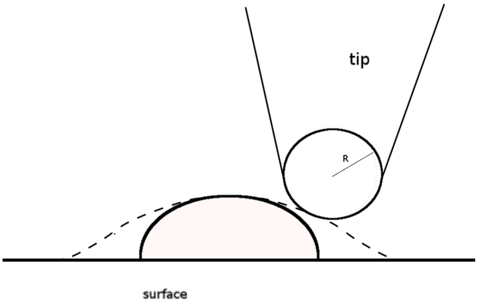

FIGURE 1: Effect of tip convolution during scanning in a contact mode AFM.

Among many advantages of investigating liposomes properties using AFM technique there are some limitations of this method. Liposomes adsorbed on solid substrates (e.g. mica, silicon wafers) modify their shapes to compressed or flattened spheroidal structures.[25–27] In order to measure the size of liposomes and obtain their shape correctly it is important to take under consideration many factors affecting liposome structures such as: a time of the sample deposition on a substrate, a type of lipids, a buffer composition, vertical and lateral forces applied by the tip during scanning, electrostatic interactions between the sample and the support and image convolution due to the tip shape and size,[23] what is schematically shown in Fig. 1.

In this work we present studies of egg yolk phosphatidylcholine (Egg PC) liposomes deposited on a mica surface using AFM (Agilent 5500). Phospholipids were dissolved in ethanol, evaporated under the stream of nitrogen and then kept under vacuum. Then thin lipid film was hydrated in the Hepes buffer (pH=7,4) in 45°C with vortexing and

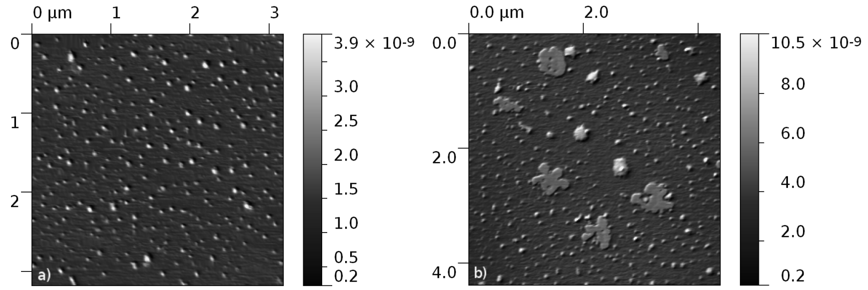

FIGURE 2: Topography images of Egg PC liposomes (10 mM HEPES pH=7,4) adsorbed on the mica surface: (left panel) A fresh sample measured after deposition; unilamellar liposomes obtained by the sonication method; lipid concentration: 100 nM, (right panel) The same sample measured 11 days after deposition. Both images were obtained in the contact mode in air.

sonicated in the ultrasonic bath for 1 h in 45°C. Lipid concentration in samples was 100 nM. All measurements were performed in the contact mode in air with adjusting the set-point as weak as possible in order not to damage the surface of liposomes. Below we present various structures of liposomes formed after their deposition on the mica surface.

In Fig. 2 we present topography images of a fresh sample adsorbed on the mica surface (left) and 11 days after its deposition (right). One can see isolated adsorbed liposomes and increased amount of flattened structures with thickness characteristic for a lipid bilayer [27] after the prolonged incubation time.

In Fig. 3 we show an example topography image of isolated liposomes (left) with corresponding cross-section analysis (right). The soft liposomes flatten on the substrate which results in meaningfully higher lateral than vertical dimensions. Additionally, in the contact mode AFM the diameter of liposomes is affected by the tip convolution.

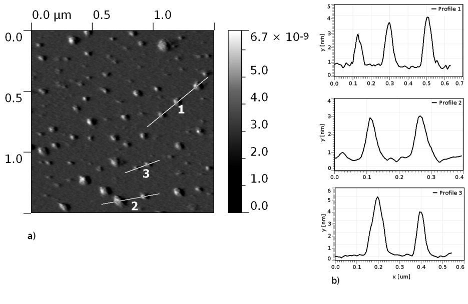

FIGURE 3: Example topography image of fresh egg PC liposomes adsorbed on the mica surface measured just after their deposition. The same sample as presented in Fig. 2a

In the next (Fig. 4) image one sees topography image of flattened structure (left) chosen from other similar structures visible in Fig. 2b with corresponding cross-section analysis (right). These flatten structures emerged when adhered on the surface.

Flatten structures formed from lipids occupying vast areas on the mica substrate were also observed. In Fig. 5 one observes these clusters with cross-section profiles.

In summary, we observed modifications of samples with increasing time of their deposi-

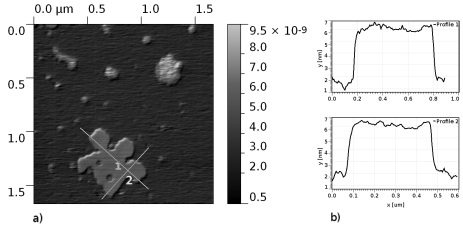

FIGURE 4: Example topography image of egg PC liposomes. The same sample as presented in Fig. 3, but measured 11 days after its deposition on the mica surface using the contact mode in air; b) Cross-section profiles of flattened structure having a mean height of 4,68 ± 0,07 nm, which corresponds to values of lipid bilayer thickness measured using AFM and reported in [25].

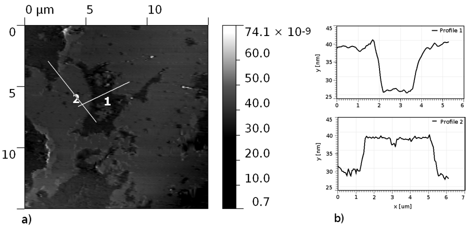

FIGURE 5: Example topography image of egg PC liposomes (10 mM; pH=7,4; lipid concentration 1 nM) deposited on the mica surface. Liposomes were obtained by 5 cycles of freezing and thawing. The image was obtained after 7 days of the sample incubation on the mica surface. Double lipid bilayers are visible due to the fussion and rupture of the liposomes. Mean height of this structures is 11,06 ± 0,42 nm.

tion on the mica surface. We observed formation of larger structures created due to the fusion of SUVs and rupture as a result of their strong adhesion to the substrate. The flattened structures showed mean thickness characteristic for a lipid bilayer. Isolated liposomes were highly flattened due to their adhesion to the substrate and tip — sample interactions.

⋆ ⋆ ⋆

[1] D. D. Lasic, *Trends Biotechnol.* **16**, 307 (1998).

[2] J. Sitterberg, M. M. Gaspar, C. Ehrhardt, U. Bakowsky, *Method. Mol. Biol.* **606**, 351 (2010).

[3] C. Socaciu, P. Bojarski, L. Aberle, H. A. Diehl, *Biophys. Chem.* **99**, 1 (2002).

[4] A. Jughans, H. Sies, W. Stahl, *Arch. Biochem. Biophys.* **391**, 160 (2001).

[5] V. P. Torchilin, *Nat. Rev. Drug. Discov.* **4**, 145 (2005).

[6] L. Paasonen, T. Laaksonen, C. Johans, M. Yliperttula, K. Kontturi, A. Urtti, *J. Control. Release* **122**, 86 (2007).

[7] Y. Huang, P. V. Palkar, L.-J. Li, H. Zhang, P. Chen, *Biosens. Bioelectron.* **25**, 1834 (2010).

[8] F. Karchemski, D. Zucker, Y. Barenholz, O. Regev, *J. Control. Release* **160**, 339 (2012).

[9] G. Angelini, S. Boncompagni, P. De Maria, M. De Nardi, A. Fontana, C. Gasbarii, E. Menna, *Carbon* **45**, 2479 (2007).

[10] D. P. Nikolelis, T. Hianik, U. J. Krull, *Electroanal.* **11**, 7 (1999).

[11] A. D. Bangham, R. W. Horne, *J. Mol. Biol.* **8**, 660 (1964).

[12] K. Akashi, H. Miyata, H. Itoh, K. Kinosita, Jr., *Biophys. J.* **71**, 3242 (1996).

[13] S. Vemuri, C. T. Rhodes, *Pharm. Acta Helv.* **70**, 95 (1995).

[14] G. Gregoriadis, Liposomes Technology: Liposome preparation and Related Techniques, Vol 1, 3rd edition (Informa Healthcare, New York 2007).

[15] L. D. Mayer, M. J. Hope, P. R. Cullis, *Biochim. Biophys. Acta* **858**, 161 (1986).

[16] M. Traïkia, D. E. Warschawski, M. Recouvreur, J. Cartaud, P. F. Devaux, *Eur. Biophys. J.* **29**, 184 (2000).

[17] M. Pons, M. Foradada, J, Estelrich, *Int. J. Pharm.* **95**, 51 (1993).

[18] F. Szoka, Jr., D. Papahadjopoulos, *P. Natl. Acad. Sci. USA* **75**, 4194 (1978).

[19] L. Mathivet, S. Cribier, P. F. Devaux, *Biophys. J.* **70**, 1112 (1996).

[20] C. Demetzos, *J. Lipos. Res.* **18**, 159 (2008).

[21] B. Ruozi, D. Beletti, A. Tombesi, G. Tosi, L. Bondioli, F. Forni, M. A. Vandelli, *Int. J. Nanomed.* **6**, 557 (2011).

[22] K. D. Jandt, *Surf. Sci.* **491**, 303 (2001).

[23] H.-J. Butt, B. Cappella, M. Kappl, *Surf. Sci. Rep.* **59**, 1 (2005).

[24] G. Mao, X. Liang, K. Y. S. Ng, The Dekker Encyclopedia of Nanoscience and Nanotechnology, (Marcel Dekker Inc., New York, 2004).

[25] X. Liang, G. Mao, K. Y. S. Ng, *Colloid. Surface. B* **34**, 41 (2004).

[26] E. F. De Souza, O. Teschke, *Rev. Adv. Mater. Sci.* **5**, 34 (2003).

[27] S. Kumar, J. H. Hoh, *Langmuir* **16**, 9936 (2000).

The activity of polyaniline sulfate — based solid acid catalysts for the formation of bio-esters in transesterification of triglycerides with methanol

Żaneta Kalemba-Jaje

Jerzy Haber Institute of Catalysis and Surface Chemistry Polish Academy of Sciences, Niezapominajek 8, 30-239 Kraków, Poland

Supervisor: Alicja Drelinkiewicz

Polyaniline sulfate catalysts were studied for the transesterification of triglycerides (triacetin) with methanol producing methyl esters (Biodiesel). Polymer powder (PANI-S) and the sample composed of polyaniline sulfate deposited on multi-wall carbon nanotubes (CNT-PANI-S) were examined. The activity of polyaniline sulfate powder and CNT-PANI-S catalysts was compared with those of commonly studied Amberlyst-15 resin and Nafion SAC-13 composite. The most active was CNT-PANI-S, whereas the activity of PANI-S powder was similar to that of Amberlyst-15 catalyst. This was related to better efficiency of active sites in the hybrid catalysts composed of polymer and inorganic matrix. The polyaniline sulfate — based catalysts and in particular the CNT supported sample seem to be promising catalysts for methanolysis of triglycerides producing methyl esters with the yield above 90%*.*

Biodiesel fuel, an alternative to classic diesel fuel, consists of methyl esters of fatty acids derived from vegetable oils or animal fats. Methyl esters are formed in transesterification of triglycerides with methanol catalysed by strong acids or bases (Fig. 1). Owing to environmental and technological reasons the substitution of homogeneous catalysts by heterogeneous ones is a desirable goal and recent studies concentrated on solid acid catalysts. A variety of solid acids has already been tested[1,2] and sulfonic acid-based catalysts seem to be the most promising ones. In this context the polyaniline sulfate-based catalysts (Fig. 2) are studied in the present work. Polymer powder (PANI-S) and the sample composed of polyaniline sulfate deposited on multi-wall carbon nanotubes (CNT-PANI-S) are examined.

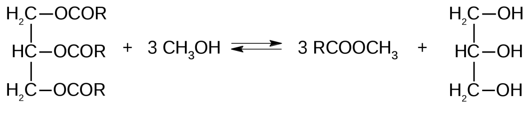

$$\begin{array}{l} H_2C{-}OCOR \\ HC{-}OCOR \\ H_2C{-}OCOR \end{array} + 3\,CH_3OH \rightleftharpoons 3\,RCOOCH_3 + \begin{array}{l} H_2C{-}OH \\ HC{-}OH \\ H_2C{-}OH \end{array}$$

FIGURE 1: Transesterification of triglycerides with methanol.

The FT-IR spectra of studied samples and polyaniline base are displayed in Fig. 3. The band at 1498 cm^{-1} assigned to the $C-C$ stretching vibration in benzenoid unit, the band at 1589 cm^{-1} originating from $C=N/C=C$ stretching vibrations in quinonoid units and the $C-C$ band at 1166 cm^{-1} appear in the spectrum of PANI-base.[3] After protonation by acids and formation of polyaniline salts, the quinonoid and benzenoid bands are shifted to 1479 cm^{-1} and 1559 cm^{-1}, respectively and new broad

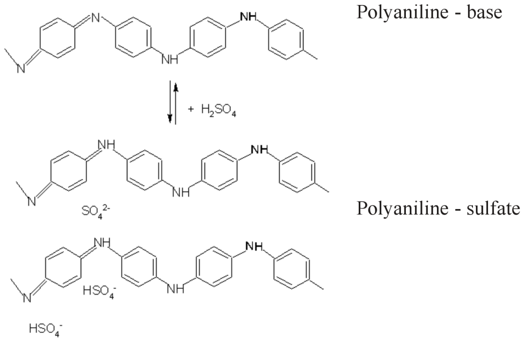

FIGURE 2: Protonation of polyaniline-base in two-step with sulfuric acid.

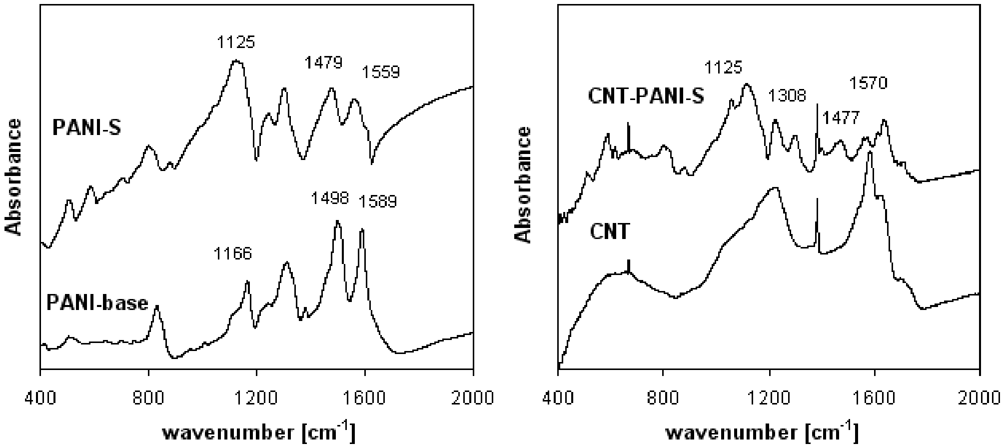

FIGURE 3: FT-IR spectra of polyaniline base, polyaniline-sulfate, initial CNT and CNT-PANI-S catalyst.

band located at 1125 cm^{-1} attributed to the protonated segments of polyaniline is formed. The FT-IR spectra of PANI-S powder and CNT-PANI-S samples exhibit spectral features characteristic of PANI-salt. However, owing to a low content of polymer in the CNT-PANI-S sample (ca. 20 wt. %) the intensity of polyaniline bands is weak. In addition, several relatively strong bands originating from initial CNT material appear thus making difficult discussion of the spectrum. Nevertheless, the bands originating from the protonated units of polyaniline can be recognized.

Textural properties of catalysts are collected in Table 1. The scanning electron microscopy (SEM) images showing the morphology of catalysts are displayed in Fig. 5. The specific surface area and porosity of PANI-S powder are low, 25,9 m^{2}g^{-1} and 0,054 cm^{3}g^{-1}, respectively. The sample of PANI-S powder exhibits rice-type granular morphology, typical of polyanilines. Surface area of CNT-PANI-S catalyst is also low, 20,3 m^2 g^{-1} and the pore volume is low, 0,11 cm^{3}g^{-1}. Previously reported data revealed that coating of CNT with polyaniline took place only at the outer surface of the CNT and the obtained coating was almost uniform.[4] Polyaniline localized exclusively at the surface of nanotubes creating uniform layer forming a structure labeled „fiber in a jacket". As Fig. 5 shows the CNT-PANI-S sample does not lose quasi-one-dimensional structure typical for nanotubes. Polyaniline sulfate — coated CNT are 40 – 60 nm thick. The coating of CNT manifests by roughness surface of coated nanotubes thus proving well extended polymer over the surface of the CNT carrier.

The activity of PANI-S powder and CNT-PANI-S catalysts is studied in the transesterification of triacetin with methanol. Their

TABLE 1: Physicochemical characteristic of studied catalysts and activity data.

Catalyst	Surface area [m^2 g^{-1}]	Pore volume [cm^3 g^{-1}]	Capacity of acid sites [mmol g^{-1}]	Initial rate [(mol TACT· ·min^{-1} g$_{\text{cat}}^{-1}$)·10^{-4}]	SPC [(min^{-1})· ·10^{-2}]
PANI-S	25,9	0,05	4,75	1,76	3,7
CNT-PANI-S	20,3	0,11	1,16	1,18	10,2
Amberlyst-15	41,6	0,24	4,70	2,26	4,8
Nafion SAC-13	164	0,56	0,15	0,61	40,6

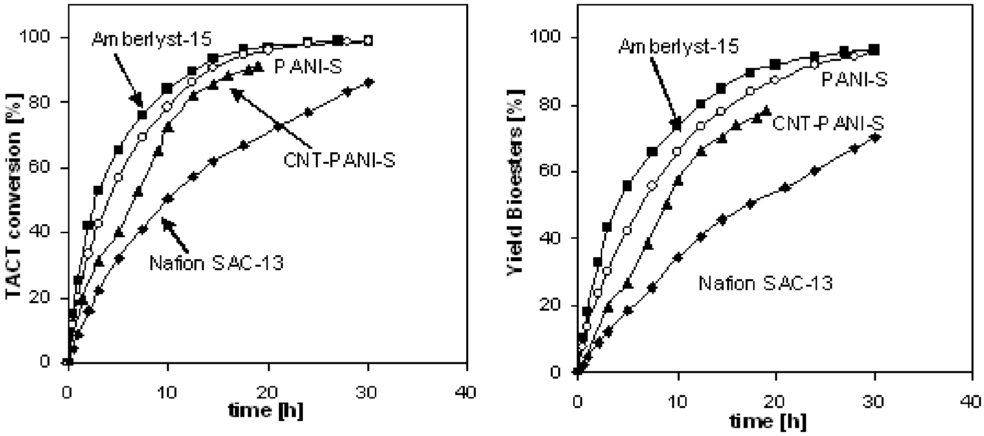

FIGURE 4: Conversion of triacetin (TACT) and the yield of methyl ester against reaction time. Reaction carried out in the presence of Nafion SAC-13, CNT-PANI-S, Amberlyst–15 and PANI-S powder.

performance is compared with those of commonly used Amberlyst-15 resin and Nafion SAC-13 composite. An interesting and advantageous property of PANI-sulfate is high content of acid sites which is close to that of Amberlyst-15 (Table 1), commonly considered to be a catalyst of high acid capacity.[5] The conversion of triacetin vs reaction time and the yield of methyl ester are shown in Fig. 4. Both polyaniline-sulfate based catalysts are active for the methanolysis of triacetin. Thus, protons in the structure of polyaniline sulfate act as the active sites for the methanolysis of triacetin.

In the presence of all studied catalysts very high conversions of triacetin are reached near to 90 – 95%. The yields of methyl esters are also high. The conversion plots show comparable activity of PANI-S powder and Amberlyst-15 resin. Moreover, after a given reaction time, higher triacetin conversion is attained on powder catalysts than in the presence of both hybrid CNT-PANI-S and Nafion SAC-13 catalysts. This could be related to lower content of polymer in the hybrid catalysts and thus lower content of acid sites in these samples. In order to compare the reactivity of active site in the catalysts, the specific activity SPC (min^{-1}) is calculated (Table 1). The initial rate (mol TACT min^{-1} $\mathrm{g}_{\mathrm{cat}}^{-1}$) referred to the acid sites capacity (mol) and expressed as min^{-1} presents the SPC. The SPC values obtained for the Amberlyst-15 and PANI-S catalysts are similar. However, the SPC values for powdered Amberlyst-15 and PANI-S catalysts are dramatically lower when compared with those for hybrid Nafion SAC-13 and CNT-PANI-S catalysts i.e. the samples with polymer dispersed through the support. This could be result of limited access of triglyceride molecules to the active sites located in bulk of powdered polymeric catalysts.

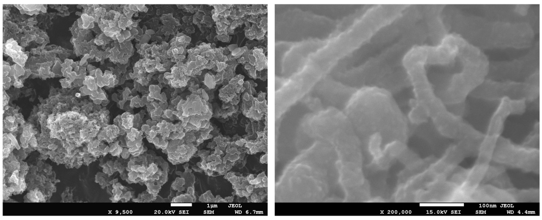

FIGURE 5: SEM micrograph of PANI-S powder and CNT-PANI-S catalysts.

Transesterification of triglycerides is reaction involving large molecules of reactants. Therefore, the access of acid sites to this bulky reactant is an important variable determining activity of solid acid catalyst in these reactions.[6,7] The SPC value for CNT-PANI-S catalyst is ca. 3-times higher then that for

PANI-S powder sample. Thus, deposition of polyaniline sulfate on CNT carrier dramatically improves the efficiency of active sites in the polymer. Hence, polyaniline-sulfate is a promising catalyst for the transesterification of triglycerides. However, in order to improve the efficiency of this polymeric catalyst, polyaniline sulfate overlayer on the carrier such as CNT material is preferred. Coating of carrier with polyaniline sulfate dramatically enhances the accessibility of triglyceride reactant to the active sites thus improving an efficiency of active sites in the catalyst.

⋆ ⋆ ⋆

[1] M. Di Serio, R. Tesser, Lu. Pengmei, E. Santacesaria, *Energy Fuels* **22**, 207 (2008).

[2] J. A. Melero, J. Iglesias, G. Morales, *Green Chem.* **11**, 1285 (2009).

[3] E. T. Kang, K. G. Neoh, K. L. Tan., *Prog. Polym. Sci.* **23** 277 (1998)

[4] J. Stejskal, I. Sapurina, M. Trchova, *Prog. Polym. Sci* **35** 1420 (2010)

[5] A. Zieba, A. Drelinkiewicz, P. Chmielarz, L. Matachowski, J. Stejskal, *Appl. Catal. A* **387**, 13 (2010).

[6] I. K. Mbaraka, K. J. McGuire, B. H. Shanks, *Ind. Eng. Chem. Res.* **45**, 3022 (2009).

[7] I. K. Mbaraka, B. H. Shanks, *J. Am. Oil Chem. Soc.* **83**, 79 (2006).

Anticorrosive polymer coatings with water barrier properties improved by water traps addition

Małgorzata Krzak

Jerzy Haber Institute of Catalysis and Surface Chemistry Polish Academy of Sciences, Niezapominajek 8, 30-239 Kraków, Poland

Supervisor: Paweł Nowak

The recent trends in improving anticorrosive polymer coatings performance by passive and active protection of the metal substrate are reviewed. As a case of the latter, a new approach to decrease the water diffusion coefficient in the anticorrosive coatings is presented. Obtained results indicate that submicron particles with high and reversible water absorption ability and low water diffusion coefficient (water traps), are able to slow down the diffusion rate when dispersed in the polymer matrix. The influence of the composite coating architecture on its properties, predicted by theoretical model, is examined by attenuated total reflection Fourier transform infrared spectroscopy (ATR-FTIR) method. Since the water traps addition results in worse adhesion to the substrate, the sandwich-structured composite with the water traps incorporated in the middle layer is considered as the most promising system with lowered water diffusion coefficient.

Polymer coatings are one of the most common methods of protecting the metal surfaces against corrosion. Such coatings applied on the metal surface play a significant role in a passive and active anticorrosive protection. They provide a physical barrier for corrosive species such as water or chloride ions but also may act as carriers for healing agents or corrosion inhibitors that can provide an active protection of the metal surface while coating is damaged.

One of the most widely investigated strategies for the active anticorrosive protection performance of polymer coatings are the self-healing systems, realized by incorporating „smart" containers,[1] capable of releasing a healing agent after the mechanical damage[2] or under some specific conditions occurring when the corrosion process starts, e.g. pH change.[3] In the field of improving the barrier properties, namely decreasing water diffusivity and permeability that are crucial for anticorrosive properties of the coatings,[4,5] the influence of addition of various nanoparticles has been widely investigated. One of the most frequently studied approaches is the addition of nanoclays. Liu et al.[6,7] developed a mathematical model of diffusion for epoxy/clay composites and proved that the water uptake and the diffusion coefficient decreased with the clay addition. The influence of the clay addition on the water diffusion coefficient was also observed in the other matrixes as polyester and polyamide.[8,9] According to these reports it is clear that the composites exhibit lower water diffusivities as compared to the pure polymer only when the clay is exfoliated in the matrix resulting in longer diffusion pathway for the water molecules. In many latest publications the idea of clay addition is combined with the adsorbed corrosion inhibitors being slowly released from the clay particles.[10,11] The similar idea of combination of the improved barrier properties and active protection performance by carriers for corrosion inhibitors was presented by Markevicius et al.[12] They investigated barrier and anticorrosive properties of the polyurethane–polyoligomeric silsesquioxane (PU-POSS) coatings with corrosion inhibitors added directly to the coating and embedded in hydrotalcite. It was found that the hardness and hydrophobicity that are responsible for barrier properties of the

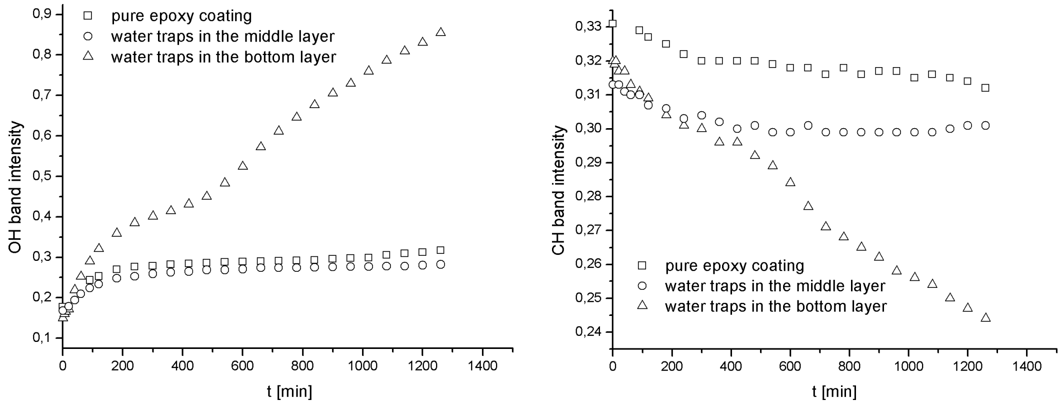

Figure 1: Changes in the OH (left panel) and CH (right panel) band intensity in the three layered sandwich-structured coatings (pure epoxy resin and the epoxy coatings with $5\%_{\mathrm{wt.}}$ addition of the water traps incorporated in the middle and the bottom layer) during sorption of water.

coating could be notably affected by the POSS addition. Good anticorrosive properties was achieved for PU-POSS coatings with inhibitor-loaded hydrotalcite particles but only in the case of benzotriazole while similar effect was observed for different corrosion inhibitor (sodium-2-mercaptobenzothiazole) added directly to the coating. In the other paper the authors described the influence of the cross-linkable monomer N,N'-bismaleimide-4,4'-diphenylmethane (BMI) on the barrier properties of the polymer coating.[13] According to this investigation the water diffusion coefficient for epoxy coating is lower after BMI addition presumably because of the subtle changes in the chemical structure and morphology of the composite film.

In this paper a new approach to reduction of the water diffusion rate in the composite polymer coatings, by addition of the water traps is presented. The water traps are the particles that exhibit an extremely low water diffusion coefficient and high water sorption capacity in comparison with the polymer matrix. The water molecules diffusing through the composite coating are trapped inside the particles and reach the substrate surface much later than diffusing through the pure coating; that results in the lower water diffusion coefficient. Since the process of the water absorption in both polymer matrix and trapping particles is fully reversible, it is possible to obtain a long-term service coating with lowered water diffusion coefficient.

As it was shown in the theoretical model developed in our previous work,[14] diffusion coefficient of the composite depends on architecture of the composite coating (besides the other factors such as: the diffusivities of dispersed particles and a host matrix, volume fraction and size of the traps, and the partition coefficient k (the ratio of volume concentrations of the diffusing medium in the host phase and in the inclusions). Namely, the effectiveness of decreasing the water diffusion coefficient is higher for sandwich-structured coatings with water traps distributed only in the one of the layers instead of the whole volume of the coating. Among the different possible architectures of sandwich-structured coatings, the most efficient is the one with the traps placed in the bottom layer that is applied directly onto the substrate surface.

However, from the experimental point of view the theoretically most effective system is not preferred since the presence of the traps in the layer contacting the substrate results in worse adhesion of the coating which eliminates the possibility of using such a system in the practical applications. In the Fig. 1 the preliminary results of ATR-FTIR measurements of the water diffusion rate for the pure water-based model epoxy coating and the composite coatings with $5\%_{\mathrm{wt.}}$ addition of water traps are presented. The spherical particles of the cross-linked poly(methacrylic acid) sodium salt with the water diffusion coefficient of $2{,}35 \times 10^{-14}$ cm^2 s^{-1} (estimated from the gravimetric measurements) were applied as water traps. Their water sorption ability measured after 24 h at 100% humidity is about 60% of the dry sample mass. In the same conditions polymer matrix absorbs about 5% of the dry sample mass which means that the partition coefficient k for this system equals 12. All the coatings were sandwich-structured films with thickness of about 40 μm. The ATR-FTIR experimental details and the method of water diffusion coefficient estimation have been reported previously.[15] In the Fig. 1 the delamination process caused by the presence of water traps is clearly shown for the sandwich-structured coating with the traps in the bottom layer. Not only the continuous increase of the water band intensity but also the decrease of the alkyl group band intensity indicates that the film was delaminated and water could penetrate into the free space between the film and the substrate. We have reported this effect previously[15] for the composite coating with the water traps distributed uniformly in the whole volume. As shown in the Fig. 1 the adhesion of the composite film with the traps in the middle layer is the same as in the case of pure polymer coating. Thus, the general recommendation for this kind of systems is application of the sandwich-structured coatings with water traps incorporated in the middle layer (Fig. 2). In the investigated system the water diffusion coefficient in the sandwich-structured coating with the traps placed in the middle layer is about 30% lower than in the pure epoxy coating. The value decreased from $0{,}82 \times 10^{-9}$ cm^2 s^{-1} in the pure film to $0{,}51 \times 10^{-9}$ cm^2 s^{-1} in the composite. It is in a good agreement with our previous work that showed the dependence of the diffusion coefficient in composite on the partition coefficient k.[14] Briefly, the higher k the lower diffusion coefficient in the composite. In the considered case k equals 12 while in the case of $k = 36$, in the composite with the same amount of added water traps the effective diffusion coefficient was reduced to almost one third of its value for pure resin.[15]

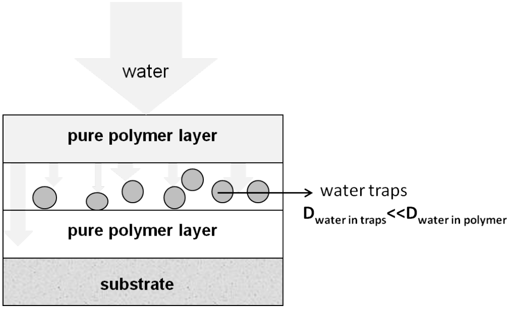

FIGURE 2: Schematic illustration of the structure of the sandwich-type coating with the water traps addition recommended for the highest efficiency of the water traps performance. The water molecules diffusing through the composite coating are trapped inside the particles in the middle layer and they reach the substrate surface much later than diffusing through the pure coating. If pure coating is applied directly at the substrate surface the delamination process does not occur.

In summary, a new idea for decreasing water diffusion coefficient by addition of water trap particles into polymer coatings to improve their performance for the passive anticorrosive protection is presented. The main difference between the water traps and widely studied additives such as water repellents or clay plates lays in the high and reversible water sorption ability of the traps. The water traps can bind water inside and delay its contact with the metal surface. Since the addition of the water traps to the polymer matrix results in lowered adhesion to the substrate it is recommended to apply sandwich-structured coatings with water traps incorporated in the middle layer. The addition of as little as a few weight percents of the water traps to such structured coating can result in significant decrease of the water diffusion coefficient but only when the trapping particles exhibit significantly lower water diffusion coefficient and much higher water sorption ability than the polymer matrix. Taking into account literature reports on active anticorrosive performance of the polymer coatings with smart containers, the combination of this idea with the water traps for improving passive anticorrosion protection properties in complex multifunctional coatings seems to be a very promising way for the effective use of both modifications.

Acknowledgment: A. Karatzas, I. A. Kartsonakis, G. C. Kordas from NCSR DEMOKRITOS are acknowledged for providing the water trapping material. Mankiewicz GmbH is acknowledged for supplying polymer system. Małgorzata Krzak has been partly supported by the EU Human Capital Operation Program, Polish Project No. POKL.04.01.01-00-434/08-02. This work was supported by the NMP3-LA-2008-214261 project „MUST”.

⋆ ⋆ ⋆

[1] M. L. Zheludkevich, J. Tedim, M. G. S. Ferreira, *Electrochim. Acta* **82**, 314 (2012).

[2] S. J. Garcia, H. R. Fischer, P. A. White, J. Mardel, Y. Gonzalez-Garcia, J. M. C. Mole, A. E. Hughes, *Prog. Org. Coat.* **70**, 142 (2011).

[3] D. Snihirova, S. V. Lamaka, M. F. Montemor, *Electrochim. Acta* **83**, 439 (2012).

[4] N. Wang, K. Cheng, H. Wu, Ch. Wang, Q. Wang, F. Wang, *Prog. Org. Coat.* **75**, 386 (2012).

[5] F. Rezaei, F. Sharif, A. A. Sarabi, S. M. Kasiriha, M. Rahmanian, E. Akbarinezhad, *J. Coat. Technol. Res.* **7**, 209 (2010).

[6] W. Liu, S. V. Hoa, M. Pugh, *Compos. Sci. Technol.* **68**, 2066 (2008).

[7] W. Liu, S. V. Hoa, M. Pugh, *Compos. Sci. Technol.* **67**, 3308 (2007).

[8] S. C. See, Z. Y. Zhang, M. O. W. Richardson, *Prog. Org. Coat.* **65**, 169 (2009).

[9] D. P. N. Vlasveld, J. Groenewold, H. E. N. Bersee, S. J. Picken, *Polymer* **46**, 12567 (2005).

[10] T. T. X. Hang, T. A. Truc, T. H. Nam, V. K. Oanh, J. B. Jorcin, N. Pebere, *Surf. Coat. Tech.* **201**, 7408 (2007).

[11] T. A. Truc, T. T. X. Hang, V. K. Oanh, E. Dantras, C. Lacabanne, D. Oquab, N. Pebere, *Surf. Coat. Tech.* **202**, 4945 (2008).

[12] G. Markevicius, S. Chaudhuri, C. Bajracharya, R. Rastogi, J. Xiao, C. Burnett, T. Q. Chastek, *Prog. Org. Coat.* **75**, 319 (2012).

[13] J. Seo, W. Jang, H. Han, *Macromol. Res.* **15**, 10 (2007).

[14] Z. Tabor, M. Krzak, P. Nowak, P. Warszynski, *Prog. Org. Coat.* **75**, 200 (2012).

[15] M. Krzak, Z. Tabor, P. Nowak, P. Warszynski, A. Karatzas, I. A. Kartsonakis, G. C. Kordas, *Prog. Org. Coat.* **75**, 207 (2012).

On the nature of Brönsted acid sites generated in MFI type of zeolite isomorphously substituted with boron

Łukasz Kuterasiński

Jerzy Haber Institute of Catalysis and Surface Chemistry Polish Academy of Sciences, Niezapominajek 8, 30-239 Kraków, Poland

Supervisor: Mirosław Derewiński

Zeolites (molecular sieves) are crystallographically defined microporous solids that could be used as catalysts. The structure (framework) of zeolites consists of corned-linked tetrahedra in which small atoms (collectively denoted T-atoms) lie at the centers of tetrahedra and oxygen atoms lie at the corners. The T-sites of zeolites are Si and Al atoms. Brönsted active centers, which can donate proton to the reacting molecule, are mainly responsible for catalytic activity of zeolites. This type of active centers are generated as a result of isomorphous substitution of tetravalent Si^{4+} *cation in the* SiO_4 *tetrahedra by trivalent cations (for example* Al^{3+}, Fe^{3+} B^{3+}*). The strength of the Brönsted acid site depends on the nature of the metal cation substituting* Si^{4+}*. Boron containing zeolites are characterized by the presence of weaker acid sites than their aluminum counterparts. In numerous chemical reactions — such as isomerization of olefins or dehydration of alcohols — where strong acid sites are not required, the borosilicate can be used as catalysts. Unfortunately, in the B containing molecular sieves the active centers are thermally unstable. During a high temperature treatment the boron is extracted from the framework and so-called internal silanol groups — of a similar acidic strength — are formed. In the undertaken study I would like to verify whether it is possible to distinguish between protonic sites generated by the framework boron and the internal silanols.*

The zeolites with a different boron content ($Si/B=10\div30$) were synthesized. There was also a negligible amount of aluminum ($Si/Al=320$) incorporated into the framework (Al was present as an impurity of the used silica source). Gels of defined chemical composition were prepared in several steps. First, aluminum nitrate nonahydrate ($Al(NO_3)_3{\cdot}9H_2O$) and sodium tetraborate decahydrate ($Na_2B_4O_7{\cdot}10H_2O$) were dissolved simultaneously in aqueous solution of sodium hydroxide (NaOH). Second solution was obtained by adding a template i.e. tetrapropylammonium bromide (TPABr) to the NaOH solution. Subsequently, the first solution was added to the second one with required amount of silica under vigorous stirring at room temperature. The prepared gels were aged for 20 hours.

The aged gels were subsequently transferred into Teflon-lined stainless-steel autoclaves, sealed and kept at 175°C for 20 hours. The autoclaves were rotated at 56 rpm. After synthesis the solids were centrifuged, washed and dried at 80°C. In order to remove organic template (TPABr) calcination of the crystallized materials was carried out at 480°C for 8 hours with temperature ramp 2°C/min.

A half of the obtained Na^+/B-ZSM-5 samples were ion-exchanged twice with a 0,1 M solution of boric acid (H_3BO_3) at 80°C for 2 h. Subsequently, ion-exchanged samples were centrifuged and washed three times with distilled water and dried. The procedure should result in formation of the Brönsted acid centers of Si–O(H)–B type as a consequence of the replacement of Na^+ by H^+ cations from boric acid.

The rest of the samples were exchanged with 0,1 M solution of NH_4NO_3 in the same conditions as mentioned above. This procedure led to replacement of Na^+ cations in the

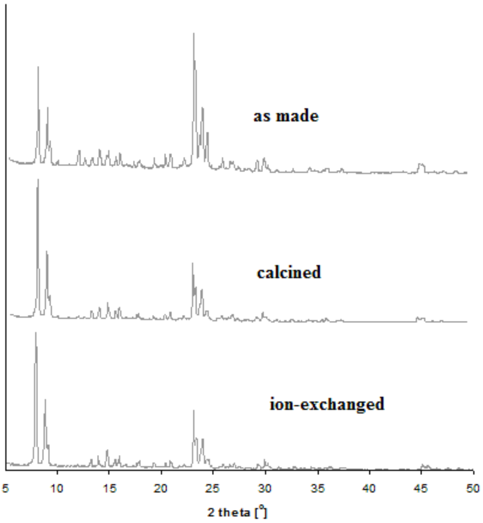

Figure 1: The diffraction image of zeolite B-ZSM-5 (Si/B=10, Si/Al=320).

synthesized materials by NH_4^+ cations. Additional, required step was deammoniation of the obtained NH_4^+/B-ZSM-5 samples by calcination, which resulted in removal of the boron from the framework and generation of defects, i.e. the internal silanol groups ($SiOH_{inter}$).

The X-ray powder diffraction (XRD) was recorded with diffractometer PANalytical X'Pert PRO MPD. The FTIR experiments were carried out using Nicolet 6700 spectrometer. The ^{11}B MAS NMR spectra were recorded with Bruker spectrometer. Scanning electron micrographs were recorded with high-resolution microscope Jeol JSM-7500F. Textural properties were determined by N_2 physisorption at −196°C using Quantachrome Nova 2000. NH_3-TPD measurements were performed using a „home made" instrument.

The XRD data obtained for exemplary sample (Si/B=10, Si/Al=320) are presented in Fig. 1. The high intensity of the reflections indicated that the samples are highly crystalline without any other crystalline phases as a contaminating desired product. The registered XRD pattern (2θ in the range of 2 – 50°) is identical where as that one, recorded for as-synthesized pure MFI type zeolite.[1]

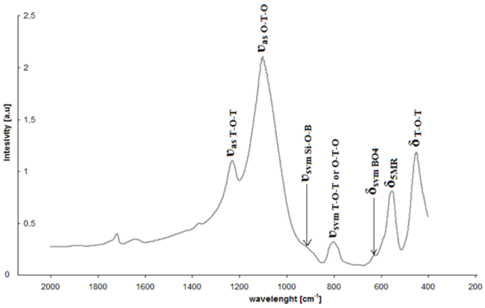

Figure 2: IR spectrum of the as-synthesized sample B-ZSM5 (Si/B=10, Si/Al=320).

The IR spectrum of as-synthesized B-ZMS-5 (Si/B=10, Si/Al=320) was also typical for pentasil zeolites (Fig. 2). The well defined band at 455, 800 cm^{-1} and ca 1100 cm^{-1} correspond to the vibration of the internal bonds in TO_4 tetrahedra (T = Si, Al). The bands at ca 1230 cm^{-1} and 550 cm^{-1} are attributed to the asymmetric stretching vibration of T-O-T bonds ($\nu_{\mathrm{as\ T-O-T}}$) between tetrahedra and vibration of five-member rings (5MR) present in the structure, respectively.[2] According to literature the band at 920 cm^{-1} reflects presence of Si-O-B symmetric stretching vibration and that one at 670 cm^{-1} corresponds to symmetric bending vibrations of tetra-coordinated framework boron.[3]

Incorporation of boron into the tetrahedrally coordinated framework positions was proved with ^{11}B MAS NMR data. The typical spectrum of the as-made boron containing zeolite is shown in Fig. 3. Narrow and symmetric resonance line positioned at ca −23 ppm (from H_3BO_3 as a reference) confirms the presence of B incorporated in the zeolitic structure.[4,5]

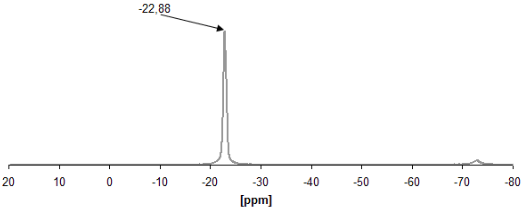

Figure 3: ^{11}B MAS NMR spectrum of the as-synthesized sample B-ZSM-5 (Si/B=10, Si/Al=320). H_3BO_3 as a reference.

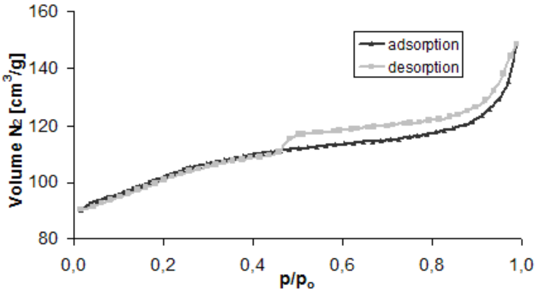

Figure 4: Adsorption/desorption isotherms of the calcined sample B-ZSM5 (Si/B=10, Si/Al=320).

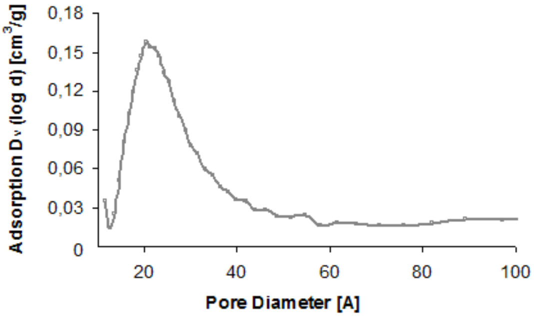

Figure 5: Pore size distribution of the calcined sample B-ZSM5 (Si/B=10, Si/Al=320).

Calcination necessary to remove the molecules of organic template (TPABr) from the micropores changes neither crystallinity nor phase purity of the obtained zeolites (Fig. 1). Changes in the intensity of the reflections were observed in the sample after calcinations. The unit cell decreases owing to removal of organic template from zeolite framework.[6] The FTIR data (not shown) revealed disappearance of bands at ca 3000 cm^{-1} and 1600 – 1700 cm^{-1} corresponding to the presence of organic template. ^{11}B MAS NMR analysis of the calcined samples (not shown) proved that only a small part of the boron has been extracted as evidence by the presence of the low intensity of resonance line of trigonally coordinated boron.

The BET specific surface area calculated from N_2 adsorption isotherms measured for the calcined borosilicates is in the range 270 – 320 m^2/g. Hysteresis loop of IV type[7] observed for the calcined samples is attributed to the presence of the intercrystalline pores between the crystals of B-MFI in the aggregates crystals (Fig. 4). Pore size distribution for the B-ZSM-5 sample is presented in Fig. 5.

The results of the TPD of ammonia and pyridine from the zeolite under study (Si/B=10, Si/Al=320) showed desertion peak at temperatures at 170°C and 280°C, respectively (Figs. 6a, 6b). Relatively low desorption temperature of NH_3/pyridine indicates the presence of only weak acid sites (mostly Na^+ cations in the ion-exchange positions of the framework).[8] Presented results reflects the strength of chemical interaction between the molecules of the used bases, nevertheless do not allow concluding on the nature of the acid sites. This point would be studied in the future by sorption of pyridine monitored with FTIR spectroscopy.

The XRD analysis showed that in both cases of H^+/B-ZSM-5 and NH^{4+}/B-ZSM-5 no changed in the crystallinity was detected. No significant changes in XRD reflections intensity were observed however, a small increase in the unit cell volume has been found for the sample exchanged with the boric acid. Discussion of the reasons for the observed phenomenon will be done after getting results for the sample exchanged with ammonium nitrate. ^{11}B MAS NMR analysis showed that ion exchange procedure led to „reinsertion" of most of the trigonal boron back to the tetrahedrally coordinated framework positions (B^{IV}frame) and obtained spectrum is similar to that one registered for as-synthesized B-ZSM-5 zeolite. The TPD of pyridine from the boric acid exchanged zeolite sample (Si/B=10, Si/Al=320) did no show any significant changes in the strength acid sites present. However, the applied method does not allow determining of the nature of the active centers (Lewis or Brönsted type). This point will be clarified after IR experiments of pyridine sorption.

The TPD, ^{11}B MAS NMR and IR experiments were not carried out yet for the NH^{4+}/B-ZSM-5 preparation (experiments in progress). On the other hand, the XRD

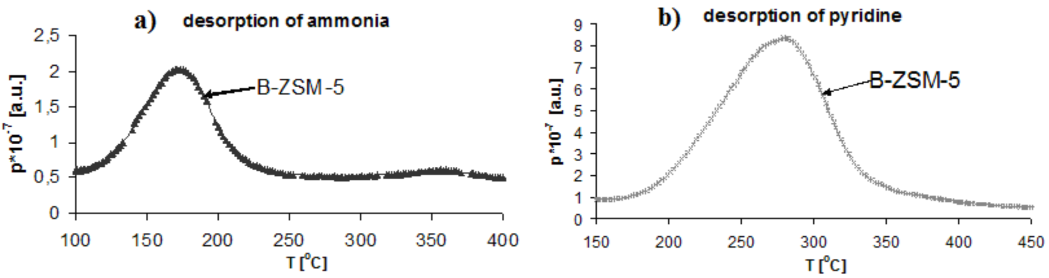

FIGURE 6: Temperature Programmed Desorption (TPD) of a) ammonia; b) pyridine from the calcined sample B-ZSM-5 (Si/B=10, Si/Al=320).

analysis and low-temperature nitrogen sorption experiments confirmed that there were not structural changes in that material.

Zeolites of the ZSM-5 type containing different amount of boron introduced into the framework position have been synthesized. The post-synthesis treatment (calcination, ion exchange procedure) did not influence both the crystallinity and textural properties of the B-ZSM-5 samples. Ion-exchange either with boric acid or ammonium nitrate has been proposed to generate Brönsted active sites.

In the next step of my work a detailed study of state of the framework boron present in both types of the samples i.e. H$^+$/B-ZSM-5 and NH^{4+}/B-ZSM-5 will be carried out. Measurements of the acidity (number and nature of the acid sites, their strength) will allow determining whether the acid centers present in both samples vary in the nature i.e. Si–OH–B or Si–OH$_{\text{intern}}$. The necessary NMR and FTIR experiments are currently in progress.

⋆ ⋆ ⋆

[1] M. J. M. Treacy, J. B. Higgins, Collection of simulated XRD powder patterns for zeolites, 15th Revised Edition, (Elsevier 2007).

[2] M. Mehdipourghazi, A. Moheb, H. Kazemian, *Microporous Mesoporous Mater.* **136**, 18 (2010).

[3] V. Sundaramurthy, N. Lingappan, *J. Mol. Catal. A: Chem.* **160**, 367 (2000).

[4] B. Sulikowski, *Heterogen. Chem. Rev.* **3**, 203 (1996).

[5] R. D. Farlee D. R. Corbin, *Int. Chem. Con. Pac., Basin.Soc.* (Honolulu, Hawaii, 1984).

[6] A. Burkat-Dulak, Ph. D. Thesis, Preparatyka materiałów mikroporowatych z wtórnym systemem mezo i makropodów syntezowanych w obecności węgla i polimerów organicznych (Institute of Catalysis and Surface Chemistry Polish Academy of Sciences, Kraków, 2008).

[7] IUPAC Reporting Physisorption Data, *Pure Appl. Chem.* **57**, 603 (1985).

[8] D. J. Parrillo, C. Lee, R. J. Gorte, *Appl. Catal. A: General* **67**, 110 (1994).

Studies on the mechanism of enzymatic reaction of non-heme (S)-2-hydroxypropylphosphonic acid epoxidase (HppE)

Anna Miłaczewska

Jerzy Haber Institute of Catalysis and Surface Chemistry Polish Academy of Sciences, Niezapominajek 8, 30-239 Kraków, Poland

Supervisor: Tomasz Borowski

Infectious diseases of the urinary tract can be treat using fosfomycin — an antibiotic which is effective against strains such as Staphylococcus aureus that are resistant to other antibiotics, e.g. vancomycin or methicillin. Fosfomycin is produced by microorganisms from a strain of Streptomyces wedmorensis. The final step in the biosynthesis of fosfomycin is catalysed by (S)-2-hydroxypropylphosphonic acid epoxidase (HppE), which is a non-heme mononuclear iron enzyme. We studied the mechanism of the catalytic oxidative epoxidation of HppE using hybrid DFT quantum chemistry methods. Three main pathways were investigated to find the most plausible mechanism of the native HppE reaction.

HppE is a tetramer and each of the identical monomers contains two domains: an α-helical domain and β-domain composed of antiparallel β-strands in a jellyroll β-barrel motif.[1] As it is known from crystallographic studies, the organic substrate of HppE, i.e. (S)-2-hydroxypropylphosphonic acid (S−HPP), binds to iron in a bidentate fashion, which actives the site for binding of molecular oxygen. In the presence of external electron donors, several types of reactive iron-oxygen intermediates can be generated at the iron center. In the subsequent step, hydrogen atom abstraction by one of those reactive species yields a radical intermediate which through formation of an epoxide ring produces fosfomycin and regenerates the iron core.

Concerning our mechanistic studies, an active site model was created from an available crystal structure solved for the HppE−Fe(II)−S−HPP complex, and it is shown in Fig. 1. Except for metal ion and coordinated substrate, the model contains first-shell ligands of iron and second-shell polar groups of residues interacting with the substrate. There are several proposed scenarios for substrate activation and cyclization in the literature.[2] They differ in the redox state of the reactive iron-oxygen species responsible for the hydrogen atom abstraction (Fig. 2). Thus, in the first mechanism (A), the substrate is directly activated by a dioxygen molecule bounded to Fe(II). In the second mechanism (B), which assumes 1-electron reduction of the Fe(II)$-$O$_2$ species prior to substrate activation, hydrogen atom is abstracted from the substrate by a Fe(III)−hydroperoxide intermediate. Third mechanism (C) requires 2-electron reduction

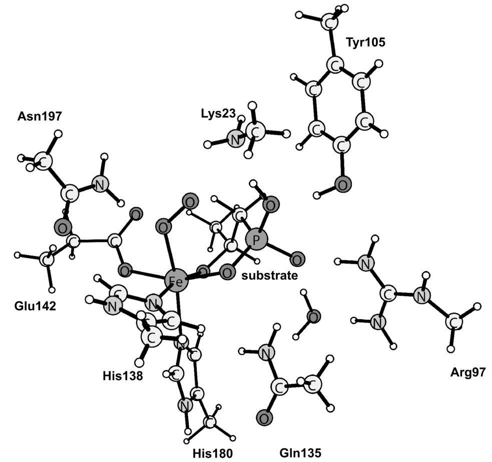

Figure 1: The optimized structure for the active site model used for theoretical investigations.

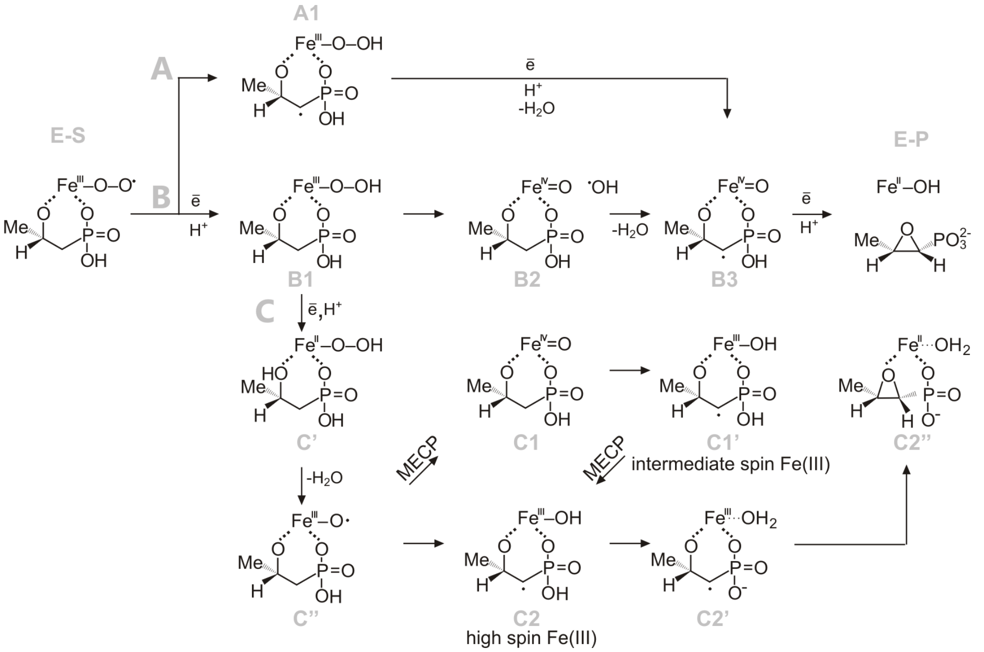

FIGURE 2: Three mechanisms investigated for epoxidation of (S)-2-hydroxypropylphosphonic acid.

of the Fe(II)$-$O$_2$ species and involves a reactive Fe(IV)$=$O species.[3] The reaction energy profiles were constructed for these three a priori plausible mechanisms by determining structures and energies of consecutive species (including transition states) lying on the reaction pathways. To this end density functional theory (DFT) with B3LYP functional was applied to the active site model. Geometry optimization was carried out with the software package Jaguar 7,[4] whereas Gaussian 09 suite of programs[5] was used to locate transition states. Optimizations were carried out using the double ζ basis set (lacvp) and then the electronic energies for optimized structures were computed using a larger basis set (cc-pVTZ(-f) for all atoms apart from iron for which a triple zeta basis with a set of diffuse functions (lacv3p+) was used). Final energies were corrected for solvent effects (using dielectric constant $\epsilon = 4$ for the active sites inside the metalloenzyme), as well as zero-point energy and the van der Waals empirical correction.[6] Results of single-point calculations with B3LYP* functional were compared with those obtained with B3LYP to check how sensible they are with respect to variations of the exchange-correlation functional.

Investigations were conducted for various plausible spin states. The lowest barrier for the hydrogen atom abstraction is observed for the proposed mechanism C, and only for this path the following step, i.e. S$-$HPP epoxidation, was investigated. In Fig. 3 we present barriers and energy effects obtained for the energetically most favorable state for each pathway: A — quintet, B — sextet, C — quintet. During a one electron reduction of B1, that leads to pathway C, the incoming proton may be placed on several atoms: oxygen of the HOO group proximal to the iron, nitrogen of Lys23 or the oxygen of the substrate (bound to carbon C2 of S$-$HPP). The last one gave the most stable structure C$'$ (vide Fig. 2) and led to a mechanism with a low energy barrier. In the next step (C$'$ → C$''$), the O$-$O bond of the HOO group is cleaved with the help of a proton transferred from the S$-$HPP alcohol group to the leaving OH. The species formed in this step is metastable with high spin Fe(III) and an oxyl radical. It is an excited state of the usual oxofer-

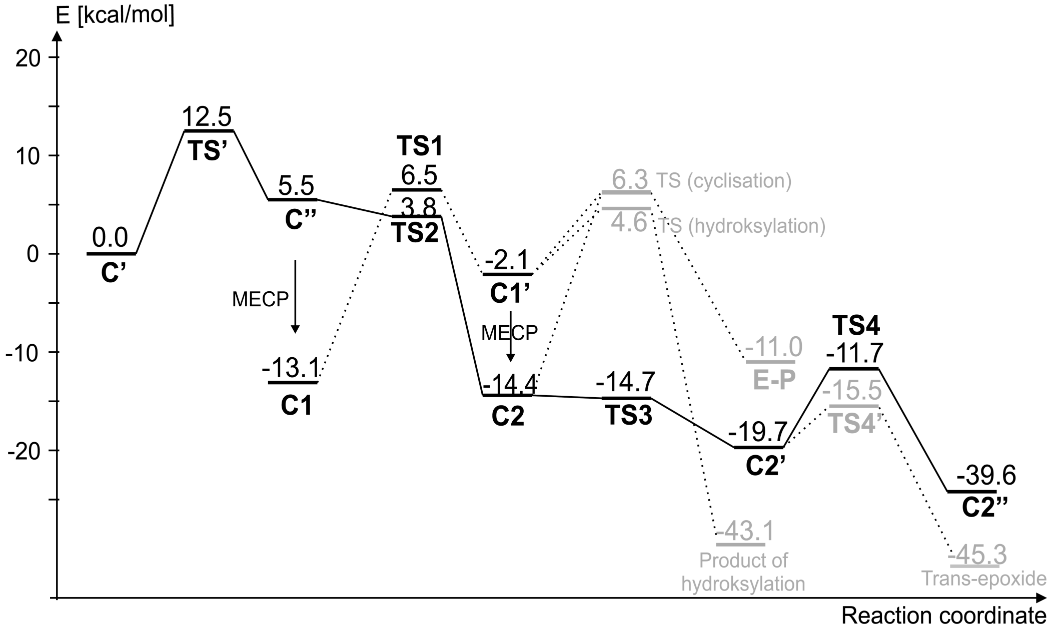

FIGURE 3: The energy profile for reaction on pathway C and the most preferred spin state — quintet. Black solid lines mark the most likely pathway and other possible routes are indicated by gray dotted lines.

ryl compound (species C1). In an attempt to estimate the energy barrier of de-excitation ($C'' \rightarrow C1$), a minimum energy crossing point (MECP) between two non-interacting PESs was located[7] and since its energy is almost identical to C'' we concluded that there is no structural barrier for de-excitation C'' to C1. Transition from species C1 to $C1'$ (with intermediate spin configuration of Fe(III)) is endothermic by about 11,0 kcal mol^{-1} (14,3 kcal mol^{-1} with B3LYP*) and involves a barrier of 19,6 kcal mol^{-1} (20,8 kcal mol^{-1} with B3LYP*). De-excitation to C2 also proceeds without any energy barrier. Nevertheless, there is another possible pathway related to the pro-R hydrogen placed only 2,04 Å away from the oxyl radical. In this case, there is also no barrier for the C−H bond cleavage leading directly to C1 (a ground state of specie C2). Thus, some part of the reaction may proceed on the excited state surface. It was also checked if the reaction could continue further from $C1'$ through hydroxylation or cyclization, but connected barriers are too large (6,7 and 8,4 kcal mol^{-1} respectively) to make these steps competitive.

In many cases oxoferryl species is involved in hydroxylation of an organic substrate, what can be understood as a transfer of the hydroxyl group from to Fe(III) to the radical carbon. Starting with C2 species, such reaction has a relatively small barrier of 6 kcal mol^{-1} (4,4 kcal mol^{-1} with B3LYP*) and yields very stable product with energy about 28,7 kcal mol^{-1} (27,8 kcal mol^{-1} with B3LYP*) lower than energy of C2. Reaction of cyclization could hardly compete with the so energetically favored reaction of hydroxylation. To understand why in the HppE catalytic cycle cyclization occurs and not hydroksylation it is important to notice that the basicity of Fe(III)−OH allows for a transfer of proton from the PO_3H−Lys23 hydrogen-bonded pair, which prevents hydroksylation and supports reduction of Fe(III) to Fe(II) by decreasing the number of negatively charged ligands in the first-shell. The barrier for closing of the epoxide ring, starting from the entity formed by a proton transfer from PO_3H−Lys23, is just 8,0 kcal mol^{-1} (6,5 kcal mol^{-1} with B3LYP*). It is significantly less then the barrier of 20,6 kcal mol^{-1}

(18,9 kcal mol^{-1} with B3LYP*) for formation of the epoxide ring straight away from C2 to E−P complex.

Applied model of the active center did not involve hydrophobic residues in the vicinity of substrate. It is a usual approach to reduce the computational burden. However, in this case the necessary simplification resulted in a model favoring production of a trans-epoxide — stereoisomer of fosfomycin. The barrier for this process is 3,8 kcal mol^{-1} lower than for the desirable formation of the cis-epoxide — fosfomycin. The ongoing computational studies will address this issue.

In conclusion, catalytic reaction of HppE for the native S−HPP substrate involves one of species $\text{Fe(III)}-\text{O}^\bullet$ or $\text{Fe(IV)}=\text{O}$ in order to cleavage the C−H bond (mechanism C). The O−O bond cleavage yields $\text{Fe(III)}-\text{O}^\bullet$, an excited state of $\text{Fe(IV)}=\text{O}$. This excited species is considered catalytically important, since it elicits cleavage of the C−H bond proceeding without any energetic barrier. Moreover, we found that formation of the epoxide ring depends on the number of negatively charged ligands in the first shell of iron, by affecting the redox potential of the Fe(III)/Fe(II) couple.[8]

⋆ ⋆ ⋆

[1] L. J. Higgins, F. Yan, P. Liu, H. Liu, C. L. Drennan, *Nature* **437**, 838 (2005).

[2] L. M. Mirica, K. P. McCusker, L. W. Munos, H. Liu, J. P. Klinman, *J. Am. Chem. Soc.* **130**, 8122 (2008).

[3] F. Yan, S. Moon, P. Liu, Z. Zhao, J. D. Lipscomb, A. Liu, H. Liu, *Biochemistry* **46**, 12628 (2007).

[4] Jaguar, version 7.8 (Schrödinger, LLC, New York, 2011).

[5] M. J. Frisch, G. W. Trucks, H. B. Schlegel, G. E. Scuseria, M. A. Robb, J. R. Cheeseman, G. Scalmani, V. Barone, B. Mennucci, G. A. Petersson, H. Nakatsuji, M. Caricato, X. Li, H. P. Hratchian, A. F. Izmaylov, J. Bloino, G. Zheng, J. L. Sonnenberg, M. Hada, M. Ehara, K. Toyota, R. Fukuda, J. Hasegawa, M. Ishida, T. Nakajima, Y. Honda, O. Kitao, H. Nakai, T. Vreven, J. A. Montgomery, Jr., J. E. Peralta, F. Ogliaro, M. Bearpark, J. J. Heyd, E. Brothers, K. N. Kudin, V. N. Staroverov, R. Kobayashi, J. Normand, K. Raghavachari, A. Rendell, J. C. Burant, S. S. Iyengar, J. Tomasi, M. Cossi, N. Rega, J. M. Millam, M. Klene, J. E. Knox, J. B. Cross, V. Bakken, C. Adamo, J. Jaramillo, R. Gomperts, R. E. Stratmann, O. Yazyev, A. J. Austin, R. Cammi, C. Pomelli, J. W. Ochterski, R. L. Martin, K. Morokuma, V. G. Zakrzewski, G. A. Voth, P. Salvador, J. J. Dannenberg, S. Dapprich, A. D. Daniels, Ö. Farkas, J. B. Foresman, J. V. Ortiz, J. Cioslowski, D. J. Fox, Gaussian 09, Revision A.1 (Gaussian, Inc., Wallingford CT, 2009).

[6] S. Grimme, *J. Comput. Chem.* **27**, 1787 (2006).

[7] J. N. Harvey, M. Aschi, H. Schwarz, W. Koch, *Theor. Chem. Acc.* **99**, 95 (1998).

[8] A. Milaczewska, E. Broclawik, T. Borowski, *Chem. Eur. J.* **19**, 771 (2013).

Cyclic voltammetry method for examining ion transport through porous layer

Magdalena Nosek

Jerzy Haber Institute of Catalysis and Surface Chemistry Polish Academy of Sciences, Niezapominajek 8, 30-239 Kraków, Poland

Supervisor: Paweł Weroński

Adsorption and deposition (irreversible adsorption) of colloids and bioparticles at the solid/liquid interface leads to a spontaneous formation of a porous layer, which may have a noticeable effect on the ion transport from the bulk solution to the adsorption surface. Some electrochemical techniques, such as the cyclic voltammetry and the rotating disk electrode, can be used to retrieve individual ionic transport parameters in thin films or membranes, as well as many important characteristics of the layer supported by a solid electrode and exposed to an electrolyte solution. We used the cyclic voltammetry method to characterize monolayers of one micrometer sulfate polystyrene latex particles. We conducted measurements of the limiting diffusion current in the 1 mM solution of potassium hexacyanoferrate(III) at various rotational speeds of the gold disk. Before each experiment the gold rotating disk electrode was carefully prepared by mechanical polishing to obtain a smooth, clear, and reproducible gold surface. We used a diffusion cell for polistyrene latex particle deposition under barrierless conditions. The coverage of the electrode surface was determined using an optical microscope. We demonstrated a good agreement between the experimental results and theoretically predicted limiting diffusion current at medium and high surface coverages of the rotating disk electrode. Our results suggest that the voltammetric method can be used for the characterization of monolayer thickness and porosity, as well as for the determination of surface concentration of deposited colloidal particles.

Adsorption of colloidal particles at a solid/liquid interface leads to a spontaneous formation of a porous layer, which may have a noticeable effect on the ion transport from the bulk solution to the adsorption surface. This phenomenon can be studied using the cyclic voltammetry (CV) method with the rotating disk electrode (RDE). The ion transport in the RDE system was first described by Levich, and it has been well understood.[1] His theoretical analysis was further extended to membrane-covered RDEs. The first research on this subject was published by Gough and Leypoldt in 1979. They also developed a mathematical model of the system and compared the model-predicted and experimental results of the mass transport through a homogenous gel membrane covering the RDE.[2] The CV method with the RDE has several important advantages. The disk surface is equally accessible to the reactant and the diffusion boundary layer thickness is precisely determined. At low rotational speed of the disk the diffusion boundary layer is relatively thick and the major contribution to the total diffusion resistance is the transport through the solution. Under these conditions, even when the RDE is covered with a membrane, the limiting diffusion current is proportional to the square root of rotation rate. At high rotational speed, the thickness of the diffusion boundary layer is small, the resistance of the electrolyte solution is negligible, and the diffusion current is determined largely by the properties of the membrane which covers the disk. In this way, the CV with the RDE can be used to evaluate quantitatively the mass transport through a membrane or other thin films.[2]

To our knowledge, no results have been reported in the literature for the important case of the ion transport through layers of colloidal particles. Therefore, the objective of our research is to compare experimental and theoretical results of the limiting diffusion current for a bare gold rotating disk electrode and for the electrode with a monolayer of 1 μm latex particles at medium and high surface coverages.

We derived the equation for the limiting diffusion current at the RDE with a layer of particles from the model developed by Gough and Leypoldt. They considered steady-state mass transfer of a solute that was consumed at the surface of the RDE covered by a homogenous gel membrane.[2] Using the method of Levich[1] and assuming no convective flow within the membrane they found the equation of the diffusion current in the case of membrane-covered RDE.[2] In our system the RDE has been covered by a porous layer of spherical particles instead of a homogeneous gel membrane. Considering that flow penetrates the porous medium only when its solid volume fraction is less than 0,1;[3] we can neglect the convective flow within the particle layer if the surface coverage $\theta > 0{,}15$. The equation for the limiting diffusion current at the RDE with an adsorbed layer of particles ($\theta > 0{,}15$) is:

$$I = I_\mathrm{L} \left\{ 1 + \frac{2r[1 + \theta(\pi/8 - 1/3)]}{\delta_\mathrm{d}(1 - 2\theta/3)^2} \right\}^{-1}, \quad (1)$$

where I_L is the current in the absence of the membrane (Levich current), r — the particle radius, θ — the surface coverage, and δ_d — the thickness of the diffusion boundary layer.

We show the results obtained with Eq. (1) in Fig. 1, where the normalized limiting diffusion current I/I_L is presented as a function of surface coverage for several values of the normalized layer thickness $2r/\delta_\mathrm{d}$. The limiting diffusion current decreases with the growth of surface coverage, when the porosity of the layer, and thus effective diffusion coefficient in the layer, decrease. This effect is more significant at high rotation rates, when the thickness of the porous layer of adsorbed particles becomes comparable to the thickness of the diffusion boundary layer. However, even at a relatively thin porous layer of the thickness $2r/\delta_\mathrm{d} = 0{,}1$, the limiting diffusion current is still reduced by more than 10%. In case of thicker layers the current is reduced by more than 30% at $2r/\delta_\mathrm{d} = 0{,}4$ and more than 50% at $2r/\delta_\mathrm{d} = 1$.

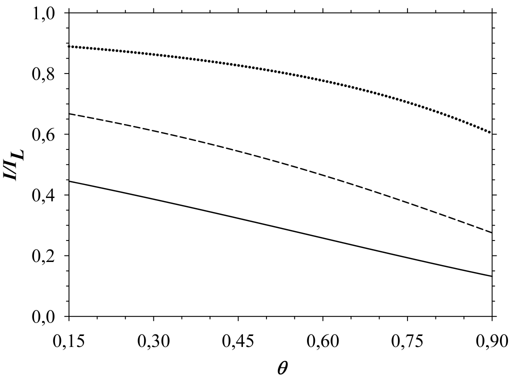

FIGURE 1: Normalized limiting diffusion current as a function of surface coverage. Solid, dash, dotted lines denote results for normalized layer thickness $2r/\delta_\mathrm{d} = 1$; 0,4 and 0,1 respectively.

We performed cyclic voltammetry measurements with the potentiostat/galvanostat Autolab PGSTAT302N. We carried out the experiments in a thermostatic glass cell using a standard three-electrode system with a working gold RDE, a platinum counter electrode, and an Ag/AgCl/sat. KCl reference electrode. Immediately before the experiment, the surface of working electrode was carefully polished for about ten minutes with a 0,05 μm Al_2O_3 MasterPrep Polishing Suspension (Buehler) with addition of isopropanol on an extruded polystyrene pad, at the pressure about 0,4 kPa, using a custom made polishing machine. Then, it was rinsed with ultrapure water and isopropanol. The CV experiments were conducted at 298 K in an aqueous solution containing 1 mM $K_3[Fe(CN)_6]$ and 0,15 M KCl as a base electrolyte. The electrolyte solution was deoxigenated before the measurements by bubbling with argon and the CV measurements were carried out under argon atmosphere. The potential was changed in the range of $-0{,}6$ V to $0{,}7$ V at the scan rate of $0{,}1\ \mathrm{V\,s^{-1}}$. Cyclic voltammograms were recorded for seven various rotational speeds: 100, 200, 400, 800, 1600, 3200, 6400 [rpm].

Particle monolayers on the gold disk were prepared using the negative latex particles (SPL) bearing sulfate groups. The particle size distributions obtained by means of laser diffractometry (Particle Size Analyzer LS 13 320 Beckman Coulter) and dynamic light scattering (Zetasizer Nano ZS of Malvern) have been similar.[4] The average diameter of the latex particles used in our experiments has been $1{,}12 \pm 0{,}02\ \mu$m. The SPL particles have been negatively charged throughout the entire pH range. The zeta potential has decreased from -54 mV at pH$\,=\,$2 to -112 mV at pH$\,=\,$11. We carried out particle deposition experiments in a diffusion cell. The bulk suspension concentration of the latex particles was $n_\mathrm{b} = 1{,}8 \times 10^{10}\ \mathrm{cm^{-3}}$, at the concentration of KCl $c = 10^{-3}$ M and pH $= 2{,}0$. After adsorption, the Au RDE with a monolayer was rinsed with distilled water and the CV measurements were performed. Then, the coverage of the electrode surface was determined using an optical microscope. During all measurements, the Au RDE with a monolayer of colloidal particles was under wet conditions.

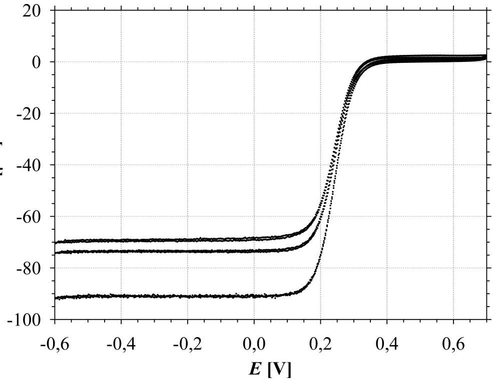

FIGURE 2: Cycling voltammograms for bare Au RDE and for Au RDE with monolayer of sulfate latex particles at surface coverage $\theta = 0{,}15$ and $\theta = 0{,}35$; from bottom to top, respectively. Experimental conditions: 1 mM $K_3[Fe(CN)_6]$ and 0,15 M KCl in aqueous solution, potential scan rate $0{,}1\ \mathrm{V\,s^{-1}}$, rotation frequency 6400 rpm.

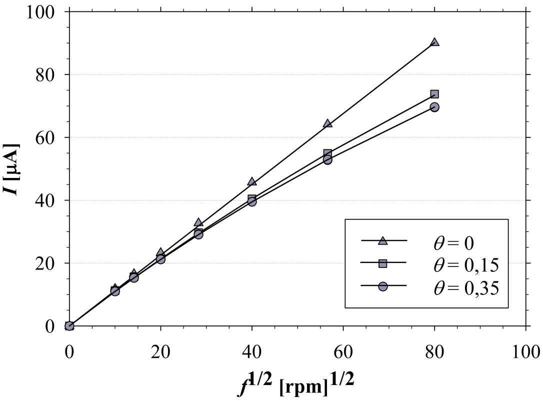

FIGURE 3: Limiting diffusion current at Au RDE with deposited colloidal particles at various surface coverage. Points represent experimental results, lines represent values calculated with Eq. (1), based on surface coverage determined by optical microscopy.

In this work we report the results of CV measurements conducted for the surface coverage of the SPL particles $\theta = 0$; 0,15 and 0,35. We have observed significant reduction of the limiting diffusion current after adsorption of the particle layer, as shown in Fig. 2. Our experimental results are consistent with the predictions of Eq. (1) with values of surface coverage and porous layer thickness determined by optical microscopy and dynamic light scattering, respectively. This agreement between our experimental and theoretical results is more evident in Fig. 3, where we have demonstrated the dependence of the limiting diffusion current on the square root of rotational speed. For a comparison, Fig. 3 shows the exemplary results for the bare electrode ($\theta = 0$) and the Au RDE with two various monolayers ($\theta\,=\,0{,}15$ and 0,35).

The results of our electrochemical measurements showed that the CV and RDE techniques can be used for characterization of the ion transport through a colloidal layer in terms of the limiting diffusion current. These techniques also allow us to determine important parameters of the adsorbed layer of colloidal particles. Specifically, with this method we can measure the particle surface coverage. We have demonstrated a very good agreement between our experimental results and theoretically predicted limiting diffusion current at medium and high surface coverages of the Au RDE. Our research suggests that in the presence of colloidal particles the Levich plot becomes non-linear. The limiting diffusion current decreases with the growth of surface coverage, when the porosity of the layer and effective diffusion coefficient in the layer decrease. This effect is more significant at high rotation rates, when the thickness of the porous layer of adsorbed particles becomes comparable to the thickness of the diffusion boundary layer. We believe that this method may have practical applications for, e.g., detection and determination of surface coverage of bacteria, cells or other objects in the micron size range.

This work was supported by the EU Human Capital Operation Program, Polish Project No. POKL.04.01.01-00-434/08-02.

⋆ ⋆ ⋆

[1] V. G. Levich, Physicochemical Hydrodynamics (Prentice-Hall, Englewood Cliffs, N. Y., 1962).

[2] D. A. Gough, J. K. Leypoldt, *Anal. Chem.* **51**, 439 (1979).

[3] D. F. James, A. M. J. Davis, *J. Fluid. Mech.* **426**, 47 (2001).

[4] M. Nosek, P. Weroński, P. Nowak, J. Barbasz, *Colloids and Surfaces A: Physicochem. Eng. Aspects* **403**, 62 (2012).

Electroactive multilayer films of polyelectrolytes and Prussian Blue nanoparticles as a sensitive tool for H_2O_2 detection

Anna Pajor-Świerzy

Jerzy Haber Institute of Catalysis and Surface Chemistry Polish Academy of Sciences, Niezapominajek 8, 30-239 Kraków, Poland

Supervisor: Piotr Warszyński

Prussian blue (PB) nanoparticles were immobilized in polyelectrolyte (PE) multilayers of various composition and thickness. Films containing nanoparticles and poly(allylamine hydrochloride) (PAH) were formed using layer-by-layer adsorption method. It was observed that the films exhibited electroactive properties, increasing with the number of deposited PB layers. The properties of PEI/(PB/PAH)$_n$ *multilayers were then compared with ones containing additionally the conductive polymer poly(3,4-ethylenedioxythiophene) poly(styrenesulfonate) (PEDOT:PSS). It was noticed that incorporation of the conductive, water soluble polyelectrolyte enhances the electroactive properties of the multilayer films. It also increased sensitivity of the multilayer covered electrodes for electrochemical detection of hydrogen peroxide.*

Prussian Blue (PB) as a mixed-valence hexacyanometalate salt is one of the longest known coordination compounds. The first reports concerning PB date back to the early XVIII century when it was only used as a blue pigment. In 1978 Neff reported that it can be deposited onto an electrode surface to produce an electroactive covering.[1] Since then the attempt have been made to use PB films in electrochemical sensors and biosensors because of its catalytic properties toward the detection of hydrogen peroxide.[2] It is an essential indicator in food, pharmaceutical, clinical, industrial and environmental analyses.[3,4] Hydrogen peroxide is also the by-product of many enzymatic reactions, so its concentration can be used as a good marker of the progress of the reaction.[5,6] Prussian Blue can catalyse the electroreduction and electrooxidation of H_2O_2. The reduction process involves the high spin iron ions, $Fe^{3+/2+}$, whereas the oxidation of H_2O_2 is the result of the redox reactions at the low-spin iron ions.[7] The possibility for selective detection of hydrogen peroxide by its reduction in the presence of oxygen on Prussian Blue modified electrodes was first demonstrated by Karyakin et al.,[8,9] while other groups used oxidation at high anodic potentials.[10,11]

In the present work Prussian Blue nanoparticles were synthesized by the reaction of $FeCl_3{\cdot}6H_2O$ and $K_4[Fe(CN)_6]$ in the presence of 10^{-2} M HCl according to the recipe given in[12]. The average PB particle size as analyzed by DLS technique, was around 10 nm. The obtained nanoparticles were negatively charged (as synthesized at $\mathrm{pH} = 2$) with the average zeta potential around -50 mV.

Fig. 1 present the comparison of the build-up of PEI/PB/(PAH/PB)$_n$ multilayer films (black line) with PEI/PB/(PEDOT:PSS/PAH/PB)$_n$ multilayer (gray line) studied by QCM-D technique. The decrease of quartz crystal frequency after each polyelectrolyte and Prussian Blue adsorption step is the evidence of mass deposition on the crystal surface. For the system containing PEDOT:PSS the observed ΔF shifts, were bigger after first few layers than for films consisted of PB and PAH only. Although PEDOT:PSS is negatively charged, it adsorbs on PB terminated films (Fig. 1, gray line). It means that PEDOT:PSS can cover local, positively

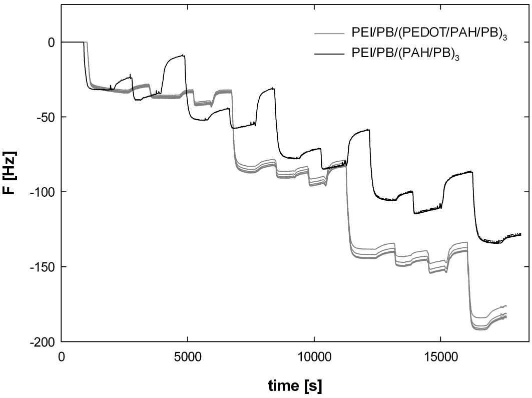

FIGURE 1: QCM results showing the frequency shift due to formation of PEI/PB/(PAH/PB)$_n$ (black line) and PEI/PB/(PEDOT:PSS/PAH/PB)$_n$ multilayer (gray line); dependency for n-layer films.

charged voids between PB nanoparticles. In this way the charge uniformity of the layer is improved, which creates favourable conditions for the deposition of next polycation and subsequent PB layers. Moreover, presence of polyanion stabilizes the whole film. One can observe in Fig. 1 that the significant mass is desorbed during the rinsing step after deposition of PAH. The desorption is much decreased when PEDOT:PSS is used for the formation of the multilayer film. Another difference between the films, which can be observed in Fig. 1 concerns their viscoelastic properties. Splitting of the frequency shifts for the quartz crystal overtones for the PEI/PB/(PEDOT:PSS/PAH/PB)n multilayers indicates on their more viscoelastic behaviour as compared with PEI/PB/(PAH/PB)$_n$, which are stiffer.

Cyclic Voltammetry (CV) was used to analyze the electroactive properties of PB films. The redox reaction of PB can be written as:[13–16]

$$\underset{\text{PB}}{\mathrm{Fe}_4^{\mathrm{III}}\left[\mathrm{Fe}^{\mathrm{II}}(\mathrm{CN})_6\right]_3} + \mathrm{e}^- \leftrightarrow \underset{\text{PW}}{\mathrm{Fe}_4^{\mathrm{II}}\left[\mathrm{Fe}^{\mathrm{II}}(\mathrm{CN})_6\right]_3} \tag{1}$$

The voltammograms obtained for the gold electrode covered with this films have two sets of characteristic peaks corresponding to the reduction of Prussian Blue (PB) to Prussian White (PW) and the reverse process, the oxidation of PW to PB. The potential separation of the peaks was around 40 mV, which was very close to the theoretical value, indicating that fast charge transfer in the modified film occurred. These are obviously not observed at the bare electrode.

Films of PEI/PB/(PAH/PB)$_n$ and-PEI/PB/(PEDOT:PSS/PAH/PB)$_n$ were formed in the identical experimental conditions as these applied for QCM experiments. Appearance of the PB redox peaks, is a clear evidence that multilayers containing PB nanoparticles have electroactive properties, enhanced by the presence of conductive polyelectrolyte (PEDOT:PSS) in the film structure. In order to compare directly the electroactive properties of PEI/PB/(PAH/PB)$_n$ multilayers with ones containing PEDOT:PSS, i.e., PEI/PB/(PEDOT:PSS/PAH/PB)$_n$ we determined the current density in the maximum of both reduction and oxidation peaks. The results are illustrated in Fig. 2. It can be observed that for both types of films the redox current increased almost linearly with number of deposited bilayers, i.e., with number of adsorbed PB layers. The current density of PB in the maximum of oxidation and reduction peak is higher in the presence of conductive polymer in the multilayer structure that means that conductive polymer improves the electroactive properties of studied films. This improvement can be attributed either to larger amount of the Prussian Blue nanoparticles adsorbed in the presence of PEDOT:PSS or to the enhancement of rapid electron transfer to the surface of the gold electrode by the presence of conductive polyelectrolyte.

In the presence of H_2O_2 characteristic peaks from reduction and oxidation of H_2O_2 appeared. We observed hydrogen peroxide reduction at cathodic potential of about −0,6 V. The product of H_2O_2 reduction was

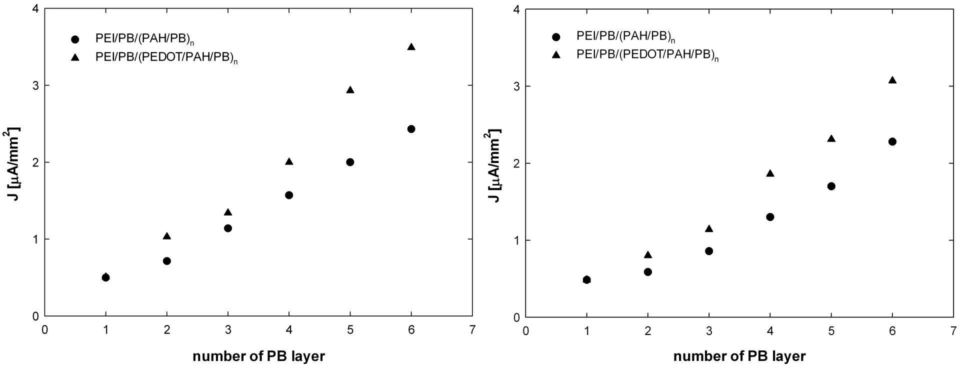

FIGURE 2: Comparison of oxidation (left panel) and reduction (right panel) current density at gold electrode covered with PEI/PB(PAH/PB)$_n$ (circle) and with PEI/PB/(PEDOT:PSS/PAH/PB)$_n$ multilayers (triangles) with increasing number of layers.

OH−. An overall reaction for the electrocatalytic reduction process can be written as:[17]

$$H_2O_2 + 2e^- \rightarrow 2OH^- \ . \qquad (2)$$

Characteristic peaks of hydrogen peroxide oxidation:

$$H_2O_2 + 2e^- \rightarrow O_2 + 2H^+ + 2e^- \qquad (3)$$

could be noticed at anodic potential about 0,6 V.

The efficiency of the polyelectrolytes and Prussian Blue multilayer films for the H_2O_2 detection was determined in 0,1 M phosphate buffer solution at pH = 7. We observed that the height of redox current peaks decrease with the number of CV cycles. For the sake of comparison we determined the value of redox current density from value of current in the peaks in the second CV cycle. Fig. 3 presents the dependence of the current density of the oxidation and reduction of H_2O_2 for gold electrode covered with PEI/PB/(PAH/PB)$_n$ and the ones modified by PEDOT:PSS, on the number of deposited PB layers.

Results presented in Fig. 3 imply that the electrocatalytic properties of PB films can be controlled by the number of adsorbed PB layers. It can be observed that the current densities for oxidation and reduction of H_2O_2 increases linearly with the number of deposited PB layers. It suggests that hydrogen peroxide molecules have ability to diffuse through the film. We can also notice that the peak values of the anodic current are smaller then cathodic ones. The films modified with con-

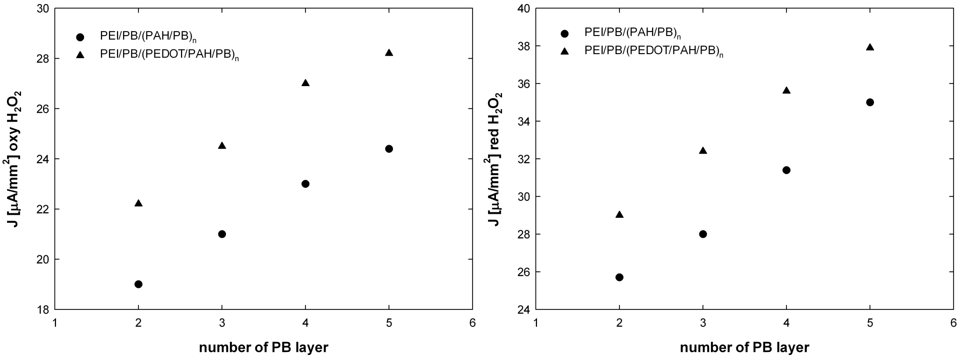

FIGURE 3: The comparison of the hydrogen peroxide oxidation (left panel) and reduction (right panel) current density for PEI/PB/(PAH/PB)$_n$ (circles) and PEI/PB/(PEDOT:PSS/PAH/PB)$_n$ (triangles) modified electrodes in the presence of 5 mM H_2O_2, obtained in pH=7 phosphate buffer solution.

ductive polymer (PEDOT:PSS) are more sensitive to the presence of hydrogen peroxide.

To summarize, we studied formation and electroactive properties of multilayer films of polyelectrolytes and Prussian Blue nanoparticles. We noticed that larger amount of PB nanoparticles were adsorbed when the PB film was covered with the layer of conductive polymer (PEDOT:PSS). Cyclic voltammetry technique provided information about the electroactive properties of studied multilayers. We observed linear increase of PB redox current with the number of adsorbed PB layers. The redox current was increased in the presence of conductive polymer, which can be attributed to larger amount of the Prussian Blue nanoparticles adsorbed in the presence of PEDOT:PSS and also to the enhancement of rapid electron transfer to the surface of the gold electrode. The PE/PB multilayer films were successfully tested for electrochemical detection of hydrogen peroxide. Polyelectrolyte multilayers containing PB are selective electrocatalysts for hydrogen peroxide reduction and oxidation. Incorporation of the PEDOT:PSS in the multilayer structure increases redox current of hydrogen peroxide. It gives possibility for application of hybrid PE/PB multilayers containing conductive polyelectrolytes for the electrochemical detection of hydrogen peroxide in various applications, however, selection of the conductive polymer, preparation and measuring conditions still need to be optimized.

The work was supported by the EU Human Capital Operation Program, Polish Project No. POKL.04.01.01-00-434/08-02.

⋆ ⋆ ⋆

[1] V. D. Neff, *J. Electrochem. Soc.* **128**, 886 (1978).

[2] A. A. Karyakin, E. A. Kotel'nikova, L. V. Lukachova, E. E. Karyakina, *Anal. Chem.* **74**, 1597 (2002).

[3] P. N. Bartlett, P. R. Birkin, J. H. Wang, F. Palmisano, G. D. Benedetto, *Anal. Chem.* **70**, 3685 (1998).

[4] O. Wolfbeis, A. Drkop, M. Wu, Z. Lin, *Angew. Chem. Int. Ed.* **41**, 4495 (2002).

[5] A. Salimi, L. Miranzadeh, R. Hallaj, H. Mamkhezri, *Electroanal.* **20**, 1760 (2008).

[6] R. H. Bhate, T. Ramasarma, *Arch. Biochem. Biophys.* **495**, 95 (2010).

[7] X. Liu, J. L. Zweier, *Biol. Med.* **31**, 894 (2001).

[8] A. A. Karyakin, O. V. Gitelmacher, E. E. Karyakina, *Anal. Lett.* **27**, 2861 (1994).

[9] A. A. Karyakin, E. E. Karyakina, L. Gorton, *Talanta* **43**, 1597 (1996).

[10] S. A. Jaffari, J. C. Pickup, *Biosens. Bioelectron.* **11**, 1167 (1996).

[11] S. A. Jaffari, A. P. F. Turner, *Biosens. Bioelectron.* **12**, 1 (1997).

[12] K. Itaya, T. Ataka, S. Toshima, *J. Am. Chem. Soc.* **104**, 4767 (1982).

[13] K. Itaya, I. Uchida, S. Toshima, *J. Phys. Chem.* **87**, 105 (1983).

[14] K. Itaya, K. Shibayama, H. Akahoshi, S. Toshima, *J. Appl. Phys. Chem.* **53**, 804 (1982).

[15] K. Itaya, T. Ataka, S. Toshima, T. Shinohara, *J. Phys. Chem.* **86**, 2415 (1982).

[16] A. Abbaspour, M. A. Kamyabi, *J. Electroanal. Chem.* **584**, 119 (2005).

[17] A. J. Bard, R. Parsons, J. Jordan, Standard Potentials in Aqueous Solution (IUPAC, 1979).

Structural and physicochemical studies of molybdenum oxo-peroxo and oxo complexes

Anna Szymańska

Jerzy Haber Institute of Catalysis and Surface Chemistry Polish Academy of Sciences, Niezapominajek 8, 30-239 Kraków, Poland

Supervisor: Wiesław Łasocha

Molybdenum complexes were synthesized and thoroughly investigated. Presented compounds contain different types and amounts of active oxygen, thus they were found to be efficient catalysts in oxidation process of cyclooctane with molecular oxygen. Results of X-ray diffraction and thermal stability studies are presented in this paper.

Molybdenum compounds are well known and widely used materials in catalysis, electronics, medicine, industry, etc.[1,2] Polymolybdates are interesting group of compounds which exhibit structural and functional diversity. They are very popular in material engineering due to possibility of designing compounds with desired features. When combining organic substrates with inorganic anions such as molybdates, new hybrid organic — inorganic materials with properties characteristic for individual component as well as new ones acquired by combination of them are obtained.[3] Some oxo-molybdenum complexes show structural and functional similarity to oxotransferases, molybdoezymes which take part in oxygen atom transfer (OAT) processes.[4] Octamolybdates are the widest group of compounds among the polymolybdates. So far, eight isomers are known: α, β, γ, δ, ϵ, ζ, η and θ.[3,5] Our attention was drawn to gamma isomer, where the core of the structure is the $[Mo_8O_{26}]^{-4}$ anion and molybdenum atoms are surrounded by oxygen atoms. The 6 Mo atoms are in octahedral and 2 in square pyramidal coordination. Number and type of oxygen atoms are as follow: 14 O_t, 6 μ_2-O, 4 μ_3-O, 2 μ_4-O. According to the literature, the isomer γ is an intermediate between octamolybdates α and β.[3]

The subgroup of polymetallates are peroxocomplexes which contain variable amounts of active oxygen. Peroxo oxygen is highly reactive but also is the main cause of instability of peroxo compounds. What is more, the reactivity of peroxocomplexes can be controlled by a proper ligand selection.[6] Strong oxidizing properties of peroxocomplexes are used in the processes of oxidation of alcohols[7] and sulfur-based compounds,[2] epoxidation of alkenes and cycloalkenes,[8] in bleaching processes and photodynamic therapy as compounds with peroxo groups are source of singlet oxygen.

During my research new polymetallates were synthesized. Two γ-octamolybdates, one polymeric hybrid material and three oxodiperoxomolybdates are described below. The compounds were characterized with the use of following techniques: single crystal X-ray diffraction, X-ray powder diffraction, DSC/TG, SEM, IR spectroscopy. In Table 1 basic crystallographic data of investigated compounds are summarized. The obtained results were the key to know the structure, thermal stability and morphology of the new complexes.

In my research two new γ-type octamolybdates of pyridine derivatives were synthesized. The compound {1} is an octamolybdate of 4-methylpyridine with formula: $\{[Mo_8O_{26}\cdot 2(C_6H_7N)]\cdot 4(C_6H_7NH)\cdot H_2O\}$ and compound {2} of 3,4-dimethylpyridine with formula: $\{[Mo_8O_{26}\cdot 2(C_7H_9N)]\cdot 3(C_7H_9NH)\cdot NH_4\cdot 2H_2O\}$. As it can be seen in Fig. 1 (only the molybdate anions are presented), in both compounds the nitrogen atom from pyridine ring is directly connected to Mo atom

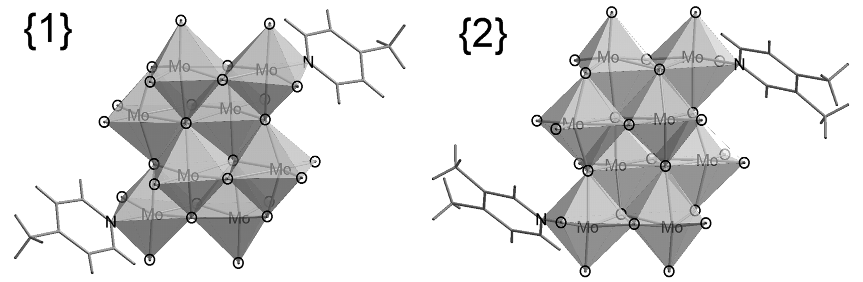

FIGURE 1: Octamolybdate anions of compounds {1} and {2}.

from the anion. Octamolybdates are stable until 100°C, then degradation occurs. During thermal decomposition of compound {1} the gamma isomer was converted into beta isomer, which agrees with published reports mentioned above. The final product of thermal decomposition is molybdenum trioxide with melting point around 795°C observed in TG/DSC curves.

A new polymeric organic-inorganic material was obtained from molybdic acid and 1,2-phenylenediamine with formula $[MoO_3 \cdot C_6H_4(NH_2)_2]_n$. The Mo atom is in octahedral coordination surrounded by four oxygen and two nitrogen atoms. The infinite chain is built of MoO_4N_2 octahedra linked to each other by O atoms. To each Mo atom a molecule of amine at an angle of 102°C (to chain axis) is attached through two Mo−N bonds (Fig. 3). XRD vs. temperature studies indicate that compound {3} is stable until 225°C, then amorphous phase occurs followed by crystallization of MoO_2 and MoO_3. Results from TG/DSC studies confirm conclusions from XRPD vs. temperature described above. Morphology of the compound {3} before and af-

TABLE 1: Crystal data for all presented compounds.

	{1}	{2}	{3}
Crystal system	Monoclinic	Triclinic	Orthorombic
SG	$C2/c$ (15)	$P-1$ (2)	$Pnma$ (62)
Cell parameters [Å, °]	a = 27,086(4) b = 11,917(2) c = 19,332(2) β = 124,42(1)	a = 10,786(3) b = 13,772(4) c = 18,358(5) α = 81,69(2) β = 83,27(2) γ = 87,35(2)	a = 19,429(6) b = 10,109(3) c = 3,8332(10)
Volume [Å^3]	5147,09(1)	2678,54(1)	752,86(5)
Weight [g/mol]	1764,32	1776,38	252,02
Z	4	2	4

	{4}	{5}	{6}
Crystal system	Triclinic	Monoclinic	Monoclinic
SG	$P-1$ (2)	$P2_1/c$ (14)	Pc (7)
Cell parameters [Å, °]	a = 6,687(4) b = 6,965(4) c = 12,012(7) α = 76,42(4) β = 77,43(4) γ = 69,48(4)	a = 7,504(2) b = 28,473(7) c = 7,777(2) β = 111,43(1)	a = 5,416(3) b = 5,350(2) c = 16,976(7) β = 106,23(3)
Volume [Å^3]	503,66(5)	1546,82(7)	472,29(4)
Weight [g/mol]	664,16	912,35	317,06
Z	1	2	2

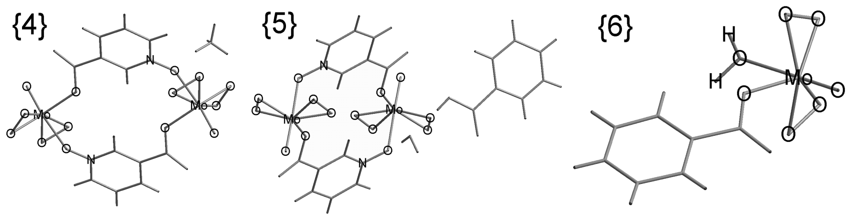

Figure 2: Compounds {4}, {5}, {6}.

ter annealing in 400°C was investigated. SEM images show layered structure of the sample before and plates with thickness of 0,25 μm after calcination.

Three oxodiperoxocomplexes of molybdenum with nicotinic acid were obtained. Their structures are presented in Fig. 2. Compound {4} and {5} consist of cyclic dimeric centrosymmetric anions. In the case of {4} negative charge of anion is compensated by ammonium cations, in {5} by protonated nicotinic acid. What is more, in both compounds characteristic N-oxide block is formed by oxidation of nicotinic acid to nicotinic acid N-oxide. General formulas of compounds are: {4} $(NH_4)_2 \cdot 2[MoO(O_2)_2 \cdot OC_6H_4NO_2]$ and {5} $(C_6H_5NO_2)_2 \cdot [MoO(O_2)_2 \cdot OC_6H_4NO_2]_2 \cdot 2(H_2O)$. As it can be noticed, the structures of {4} and {5} are similar to each other, while the {6} is quite different. Compound {6} is an inner salt, where negative charge of oxodiperoxomolybdate fragment is compensated by protonated nicotinic acid fragment: $[MoO(O_2)_2(H_2O)C_6H_5NO_2]$. Although, all mentioned oxodiperoxocomplexes contain the same organic ligand, the methods of syntheses caused differences in their structures. The time of synthesis plays a crucial role, the formation of {4} and {5} takes at least 24 hours, whilst the compound {6} is obtained after 1 hour. Another interesting fact is that during synthesis of compounds {4} and {5} an intermediate product was detected and it turned out to be the compound {6}. Yellow needle or plate shaped crystals were obtained and investigated with the use of single crystal X-ray diffraction method. Phase purity was tested with the use of X-ray powder diffraction technique. The spectra obtained with the use of FTIR spectroscopy verified presence of $[Mo{=}O]$, $[Mo{-}(O)_2]$ and $[O{-}O]$ groups. All the synthesized complexes are stable in the room temperature. During thermal decomposition they undergo degradation after 100 – 125°C, next amorphous phase is observed and above 300°C recrystallization of MoO_3 occurs. In the case of compound {5} phase of MoO_2 is observed between 200 – 250°C, which next is oxidized to molybdenum trioxide. The TG/DSC studies agrees with the results of XRPD vs. temperature. The final product of degradation processes is molybdenum trioxide with melting point around 795°C, for compound {5} endothermic peak corresponding to the melting of MoO_3 was shifted towards higher temperatures due to presence of MoO_2 in the heated sample (melting point 1100°C). The morphology of the samples after annealing in 600°C was also examined, rounded rectangular plates of MoO_3 with thickness of 0,15 – 0,25 μm were observed.

{3}

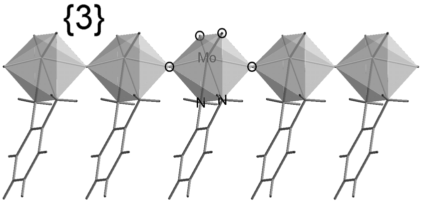

Figure 3: Compound {3}.

Tests for catalytic activity of presented compounds were performed. In oxidation reaction of cyclooctane (Fig. 4) investigated compounds show various ability to converse cyclooctane to cyclooctanone and cyclooctanol. It is very possible that these compounds will be also active in oxidation of other alkanes, therefore will find application in reaction used in industry. For example, through oxidation of cyclohexane with H_2O_2 adipic acid is produced.[9] Also a lot of molybdenum compounds together with hydrogen

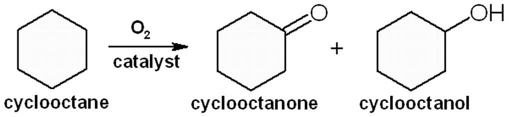

FIGURE 4: Cyclooctane oxidation.

peroxide are known and used in the design and syntheses of catalysts for „cleaner industrial processes".[10] The reaction was carried out in a batch type reactor with temperature $T = 120°\mathrm{C}$ and pressure $p = 10$ atm. The oxidizing agent used in the reaction was molecular oxygen and the ratio of cycloalkane to oxygen was 6,5[a]. All but one of presented complexes were tested and showed the ability to catalyze reaction of cyclooctane oxidation. The highest total cyclooctane conversion (around 53%) occurred for peroxocomplexes {5} and {4}, the lowest for γ-octamolybdate (22%). Catalytic activity of investigated compounds was as follows: $\{5\} > \{4\} > \{3\} > \{6\} > \{1\}$. However, the best selectivity to cyclooctanone was observed for compound {3}. The exact reaction path is not known yet. Further tests must be undertaken.

For all newly synthesized compounds structural and physicochemical investigations were performed. The main properties of the complexes were described in this paper. As for practical use, it was shown that these polymetallates are active and enable high conversion of cyclooctane.

⋆ ⋆ ⋆

[1] W. Łasocha, M. Grzywa, M. Oszajca, *Z. Kristallogr. Suppl.* **30**, 387 (2009).
[2] M. Bagherzadeh, M. M. Haghdoost, M. Amini, P. G. Derakhshandeh, *Catal. Commun.* **23**, 14 (2012).
[3] D. G. Allis, R. S. Rarig, E. Burkholder, J. Zubieta, *J. Mol. Struct.* **688**, 11 (2004).
[4] G. Lyashenko, G. Saischek, M. E. Judmaier, M. Volpe, J. Baumgartner, F. Belaj, V. Jancik, R. Herbst-Irmer, N. C. Mösch-Zanetti, *Dalton T.* **5655** (2009).
[5] F. R. Sensato, Q. B. Cass, E. Longo, J. Zukerman-Schpector, R. Custodio, J. Andrés, M. Zaldini Hernandes, R. L. Longo, *Inorg. Chem.* **40**, 6022 (2001).
[6] O. Bortolini, S. Campestrini, F. Di Furia, G. Modena, G. Valle, *J. Org. Chem.* **52**, 5467 (1987).
[7] M. Abrantes, T. R. Amarante, M. M. Antunes, S. Gago, F. A. A. Paz, I. Margiolaki, A. E. Rodrigues, M. Pillinger, A. A.Valente, I. S. Goncalves, *Inorg Chem.* **49**, 6865 (2010).
[8] D. G. Allis, E. Burkholder, J. Zubieta, *Polyhedron* **23**, 1145 (2004).
[9] W. Zhu, H. Li, X. He, Q. Zhang, H. Shu, Y. Yan, *Catal. Com.* **551** (2008).
[10] W. R. Sanderson, *Pure Appl. Chem.* **72**, 1289 (2000).

---

[a] Catalytic tests were performed in the group of dr J. Połtowicz, lab. Homogeneous Catalysis in J. Haber Institute of Catalysis and Surface Chemistry PAS.

Tape-casting method for the preparation of the carbonate eutectic filled lithium aluminate electrolyte matrix used in the carbonate fuel cells

Maciej Tatko

Jerzy Haber Institute of Catalysis and Surface Chemistry Polish Academy of Sciences, Niezapominajek 8, 30-239 Kraków, Poland

Supervisor: Paweł Nowak

Matrices made of $LiAlO_2$ and containing eutectic lithium and potassium carbonate in the Li/K molar proportion 62/38 were prepared using the method of tape-casting. The stability over time, and during the warm-up and cool-down cycles of the matrices obtained by this method was investigated by electrochemical impedance spectroscopy.

The most important part of a fuel cell is the matrix. It has to fulfill three basic requirements. Firstly, it ought to be gas-tight, to assure that there is no mixing of gases between the anodic and cathodic compartments. Secondly, it must be a good ionic conductor. Finally it must not be electronically conductive. Only matrices satisfying these three conditions can be used in fuel cells.[1] Preparation of such a matrix is not an easy task.

Eutectic mixtures of alkali metal carbonates are usually used as electrolytes in carbonate fuel cells, because they show lower melting temperatures in comparison to monometallic carbonates. There are several methods for producing matrices containing carbonate eutectic. Currently, the most popular is the method consisting of mixing the $LiAlO_2$ powder with powdered carbonates and pressing them into the form of pellets.[2] Unfortunately, this method requires a high pressure press. In the other method one makes two carbonate films by tape-casting method.[3] $LiAlO_2$ matrix is saturated with carbonates by heating the matrix between such films at the temperature higher than the melting temperature of carbonates. That method gives better dispersion of carbonates, because $LiAlO_2$ matrix porosity can be measured and the amount of carbonates needed to saturate the matrix can be calculated. However, that method does not guarantee the even distribution of the eutectic in the matrix. Given all these problems we decided to use the tape-casting method in a slightly altered form. The method consists in preparing $LiAlO_2$ matrix containing carbonate eutectic in a single technological process. It provides a mechanically robust and chemically resistive matrix with well dispersed carbonates. The paper describes in details the preparation, and preliminary investigations of the conductivity of such prepared matrices.

The first stage of tape-casting method is a thorough mixing of $LiAlO_2$ powder and potassium lithium carbonate eutectic in a solvent in the presence of a dispersant. The mixture is than subjected to 24 h grinding before adding of the binder and the plasticizer. The mixture is again milled for 24 hours and then poured onto a PTFE foil, dried, separated from the foil and finally fired at 750°C. Scheme of the casting process of the matrix together with the electrolyte is shown in Fig. 1. Refining of the procedures required multiple tests with different proportions of the matrix material, electrolyte, binder, plasticizer and solvent. In the first trials the solution was not degassed before pouring the film. That caused the nonuniformity of prepared films. The air bubbles formed in the film weakened its structure and caused cracking of the films during the firing. Only thorough degassing of sample, which was performed in a desiccator, enabled preparation of more homogeneous samples. Another problem is the process of grind-

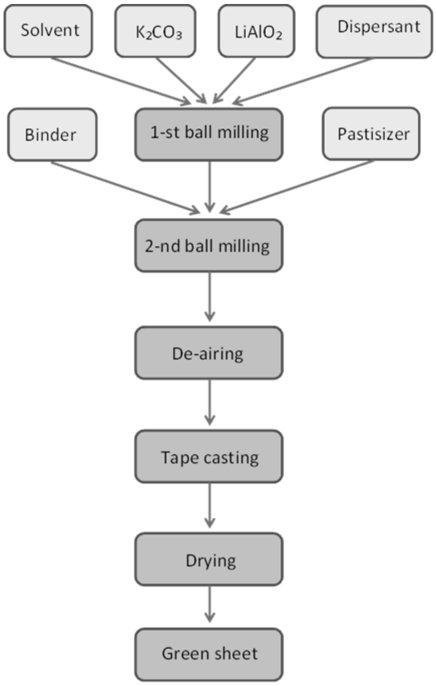

Figure 1: Scheme of the process of the preparation of the matrix with the electrolyte by tape-casting method.

ing. Choosing of the right grinding time is one of the most important factors affecting the quality of the film.

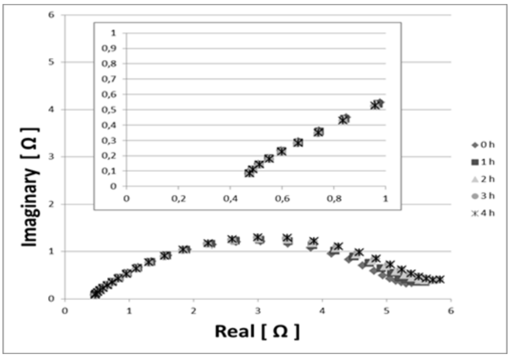

Figure 2: Changes of the impedance of matrix filled with electrolyte in time.

The carbonates present in the matrix may evaporate, changing the matrix conductivity, and the freezing and melting of carbonates present in the pores of the matrix can cause degradation of the cell structure. So, the films after firing underwent testing by impedance spectroscopy to check the stability of the ionic conductivity parameters at the temperature of work and during heating and cooling cycles. The measurements were conducted at 650°C in air. The tested films were placed between two silver plates, which constituted the anode and the cathode of our measuring system. As shown in Fig. 2 the resistance of the matrix, estimated as the intersection of the tangential to the high-frequency part of the impedance plot with the real axis did not change within a few hours. The full test took about 24 hours and after that time no changes in the resistance of the matrix were observed. The situation is somewhat different during subsequent annealing of the sample. As shown in the Fig. 3 the resistance of the sample diminishes between consecutive cycles. That phenomenon can be explained by the formation of microcracks in the matrix structure due to expansion of the carbonates during cooling/heating cycles. In the next cycle those microcracks are filled with molten carbonates and created a kind of micro-channels that increase the ionic conductivity. Despite the formation of microcracks in the internal structure of the matrix the leaking of the gas did not occur up to at least 10 cycles as observed in our experiments. It means that the matrix made of $LiAlO_2$ and carbonate electrolyte, produced by tape-casting method, is mechanically stable and no leakage of carbonates occurs.

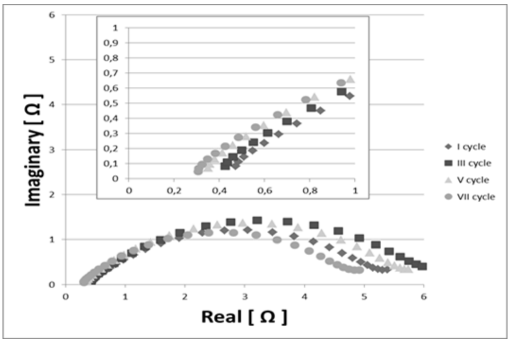

Figure 3: Changes of the impedance of matrix during subsequent subsequent heating-cooling cycles.

Currently, our investigations are focused on the use of SDC powder ($Sm_{0,2}Ce_{0,8}O_2$) to produce this type of matrices. The choice of this compound is dictated by the high ionic conductivity of SDC which would result in dual-electrolyte system. In such a system the charge is transported both by the O^{2-} ions derived from SDC as well as CO_3^{2-} ions derived from carbonates. In addition, studies are planned with the use of other carbonate eutectics (lithium sodium eutectic and potassium sodium lithium triple eutectic) to select a eutectic with the best ionic conductivity and stability.

In summary, among the various methods of obtaining carbonate filled electrolyte matrix tested up to now, the method of preparing a matrix with a eutectic carbonate in one process proved to be the best solution. That solution provides a very good dispersion of the eutectic in the matrix. At the same time the obtained matrix shows a relatively high resistance to cyclic warming and cooling and especially the stability of the resistance of the electrolyte over time. With prolonged annealing no changes in the impedance were observed which means that the carbonates did not evaporate from the matrix. After 10 cycles of warming and cooling no mechanical degradation nor gas leaking was observed.

⋆ ⋆ ⋆

[1] P. G. Glugla, V. J. DeCarlo, *J. Electrochem. Soc.* **129**, 1745 (1982).
[2] M. Farooque, *MRS Bull.* **30**, 602 (2008).
[3] A. Kulkarni, S. Giddey, *J. Solid State Electrochem.* **16**, 3123 (2012).

The use of X-Ray Fluorescence Analysis and X-Ray Absorption Spectroscopy in studies of glial brain tumours

Aleksandra Wandzilak

Faculty of Physics and Applied Computer Science, AGH University of Science and Technology, Mickiewicza 30, 30-059 Kraków, Poland

Supervisor: Marek Lankosz

Glial brain tumours are currently one of the least understood types of cancer. It is believed that transition metals play a particular role in both the formation of cancer and protection against carcinogenic agents. In this study, maps of the distribution of selected elements in specific areas of cancerous tissue have been drawn up. In addition, analysis of the XANES spectra enabled us to determine the average oxidation state of iron present in the brain tissues examined. This study showed that the ratio of Fe^{2+} *to* Fe^{3+} *content increases with the brain tumour malignancy grade. It has also demonstrated the advantage of using cryogenic conditions over other methods of sample preparation for the analysis of the oxidation states of elements present in the tissues.*

Cancer currently causes nearly as many deaths as cardiovascular diseases.[1] Tumours of the brain and central nervous system are among the ten most common types of cancer,[2] and are among the tumours with the smallest survival rate,[3] with most patients living for less than one year after diagnosis.[4]

Despite the significant progress made in medicine in recent years, glial brain tumours are still considered one of the less known types of cancer. Information about the chemical changes occurring during carcinogenesis in some selected elements present in the tissue may well contribute to this knowledge. It is believed that carcinogenesis is stimulated by free radicals, whose formation is controlled by some transition elements. Their increased concentration causes modifications in DNA bases, enhances lipid peroxidation and causes a lot of other effects that disturb metabolism.[5] The most important transition element in terms of carcinogenesis is iron, because it controls the formation of the most reactive free radicals via the Fenton reaction.[6]

$$\mathrm{Fe(II)}+\mathrm{H_2O_2}\rightarrow\mathrm{Fe(III)}+{}^{\bullet}\mathrm{OH}+\mathrm{OH}^{-}. \qquad (1)$$

It is therefore important that iron atoms be protected from oxygen molecules so as to prevent them from catalyzing redox reactions. This protection is carried out by binding iron in chelates, such as hemoglobin.[7] For this reason, it is important to attempt to determine the oxidation states of iron in tumour tissues and the chemical environment of iron atoms. Copper also has toxic properties because, like iron, it takes part in the Fenton reaction, causing the formation of free radicals. On the other hand, copper is a component of many enzymes that scavenge free radicals. The most important among them is superoxide dismutase CuZn (CuZnSOD) because it binds as much as 25% of the copper contained in the human brain.[8] CuZnSOD provides protection against the superoxide radical ($O_2^{\bullet-}$) by catalysing this reaction:

$$\mathrm{O_2^{\bullet-}}+\mathrm{O_2^{\bullet-}}+2\mathrm{H^+}\rightarrow\mathrm{H_2O_2}+\mathrm{O_2}. \qquad (2)$$

This enzyme is necessary for the survival of all cells that metabolize oxygen, so it must not be damaged.[9] Also, an increased copper to zinc ratio was observed in tumour tissues in relation to non-tumour ones.[10]

In order to study tissues of glial brain tumours, we chose X-Ray Fluorescence (XRF) to determine the concentrations of chemical elements, and the XANES method to determine the mean oxidation state of some selected elements present in the tissue.

The samples were collected intraoperatively during the resection of a brain tumour. Samples were cut from the material for three purposes: histopathological analysis, to map the distribution of chemical elements, and for the bulk analysis of the mean oxidation state. Samples of the first type were cryosectioned to a thickness of 5 μm and stained with hematoxylin-eosin and then subjected to histological examination to identify the type and malignancy grade of the tumour. An adjacent piece of tissue was cut to a thickness of 20 μm and then placed on X-ray-transparent Ultralene foil, stretched on a polymer disc. Next the sample was dried at a sub-zero temperature. The samples for the bulk analysis were trimmed to a volume of about 1 cm^3 and placed in polymer containers covered with Ultralene foil on the side exposed to X-rays. The samples were immediately frozen at -80°C and stored at this temperature to minimize biochemical processes such as oxidation.

Among the samples analyzed, there were tumours with different degrees of malignancy, according to the latest World Health Organisation (WHO) classification. Among the samples examined were such cancers as glioblastoma multiforme (WHO IV), anaplasticum astrocytoma (WHO III), oligodendroglioma anaplasticum (WHO III) and meningioma atypicum (WHO II). As a non-cancerous control sample, brain abscess wall was used. The samples were taken from the Institute of Neurology, Medical College, Jagiellonian University in Cracow. The study was approved by the Jagiellonian University Bioethics Committee (KBET/101/B/2012). FeO and Fe_2O_3 were used as the reference materials of iron in different oxidation states.

The XANES study was carried out at beamline C of DORIS III synchrotron in the HASYLAB at DESY in Hamburg. The samples were measured in a vacuum at the temperature of liquid nitrogen. In the measurements, the fluorescent mode was used and the energy of the incident radiation ranged from 7,05 keV to 7,70 keV. XRF studies were carried out at beamline I18 at Diamond Light Source. Distribution maps of chemical elements were collected from rectangular sections of the tissue with side lengths of up to several hundred microns. The beam size was 2 μm × 5 μm. The sampling time at a single point was 1 s. Spectra of iron and zinc present in the bulk samples were measured near the K edges of the elements. The spectra were normalized by the radiation intensities measured in the ionization chamber before the sample in order to compensate for the effects associated with changes in beam current excitation. The background was subtracted and the spectrum normalized by the average value of the absorption coefficient above the edge. The data were analyzed using the Athena program from the IFEFFIT package. An attempt to determine energies at which the absorption edges occur proved problematic with the first derivative method commonly used for this purpose. The difficulties arose from the overlapping of the absorption edges coming from different oxidation states of the same element. We therefore decided to use an integral method involving the determination of the centre of gravity of the absorption curve in the region of the absorption edge:

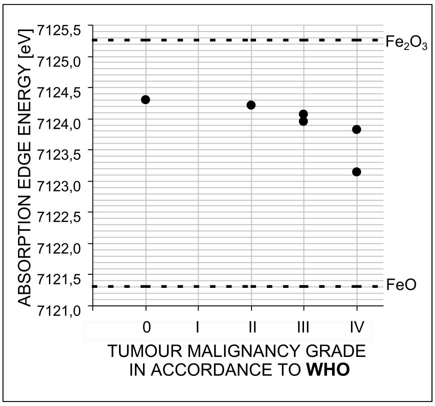

FIGURE 1: Absorption edge energies of Fe for various malignancy grades (according to World Health Organization scale) and adsorption edge energies for Fe^{2+} and Fe^{3+}.

$$E_0 = E(\mu_1) + \frac{1}{\mu_2 - \mu_1} \int_{E(\mu_1)}^{E(\mu_2)} [(\mu_2 - \mu(E)]\, dE, \quad (3)$$

where μ_1 and μ_2 are the absorption coefficients which were assumed to be the beginning and end of the absorption edge.[11]

The energies at which the absorption edges occur for iron in the analyzed samples of glial brain tumours are plotted in Fig. 1 as a function of the malignancy grade. In the chart it can be seen that the higher the malignancy grade of the tumour, the higher the ratio of the Fe^{2+} to Fe^{3+} content in the tissue. This relationship has been observed so far for a small number of samples due to the limited availability of tissues of glial brain tumours. These results offer hope, however, for differentiating between tumour grades based on the average oxidation state of the iron contained in the tissue.

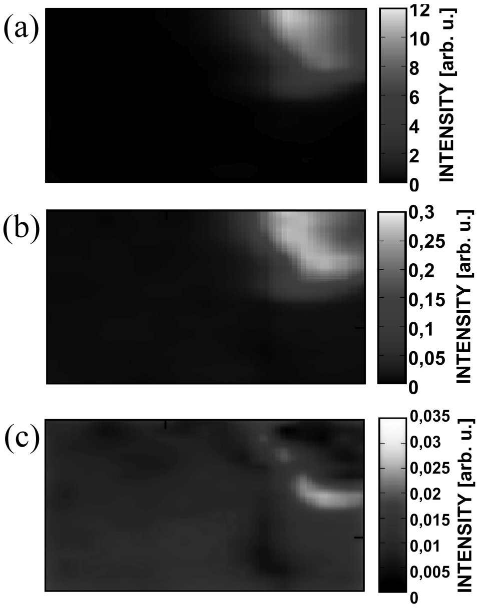

FIGURE 2: Concentration distribution maps of: (a) calcium, (b) zinc, and (c) copper in a scrap of slightly cancerous tissue including a calcifications area, sized 30 μm × 60 μm.

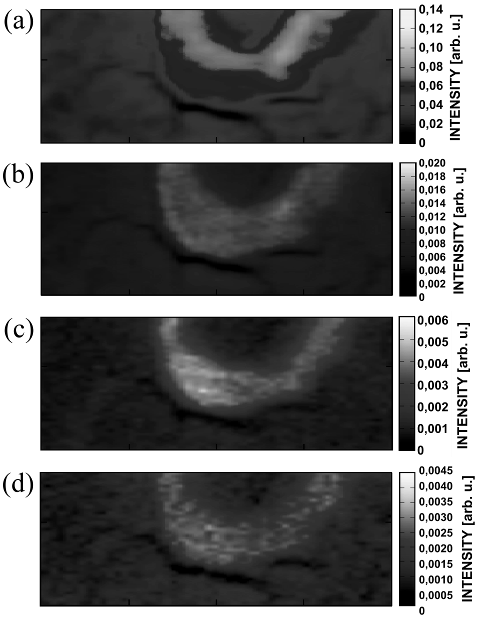

FIGURE 3: Concentration distribution maps of: (a) iron, (b) zinc, (c) bromine, and (d) rubidium in a scrap of tissue affected by anaplastic oligodendroglioma (WHO III), sized 200 μm × 80 μm including a blood vessel area.

For X-ray fluorescence analysis, areas of the tissue characteristic of the various malignancy grades were selected. These included a homogeneous area, a blood vessel and a calcification area. These areas were identified by comparing the X-ray-studied sample with the adjacent scraps of the tissue stained for histological examination. The results were analyzed using the QXAS program developed by the IAEA. Based on the calculated intensities of the fluorescence lines of selected the chemical elements, maps of their distribution were drawn. Fig. 2 shows distribution maps of calcium, zinc and copper present in the calcification of a tissue slightly affected by cancer. In addition to the higher calcium level in the calcification area, the zinc level was also elevated. Note also that the ratio of copper to zinc is higher in the cancerous tissue surrounding the calcification than in the calcification itself. Fig. 3 shows a map of the distribution of elements in the wall of a blood vessel located in the tissue of anaplastic oligodendroglioma — cancer of the third malignancy grade according to the WHO scale. Increased levels of iron, zinc, bromine, and rubidium in the wall of the blood vessel were observed, as was slight penetration of these elements into the tissue surrounding the vessel. Analysis of the XANES spectra measured for tumours with various malignancy grades showed that iron in these samples occurs almost entirely in the third oxidation state (Fig. 4). These

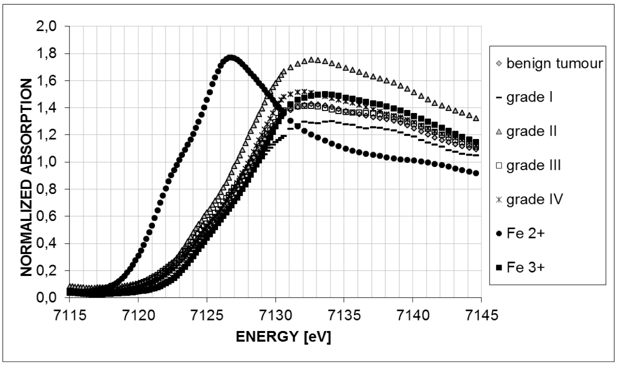

FIGURE 4: XANES spectra for Fe^{2+}, Fe^{3+} and brain glioma samples (grade I — meningeoma monstrocellulare et microcysticum WHO I, grade II — astrocytoma diffusum partim microcysticum WHO II, grade III — astrocytoma anaplasticum WHO III, grade IV — glioblastoma multiforme WHO IV).

results do not reflect the results obtained in bulk analysis, in which the average oxidation state of iron varied for various types of brain cancer. This may be caused by the differences in the preparation of samples, because the samples for bulk analysis were stored from the moment of collection at a temperature not higher than −80°C, whereas thin samples were stored at room temperature. These results show the importance of the cryogenic conditions we used for the measurements.

The results show that the analysis of the average oxidation state of iron present in the tissues of glial brain tumours may be useful for assessing the malignancy grade of glial brain tumours. This type of analysis could contribute information to complement histological analysis. The only requirement of the analyzed samples is that they be as similar as possible to their natural form, hence the need to freeze the samples immediately upon collection.

The research leading to these results has received funding from: the European Community's Seventh Framework Programme (FP7/2007-2013) under grant agreement No. 226716, Diamond Light Source Ltd, Didcot Oxfordshire, European Synchrotron Radiation Facility, Grenoble, France, HASYLAB, Hamburg, Germany and the Ministry of Science and Higher Education (Warsaw, Poland) grant No. N N518 377 537. I would also like to thank Mateusz Czyżycki for his assistance in the measurements and data preparation.

⋆ ⋆ ⋆

[1] P. Mladowsky, S. Allin, C. Masseria, C. Hernandez-Quevedo, D. McDaid, E. Mossialos, Health in the European Union. Trends and analysis, (World Health Organisation, 2009).

[2] http://www.cancerresearchuk.org, (available 04.12.2012).

[3] M. P. Coleman, D. M. Alexe, T. Albrecht, M. McKee, Responding to the challenge of cancer in Europe (Institute of Public Health of the Republic of Slovenia, 2008).

[4] http://www.oncologynews.biz/mayjune10.html (available 04.12.2012).

[5] S. P. Hussain, L. J. Hofseth, C. C. Harris, *Nat. Rev. Cancer* **3**, 276 (2003).

[6] S. Toyokuni, *Cancer Sci.* **100**, 9 (2009).

[7] M. Valko, H. Morris, M. T. D. Cronin, *Curr. Med. Chem.* **12**, 1161 (2005).

[8] H. R. Lieberman, R. B. Kanarek, C. Prasad, Nutritional Neuroscience, 1st edition (Taylor & Francis Inc., 2005).

[9] L. W. Oberley, G. R. Buettner, *Cancer Res* **39**, 1141 (1979).

[10] M. Diez, F. J. Cerdan, M. Arroyo, J. L. Balibrea, *Cancer* **63**, 726 (1989).

[11] H. Dau, P. Liebish, M. Haumann, *Anal. Bioanal. Chem.* **376**, 562 (2003).

THIN FILMS AND NANOSTRUCTURES

Deposition of zeolite nanoparticles onto silica monolith

Mariusz Gackowski

Jerzy Haber Institute of Catalysis and Surface Chemistry, Polish Academy of Sciences, Niezapominajek 8, 30-239 Kraków, Poland

Supervisor: Mirosław Derewiński

Highly porous silica monoliths can be used for deposition of different active phases/materials. They can form assemblies for variety of purposes, for example for separation, encapsulation of biomolecules[1] and for catalysis.[2] One of the active phases providing active centers for catalytic reactions are small zeolite particles. A shorter diffusion path, being the result of nanosize of the crystals, enables better accessibility to the Brønsted acid sites located in the network of zeolitic channels. The aim of this study was to determine how various parameters of the procedure of the deposition of the zeolite nanoparticles on the walls of meso-/macroporous silica monolith influences effectiveness of the process. In order to enhance the interaction between the monolith surface and zeolite nanoparticles the surface charge of the latter was reversed by polycation adsorption. The effect of: i) type of a polyelectrolyte used, and ii) duration of the deposition of nanoparticles was examined.

Silica monoliths and suspension of the MFI type zeolite nanocrystals (c.a. 100 nm in size) were used. Poly(ethyleneimine) (PEI) and poly(diallyldimethylammonium chloride) (PDADMAC) were applied to generate positive charges on the surface of zeolite nanoparticles prior to their deposition on the walls of monolith. Duration of the deposition varied from 1 h to 3 h.

Silica monoliths were synthesized by sol-gel method developed by Nakanishi.[3] 0,5 g of polyglycol ethylene (PGA) was added to HNO_3 (1 mole/dm^3). Then 4,5 ml of tetraethylortosilicate (TEOS) was added to obtain a clear solution. Subsequently, 0,2 g of cetyltrimethylammonium bromide (CTAB) was added under stirring conditions. After obtaining a clear solution, the mixture was poured into straws to form desired shape and dried at 400°C for 14 days. Synthesized monoliths were washed with distilled water and immersed in a NH_4OH solution (1 mole/dm^3) at 90°C for 9 h. After this treatment they were washed in distilled water and dried at 60°C. Finally, dry monoliths were calcined at 550°C for 5 hours in dry air.

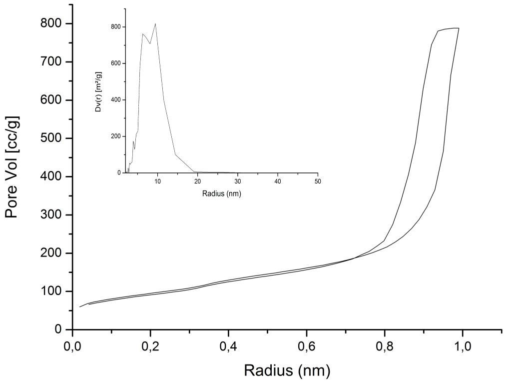

FIGURE 1: Adsorption/desorption isotherms of silica monolith.

The SEM analysis proved a sponge resembling structure of the monoliths with hierarchical pore size distribution. Specific surface area of the prepared monoliths as well as size and distribution of the mesopores were examined with N_2 sorption technique. Shape of adsorption/desorption isotherms and hysteresis loop (of H1 type) showed in Fig. 1 are characteristic for mesoporous structure.[4] The BET specific surface area of the monoliths was in the range 340 – 390 m^2/g. Pore size distribution analysis showed that mean diameter of mesopores is approx. 10 nm. Macropores presented in the SEM micrograph (Fig. 2)

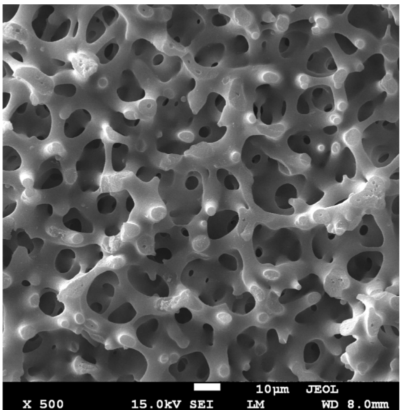

FIGURE 2: SEM image of silica monolith.

are of micrometers size. The deposition of nanocrystals occurred mainly on the wall of these macropores.

Zeolite nanocrystals were synthesized from solution of molar ratio:

$$103SiO_2 \ : \ 1\ Al_2O_3 \ : \ 1\ Na_2O \ : \\ : \ 272\ H_2O \ : \ 90\ (TPA)_2O \ .$$

The synthesis from the clear solutions in stirring conditions was carried out in an oil-bath at 85°C. After 44 hours of synthesis a monodispersed colloid gel was obtained with crystals' size of ca. 100 nm (Fig. 3). The suspension was centrifuged, washed with distilled water and alkalized with ammonium hydroxide solution (to pH = 10) to protect against aggregation of the nanocrystals in suspension. The X-ray diffraction pattern proved that obtained nanoclusters have the MFI structure (Fig. 4).

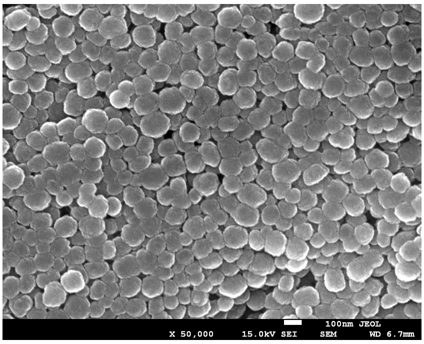

FIGURE 3: SEM image of MFI zeolite nanocrystals.

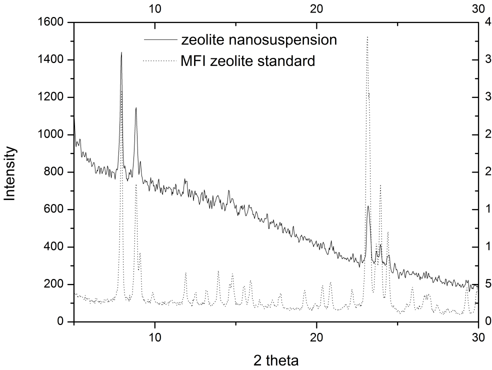

FIGURE 4: The diffraction pattern of MFI zeolite nanocrystals.

The surface of the silica monoliths and zeolite nanoclusters are usually negatively charged. In order to make their interaction possible, a charge-changing agent has to be used for the components i.e. for monoliths or nanoparticles. For this purpose, polyelectrolytes, i.e. polyethylene imine (PEI) and poly(diallyldimethylammonium chloride) (PDADMAC) were chosen to change surface charge of the zeolite nanoparticles.

First, the solution of PEI has been prepared (in concentration of 1000 ppm in water solution of 10^{-2} mol/dm^3 NaCl). Zeta potential of this solution was +26,2 mV, whereas zeta potential of zeolite nanocrystals suspension was −47,7 mV. In order to estimate the optimal proportion of the polyelectrolyte and nanocrystals, which protects the system against nanoparticles aggragation, an increas-

TABLE 1: Zeta potentials of the zeolite suspension-PEI polyelectrolyte.

zeolite suspension:PEI [cm^3:cm^3]	ζ [mV]
1,0 : 1,0	12,7
1,0 : 1,5	20,8
1,0 : 2,0	25,3
1,0 : 2,5	28,2
1,0 : 3,0	27,0
1,0 : 3,5	31,4
1,0 : 4,0	32,2
1,0 : 4,5	1,0

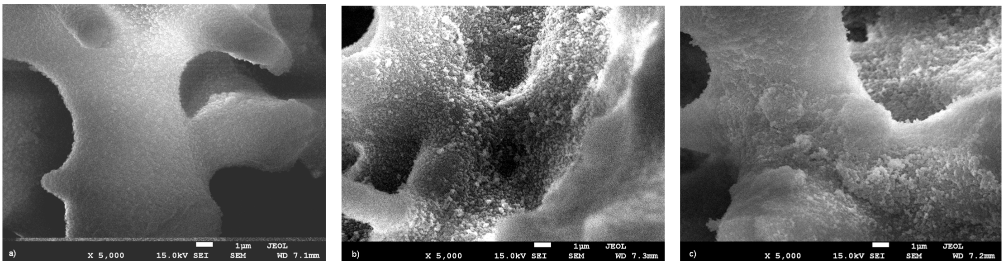

FIGURE 5: SEM images of nanoparticles deposited on the walls of monolith modified with PEI after: a) 1 h, b) 2 h, c) 3 h.

TABLE 2: Zeta potentials of the zeolite suspension-PDADMAC polyelectrolyte.

zeolite suspension:PDADMAC [cm^3:cm^3]	ζ [mV]
10 : 1	46,8
20 : 1	43,8
40 : 1	39,4
50 : 1	0,2

ing amount of the polyelectrolyte solution was added to the zeolite suspension. After each portion added, Zeta potential of the mixture was measured. Such titration was carried out till the aggregation has been observed and evidenced by a sharp decrease of the Zeta potential value (c.a. 0 mV). The optimal ratio of PEI solution to the zeolite suspension for which no aggregation occurred has been determined i.e. 1 ml PEI/16 ml zeolite suspension (Table 1).

In order to deposit nanoparticles the monolith was submerged into the mixture of this composition and placed in an ultrasound bath. Time of the deposition varied from 1 h to 3 h. After every hour sample was taken for analysis.

Samples were examined by scanning electron microscopy (SEM). The extent of coverage showed a strong dependence on the time of deposition. After 1 hour of deposition the surface was not completely covered whereas a monolayer of zeolite nanocrystals was observed after 2 hours. After 3 hours formation of a multilayer was observed (Fig. 5).

Similar deposition procedure has been performed using second polyelectrolyte i.e. PDADMAC solution (prepared in concentration as that one of PEI). The Zeta potential of polyelectrolyte solution was found to be +32,6 mV. Optimal proportion of zeolite suspension and polyelectrolyte solution has been determined in the same way as in the case of PEI. The optimal ratio found was: 0,1 ml PDADMAC/4,0 ml of the zeolite suspension (Table 2). Deposition was carried out as described for PEI, i.e. by submerging the monolith in the mixture of polyelectrolyte and zeolite (placed in an ultrasound bath). Results of SEM analysis of the samples after 1, 2, and 3 hours of the deposition are shown in Fig. 6.

The obtained results revealed that more PEI solution — in comparison to PDADMAC

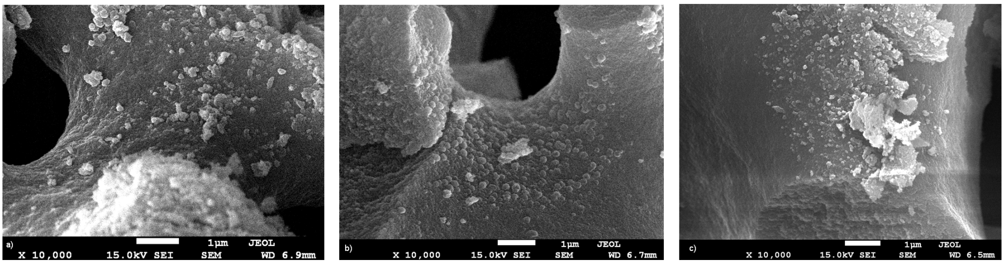

FIGURE 6: SEM images of nanoparticles deposited on the walls of monolith modified with PDADMAC after: a) 1 h, b) 2 h, c) 3 h.

— can be used for an effective nanoparticles deposition. This is mainly due to the fact that PDADMAC is a stronger polyelectrolyte. It does not mean, however, that it is more suitable for effective deposition of nanoparticles onto silica monoliths. As seen in the SEM micrographs the use of PEI polyelectrolyte leads to better coverage than that observed when PDADMAC has been applied.

The obtained data proved that use of the PEI — from the solution of high ionic strength — leads to better and more homogenous deposition of the nanoparticles on the walls of the monolith in comparison to PDADMAC. The increased duration of the deposition resulted in formation of multilayer of the nanocrystals.

⋆ ⋆ ⋆

[1] M. Kato, K. Sakai-Kato, T. Toyo'oka, *J. Separation Sci.* **28**, 1893 (2005).

[2] A. El Kadib, R. Chimenton, A. Sachse, F. Fajula, A. Galarneau, B. Coq, *Angew. Chem. Int. Ed.* **48**, 4969 (2009).

[3] K. Nakanishi, *J. Porous Mater.* **4**, 67 (1997).

[4] K. S. W. Sing, D. H. Everett, R. A. W. Haul, L. Moscou, R. A. Pierotti, J. Rouquerol, T. Siemieniewska, *Pure and Appl. Chem.* **57**, 603 (1986).

Investigation of Multi-Wall Carbon Nanotubes properties

Agnieszka Jamrozik

Faculty of Physics and Applied Computer Science, AGH University of Science and Technology, Mickiewicza 30, 30-059 Kraków, Poland

Supervisor: Květoslava Burda

Carbon nanotubes (CNTs), nanocylindrical forms of pure sp^2 *carbon, are one of the most exciting and interesting discoveries of this century. The objects of our study are MWCNTs containing iron, which was used as catalyst during their synthesis. The knowledge about the character of iron compounds present in CNTs is very important for their future potential technical applications. We investigated Fe-phases included in non-functionalized (as prepared) and functionalized (variously modified) MWCNTs using Mössbauer spectroscopy. This technique is a unique tool to study chemical properties of iron compounds embedded in MWCNTs. Additionally, we present the images of our samples, measured using Atomic Force Microscopy (AFM). This method allows to get high resolution topography of nano-objects. The Mössbauer results show that the chemical treatment of as prepared MWCNTs causes modification of iron compounds built into them. These iron states may create new physico-chemical properties of functionalized MWCNTs. Our AFM data confirms that functionalization leads to MWCNTs purification.*

Carbon nanotubes were discovered by Sumio Ijima in 1991 while analysing soot samples under an electron microscope. He found long strands with a diameter of several nanometers and several micrometers in length.[1–3] Carbon nanotubes can be imagined as a plane of graphene rolled into different kinds of cylinders. CNTs are classified into single-walled carbon nanotube (SWCNT), double-walled carbon nanotube (DWCNT), and multi-walled carbon nanotube (MWCNT) according to the rolling layers of graphene sheets. The unique carbon nanotube structures result in numerous superior physical and chemical properties.[3–5] Synthesis, even using the same method, leads to the production of a mixture of various types of carbon nanotubes exhibiting different features. For practical applications carbon nanotubes with uniform properties are sought. Researchers have developed some effective methods to functionalize CNT surfaces such as covalent modification or non-covalent approaches including polymer wrapping, biomolecule binding, and metal ion binding.[6] Additionally, functionalization of carbon nanotubes (CNTs) may improve their chemical and physical properties and make them more useful.

The objects of our study are MWCNTs containing iron, which was used as catalyst during their synthesis. Fe-MWCNTs promise to be a good candidate for instruments, such as sensors for magnetic scanning probe microscopy, for spintronic devices or highly density magnetic memory materials.[4,5] We studied three kinds of multi-walled carbon nanotubes: (i) as prepared, non-functionalized MWCNTs, (ii) carboxylated MWCNTs-COOH and (iii) the ammonium salt of carboxylated nanotubes MWCNTs-COONH$_4$. Non-functionalized MWCNTs (CTube100) were manufactured by CNT Co., Ltd, South Korea. MWCNTs-COOH were prepared by oxidation of MWCNTs in an aqueous solution of concentrated (68%) HNO$_3$ at 120°C for 50 h under reflux. After oxidation the nanotubes were washed with distilled water during filtration until the pH value of the filtrate approached 6. Subsequently, carboxylic-functionalized CNTs (MWCNTs-COOH) were treated with a 10%

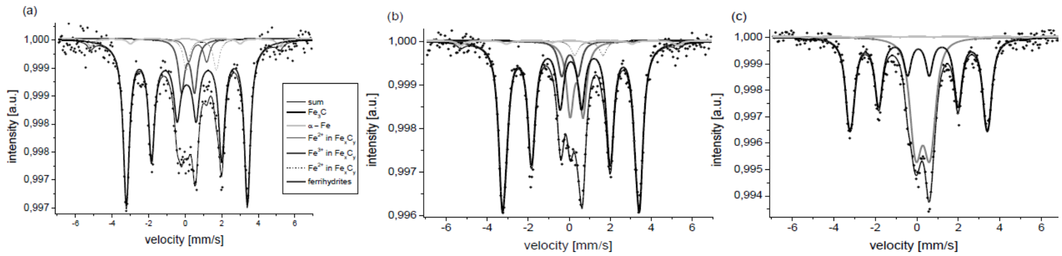

FIGURE 1: The Mössbauer spectra: (a) as prepared MWCNTs, (b) MWCNTs-COOH, (c) MWCNTs-COONH$_4$, measured at R.T.

ammonia solution and rinsed with distilled water during filtration to obtain their ammonium salt. We investigated our samples using Mössbauer spectroscopy and Atomic Force Microscope (AFM).

Mössbauer spectroscopy is a selective and highly sensitive method which is used to monitor the valence and spin states of the probing atom, in our case it is an isotope of ^{57}Fe with a natural abundance of 2,2%. Hyperfine parameters fitted to the Mössbauer spectra provide information on the chemical surrounding of iron and its local magnetic properties. We applied Mössbauer spectroscopy to study iron compounds formed in different types of MWCNTs. The Mössbauer spectra were recorded at 80 K, 220 K, and R.T. using a home made cryostat and ^{57}Co(Rh) as a source of 14,4 keV γ-radiation. An isomer shift is given in relation to the metallic iron. The spectra are fitted using Recoil software.[7] The Mössbauer spectra for as prepared MWCNTs, MWCNTs-COOH and MWCNTs-COONH$_4$ measured at R.T. are shown in Fig. 1. The fitted hyperfine parameters are collected in Table 1. The Mössbauer spectra and hyperfine parameters obtained at 85 K and 220 K are precisely reported in our previous work.[8]

TABLE 1: Hyperfine parameters fitted to the Mössbauer spectra measured at R.T. (IS — isomer shift related to the metallic Fe, QS — quadrupole splitting, H — hyperfine magnetic field, ΔQ — quadrupole splitting distribution, ΔH — magnetic field distribution, A — relative contribution, Γ — line width).

Types of MWCNTs	Component	R.T. IS [mm s^{-1}]	 QS [mm s^{-1}]	 H [T]	 A [%]
	Fe_3C	0,08±0,01	0,007±0,009	18,69±0,01	77,6±3,7
as prepared				ΔH=3,89	
MWCNTs	α-Fe	0	0	32,09±1,26	2,9±2,4
	Fe^{3+} in Fe_xC_y	0,15±0,04	0,71±0,07	-	9,5±2,7
Γ=0,19±0,01	Fe^{2+} in Fe_xC_y	0,68±0,09	0,98±0,05	-	4,2±0,4
	Fe^{2+} in Fe_xC_y	0,88±0,05	1,65±0,12	-	5,7±1,7
	Fe_3C	0,08±0,01	0,001±0,007	20,50±0,33	74,4±2,6
MWCNTs-				ΔH=0,73	
COOH	α-Fe	0	0	32,78±1,46	2,0±1,9
	Fe^{3+} in Fe_xC_y	0,03±0,05	0,79±0,09	-	6,7±1,5
Γ=0,19±0,01	Comp 1$^{(1)}$	0,36±0,03	0,63±0,04	-	14,0±1,6
	Fe^{2+} in Fe_xC_y	0,96±0,10	1,39±0,20	-	2,9±1,4
	Fe_3C	0,08±0,01	0,008±0,010	20,53±0,03	50,0±6,1
MWCNTs-				ΔH=0,11	
COONH$_4$	α-Fe	0	0	33,24±1,24	2,8±0,4
	Comp 1$^{(1)}$	0,28±0,01	0,69±0,02	-	47,2±0,6
Γ=0,19±0,01			ΔQ=0,37		

(1) These hyperfine parameters are characteristic of Fe in Fe_xC_y with O in the second coordination sphere of iron as well as of ferrihydrite Fe_2O_3, for example, $5\,Fe_2O_3 \cdot 9\,H_2O$.[11–13]

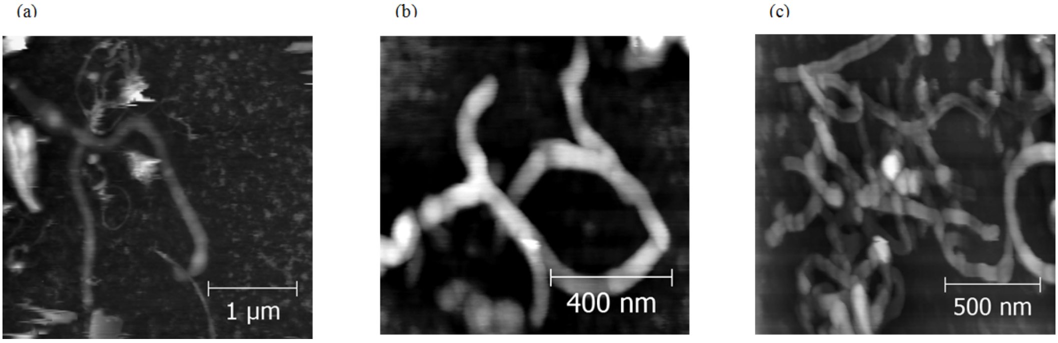

FIGURE 2: AFM topography images of MWCNTs, placed on a glass substrate: (a) as prepared MWCNTs — scan size: 3,5 μm × 3,5 μm, (b) MWCNTs-COOH — scan size: 1 μm × 1 μm, (c) MWCNTs-COONH$_4$ — scan size: 1,6 μm × 1,6 μm.

In the non-functionalized MWCNT cementite, Fe$_3$C predominates with a small amount of α-Fe and Fe$_x$C$_y$ complexes.[9] Fe$_3$C and α-Fe particles have sufficient size to result in observable magnetic ordering even at room temperature. The hyperfine parameters of iron in the Fe$_x$C$_y$ complexes suggest that there is a wide distribution of Fe$_x$C$_y$ aggregates which vary in the number of C atoms in the Fe surrounding as well as in the symmetry of their arrangement. The charge distribution and the stabilized magnetic moment on Fe atoms is modulated depending on the amount of carbons in the iron neighborhood.[10] We observe one low spin ferric state and two different high spin ferrous states in Fe$_x$C$_y$ (Table 1) in the as prepared MWCNTs. We do not observe significant changes in the hyperfine parameters at lower temperatures. The small decrease in isomer shift values with increasing temperature is related to a second order Doppler effect. The chemical treatments modify the Fe phases in the remaining iron grains. None of the functionalization methods influences the relative fraction (percentage) of α-Fe in built-in iron complexes in the nanotubes. However, the relative content of Fe$_3$C in the Mössbauer spectra of oxidized MWCNTs decreases (by about 10%) and simultaneously superparamagnetic particles of ferrihydrates ($x \cdot$ Fe$_2$O$_3$ $y \cdot$ H$_2$O) and Fe$_x$C$_y$ with Fe-C-O coordinations appear.[11–13] Further treatment of MWCNTs-COOH with ammonia water causes a decrease in Fe$_3$C contribution in the Mössbauer spectra by a factor of 2 in comparison with as prepared MWCNTs. At the same time the relative content of superparamagnetic ferrihydrates and Fe$_x$C$_y$O$_z$ in MWCNTs-COONH$_4$ increases twofold in comparison with MWCNTs-COOH (both samples contain the same amount of Fe in the studied material). In both functionalized samples the hyperfine parameters of Fe$_x$C$_y$ complexes change due to modifications of the type and arrangement of ligands. In contrast with other works in our samples we did not detect γ-Fe.[14–18]

The AFM technique captures precise images by moving a nanometer sized tip across the investigated surface. In our investigations we used the Agilent 5500 AFM working in a contact mode. All measurements were done in ambient environment at room temperature. MWCNTs suspended in distilled water were sonicated for 20 minutes, at 25°C in order to minimize a number of nonstable nanostructured aggregates, such as C–C complexes, graphite planes and amorphous carbon. Then, the suspensions were dropped on a glass surface. The main goal of our AFM study was to observe the arrangement of various types of MWCNTs. Differences between the as prepared and functionalized MWCNTs are visible (Fig. 2).

Most of as prepared MWCNTs are predominantly longer and have a greater distribution of diameters than functionalized nanotubes. Non-functionalized MWCNTs form clusters of about several micrometers in size because of a high content of magnetic Fe_3C. The amount of iron complexes decreases two-fold during the functionalization process, and that why the surface of functionalized MWCNTs is plane in comparison to that one of non-functionalized nanotubes.

In conclusion, our studies show that that the traces of Fe catalyst can be easily deposited inside the MWCNTs material during their synthesis, and the Fe aggregates can be removed by the oxidation process. Further functionalization of MWCNTs-COOH does not remove more iron impurities but only changes the iron states. The main component in *as prepared* MWCNTs is Fe_3C (cementite) and it is transformed into ferrihydrites during the oxidation process. Additionally, the hyperfine parameters of Fe_xC_y components are modified due to the functionalization. The relative content of α-Fe remains unchanged. Differences between the as prepared and functionalized MWCNTs are also visible on AFM images: MWCNTs after purification do not form clusters, are predominantly shorter and have a smaller distribution of diameters.

⋆ ⋆ ⋆

[1] S. Iijima, *Nature* **354**, 56 (1991).

[2] M. Daenen, R. D. de Fouw, B. Hamers, P. G. A. Janssen, K. Schouteden, M. A. J. Veld, The wondrous world of carbon nanotubes — A review of current carbon nanotube technologies (Eindhoven University of Technology, Eindhoven, The Netherlands, 2003).

[3] P. J. F. Harris, Carbon nanotubes: synthesis, properties and applications (Science Cambridge University Press, 2009).

[4] R. H. Baughman, A. A. Zakhidov, W. A. Heer, *Science* **297**, 787 (2002).

[5] C. Pham-Huu, N. Keller, V. V. Roddatis, G. Mestl, R. Schloegl, M. J. Ledoux, *Phys. Chem. Chem. Phys.* **4**, 514 (2002).

[6] E. Borowiak-Palen, E. Mendoza, A. Bachmatiuk, M. H. Rummeli, T. Gemming, J. Nogues, V. Skumryev, R. J. Kalenczuk, T. Pichler, S. R. P. Silva, *Chem. Phys. Lett.* **421**, 129 (2006).

[7] D. G. Rancourt, J. Y. Ping, *Nucl. Instrum. Methods B* **58**, 85 (1991).

[8] A. Jamrozik, M. Mazurkiewicz, A. Małolepszy, L. Stobiński, K. Matlak, J. Korecki, K. J. Kurzydłowski, and K. Burda, *Phys. Status Solidi A* **208**, 1783 (2011).

[9] J. Jorge, E. Flahaut, F. Gonzalez-Jimenez, G. Gonzalez, J. Gonzalez, E. Belandria, J. M. Broto, B. Raquet, *Chem. Phys. Lett.* **457**, 347 (2008).

[10] M. Perez-Cabero, J. B. Taboada, A. Guerrero-Ruiz, A. R. Overweg, I. Rodriguez-Ramos, *Phys. Chem. Chem. Phys.* **14**, 1230 (2006).

[11] V. J. Goldanskii, R. H. Herbert, Chemical applications of Mössbauer spectroscopy (Academic Press, NewYork, 1968).

[12] E. Murad, L. H. Bowen, G. J. Long, and G. Quin, *Clay Miner.* **23**, 161 (1988).

[13] J. L. Jamber, J. E. Dutrizac, *Chem. Rev.* **98**, 2549 (1998).

[14] T. Ruskov, I. Spirov, M. Ritschel, C. Müller, A. Leonhardt, *J. Appl. Phys.* **100**, 084326 (2006).

[15] L. Qun-qing, F. Shou-shan, H. Wei-qiang, G. Nai-fei, W. Xin-rong, *Chin. Phys. Lett.* **1**, 68 (1998).

[16] P. Coquay, E. De Grave, R. E. Vanderberghe, C. Dauwe, E. Flahaut, Ch. Laurent, A. Peigney, A. Rousset, *Acta Mater.* **48**, 3015 (2000).

[17] A. B. Gonzalez-Guerrero, E. Mendoza, E. Pellicer, F. Alsina, C. Fernandez-Sanchez, L. M. Lechuga, *Chem. Phys. Lett.* **462**, 256 (2008).

[18] V. G. de Resende, A. Peigney, E. de Grave, Ch. Laurent, *Termochim. Acta* **494**, 86 (2009).

Optimization of growth parameters of CVD diamond for thermoluminescence

Agnieszka Karczmarska

The Henryk Niewodniczański Institute of Nuclear Physics Polish Academy of Sciences, Radzikowskiego 152, 31-342 Kraków, Poland

Supervisor: Marta Wolny-Marszałek

Diamond is believed to be an attractive material for thermoluminescence (TL) dosimetry applications. Growth conditions strongly affect morphology and structure of polycrystalline diamond and its thermoluminescent properties. In this work effects of the deposition parameters on grain size and quality of CVD diamond were investigated.

Diamonds are well known for their extraordinary physical and chemical properties which explain their ever-increasing interest in extreme applications. [1,2] Diamonds have their place in medicine, industry, dosimetry. [3,4] Remarkable properties such as human soft tissue equivalence, non-toxicity and a wide gap energy (5,5 eV), make diamond suitable for medical application as thermoluminescent dosimeter (TLD). [5,6]

The great potential generates high demand, but diamonds are a scarce natural resource, and therefore the production and study of synthetic diamonds are carried out for many years. CVD — Chemical Vapour Deposition — is one of the more promising methods of producing diamonds. CVD is a process where diamond is deposited under the influence of chemical reactions happening at the substrate surface. For reactions to take place, gases are first excited — e.g. by microwaves — to the plasma state. Gases that are most commonly used are hydrogen, methane and oxygen. Microwaves ionize gases, and created electrons collide with gas particles causing them to dissociate, produce reactive chemical radicals and start a series of chemical reactions. Gas mixture and pressure within CVD chamber, substrate temperature and substrate preparation are all very important factors for the resultant diamond quality. It is thus of great importance to optimize these parameters for the application. We worked on optimizing CVD process parameters for diamonds to be used in thermoluminescence. Among methods used to study the structure, chemical properties and surface morphology of prepared samples were X-ray diffraction, Raman spectroscopy, Scanning Electron Microscopy (SEM) and Atomic Force Microscopy (AFM). Results were correlated with deposition parameters and thermoluminescence properties of produced diamonds. TL properties were examined by standard laboratory reader and 2D TL reader. Measurements were then used to determine linearity range, reproducibility and decay of registered thermoluminescence signal. In this work some of these results were presented.

Presence of other allotropic forms of carbon such as amorphous carbon and graphite in diamond coating reduce TL signal. [7] Fig. 1 shows Raman spectra of two samples pre-

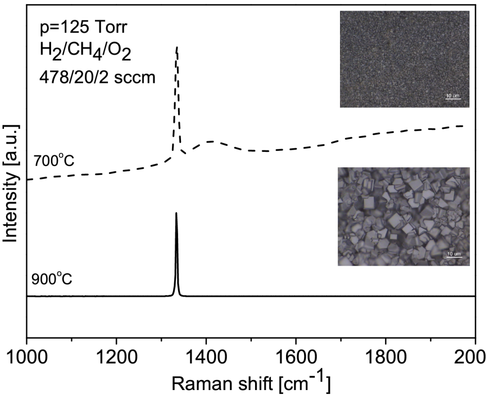

FIGURE 1: Raman spectra of polycrystalline diamond films prepared at 700°C and 900°C. The inset shows the corresponding optical images.

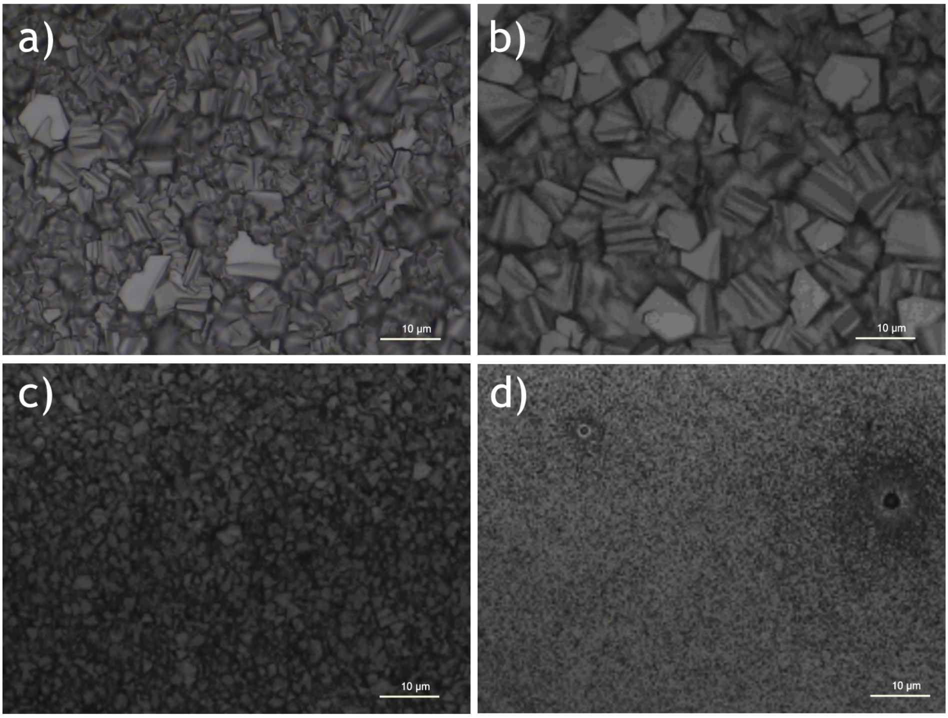

FIGURE 2: Optical micrographs of diamond prepared with oxygen concentrations of: a) 0%, b) 0,4%, c) 1%, d) 2%.

pared at temperatures of 700°C and 900°C. The other parameters of deposition process were identical and are shown in Fig. 1. Spectrum of the sample fabricated at 700°C contains broad peak centered on 1420 cm^{-1}, next to narrow 1332 cm^{-1} diamond line. This peak was fitted with two Voigt distributions at 1380 cm^{-1} and 1460 cm^{-1}. The 1380 cm^{-1} line is often referred to as D peak of disordered graphite, and its intensity characterizes the contribution of this carbon form. During CVD deposition atomic hydrogen plays important role, its degree of dissociation is a function of temperature. Lower temperature decreases the dissociation of H which causes sp^2 bonds to be etched faster than sp^3. This, in turn, affects not only grain size but also grain boundary volume. The line of 1460 cm^{-1} may be attributed to trans-polyacetylene, which frequently appears in grain boundaries.

TL signal intensity increases together with the grain size of tested material.[8] Gomez-Aleixandre et al. showed that 2% oxygen contribution to the CH_4/H_2 mixture causes increase of deposition rate.[9] Gracio et al. presented improved layers quality as a result of introduction of small amount of oxygen to plasma containing CH radicals.[10] The presence of oxygen will also positively affect purity of diamond phase due to increase of grain size, but also by etching of non-diamond carbon forms.[10] Fig. 2 shows diamond layers deposited with different oxygen concentrations imaged with optical microscope. Common deposition parameters were: methane concentration — 4%, microwave power — 4,9 kW, reactive gases pressure — 120 Torr. Grain shapes of layers produced with no oxygen are random and do not contain distinct boundaries (Fig. 2a). Fig. 2b shows large {111} faceted grains in polycrystalline layer obtained for 0,4% oxygen concentration. A further increase of oxygen contents (1%) shows clear reduction of grain size (Fig. 2c). When oxygen amounts to 2% of reactive gases

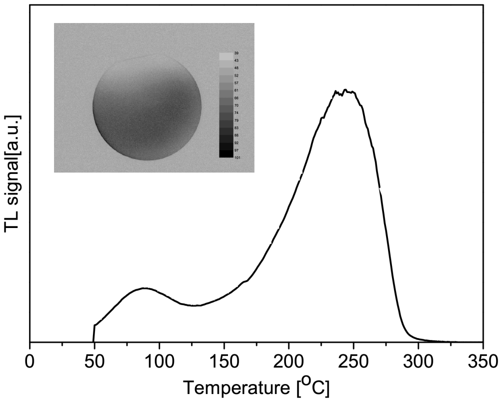

FIGURE 3: Thermoluminescence (TL) glow curve of CVD diamond films exposed to 40 Gy gamma irradiation dose. The inset shows the corresponding thermoluminescence signal of this sample.

volume deposition is stopped and a dominant process becomes silicon substrate etching (Fig. 2d).

Thermoluminescence phenomenon is the best described by band theory of solids. Structure imperfections, resulting from wrong localization or lack of basic ions or presence of additional ions in lattice sites, are of crucial importance to TL processes.[11] These defects form separated centers which are potential traps for electrons and holes. The presence of these defects in the band gap area results in electron traps close to conduction band and hole traps close to valence band. Thermoluminescence phenomenon may be divided into two stages. The first one comes with the irradiation of TL material by ionizing radiation or by light. The electron-hole pairs are created. Some number of electrons is catched by electron traps. This number is proportional to absorbed energy of used dose. In the second stage trapped electrons are heated and recombine with hole traps. Light is emitted and the system returns to its ground state. Registration of emitted light with temperature increase gives a dependence called TL curve.

Typical TL curve of diamond sample irradiated with a dose of 40 Gy obtained with laboratory reader is shown in Fig. 3. Two peaks at temperatures of 85°C and 240°C are easily visible on the TL curve. High-temperature peak is a result of diamond thermoluminescence caused by ionizing radiation and gives information about applied dose. A 2D map of dose distribution of this sample is shown in the inset of Fig. 3. It shows heterogeneity of TL signal due to the not uniform grain sizes on the whole sample surface.[12] On the other hand a reason for signal attenuation may be appearance of graphite phase.

This work presents the influence of deposition parameters (substrate temperature and oxygen concentration) on the structure and morphology — and thus TL properties — of prepared diamond coatings. TL signal registered at 240°C gives information about applied radiation dose. Relationship between TL signal and grain size within diamond layers was shown. TL signal linearity for a broad spectrum of ionizing radiation doses makes diamond a very promising material for thermoluminescence dosimetry.

⋆ ⋆ ⋆

[1] J. J. Gracio, Q. H. Fan, J. C. Madaleno, *J. Phys. D: Appl. Phys.* **43**, 374017 (2010).

[2] P. W. May, *Phil. Trans. R. Soc. Lond. A* **358**, 473 (2000).

[3] M. Vandrovcovà, L. Bačàkovà, *Physiol. Res.* **60**, 403 (2011).

[4] C. Popov, W. Kulisch, M. Jelinek, A. Bock, J. Strnad, *Thin Solid Films* **494**, 92 (2006).

[5] C. Descamps, D. Tromson, M. J. Guerrero, C. Mer, E. Rzepka, M. Nesladek, P. Bergonzo, *Diam. Relat. Mater.* **15**, 833 (2006).

[6] B. Marczewska, P. Olko, M. Nesladek, M. P. R. Waligórski, Y. Kerremans, *Radiat. Prot. Dosim.* **101**, 485 (2002).

[7] A. Karczmarska, M. Mitura-Nowak, T. Nowak, M. Marszałek, *Acta Phys. Pol. A* **121**, 510 (2012).

[8] S. Gastélum, E. Cruz-Zaragoza, V. Chernov, R. Melendrez, M. Pedroza-Montero, M. Barboza-Flores, *Nucl. Instr. Methods B* **260**, 592 (2007).

[9] C. Gómez-Alexandre, M. M. García, O. Sánchez, J. M. Albella, *Thin Solid Films* **303**, 34 (1997).

[10] C. J. Tang, A. J. Neves, A. J. S. Fernandes, *Diam. Relat. Mater.* **13**, 203 (2004).

[11] T. Niewiadomski, Dozymetria termoluminescencyjna w praktyce (IJF PAN, Kraków, 1991).

[12] A. Karczmarska, M. Mitura-Nowak, M. Kulij, B. Marczewska, M. Marszałek, *Phys. Stat. Sol. A* **209**, 1774 (2012).

Nonstoichiometric TiO_{2-x} thin films for renewable energy sources

Kamila Kollbek

Faculty of Physics and Applied Computer Science, AGH University of Science and Technology, Mickiewicza 30, 30-059 Kraków, Poland

Supervisors: Czesław Kapusta, Katarzyna Zakrzewska

Nonstoichiometric TiO_{2-x} thin films have been deposited by magnetron sputtering of Ti target in Ar+O_2 atmosphere controlled by the plasma emission method. Systematic studies with X-ray Diffraction in Grazing Incidence, GID, impedance spectroscopy, optical spectrophotometry, 1s3p Resonant Inelastic X-ray Scattering, RIXS have been performed. The obtained stoichiometric thin films of TiO_2 turned out to be composed of a well-crystallised anatase-rutile mixture with predominantly anatase form while the films with higher oxygen deficit indicated rutile and then became amorphous. Oxidation state changes from Ti^{4+} in stoichiometric films towards Ti^{3+} upon increasing departure from stoichiometric composition. This change is accompanied by a significant decrease in the electrical resistivity.

Titanium dioxide thin films have been extensively investigated because of their numerous applications in gas sensing, photodegradation of organic contaminants, bacteria deactivation as well as photoanodes in photoelectrochemical cells for water decomposition as renewable energy sources.[1–5] The main advantage of TiO_2 considered as a photoanode for hydrogen generation is its high chemical stability towards corrosion and photocorrosion as compared to other proposed semiconductors. However, stoichiometric TiO_2 suffers from too wide band gap (>3,0 eV) that results in a considerable mismatch between its absorption spectrum and the solar spectrum. This difference is the main cause of the fact that the solar conversion efficiency is not sufficient for industrial applications. Also too high electrical resistivity of stoichiometric TiO_2 limits the solar conversion efficiency. Many attempts were undertaken in the past in order to improve the photoconversion efficiency of TiO_2 in order to benefit from the whole light spectrum and decrease the electrical resistivity. Modifications of TiO_2 cationic as well as anionic sublattices, including those creating oxygen deficiency have been proposed. The effect of deviation from stoichiometry x in TiO_{2-x} on the structural, optical, and photoelectrochemical, properties has been studied.[6–8] However, there is still a disagreement about the extent of nonstoichiometry and the mechanism by which it is accommodated. It is well known that oxygen non-stoichiometry helps to reduce electrical resistivity and makes electrical conductivity sufficient.[7,8] However, for TiO_{2-x} close to the stoichiometric composition, i.e. with small x, the band gap has been found to increase with the increasing departure from stoichiometry. It is believed that large deviations from stoichiometry in TiO_{2-x} could resolve the problem of too wide band gap. Therefore, the present work extends the range of non-stoichiometry to include higher oxygen deficit.

Thin films of TiO_{2-x} with thickness of 250 nm have been deposited by dc pulsed magnetron sputtering onto amorphous silica substrates. Reactive sputtering from Ti target has been carried out in a flow-controlled Ar+O_2 gas atmosphere which leads in consequence to a certain oxygen excess or deficit x in the growing thin films of TiO_{2-x}. Deposition process is controlled by means of the Optical Emission Spectroscopy (OES). Nonstoichiometry of TiO_{2-x} thin films is a function of the controllable technological parameter I/I_0 which is related to Ti target sputtering rate. Details of the technological procedure are presented elsewhere.[9]

X-ray diffraction patterns have been measured by means of X-ray Diffraction at Grazing Incidence (GID) on Philips X'Pert MPD diffractometer with Cu $K\alpha$ radiation. Optical transmittance and reflectance spectra have been obtained by Lambda 19 Perkin-Elmer double beam spectrophotometer with a 150 mm integration sphere over a wide wavelength range from 250 to 2500 nm. Impedance Spectroscopy (IS) data have been recorded with dielectric interface Solatron 1296 and frequency response analyzer Solatron 1260. A frequency range of 1 – 10^6 Hz has been covered, with 10 mV amplitude.

Synchrotron measurements have been carried out under ambient conditions at Super XAS (X10DA) beamline of Swiss Light Source, Villigen, Switzerland. Energy scans have been performed with a Si(111) double crystal monochromator. Resonant Inelastic X-ray Scattering spectra (RIXS) have been collected using high-resolution von Hamos bent crystal spectrometer equipped with Ge(440) crystal analyser and position sensitive MYTHEN II detector. Samples have been set up at grazing incidence (~5° to the X-ray beam) in order to enhance emission efficiency.[10]

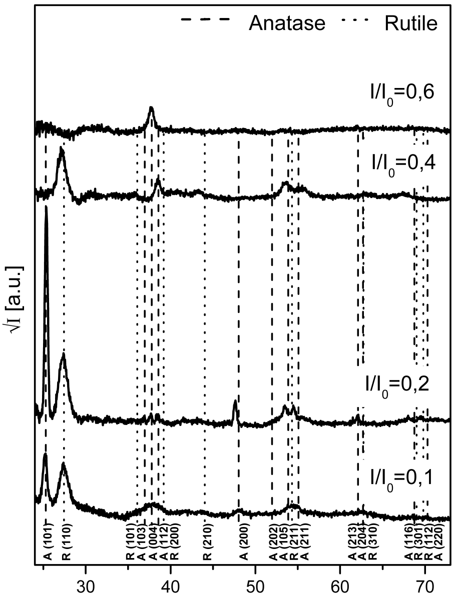

FIGURE 1: XRD GID patterns of nonstoichiometric TiO_{2-x} thin films deposited at different I/I_0; A — anatase, R — rutile, I — intensity of Ti plasma emission line at $\lambda = 500$ nm under conditions of the reactive sputtering in $Ar+O_2$ mixture, I_0 — intensity of the same line at 100% Ar.

$1s3p$ 2D RIXS plane of Ti exhibits a strong non-dispersive feature at the emission energy of approx. 4933 eV that corresponds to $K\beta_{1,3}$ emission line and a dispersive feature due to elastic and quasi-elastic scattering of the incident beam which have been used for calibration of the emission energy scale X-ray emission spectra of $K\beta_{1,3}$, $K\beta_{2,5}$ and $K\beta$ satellite (XES) and K-edge High Energy Resolution Fluorescence Detected X-ray Absorption Near-Edge Structure (HERFD-XANES) spectra have been extracted from 2D RIXS planes along incident and emission energy, respectively. The former have been obtained by integration of the 2D RIXS intensities along incident energy over the range from 4992 eV to 5200 eV, while the latter by integration along emitted energy over the range from 4930 eV to 4935 eV.

X-ray diffraction patterns of nonstoichiometric TiO_{2-x} thin films deposited at different values of the technological parameter I/I_0 are shown in Fig. 1. Thin films with nearly stoichiometric composition (TiO_2) deposited at $I/I_0 = 0{,}1$ and 0,2 are well crystallized and contain a mixture of anatase and rutile polymorphic forms in the amorphous background. Anatase predominates at $I/I_0 = 0{,}1$ and 0,2 because sputtering performed from the oxidized Ti target surface creates conditions more favourable for anatase formation. However, for sample obtained at $I/I_0 = 0{,}4$ anatase disappears while rutile grows. Under higher sputtering rates and lower oxygen content, deposition process is performed from the metallic-like target surface which creates more favourable conditions for rutile formation. XRD pattern for oxygen deficient TiO_{2-x} deposited at $I/I_0 = 0{,}6$ contain only one

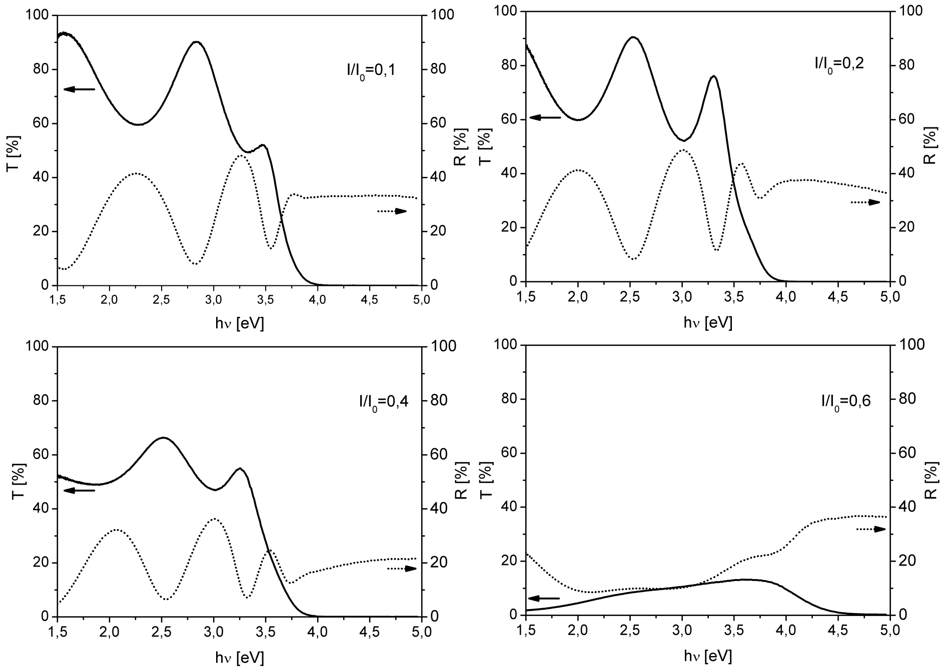

FIGURE 2: Transmittance T and reflectance R spectra of TiO_{2-x} thin films deposited at different I/I_0; $h\nu$ — photon energy. Thickness d of the samples is $d = 250$ nm.

diffraction peak. The most prominent anatase (101) and rutile (110) diffraction peaks disappear. It is not possible to distinguish between these two polymorphic forms and neglect the presence of other phases. In order to verify this result more work is still necessary.

The determined resistances for thin film deposited at $I/I_0 = 0{,}1$ and $I/I_0 = 0{,}6$ using Impedance Spectroscopy measurements are $R_{I/I_0=0,1} = 21260$ Ohm, $R_{I/I_0=0,1} = 8{,}08 \times 10^9$ Ohm, respectively. The results from the Impedance Spectroscopy measurements have been obtained by fitting with a simple electrical model in which the resistance R is connected in parallel with CPE (Constant Phase Element). A constant phase element (CPE) is used instead of a pure capacitor to compensate for the non-ideal capacitive response of the interface.

Example of the optical measurements of the transmittance $T(h\nu)$ and reflectance $R(h\nu)$ coefficients for thin films deposited at $I/I_0 = 0{,}1$, $I/I_0 = 0{,}2$, $I/I_0 = 0{,}4$, $I/I_0 = 0{,}6$ are given in Fig. 2. Spectra for films grown at $I/I_0 = 0{,}1$, 0,2 and 0,4 reveal periodic oscillations due to the interference effect below the fundamental absorption edge, which is characteristic for transparent titanium dioxide thin films with small oxygen deficit. The samples are homogeneous because $T_{\min}(h\nu)$ in transmittance spectra are in alignment with $R_{\max}(h\nu)$ in reflectance spectra and vice versa. For highly nonstichiometric sample ($I/I_0 = 0{,}6$) oscillations become strongly attenuated and the plasma reflectance edge is clearly seen. Oxygen deficit results in an enhanced absorption of light and shifts absorption edge towards UV range. Moreover, the occurrence of the plasma reflectance edge in the reflectance spectra for oxygen deficient TiO_{2-x} thin film ($I/I_0 = 0{,}6$) is consistent with the decreased electrical resistivity (by 6 orders of magnitude) as indicated by the Impedance Spectroscopy and confirms the transition from stoichiometric TiO_2 to semiconducting, oxygen deficient TiO_{2-x}.

Ti $K\beta$ detected K-edge HERFD-XANES of TiO_{2-x} thin films is shown in Fig. 3. The K-edge HERFD-XANES spectra show a significant change in the pre-edge structure and a shift of the absorption edge to lower photon energies upon an increased oxygen deficit. Po-

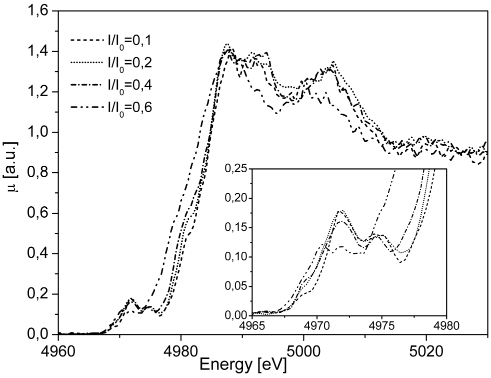

FIGURE 3: HERFD-XANES spectra of non-stoichiometric titanium dioxide (TiO_{2-x}) thin films at Ti-*K*-edge. Insets show the close-up of the pre-edge structure.

sition of the absorption edge is taken at the intensity of half of the absorption threshold. Such a shift can be attributed to a gradual decrease in the inter atomic distances that leaves local symmetry of Ti ions almost unaffected up to $I/I_0 = 0{,}4$, since the shape of the XANES spectra remains unchanged. The spectrum of the most non-stoichiometric sample ($I/I_0 = 0{,}6$) is significantly different and this fact can be attributed to a considerable evolution of the local structure. Moreover, the shape of the Ti K pre-edge peaks is similar for all samples except for that sputtered at $I/I_0 = 0{,}6$. This means that the formal valence and local structure are modified significantly only for TiO_{2-x} deposited at $I/I_0 = 0{,}6$.

In summary, thin films of nonstoichiometric TiO_{2-x} deposited by means of reactive sputtering were studied in order to observe the changes in their structure and optical properties. XRD measurements of nonstoichiometric TiO_{2-x} thin films show that well-crystallised films obtained at $I/I_0 = 0{,}1$ and $I/I_0 = 0{,}2$ contain a mixture of mostly anatase and rutile polymorphic form. Anatase is no longer formed while rutile phase still exists for thin film sputtered at $I/I_0 = 0{,}6$. At higher departures from stoichiometric composition (film obtained at $I/I_0 = 0{,}6$) the film becomes amorphous and it is difficult to reach reliable phase identification. Optical properties have been found to be equally sensitive to the changes in the oxidation state of the sputtered target and correlate with the results of XRD measurements. Corresponding changes in the transmittance T and reflectance R spectra confirm the transition from stoichiometric TiO_2 to semiconducting, oxygen deficient TiO_{2-x}. The presence of the plasma reflectance edge for oxygen deficient TiO_{2-x} ($I/I_0 = 0{,}6$) is consistent with the decrease in the electrical resistivity measured by the Impedance Spectroscopy. Local structure of Ti ions changes for the films sputtered at the highest oxygen deficit. Moreover, XANES confirms that the oxidation state changes from Ti^{4+} towards Ti^{3+}.

⋆ ⋆ ⋆

[1] G. Sberveglieri, *Sens. Actuators, B, Chem.* **23**, 103 (1995).

[2] U. I. Gaya, A. H. Abdullah, *J. Photochem. Photobiol. C: Photochemistry Reviews* **9**, 1 (2008).

[3] C. M. Teh, A. R. Mohamed, *J. Alloys Compd.* **509**, 1648 (2011).

[4] A. Fujishima, K. Honda, *Nature* **238**, 37 (1972).

[5] M. Radecka, M. Rekas, A. Trenczek-Zajac, K. Zakrzewska, *J. Power Sources* **181**, 46 (2008).

[6] D. C. Cronemeyer, *Phys. Rev.* **87**, 876 (1952).

[7] M. Radecka, A. Trenczek-Zajac, K. Zakrzewska, M. Rekas, *J. Power Sources* **173**, 816 (2007).

[8] F. Vratny, F. Micale, *Trans. Faraday Soc.* **59**, 2739 (1963).

[9] A. Brudnik, A. Gorzkowska-Sobaś, E. Pamuła, M. Radecka, K. Zakrzewska, *J. Power Sources* **173**, 774 (2007).

[10] J. Szlachetko, M. Nachtegaal, E. de Boni, M. Willimann, O. Safonova, J. Sa, G. Smolentsev, M. Szlachetko, J. A. van Bokhoven, J.-Cl. Dousse, J. Hoszowska, Y. Kayser, P. Jagodzinski, A. Bergamaschi, B. Schmitt, C. David, A. Lücke, *A. Rev. Sci. Instrum.* **83**, 103105 (2012).

Silver nanoparticle deposition on mica and oxidized silicon surface

Katarzyna Kubiak

Jerzy Haber Institute of Catalysis and Surface Chemistry Polish Academy of Sciences, Niezapominajek 8, 30-239 Kraków, Poland

Supervisor: Zbigniew Adamczyk

A stable silver nanoparticle suspension was synthesized via the reduction of silver nitrate using sodium borohydride in the presence of sodium citrate. Characterization of these particles was done in the bulk and at a surface using such methods as UV-Vis spectrophotometry, Dynamic Light Scattering (DLS), Scanning Electron Microscopy (SEM), Atomic Force Microscopy (AFM) and Transmission Electron Microscopy (TEM). Kinetics of silver particles adsorption on modified by cationic polyelectrolyte PAH surface of mica and silicon was determined for ionic strength (I) of 0,01 M NaCl. Characterization of silicon surface modified by various methods was done by X-ray Photoelectron Spectroscopy (XPS), Atomic Force Microscopy (AFM) and wetting angle measurements.

Silver nanoparticles are known to possess unique properties such as high biological activity,[1] the ability to promote oxidation processes and high electric conductivity.[2] These particles find practical applications in many fields of science e.g. medicine,[1] pharmacology, cosmetology and catalysis.

There are several methods for obtaining silver nanoparticles such as the chemical reduction of silver nitrate using: sodium borohydride,[2] hydrazine,[3] formaldehyde,[4] sodium citrate[5] and β-D-glucose.[6] Also in common usage is electrochemical method,[7] preparation in reverse micelles[8] and bacterial biosynthesis.[1]

One of the most efficient and reliable method is the chemical reduction in aqueous environment. Silver nanoparticle suspension obtained in this way is monodispersed and size of particles can be regulated by choosing a proper concentration of the precursor salt, varying reaction temperature and time.[9]

Silver nanoparticles in a form of monolayers find practical applications in medicine, opto-electronics,[2] catalysis and environmental protection technologies. There are several methods to prepare silver particle monolayers e.g. chemical vapor deposition[10] and chemical bath deposition,[11] but they do not give satisfying results in surface coverage, particle distribution uniformity and stability of these monolayers. The simplest method which gives stable and homogeneous monolayer of high particle coverage is self-assembly from suspensions under diffusion controlled transport conditions. This method produce monolayers in controlled by the bulk concentration of the sol, the ionic strength, pH and adsorption time conditions.

Park et al.[5] described silver nanoparticle deposition on glass surface modified by silane compounds having bifunctional moieties. No information of particle size, zeta potential and also stability, polidispersity or deposition conditions of a sol were performed. Only the AFM and UV-vis measurements were studied. Flores et al.[12] reported adsorption of silver nanoparticles on Ti/TiO_2 surface. These monolayers were used as antibacterial coatings. Bandyopdhyay et al.[13] using high polidispersed sol performed a method of obtaining silver nanoparticle layers on Al-coated silicon wafers functionalized by thiophenol derives. The maximum surface coverage of silver particles obtained in this study was equal to 10%.

This work was concentrated on the synthesis of stable silver nanoparticle suspension via the reduction of silver nitrate using sodium borohydride and sodium citrate.

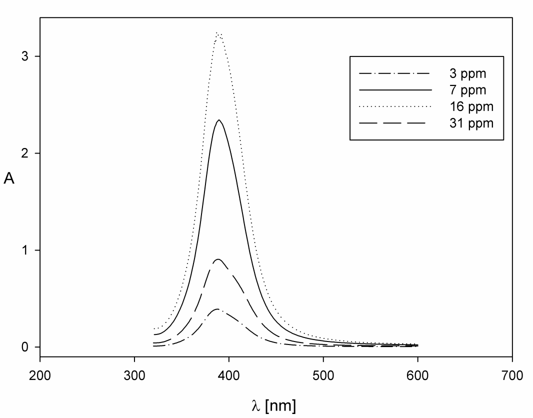

FIGURE 1: The UV-vis spectrum of the silver nanoparticles suspension for bulk concentration of 3, 7, 16, 31 ppm.

The UV-Vis method was used for studying the stability of the sol as a function of concentration for four silver suspension solutions 3, 7, 16, 31 ppm. It was determined that the maximum excitation band is near 389 nm, attributed to the surface plasmon excitation of silver particles and is narrow and symmetric, what indicates that the silver suspension does not contain agglomerated particles and is fairly monodispersed. This method also indicated that the absorption value increased with particles concentration Fig. 1.

Characterization in the bulk also involved particles' size distribution, which was determined via the diffusion coefficient measurements executed by the Dynamic Light Scattering (DLS) using the Zetasizer Nano ZS Malvern. Knowing the diffusion coefficient D one can determine the hydrodynamic diameter of a particle, which is defined via the Stokes-Einstein relationship

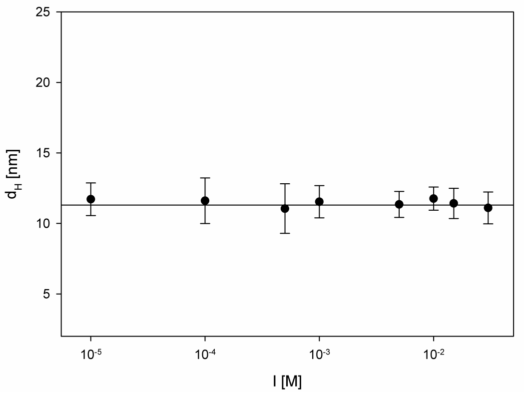

FIGURE 2: The hydrodynamic diameter vs. ionic strength (pH = 5,5).

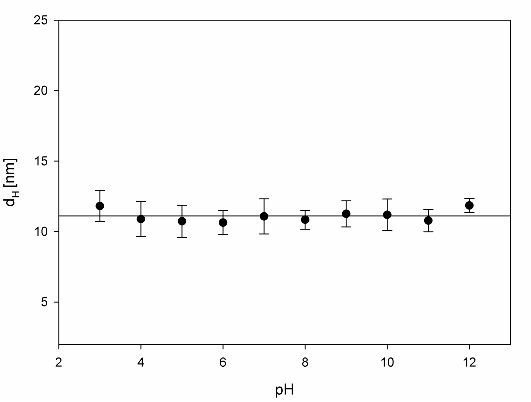

FIGURE 3: The hydrodynamic diameter vs. pH ($I = 10^{-2}$ M).

$$d_{\mathrm{H}} = \frac{kT}{3\pi\eta D}, \tag{1}$$

where d_{H} is the hydrodynamic diameter, k is the Boltzman constant, η is the viscosity of water and T is the absolute temperature.

Changes in the hydrodynamic diameter of particles was determined as a function of ionic strength and pH. As can be seen, the hydrodynamic diameter was stable, equal to 11 nm for ionic strengths I in the range of 10^{-5} M NaCl to 3×10^{-2} M (for pH = 5,5 regulated by NaCl) Fig. 2. This parameter was also unchanging in respect to pH in the range of 3 to 12 (for $I = 10^{-2}$ M NaCl) (Fig. 3).

The physicochemical characteristics of the silver nanoparticle sol was complemented by the electrophoretic mobility measurements performed by the Laser Doppler Velocimetry technique (LDV). Knowing this parameter one can calculate the zeta potential of particles using Henry-Smoluchowsky formula

$$\zeta_{\mathrm{p}} = \frac{3\eta}{2\varepsilon f(\kappa d_{\mathrm{p}})} \mu_{\mathrm{e}}, \tag{2}$$

where ζ_{p} is the zeta potential of particles, μ_{e} is the electrophoretic mobility, ε is the electric permittivity of the solution, $f(\kappa d_{\mathrm{p}})$ is the

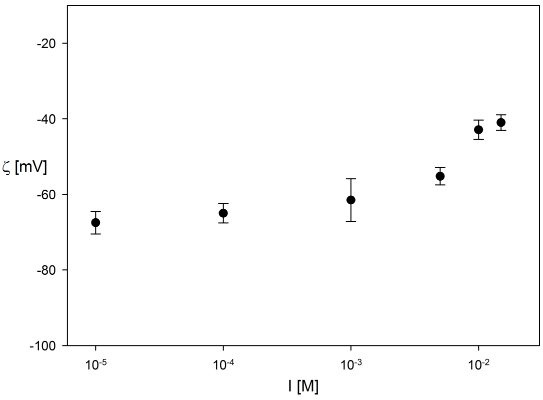

FIGURE 4: The zeta potential vs. ionic strength (pH = 5,5).

correction function of the dimensionless parameter (κd_p) and $\kappa^{-1} = (\varepsilon kT/2e^2I)^{1/2}$ is the double-layer thickness.

The zeta potential measurements reveal that these silver particles were negatively charged in the full range of measurements. The zeta potential increased with the ionic strength varying from -68 mV for 10^{-5} M to -41 mV for ionic strength of 3×10^{-2} M NaCl (for pH = 5,5 regulated by NaCl) and its value is equal on average to -49 mV for pH between 4 to 10 (for $I = 10^{-2}$ M NaCl) (Figs. 4 and 5).

The above mentioned parameters were essential for a proper interpretation of kinetic adsorption measurements. Adsorption experiments on mica and silicon modified by cationic polyelectrolyte poly(allylaminehydrochloride) (PAH) were conducted under diffusion-controlled transport. The kinetic runs were performed for 11 ppm concentration of silver nanoparticle sol, ionic strength $I = 10^{-2}$ M NaCl and pH = 5,5. The silver monolayers were formed via colloid self assembly process on a modified surface of mica and silicon and the adsorption kinetic runs were adequately reflected for the entire range of time by the random sequential adsorption (RSA) model Fig. 6.

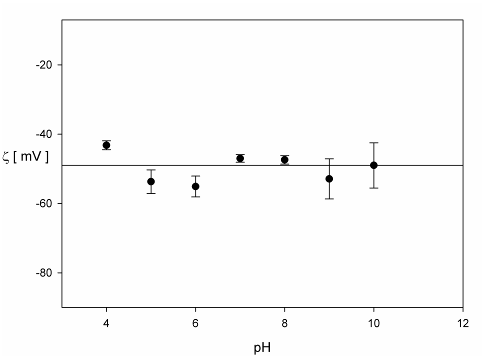

FIGURE 5: The zeta potential versus pH ($I = 10^{-2}$ M).

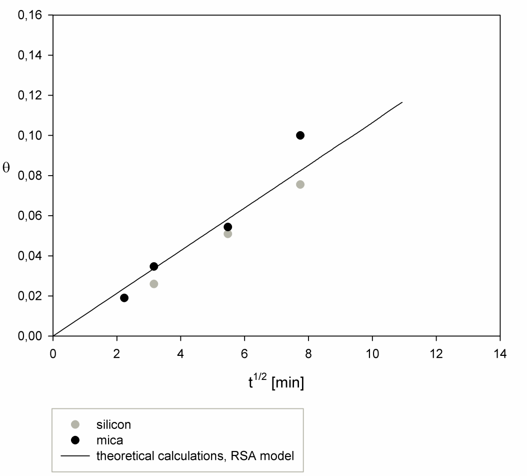

FIGURE 6: The kinetics of silver nanoparticle deposition at mica and silicon modified by the PAH monolayer, determined for ionic strength $I = 10^{-2}$ M, pH = 5,5.

Moreover, characterization of silicon surface was also performed. Using a few methods, the surface roughness and elemental composition of silica were investigated. This description involved Atomic Force Microscopy (AFM), Scanning Electron Microscopy (SEM) and X-Ray Photoelectron Spectroscopy (XPS) measurements.

Silicon surface was modified by acetone, ethanol 96%, piranha solution ($H_2O_2 + H_2SO_4$) and warmed in two temperatures 200 and 400 degrees Celsius in tube furnace. It was determined that the lowest surface roughness occured for modification by the piranha solution with heating in 400°C.

Additionally, characterization of modified silicon surface was done by wetting angle measurements. Its value was equal on average to 30° what means that the surface is hydrophilic. The angle was checked every day

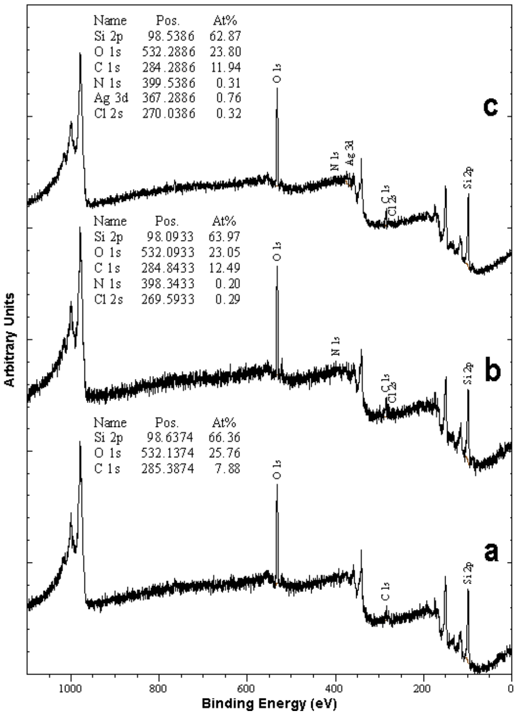

FIGURE 7: The XP spectra of elemental composition of silicon samples; a: purified silicon, b: silicon + polyelectrolyte PAH, c: silicon + PAH + silver nanoparticles.

for three day period of time and during this time no changes were observed, what gives an information that Si/SiO_2 surface is stable in time.

The X-ray Photoelectron Spectroscopy (XPS) measurements were also carried out. It determined an elemental of three silicon samples: pure silicon (a probe), silicon modified by cationic polyelectrolyte PAH (b probe) and silicon modified by PAH with silver monolayer (c probe). It was measured that the a probe contains silicon Si, oxygen O and carbon C; the b probe comprises silicon Si, oxygen O, carbon C and also nitrogen N and chlorine Cl which origin was from polyelectrolyte; the c probe includes what b probe with silver Ag addition (Fig. 7). No other elements were found that showed that all of these samples were not included any pollution.

⋆ ⋆ ⋆

[1] K. K. Y. Wong, X. Liu, *MedChemComm*, (revive 2010).

[2] A. Michna, Z. Adamczyk, M. Oćwieja, E. Bielańska, *Colloids and Surfaces A: Physicochem*, **377**, 261 (2011).

[3] U. Nickel, Zu. Castell, K. Poppl, S. Schneider, *Langmuir* **16**, 9087 (2000).

[4] K. Chou, C. Ren, *Mater. Chem. Phys.* **64**, 241 (2000).

[5] S.-H. Park, J.-H. Im, J.-W. Im, B.-H. Chun, J.-H. Kim, *Microchem. J.* **63**, 71 (1999).

[6] P. Raveendran, J. Fu, S. L. Wallen, *J. Am. Chem. Soc.* **125**, 13940 (2003).

[7] B. Nikoobakht, Z. L. Wang, M. A. El-Sayed, *J. Phys. Chem. B* **104**, 8635 (2000).

[8] W. Zhang, X. Qiao, J. Chen, H. Wang, *J. Colloid Interface Sci.* **302**, 370 (2006).

[9] H. Jiang, K.-S. Moon, Z. Zhang, S. Pothukuchi, C. P. J. Wong, *J. Nanopart. Res.* **8**, 117 (2006).

[10] Z. Yuan, N. H. Dryden, J. J. Vittal, R. J. Puddephatt, *Chem. Mater.* **7**, 1696 (1995).

[11] I. C. Estrada-Raygoza, M. Sotelo-Lerma, R. Ramirez-Bon, *J. Phys. Chem. Solids* **67**, 782 (2006).

[12] C. Y. Flores, C. Diaz, A. Rubert, G. A. Benitez, M. S. Moreno, M. A. Fernandez Lorentzo de Mele, R. C. Salvarezza, P. L. Schilardi, C. Vericat, *J. Colloid Interface Sci.* **350**, 402 (2010).

[13] K. Bandyopdhyay, V. Patil, K. Vijayamohanan, M. Sastry, *Langmuir* **13**, 5244 (1997).

Preparation of silver nanoparticle films of controlled coverage and structure

Magdalena Oćwieja

Jerzy Haber Institute of Catalysis and Surface Chemistry Polish Academy of Sciences, Niezapominajek 8, 30-239 Kraków, Poland

Supervisor: Zbigniew Adamczyk

Precisely characterized silver nanoparticles were used to obtain silver monolayers on mica modified by poly(allylamine hydrochloride) (PAH). The deposition of nanoparticles was carried out under diffusion-controlled transport from silver suspensions. Monolayers coverage, quantitatively determined by AFM and SEM, was regulated within broad limits by adjusting the nanoparticle deposition time. The adsorption kinetic runs were adequately reflected by the random sequential adsorption (RSA) model. It was revealed that the structure of monolayers, especially the average distance between particles, can be regulated via the ionic strength variations.

There are several ways to prepare silver particle monolayers. The most frequently used methods are chemical vapor deposition (CVD), chemical bath deposition (CBD), sputtering and evaporation. However, these techniques require sophisticated equipment, which make them expensive. Moreover, in the CBD method, the purity and stability of silver particle monolayers is not satisfactory. Other disadvantages include a poor control of coverage and particle distribution homogeneity within monolayers. These problems can be avoided using the colloid self-assembly methods based on deposition of silver particles from stable suspensions. Therefore, the goal of this work is to quantitatively determine the kinetics of silver particle self-assembly on solid substrates from well-defined aqueous suspensions. In particular the role of the ionic strength in these processes is evaluated, which is significant for basic colloid science. Additionally, these measurements allow us to develop an efficient method for obtaining uniform monolayers of silver nanoparticles, of high and controlled density.

Three types of silver nanoparticle suspensions used in the experiments were synthesized via the reduction of silver nitrate using sodium borohydride and sodium citrate. Bulk characteristic of silver nanoparticles in aqueous solution was carried out by measuring their plasmon absorption spectrum, diffusion coefficients, and the electrophoretic mobilities. The average hydrodynamic diameter of silver particles (d_{H}) was 15, 28 and 54 nm respectively. The stability of the silver sols was studied by determining the dependence of the hydrodynamic diameter of particles on ionic strength varied between $0{,}0001 - 0{,}05$ M (Fig. 1). As can be seen, a significant increase in the hydrodynamic diameters was observed for ionic strength approaching 0,05 M. Above this value of ionic strength the nanoparticles aggregate and the sols lose stability. Another most important parameter, which characterizes the stability of suspension, the electrokinetic charge of particles as well as the electrostatic interaction among them is the electrophoretic mobility (μ_{e}), defined as the average translation velocity of colloidal particles under given electric field. The dependence of electrophoretic mobility of silver nanoparticles on ionic strength for $\mathrm{pH} = 6{,}2$ was shown in Fig. 2. The electrophoretic mobility of silver nanoparticles is negative in entire range of ionic strength, indicating that the particles acquired a net negative charge. As can be seen, for given ionic strength the electrophoretic mobility depends on the size of nanoparticles. For $I = 0{,}0001$ M the differences in the value of electrophoretic mobility are the greatest but when ionic strength

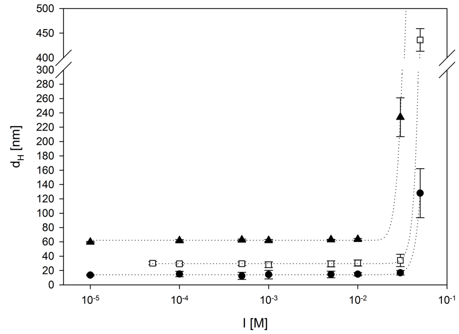

FIGURE 1: The dependence of the hydrodynamic diameter of silver nanoparticles on ionic strength, determined by DLS for silver suspension concentration 100 ppm, pH$=$ 6 $-$ 6,2; $T=293$ K, the average particle size: (●) 15 nm, (□) 28 nm, (▲) 54 nm. The solid line represents non-linear fit of experimental data.

increases it reaches a similar value about $-2{,}75$ μm cm $(\mathrm{Vs})^{-1}$ for $I = 0{,}03$ M. For a quantitative interpretation of adsorption kinetic, it is necessary to know the value of zeta potential of particles in the bulk. Knowing the electrophoretic mobility, this quantity was calculated using Henry's equation and the Ohshima's model,[1] which includes the relaxation effect of double layer around particles especially for low ionic strength when the thickness of electric double layer reaches a considerable size. The values of the zeta potential of the particles calculated from three models are given in the Table 1.

For silver particle adsorption experiments, the mica sheets modified by positively charge poly(allylamine hydrochloride) (PAH) were used as a well-defined substrate. The quantitative analysis of PAH monolayer formation on mica substrate was investigated using streaming potential method according to the procedure widely described in literature.[2,3] As previously mentioned, the silver particle adsorption was carried out under diffusion controlled regime for a desired period of time ranging from 5 to 1500 min. The samples with deposited silver nanoparticles were examined using Atomic Force Microscopy (AFM) and Scanning Electron Microscopy (SEM). The number of silver particles was determined over

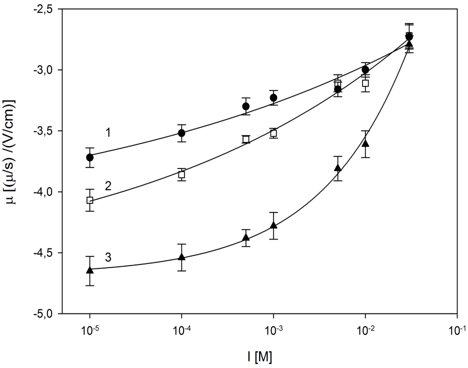

FIGURE 2: The dependence of the electrophoretic mobility of silver particles on ionic strength for pH $=$ 6,2 and silver suspension concentration 100 $-$ 150 ppm: (●) 15 nm, (□) 28 nm, (▲) 54 nm. The solids lines denote a non-linear fits of experimental data.

10 $-$ 15 equally sized areas chosen randomly over the PAH precovered mica sheet. The obtained results were expressed as the surface concentration of particles N_s, defined as the number of particles per unit area of the substrate. For the sake of convenience, this area was assumed to be one square μm; thusly N_s has the dimension of $[\mu\mathrm{m}^{-2}]$. Particle deposition kinetics was evaluated in a discontinuous way by stopping the adsorption experiment after a given adsorption time and determining the average surface concentration of particles. In this way, kinetic runs showing the dependence of N_s on t can be derived for a discrete set of points.

Moreover, knowing the average number of silver particles per unit area, the size of particle d_p and the surface area ΔS the surface concentration can be converted to dimensionless coverage defined as:

$$\Theta = \frac{\pi d_\mathrm{p}^2 N_\mathrm{s}}{4} \ . \qquad (1)$$

However, it should be mentioned that for the diffusion-controlled transport, it is appropriate to express the kinetic runs in terms of the square root of deposition time $\sqrt{t}$, rather than the primary time variable t. This is so because for a not too high coverage, where the surface blocking effects remain negligible,[4] the kinetics of particle adsorption is described by

TABLE 1: The electrophoretic mobility, number of elementary charge and zeta potential of silver nanoparticles for various pH and ionic strength (* — Ohshima model fails).

pH	Ionic strenght [M]	μ_e [μm cm (Vs)$^{-1}$]	N_c [e]	ζ_p [mV] Smoluchowski model	ζ_p [mV] Hückl model	ζ_p [mV] Ohshima model
3	0,001	−2,60	−43	−36,6	−52,4	−59,2
	0,01	−2,35	−40	−33,1	−43,6	−48,1
	0,1	−2,19	−36	−30,8	−37,9	−40,3
6,2	0,0001	−3,86	−64	−54,4	−80,5	−95,1
	0,001	−3,25	−54	−45,8	−65,5	−87,3
	0,01	−2,84	−47	−40,0	−52,7	−62,8
	0,03	−2,72	−44	−38,3	−47,1	−52,3
9	0,001	−4,10	−68	−57,7	−85,5	−105
	0,01	−3,50	−58	−49,3	−70,5	—*
	0,1	−3,06	−50	−43,1	−56,8	—*

the theoretical formula:

$$\langle N_s \rangle = 2\left(\frac{D}{\pi}\right)^{\frac{1}{2}} \sqrt{t} n_b \ , \qquad (2)$$

where n_b is the bulk number concentration of particles connected with the weight concentration c_p (expressed in ppm) via the linear dependence

$$n_b = \frac{6 \cdot 10^{-6}}{\pi d_p \rho_p} c_p \ , \qquad (3)$$

where ρ_p is the specific density of silver and equals 10,49 g cm^{-3}.

Typical kinetic runs of silver particles (average size 15, 28 and 54 nm) obtained for deposition conditions $I = 0{,}0001 - 0{,}01$ M NaCl, pH $= 5{,}8 - 6{,}2$ and $T = 293$ K are shown in Fig. 3. It is worth mentioning, that the efficiency of the adsorption process under diffusion controlled regime, strongly dependent on the suspension concentration. Hence, the suspension concentration used in the experiments increases with the average size of particle and it attains the value 50 ppm, 150 ppm and 400 ppm for silver particle 15, 28 and 54 nm respectively. Characteristic features of these kinetic runs (Figs. 3a – c) are a linear increase in N_s with $t^{1/2}$ for shorter times and then, after reaching some critical time, an abrupt stabilization of the surface concentration at a constant value. This behavior was quantitatively described in terms of the random sequential adsorption (RSA) model[4] depicted by the solid lines. As can be seen, the theoretical results obtained from RSA model are in a good agreement with the experimental value for in all three cases (Figs. 3a – c). It has been determined that the maximum surface coverage (for $I = 0{,}01$ M; pH$=5{,}8 - 6{,}2$) equals $\Theta_{mx} = 0{,}29$; $\Theta_{mx} = 0{,}33$ and $\Theta_{mx} = 0{,}36$ in the case of nanoparticles 15, 28 and 54 nm respectively. Additional series of kinetic measurements was performed with the aim of determining the influence of electrostatic interactions, whose range can be regulated by the ionic strength, on the maximum particle coverage. As can be seen, the maximum particle coverage Θ_{mx} (regardless of the size) increased systematically with ionic strength e. g. from 0,15 ($I = 0{,}0001$ M) to 0,34 ($I = 0{,}03$ M) (Fig. 3a). However, it is to be mentioned that the this maximum coverage value is significantly smaller than the jamming coverage for hard (noninteracting) particles, $\Theta_\infty = 0{,}547$.[4] This effect is attributed to the lateral electrostatic interactions among adsorbing particles as demonstrated previously for polystyrene latex particles, and gold nanoparticles. This interaction potential between a particle pair ϕ_{12} is described quantitatively by the formula:

$$\phi_{12} = \phi_0 \frac{\Theta_p}{2a_p + h} e^{-kh} \ , \qquad (4)$$

where: h is the gap distance between particle

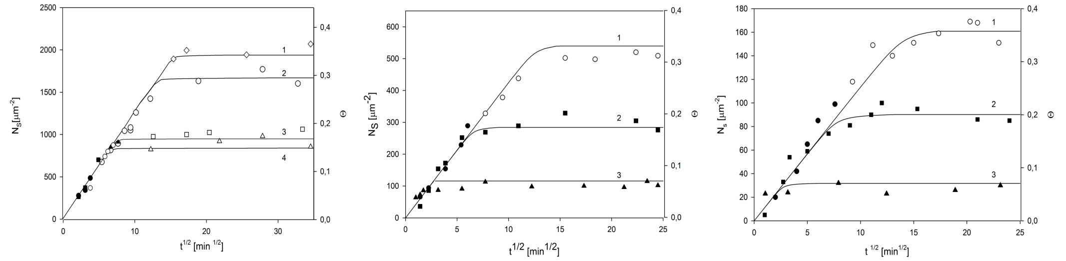

FIGURE 3: The kinetics of silver particle deposition at mica modified by the PAH monolayer, determined for various ionic strengths and particles: (left panel) 15 nm, (middle panel) 28 nm, (right panel) 54 nm, using AFM (full points) and SEM (empty points) methods. Particle deposition conditions: pH=6,2, $T=293$ K, silver sol concentration: (left panel) $c_{\mathrm{b}}=50$ ppm, (middle panel) $c_{\mathrm{b}}=150$ ppm, (right panel) $c_{\mathrm{b}}=400$ ppm. The points denote experimental results obtained for: (1) (♦, ◊) $I=0{,}03$ M, (2) (•, ∘) $I=0{,}01$ M, (3) (■, □), $I=0{,}001$ M, (4) (▲, △), $I=0{,}0001$ M, and the solid lines denote the theoretical results calculated from the RSA model.

surfaces and $0{,}5\phi_0$ is the limiting interaction energy of two particles at close separations, given by the expression:[4]

$$\phi_0 = 32\pi\varepsilon a_{\mathrm{p}} \left(\frac{kT}{e}\right)^2 \mathrm{tgh}\left(\frac{\zeta e}{4kT}\right) . \quad (5)$$

Using this potential, the effective interaction range of two particles can be calculated from the formula

$$H^\star = \frac{h^\star}{a_{\mathrm{p}}} = \\ = \frac{1}{2\kappa a_{\mathrm{p}}}\left\{\ln\frac{\phi_0}{2\phi_{\mathrm{ch}}} - \ln\left[1+\frac{1}{2\kappa a_{\mathrm{p}}}\ln\frac{\phi_0}{2\phi_{\mathrm{ch}}}\right]\right\}, \quad (6)$$

where: $h^\star$ is the dimensional interaction range and ϕ_{ch} is the characteristic interaction energy, close to the kT unit.[4] Hence, according to this effective hard particle concept, the interacting (soft) particle is replaced by a hard particle having the effective radius of $a_{\mathrm{p}}+h^\star$. Accordingly, the maximum coverage of such interacting particles can be calculated from the formula:

$$\Theta_{\mathrm{mx}} = \Theta_\infty \frac{1}{(1+H^\star)^2} . \quad (7)$$

The systematic studies of silver particle adsorption kinetics on PAH modified mica carried out by AFM and SEM methods confirmed that this process was diffusion controlled, with the initial rate proportional to the bulk concentration of particles. On the other hand, for long adsorption times, the saturation coverage was attained, which increased systematically with the ionic strength of the particle suspension. The adsorption kinetic runs were adequately reflected for the entire range of times and bulk concentrations by the random sequential adsorption (RSA) model. The experimental results proved, therefore, that it is feasible to produce uniform silver particle monolayers of desired coverage using the self-assembly process involving aqueous suspensions. The coverage, governing average spacing among deposited particles, can be regulated within broad limits by adjusting the ionic strength and the deposition time.

⋆ ⋆ ⋆

[1] H. Ohshima, Interface Science and Technology: Theory of Colloid and Interfacial Electric Phenomena, 1st edition (Elsevier, Amsterdam, 2006).

[2] K. Lowack, C. A. Helm, *Macromolecules* **28**, 2912 (1995).

[3] J. Schmitt, P. Mächtle, D. Eck , H. Möhwald, C. A. Helm, *Langmuir* **15**, 3256 (1999).

[4] Z. Adamczyk, Interface Science and Technology — Particles at Interfaces: Interactions, Deposition, Structure, 1st edition (Elsevier, Amsterdam, 2006).

Zeolite seeds precursors incorporated in the mesoporous framework: physicochemical and catalytic properties

Katarzyna Onik

Jerzy Haber Institute of Catalysis and Surface Chemistry Polish Academy of Sciences, Niezapominajek 8, 30-239 Kraków, Poland

Supervisor: Mirosław Derewiński

Synthetic zeolites are widely used as catalysts in petroleum refining, petrochemical processes and fine chemistry. Base elements of the zeolite are silicon, aluminum and oxygen. They are connected together in a form of a tetrahedron (SiO_4), (AlO_4) — called Primary Building Units (PBUs) — with a silicon atom in the middle and oxygen atoms at the corners. These tetrahedra are linked together by their corners. In some cases the presence of micropores limits the catalytic performance of the zeolites due to diffusion limitation, so the conception of using protozeolitic nanoclusters of few nanometers in size as precursors, which are introduced into thin layers enable to reach full catalytic potential by the increased accessibility to the active centers and facilitated transport of the reacting molecules.[1–3] *The aim of the work was preparation of the layered mesoporous materials containing protozeolitic species, their physicochemical characteristics and applications in a liquid phase isomerization.*

Synthesis of the new mesoporous solids based on the protozeolitic nanoclusters was carried out according to the method reported in literature.[4–6] Formations of very small particles (~ 5 nm in size) was proved with Dynamic Light Scattering (DLS) method. Zeolitic character of the protozeolitic species was confirmed by Fourier Transform Infrared (FTIR) spectroscopy. Band at ~550 cm^{-1} in the FTIR spectra of the protozeolitic particles indicated presence of five member rings, i.e. secondary building units (SBU), characteristic for the MFI structure. Bands corresponding to Si–O–Si inter-tetrahedral asymmetric and symmetric stretching (respectively 1225 and 753 cm^{-1}) were also observed. Scanning Electron Microscopy (SEM), Transmission Electron Microscopy (TEM), powder X-Ray Diffraction (XRD) and nitrogen adsorption-desorption measurements were used to investigate the textural properties of the obtained materials. The SEM and TEM analysis confirmed the layered structure of the samples (Fig. 1). Also, the XRD results confirmed the lamellar morphology of these materials. A low-angle X-ray diffraction pattern showed series of reflections characteristic for a well-ordered layered structures in the direction perpendicular to the [00l] plane, according to the relation interplanar spacing $(d_1/d_1) = 1$, $(d_1/d_2) = 2$, $(d_1/d_3) = 3$, etc. On the other hand the high-angle X-ray diffraction pattern pointed out reflections at $2\Theta =$ 5,7°; 21,8° and 23,0° which can be attributed to the zeolite structure. Post-synthesis high-temperature treatment resulted in disappearance of those reflections. Nitrogen adsorption-desorption experiments performed at 77 K showed isotherm type IV and characteristic hysteresis loop, associated with capillary condensation in the mesopores. The most common BET (Brunauer-Emmett-Teller)[7] method has been used to calculated specific surface area (from the linear part of the BET plot ($p/p_0 = 0{,}05 - 0{,}30$)). Pore size distributions has been calculated from the adsorption branch of the isotherm by the BJH (Barrett–Joyner–Halenda)[8] approach based on the modified Kelvin equation. Total pore volume was estimated from the amount of sorbent (N_2) at $p/p_0 = 0{,}95$. The N_2 sorption data proved a very high BET specific surface

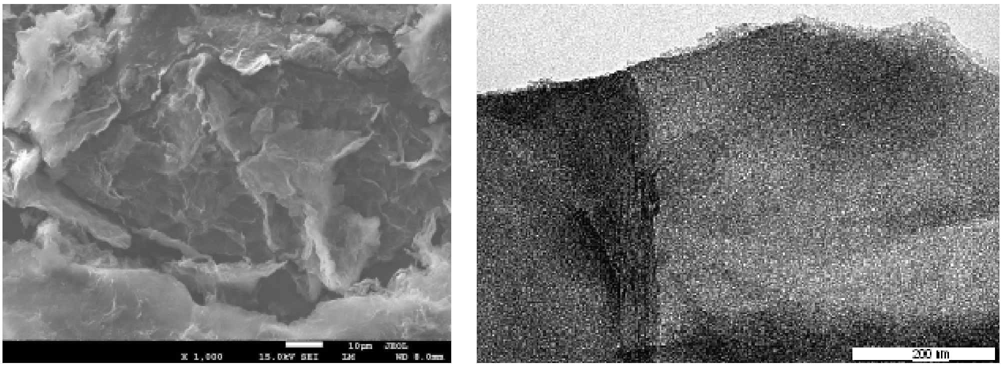

Figure 1: SEM and TEM images (mesoSi/Al(12)).

area (~ 1000 m^2/g), high sorption capacity (~1 cc/g) as well as presence of the mesopores (~2,5 nm). ^{27}Al MAS NMR data of the calcined materials showed that most of Al was tetrahedrally coordinated (peak at chemical shift of ~60 ppm), thus could generate protonic active centres. This calculation was supported by measurements of the acidity with pyridine sorption monitored with FTIR spectroscopy. Bands attributed to the vibration of pyridine molecules bonded to the protonic active centres (band at 1545 cm^{-1}) were found in the IR spectra recorded after desorption of pyridine at 150 – 400°C. The prepared mesoporous systems (denoted as mesoSi/Al(12), mesoSi/Al(40), where 12 and 40 is a Si/Al molar ratio of gels) showed remarkable catalytic performance for a liquid phase isomerization of α-pinene at 75°C, considerably better than that of amorphous aluminosilicate (SA, Si/Al(7)) and a standard MFI zeolite (Si/Al(40)) (Fig. 2). Effect of loading of the mesoSi/Al catalyst (25 – 250 mg) on conversion of α-pinene is presented in Fig. 3. In most cases, camphene and limonene (~50 and 40%, respectively) were major reaction products (Fig. 4). After a small decrease in selectivity to both products (~10%) their content remained almost unchanged during next 3 h of the reaction. Whereas, the selectivity to camphene did not change considerably with catalyst loading, lower loading of the mesoSi/Al (150 – 250 $mg_{catal}/5\ ml_{\alpha-pinene}$) resulted in a secondary transformation of limonene to other products (mainly α-terpinene and p-cymene).

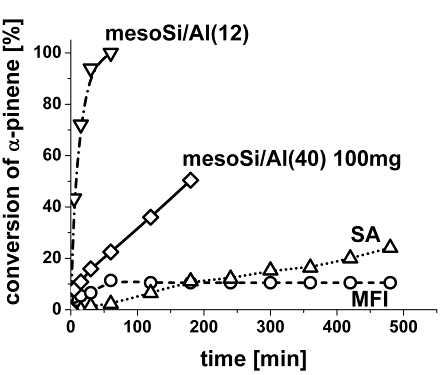

Figure 2: Conversion of α-pinene in the presence of selected catalysts (m_{cat} = 250 mg, $v_{\alpha-pinene} = 5$ ml).

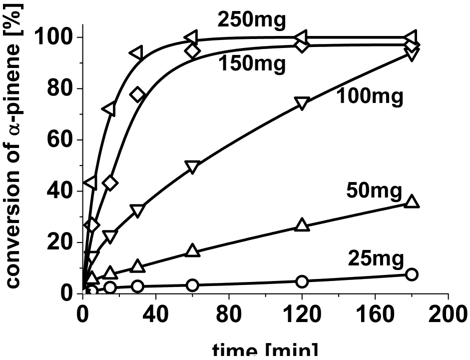

Figure 3: Effect of loading of mesoSi/Al(12) catalyst on conversion of α-pinene (in all experiments $v_{\alpha-pinene} = 5$ ml).

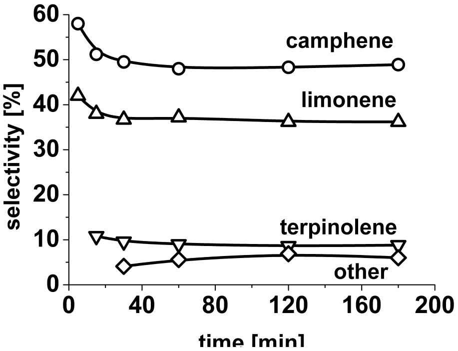

FIGURE 4: Isomerization selectivity of α-pinene to different products ($m_{\mathrm{cat}} = 50$ mg, mesoSi/Al(12), $v_{\alpha-\mathrm{pinene}} = 5$ ml).

The presented results have proved that synthesis of new mesoporous materials based on the MFI zeolite nanoclusters below 10 nm in size, led to highly active catalysts for low temperature, liquid phase isomerization of terpene hydrocarbons.

⋆ ⋆ ⋆

[1] Z. T. Zhang, Y. Han, F,-S. Xiao, S. I. Siu, L. Zhu, R. W. Wang, Y. Yu, Z. Zhang, B. S. Zou, Y. Q. Wang, H. P. Sun, D. Y. Zhao, Y. Wei, *J. Amer. Chem. Soc.* **123**, 5014 (2001).

[2] A. Corma, M. J. Diaz-Cabanas, *Microporous Mesoporous Mater.* **89**, 39 (2006).

[3] Y. Liu, W. Zhang, T. J. Pinnavaia, *Angew. Chem. Int. Ed.* **40**, 1255 (2001).

[4] C. J-M. Y. Houssin, Ph. D. Thesis, Nanoparcticles in zeolite synthesis (Technische Universiteit Eindhoven, Eindhoven, 2003).

[5] Y. Liu, T. J. Pinnavaia, *Chem. Mater.* **14**, 3 (2002).

[6] Y. Liu, W. Zhang, T. J. Pinnavaia, *Angew. Chem.* **113**, 1295 (2001).

[7] S. Brunauer, P. H. Emmet, E. Teller, *J. Am. Chem. Soc.* **60**, 309 (1938).

[8] E. P. Barrett, L. G. Joyner, P. P. Halenda, *J. Am. Chem. Soc.* **73**, 373 (1951).

Epitaxial layers of manganese oxides — surface properties and reactivity

Magdalena Szczepanik-Ciba

Faculty of Physics and Applied Computer Science, AGH University of Science and Technology, Mickiewicza 30, 30-059 Kraków, Poland
Jerzy Haber Institute of Catalysis and Surface Chemistry Polish Academy of Sciences, Niezapominajek 8, 30-239 Kraków, Poland

Supervisors: Józef Korecki, Robert Socha

Manganese oxides and mixed manganese-iron oxides on MgO(100) substrate were prepared under ultrahigh vacuum conditions and characterized in situ using Low Energy Electron Diffraction (LEED), X-Ray Photoelectron Spectroscopy (XPS) and ex-situ using Conversion Electron Mössbauer Spectroscopy (CEMS). Post-preparation oxidation of metallic Mn layers in a wide range of O_2 pressures and temperatures leads to formation of a MnO(100)-like surface structure, according to the LEED pattern. Mn 2p core excitation XPS spectra show the presence of Mn^{2+} cations with binding energy assigned to MnO. Two different mixed manganese-iron oxides were obtained under different preparation conditions on the MgO(100) substrate. $Fe_xMn_{1-x}O$ and $Fe_xMn_{3-x}O_4$ structures were confirmed by LEED, XPS and CEMS investigations.

The molecular level understanding of the catalytic reaction mechanisms, relaying on the model catalysts, is crucial for the design and optimization of industrial catalysts. However, while the field of heterogeneous catalysts is focused on the high-surface area catalytic materials studied under high pressure, the model approach to catalysis consists in investigations under idealized conditions (on single crystals surfaces at low pressures). It results in so called „pressure and material gap". To bridge these gaps, more sophisticated model catalysts, like metal nanoparticles supported on well-defined oxide surfaces are developed, called supported model catalysts. The variety of oxide surfaces is considerably increased, when thin epitaxial oxide films are used. On the other hand, to recognize the influence of the oxide substrate morphology on the catalytic reactions, the inverse model catalysts (oxide nanostructures deposited on metallic single crystal) can be employed.

Supported and unsupported manganese oxides were found to be active in various catalytic reactions, such as oxidation of carbon monoxide, methane and hydrocarbons and selective reduction of NO.[1–5] Thin epitaxial films of MnO_x have been studied on different single crystal substrates.[6–9] Such low dimensional oxide structures are very often a mixture of the most common and stable oxide phases (MnO, MnO_2, Mn_2O_3 and Mn_3O_4). It appears that synthesis of stoichiometric layers, important from the catalytic point of view, is difficult due to a large variety of possible Mn-oxidation states.

This paper is dedicated to the efforts towards fabrication of well-defined single-phase manganese oxide epitaxial films (MnO,

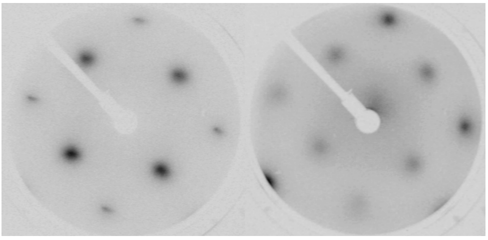

FIGURE 1: LEED pattern for the clean MgO(100) surface (left) and epitaxial MnO layer (right). Both images were collected at the electron energy 86 eV.

TABLE 1: Fitted parameters of Mn $2p$ XPS spectrum for MnO-stoichiometry oxide grown on MgO(001) substrate.

Component	BE [eV]	[%]	Interpretation
B	640,6	15,9	MnO_{1-x}
C	641,7	47,5	MnO
D	643,3	36,6	Mn^{3+} and Mn^{4+} in oxides
s	645,2 – 649,6	–	Shake-up satellites

$\mathrm{Fe}_x\mathrm{Mn}_{3-x}\mathrm{O}_4$, $\mathrm{Fe}_x\mathrm{Mn}_{1-x}\mathrm{O}$) on the MgO(100) single crystals used as model catalysts or oxide supports.

MnO_x epitaxial layers were fabricated by post oxidation of metallic Mn films with the thickness of approximately 20 nm at elevated temperatures. Satisfactory results were obtained for temperatures in the range 520 – 620 K and oxygen pressures from $1 \cdot 10^{-7}$ mbar to $1 \cdot 10^{-6}$ mbar. Fig. 1 shows a LEED pattern for the clean MgO(100) substrate (left) and for the MnO_x layer (right) at the electron energy 86 eV. Similarly to the MgO(100) substrate, the MnO_x surface unit cell is square, and both structures have similar lattice constants, which suggests that the MnO_x film might have the same crystallographic structure as MgO, i.e. the rock salt one. This would point toward the MnO-stoichiometry oxide, which crystallizes in this structure. Such a conclusion is consistent with the XPS measurements. Fig 2 shows the Mn $2p$ XPS spectrum, which fitted parameters are listed in Table 1. The most intensive component at the electron binding energy (BE) of 640,6 eV corresponds to stoichiometric bulk-like MnO, the component at lower BE can be ascribed to not fully oxidized manganese deep layers. The peak at BE of 643,3 eV can be assigned to Mn^{3+} and Mn^{4+} in higher oxides.[10]

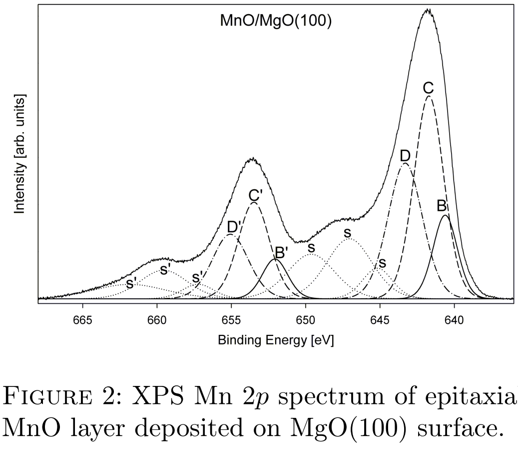

FIGURE 2: XPS Mn $2p$ spectrum of epitaxial MnO layer deposited on MgO(100) surface.

The comparison of pure and mixed oxide systems can show potential routes for the synthesis of catalytic systems. Therefore, the synthesis of mixed iron-manganese oxides was compared to that of MnO and $\mathrm{Mn}_3\mathrm{O}_4$. Our attempts to obtain the spinel $\mathrm{Mn}_3\mathrm{O}_4$ phase by the direct reactive deposition of Mn on MgO(100), revealed an experimental problem connected with the oxidation of manganese in the evaporator. Thus, $\mathrm{Fe}_x\mathrm{Mn}_{3-x}\mathrm{O}_4$ layers were obtained on a magnetite epitaxial thin film seed layer. The procedure of preparing the (100)-oriented $\mathrm{Fe}_3\mathrm{O}_4$ films is well-known[11] and the main idea was to allow Mn

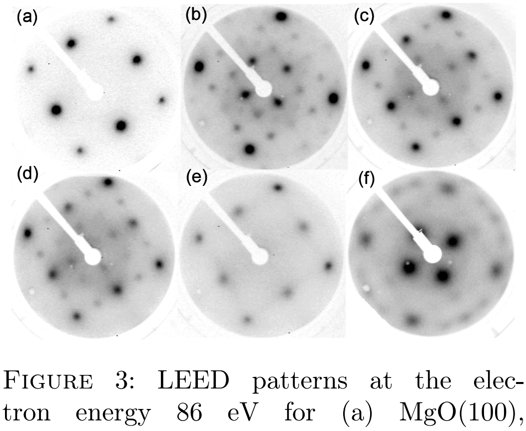

FIGURE 3: LEED patterns at the electron energy 86 eV for (a) MgO(100), (b) $\mathrm{Fe}_3\mathrm{O}_4$/MgO(100), post oxidized ($p_{\mathrm{O}_2} = 1 \cdot 10^{-7}$ mbar, $T = 520$ K) deposits of (c) 2 Å Mn/$\mathrm{Fe}_3\mathrm{O}_4$/MgO(100), (d) 6 Å Mn/$\mathrm{Fe}_3\mathrm{O}_4$/MgO(100), (e) 50 Å Mn/$\mathrm{Fe}_3\mathrm{O}_4$/MgO(100), and (f) post oxidized ($p_{\mathrm{O}_2} = 1 \cdot 10^{-5}$ mbar, $T = 770$ K) deposit of 50 Å Mn/$\mathrm{Fe}_3\mathrm{O}_4$/MgO(100).

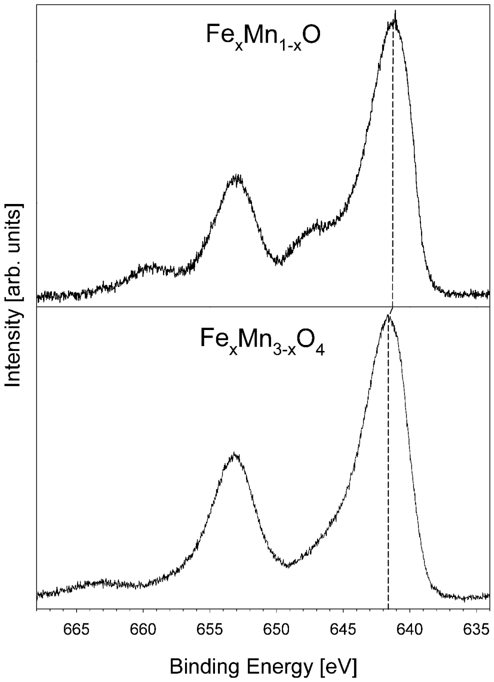

FIGURE 4: XPS Mn 2p spectra for the $Fe_xMn_{1-x}O$ and $Fe_xMn_{3-x}O_4$ systems.

atoms to diffuse into magnetite structure and to replace iron in the spinel lattice. Fig. 3 illustrates the LEED patterns of the 16 nm $Fe_3O_4(100)$ film and for the further steps of preparation, i.e. deposition of thin metallic-Mn films (total thickness of 5 nm) followed by oxidation ($p_{O_2} = 1\cdot10^{-7}$ mbar) at 520 K. It can be observed that the surface unit cell changes from spinel-like to $Fe_{1-x}Mn_xO$ rock salt-like with the increase of the nominal thickness of the Mn deposit.

However, by modifying of the oxidation conditions one can synthesize the spinel structure (Fig. 3f). Fig. 4 shows that post-oxidation of the MnO-like structure under $1\cdot10^{-5}$ mbar O_2 for 20 minutes at 770 K[12] significantly changes the shape of Mn 2p spectra indicating increased contribution of higher oxidation states (Mn^{3+} and Mn^{4+}). The corresponding CEMS spectrum (Fig. 5 bottom) shows a pattern with two magnetic and one paramagnetic component, which can be compared with the one of a 10 nm thick stoichiometric magnetite epitaxial layer on MgO(100) (Fig. 5 top). The fingerprint of magnetite are two spectral components corresponding to the Fe^{3+} ions at tetrahedral A sites (hyperfine magnetic field $B_{\mathrm{hf}} = 47{,}9$ T and isomer shift $IS = 0{,}27$ mm s^{-1}) and to $Fe^{2,5+}$ (Fe^{2+} and Fe^{3+}) ions at octahedral B sites ($B_{\mathrm{hf}} = 43{,}5$ T and $IS = 0{,}65$ mm s^{-1}). The A/B intensity ratio is close to 0,5. For the manganese-iron oxide, it is clearly seen that the manganese atoms diffused into the spinel structure, which strongly affects the intensity and width of the components. The component A remains narrow (population of 20,2%) while the component B shows a wide hyperfine magnetic field distribution and a larger population (78,6%). The A/B ratio is equal to 0,26. Moreover, the hyperfine field of the component A remains almost unchanged (47,5 T) and the isomer shift is only slightly larger (0,29 mm s^{-1}) while the average B_{hf} and the isomer shift of B component are strongly reduced (0,43 mm s^{-1} and

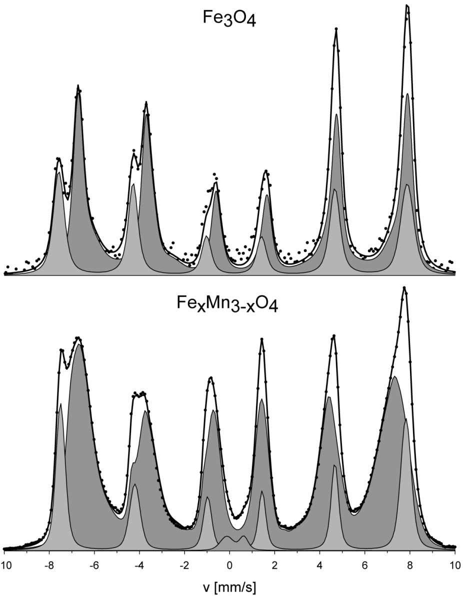

FIGURE 5: CEMS spectra of the epitaxial $Fe_3O_4(100)$ (top) and $Fe_xMn_{3-x}O_4(100)$ (bottom) films on the MgO(100) substrate. Lighter components correspond to tetrahedral sites (A), darker ones are assigned to octahedral sites. FeO-like component also appears in $Fe_xMn_{3-x}O_4$.

39,3 T) as compared to pure magnetite. It is worth mentioning that, in the inverse spinel structure, the tetrahedral sites are situated far away from each other and from the octahedral sites. Hence we conclude that the Mn atoms predominantly substitute the Fe atoms in the tetrahedral sites, which reduces the intensity of the A component, without leaving its Mössbauer parameters unchanged. Additionally, because manganese prefers higher valence states, the Mn ions in the spinel lattice can have the oxidation state higher than 3+, in agreement with the XPS results (compare Fig. 4). For the charge neutrality this requires that some Fe^{3+} cations at the A sites were reduce to Fe^{2+}. It might be the reason of increasing IS for the component A and broadening of component B. This conclusion is in agreement with Takaobushi et al.[13] and in opposition to the statement of Oliveira et al.[14]

In summary, epitaxial MnO, $Fe_xMn_{x-1}O$ and $Fe_xMn_{3-x}O_4$ layers on MgO(100) were synthesized and characterized. It was found that Mn atoms enter preferentially the tetrahedral sites of the spinel structure.

⋆ ⋆ ⋆

[1] W. S. Kijlstra, D. S. Brands, E. K. Poels, A. Bliek, *J. Catal.* **171**, 208 (1997).

[2] A. Nishino, *Catal. Today* **10**, 107 (1991).

[3] M. A. Baltanas, A. B. Stiles, J. R. Katzer, *Appl. Catal.* **28**, 13 (1986).

[4] G. J. Hutchings, M. S. Scurrell, J. R. Woodhouse, *Appl. Catal.* **38**, 157 (1988).

[5] M. Kramer, T. Schmidt, K. Stowe, W. F. Maier, *Appl. Catal. A* **302**, 257 (2006).

[6] A. Chassé, Ch. Langheinrich, M. Nagel, T. Chassé, *Surf. Sci.* **605**, 272 (2011).

[7] F. Li, G. Parteder, F. Allegretti, C. Franchini, R. Podloucky, S. Surnev, F. P. Netzer, *J. Phys.-Condens. Matter* **21**, 134008 (2009).

[8] G. A. Rizzi, R. Zanoni, S. Di Siro, L. Perriello, G. Granozzi, *Surf. Sci.* **462**, 187 (2000).

[9] X. J. Xing, Y. P. Yu, L. M. Xu, S. X. Wu, S. W. Li, *J. Phys. Chem. C* **112**, 15526 (2008).

[10] H. W. Nesbitt, D. Banerjee, *Am. Mineral.* **83**, 305 (1998).

[11] N. Spiridis, R. P. Socha, B. Handke, J. Haber, M. Szczepanik, J. Korecki, *Catal. Today* **169**, 24 (2011).

[12] F. Allegretti, C. Franchini, V. Bayer, M. Leitner, G. Parteder, B. Xu, A. Fleming, M. G. Ramsey, R. Podloucky, S. Surnev, F. P. Netzer, *Phys. Rev. B* **76**, 165428 (2007).

[13] J. Takaobushi, M. Ishikawa, S. Ueda, E. Ikenaga, J. Kim, M. Kobata, Y. Takeda, Y. Saitoh, M. Yabashi, Y. Nishino, D. Miwa, K. Tamasaku, T. Ishikawa, I. Satoh, H. Tanaka, K. Kobayashi, T. Kawai, *Phys. Rev. B* **76**, 205108 (2007).

[14] L. C. A. Oliveira, J. D. Fabris, R. R. V. A. Rios, W. N. Mussel, R. M. Lago, *Appl. Catal. A-Gen.* **259**, 253 (2004).

STRUCTURAL, MAGNETIC AND ELECTRONIC PROPERTIES OF CONDENSED MATTER

Comparison of two methods of determinig the critical exponents of thallium-based superconductor

Maciej Chrobak

Faculty of Physics and Applied Computer Science, AGH University of Science and Technology, Mickiewicza 30, 30-059 Kraków, Poland

Supervisors: Wiesław Marek Woch, Andrzej Kołodziejczyk

In this paper the two ways of obtaining the critical exponents was compared. The Calculations were done from the resistance measurements of the bulk $(Tl_{0,5}Pb_{0,5})Sr_2(Ca_{0,7}Gd_{0,3})Cu_2O_z$ *high temperature superconductor. The calculations were performed from the zero resistance critical temperature* T_{c0} *up to 116 K which was above onset critical temperature* T_{c_onset}*. The results obtained by these two methods are similar to each other.*

The very short coherence length as well as the large anisotropy of high temperature superconductors (HTS) affect on the thermal fluctuations around the superconducting transition. Within the critical region one can notice the competition between the critical fluctuations at lower temperatures and the Gaussian (stochastic) fluctuations at the temperatures well above the critical temperatures that depend on the applied magnetic field as well as the applied pressure.[1–3] The Gaussian fluctuations can give the information on the effective dimensionality of superconductivity in HTS materials. The thallium based superconductors are very rewarding subjects of these studies because of their special behavior of widening of the resistive transitions upon the influence of the applied magnetic field. Because of huge anisotropy the superconductors have generally the three-dimensional (3D) to the two-dimensional (2D) transition in the critical region for polycrystalline, single crystal as well as for thin film samples.[4–7]

In this paper the two methods were compared themselves to determine the critical exponents above the critical temperature T_c. This comparison was performed on the $(Tl_{0,5}Pb_{0,5})Sr_2(Ca_{0,7}Gd_{0,3})Cu_2O_z$ bulk superconductor that superconducting properties ware measured and analyzed in the paper.[8]

The sample was prepared by the sol-gel method according to the procedure described in details in the paper.[9] The temperature dependence of the resistance was carried out using the four-point ac method using Stanford SR 830 lock-in nanovoltometer. The temperature from 77 K to 130 K was monitored by a Lake Shore temperature controller employing a chromel-gold-0,07% Fe thermocouple with an accuracy of ±0,05 K. The electrical contacts were made by silver paint which were sintered at 300°C. The critical temperatures of this sample are as follows: $T_{c\_50\%}$ = 102,7 K; T_{c0} = 90,8 K and the onset temperature T_{c_onset} = 109,3 K. The transition width $\Delta T_{90\%–10\%}$ = 8,9 K without the applied magnetic field. The measurements were repeated ten times to suppress the noise presents in the measurement system. The resistance versus temperature of $(Tl_{0,5}Pb_{0,5})Sr_2(Ca_{0,7}Gd_{0,3})Cu_2O_z$ with marked T_{c0}, $T_{c\_50\%}$ and T_{c_onset} is shown in the Fig. 1. The inset shows the temperature derivative of the resistance.

In this paper the thermal fluctuations were studied using the following formula:[10]

$$\Delta\sigma = K\varepsilon^{-\lambda} , \tag{1}$$

where $\varepsilon = (T - T_c)/T_c$, λ is a critical exponent and K is a constant. The temperature dependence of conductivity is defined within the Ginzburg-Landau mean field approximation:[11]

$$\Delta\sigma(T) = \frac{1}{R(T)} - \frac{1}{R_R(T)} , \tag{2}$$

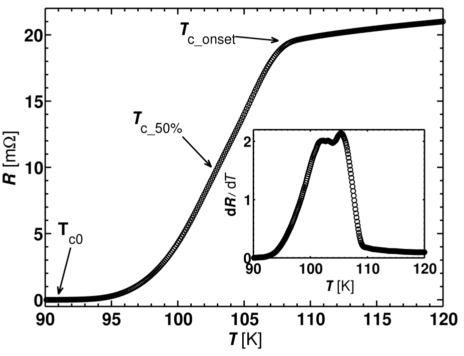

FIGURE 1: Resistance versus temperature of $(Tl_{0,5}Pb_{0,5})Sr_2(Ca_{0,7}Gd_{0,3})Cu_2O_z$ with marked T_{c0}, $T_{c\_50\%}$ and T_{c_onset}. Inset shows the temperature derivative of the resistance.

where $R(T)$ is the measured resistivity and $R_R(T)$ is the resistivity obtained by the linear extrapolation of the resistivity data from about 130 K down to the onset temperature.[12]

Assuming that the resistivity $R(T)$ follows a linear temperature dependence at higher temperatures, it is obtained by linear fitting of the resistivity curve. The determination of $\Delta\sigma$ involved the determination of R_R for temperatures near T_c by extrapolating the high temperature behavior of as follows:

$$R_R(T) = R_0 + \left(\frac{dR}{dT}\right) T \ , \qquad (3)$$

where R_0 and dR/dT are constants.

The first approach (method I) to determine critical exponents was proposed in the paper[1]. To obtain values of critical exponents λ the Eq. (1) was transformed in to the following formula:

$$\chi^{-1} = -\left(\frac{d\ln(\Delta\sigma)}{dT}\right)^{-1} = \frac{1}{\lambda}(T - T_c) \ , \qquad (4)$$

and the inverse slope of fitted line to linear regions of the χ^{-1} versus temperature dependence is the searched critical exponent λ value. The temperature dependence of the χ^{-1} was plotted in the Fig. 2.

The second way (method II) to determine critical exponents was described in the paper[12]. In this approach we transform Eq. (1) into:

$$\log_{10}(\Delta\sigma) = -\lambda \log_{10}(\varepsilon) \ , \qquad (5)$$

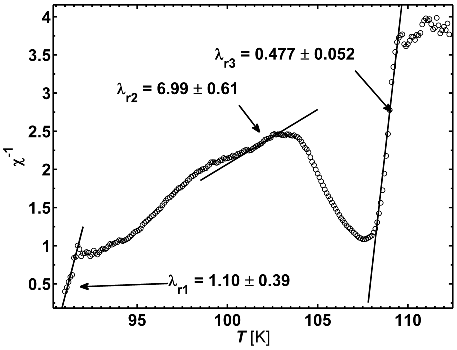

FIGURE 2: χ^{-1} versus temperature for $(Tl_{0,5}Pb_{0,5})Sr_2(Ca_{0,7}Gd_{0,3})Cu_2O_z$ with lines fitted to Eq. (4) in selected regions.

where the searched value of critical exponent λ is equal to negative value of the slope of the fitted line to linear parts of the dependence from Eq. (5). The above dependence was plotted in the Fig. 3.

To compare those two methods of determining critical exponents we chose three regions near the characteristic points of superconducting transition: above T_{c0}, near $T_{c\_50\%}$ and around T_{c_onset}. The complete list of selected regions with details is shown in Table 1.

λ value obtained from method I in the first region „r1" is 1,1±0,4. The result is saddled with a big measurement uncertainty, the relative uncertainty is 36%. This is caused by use of the derivative to calculate the value of χ^{-1}. The value of λ acquired from method II is

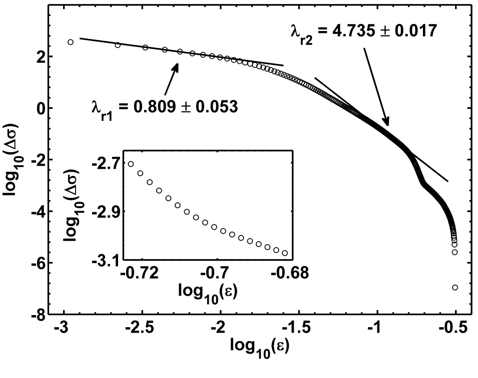

FIGURE 3: $\log_{10}(\Delta\sigma)$ versus $\log_{10}(\varepsilon)$ for $(Tl_{0,5}Pb_{0,5})Sr_2(Ca_{0,7}Gd_{0,3})Cu_2O_z$ with lines fitted to Eq. (5) in selected regions. Inset shows extended „r3" region where we did not obtain linear region.

TABLE 1: Obtained values of critical exponents λ from both methods in selected regions.

Region	Temperature range	method I	$\log_{10}(\varepsilon)$ range	method II
r1	91 ÷ 91,70	1,1 ± 0,4	$-2,66 \div -2,00$	0,81 ± 0,05
r2	101 ÷ 103	7,0 ± 0,6	$-0,95 \div -0,87$	4,74 ± 0,02
r3	108,1 ÷ 109,5	0,48 ± 0,05	T_c used to calculate ε was 107,8 K	
			$-2,56 \div -1,80$	0,473 ± 0,011

$0{,}81 \pm 0{,}05$. This result is more accurate compared to the previous one, the is 6%. There is a big difference between results obtained from the methods we used. The result from method I is 35% higher than the result from method II. The difference in the results achieved and less accurate result for method I can be caused by using a larger number of numerical calculations.

In the second region „r2" there was larger discrepancy between obtained results, $\lambda = 7{,}0 \pm 0{,}6$ (method I) and $\lambda = 4{,}74 \pm 0{,}02$ (method II). In this case the value obtained from method I is larger than value from method II by 48%. Relative uncertainty values are respectively 9% and 0,5%. As we can see linear fit in both methods were more accurate but still like in the region „r1" we did not obtain comparable results.

In the third region „r3" we obtain the value of critical exponent at level $0{,}48 \pm 0{,}05$ using method I. Unfortunately we did not get confirmation of this fact by using method II. In the same temperature range we did not obtain linear region (see inset Fig. 3). This may be caused by either too much number of inaccurate numerical calculations in method I or from T_c used to calculate function ε in method II. Considering the problem of the difference between the results obtained in the region „r3" we decided to use a different T_c to check how strongly the choice of T_c influences on the value of critical exponent achieved from method II. As T_c we have taken center of the peak of the first derivative of measured resistance. This value was 107,8 K. The obtained results are shown in the Fig. 4. After changing T_c the boundaries of „r3" region have changed to $-2,56 \div -1,80$. From fitting line to Eq. (5) in this region we got that the λ is $0{,}473 \pm 0{,}011$. This result is equal in the limit of measurement uncertainty to the result achieved from method I in the same area. This shows how strongly the results from method II depend on chosen T_c.

Comparing these two methods of determining critical exponents we can say that in method I, which was based on formula (4), obtained data is not smooth because of using derivative to calculate it. This fact causes problems in determining the linear regions and the result of fitting is saddled with large uncertainty. In the method II, which is based on formula (5), there is only a function of decimal logarithm thus obtained data are much smoother compared to the previous method. When a more detailed analysis of formulas used in these two methods is done, we see that the first method does not depend on T_c while the second one does. The domain of Eq. (4) is between $R > 0$ and $1/R(T) > 1/R_R(T)$ and we can analyze the whole area of superconducting transition. The domain of Eq. (5) is more complicated because of logarithm function on the two sides of equation. On the left side we have the same restrictions as in the first case. Additional terms implies from the right side of the equation, which are as follows: $\varepsilon > 0$ and $T_c \neq 0$. This makes that the final result

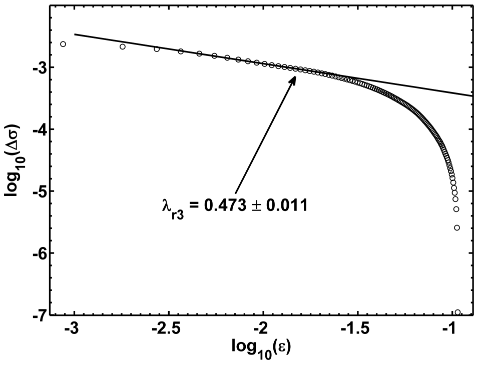

FIGURE 4: $\log_{10}(\Delta\sigma)$ versus $\log_{10}(\varepsilon)$ for $(Tl_{0,5}Pb_{0,5})Sr_2(Ca_{0,7}Gd_{0,3})Cu_2O_z$ where T_c was 107,8 K. Line was fitted to Eq. (5) in the region corresponding to the „r3" region.

depends on the temperature which was used to calculate ε.

In conclusion we calculated critical exponents of bulk $(Tl_{0,5}Pb_{0,5})Sr_2(Ca_{0,7}Gd_{0,3})Cu_2O_z$ high temperature superconductor using the two different ways. The calculation were performed in three regions above T_{c0}, near $T_{c\_50\%}$ and around T_{c_onset}. The obtained results do not fit well together which was caused by the use of the derivative in the calculation (method I) and strong dependence of ε from T_c (method II). The results obtained using the method I were determined with large uncertainty about several times greater than the results from the method II.

Based on the analysis carried out by us in this work, we are not in the position to determine which method is better to determine the critical exponents. The method I gives a picture of the whole superconducting transition but the received data is not smooth. To obtain more accurate results from this method the measurements must be repeated more times. The results from method II are more precise but it is impossible to analyze the entire superconducting transition. Therefore, to get the best results it is best to use both methods simultaneously.

Author would like to thank Professor G. Gritzner and his team from Institute for Chemical Technology of Inorganic Materials, Johannes Kepler University, A 4040 Linz, Austria for providing the sample.

⋆ ⋆ ⋆

[1] P. Pureur, R. Menegotto Costa, P. Rodrigues Jr., J. Schaf, J. V. Kunzler, *Phys. Rev. B* **47**, 11420 (1993).

[2] R. Menegotto Costa, P. Pureur, M. Gusmao, S. Senoussi, K. Behnia, *Phys. Rev. B* **64**, 214513 (2001).

[3] L. Mendoca Ferreira, P. Pureur, H. A. Borges, P. Lejay, *Phys. Rev. B* **69**, 212505 (2004).

[4] D. H. Kim, K. E. Gray, M. D. Trochet, *Phys. Rev. B* **45**, 10801 (1992).

[5] H. M. Duan, W. Kiehl, C. Dong, A. W. Cordes, M. J. Saeed, D. L. Viar, A. M. Hermann, *Phys. Rev. B* **43**, 12925 (1991).

[6] W. M. Woch, M. Chrobak, A. Kołodziejczyk, *Acta Phys. Pol. A* **118**, 389 (2010).

[7] N. H. Ahmad, N. A. Khan, A. K. Yahya, *J. Alloys Comp.* **492**, 473 (2010) and references therein.

[8] W. M. Woch, R. Zalecki, A. Kołodziejczyk, H. Sudra, G. Gritzner, *Supercond. Sci. Technol.* **21**, 085002 (2008).

[9] H. Sudra, G. Gritzner, *Physica C* **443**, 57 (2006).

[10] L. G. Aslamazov, A.I. Larkin, *Sov. Phys. Solid State* **10**, 875 (1968); A. I. Larkin, A. A. Varlamov, in: Superconductivity, Eds. K.H. Bennemann, J.B. Ketterson, (Vol. 1, Springer-Verlag, Berlin 2008), p. 369.

[11] V. I. Ginzburg, L. D. Landau, *Zh. Exp. Teor. Fiz.* **20**, 1064 (1950).

[12] A. Mohanta, D. Behera, *Physica C* **470**, 295 (2010).

Characterization of recrystallization phenomena in commercially pure titanium based on EBSD technique

Mariusz Jędrychowski

Faculty of Physics and Applied Computer Science, AGH University of Science and Technology, Mickiewicza 30, 30-059 Kraków, Poland

Supervisors: Jacek Tarasiuk†, Paul Lipinski‡
† AGH University of Science and Technology, Kraków, Poland
‡ Ecole Nationale d'Ingénieurs de Metz, Metz Cedex, France

Characterization of texture and microstructure evolution during a complete thermo-mechanical treatment of commercially pure titanium (HCP-Ti) based on the data obtained from EBSD (Electron Backscatter Diffraction) experiment is presented. Examined HCP titanium was cold rolled to reach various degrees of thickness reduction: 20%, 40% *and* 60%. *Next, annealing in air atmosphere was conducted at different conditions to achieve the recrystallized state. EBSD topological maps were measured on surface of each sample. Strong heterogeneity of deformed titanium microstructures is described with focus on the important role of twinning mechanisms. Texture evolution in investigated titanium appears to be limited, especially in recrystallized state. However, some subtle mechanisms are discussed.*

A thorough understanding of the physical and metallurgical phenomena occurring in a polycrystalline metal over its thermo-mechanical processing, recrystallization is one of the most important among them,[1] is essential for the control of its final properties. Therefore, the role played by this phenomena is valid from industry and technological application points of view. For instance, many applications of aluminum and steel alloys such as car bodies or beverage cans involve deep-drawn process. Such deformation can be highly inhomogeneous due to the material texture (non-random distribution of grains orientation) and thus the formability of final product is reduced. For example, wavy folds have been observed on the top of an aluminum can at the end of the production process. However, appropriate thermo-mechanical treatment (deformation and annealing) has been successfully applied to balance aluminum texture and solve this problem.[2]

Modern technologies more often make use of hexagonal metals, due to their exceptional properties. Today, mentioned metals are applied in various industry branches, such as bioengineering, implantology (titanium implants), nuclear power engineering (zirconium envelopes of fuel pencils), aircraft industry (magnesium alloys sheets), stomatology (zirconium and titanium implants) and modern metallurgy (titanium steels).

Titanium is one of the most popular hexagonal metal being investigated. However, the satisfactory theory of the physical phenomena taking place during cold rolling deformation and following annealing treatment of titanium is still far from being achieved.

The main purpose of this work is thus to focus on the characterization of texture and microstructure evolution in hexagonal titanium during complete thermo-mechanical treatment, especially at recrystallization stage. In order to achieve this goal, EBSD (Electron Backscatter Diffraction) equipment is used.

EBSD (Electron Backscatter Diffraction) is a modern and promising experimental technique which allows to represent the information about texture and microstructure in the form of a topological map comprised of a very large number of acquisitioned orienta-

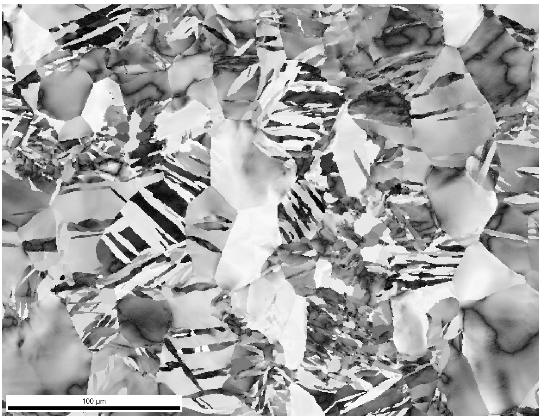

FIGURE 1: EBSD map of Ti microstructure rolled to 20% of reduction.

tion points. From these huge amounts of data, many material parameters may be obtained directly and analyzed statistically.

Commercially pure HCP titanium (grade 2) in a fully recrystallized state was cold rolled in several passes to reach different thickness reduction ratios: 20%, 40% and 60%. Sample reference system is thus defined by Rolling Direction (RD), Transverse Direction (TD) and Normal Direction (ND). For recrystallization study, the deformed samples were then heat-treated in air at various annealing temperatures (500°C, 600°C, 715°C, 750°C) and times (5 min, 15 min, 1 h, 4 h). To characterize both deformed and recrystallized states, EBSD topological maps were measured on RD-TD and RD-ND surface of each sample. The measurements were carried out in the middle cross-section of each sample to avoid the influence of potential surface effects. Moreover, special attention was given to reach statistically representative and trustworthy data.

Initial state microstructure of investigated titanium comprise of equiaxed grains, whose average diameter grain size is 22 μm.

The beginning of deformation process in titanium is mainly governed by twinning deformation mode, which plays significant role in the accommodation of externally imposed strain. In the sample rolled up to 20%, twins appear in the form of narrow and highly elongated grains. Moreover, it is seen that secondary twins are created in the most of already twinned grains (Fig. 1).

As a result of twinning, the high fragmentation of most of the initially equiaxed grains is seen. However, some of the grains resist to this mechanism and remain untwined. Observation of RD-TD surface reveals that these grains can be described as wide and broad oval areas of continuous orientation change probably produced by slip deformation mode, some of them can be seen in the Fig. 2. The main feature of the deformed microstructure is thus a strong heterogeneity.

As deformation proceeds, the RD-TD section of the microstructure can be described by big isolated islands of untwined areas surrounded by a sea of fragmented grains. In the case of RD-ND section, untwined areas are much more elongated, hence lamellar structure is formed.

Extensive twinning can be analyzed using misorientation parameter, which is defined as a difference in crystallographic orientation between two grains in a polycrystalline material. Fig. 3 presents the distribution of the lowest misorientations calculated for a particular crystallographic direction.

Two main peaks are observed for the data obtained from RD-TD surface (Fig. 3).

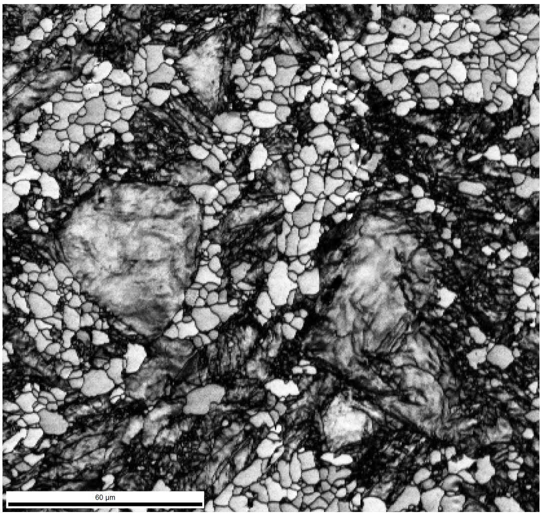

FIGURE 2: EBSD map presenting new grains, which appeared after annealing (1 h, 500°C) of sample rolled by 20%.

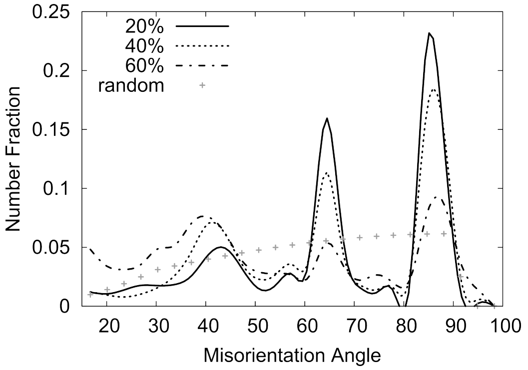

FIGURE 3: Misorientations distribution at various thickness reductions.

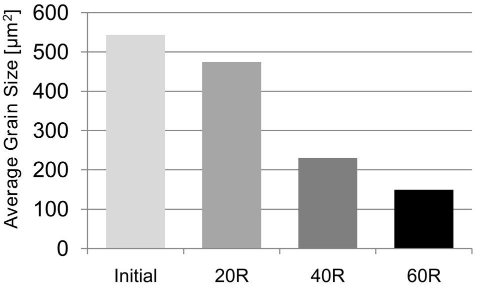

FIGURE 4: Average area grain size in μm^2 (RD-TD plane). The names of last three bars (20R, 40R and 60R) refer to annealed state of samples, which were previously deformed to 20%, 40%, 60% of thickness reduction.

Based on their position, active twin systems can be determined: tensile $\{10\bar{1}2\}\langle 10\bar{1}\bar{1}\rangle$ (85° around $\langle 2\bar{1}\bar{1}0\rangle$ axis) and compressive $\{11\bar{2}2\}\langle 11\bar{2}\bar{3}\rangle$ (64° around $\langle 10\bar{1}0\rangle$ axis) twins.[3] Increasing deformation results in a decrease of twin misorientations fraction, what is expected due to grain refinement process. The same tendency appears on RD-ND surface. The only difference is the opposite fraction ratio of twin misorientations.

It is concluded that annealing performed at 715°C over 1 h leads to fully reconstructed microstructures in all investigated samples, due to the activation of recrystallization process. Detailed analysis of the beginning of annealing treatment reveals that newly created grains tend to gather in form of clusters. Such grains are located in highly fragmented areas (Fig. 2), which suggests that these regions are preferred places for nucleation of new grains, whereas big, untwined grains are replaced by new population of grains rather at final stage of recrystallization.

The influence of the prior deformation degree on average grain size after recrystallization has been also analyzed. Based on the results presented in the Fig. 4, it is noted that the higher deformation before annealing, the smaller grain size after annealing.

Concerning texture evolution in investigated titanium, it is analyzed using Orientation Distribution Functions — ODF's which were calculated from EBSD data with imposed orthotropic sample symmetry. Grain orientations are described using Euler angles (φ_1, ϕ, φ_2) according to Bunge definition.[4] Crystal coordinate system is defined as: $X = [2\bar{1}.0]$, $Y = [10.0]$, $Z = [00.1]$. It is common to focus on selected ODF cross-sections, as it is difficult to analyze whole three-dimensional ODF. In the case of titanium the chosen cross-section is $\varphi_1 = 0°$,(Fig. 5) because it contains the most important information about texture changes. The information about annealing treatment and obtained average diameter grain size (calculated with the grain boundary limit of 15° is also presented in the Fig. 5.

Deformation of the investigated titanium results in continuous strengthening of one main texture component (0°, 35°, 30°). During annealing textures evolve in a more complex way, which clearly depends on the amount of stored energy. It has been reported[5] that in titanium deformed by 80% cold rolling, primary recrystallization does not affect the stability of the main texture component obtained after deformation, which is (0°, 35°, 30°) according to crystal reference system used in this letter.

Only extensive annealing gives rise to more significant texture evolution in the aftermath of grain growth process. This evolution is described by a movement from (0°, 35°, 30°) to (0°, 35°, 0°). The results presented in this paper reveal that grain growth is also necessary to start texture evolution. However, in this case, the final texture depends much more on the prior deformation degree. For instance, the texture of the sample deformed by 20% of thickness reduction evolves not much —

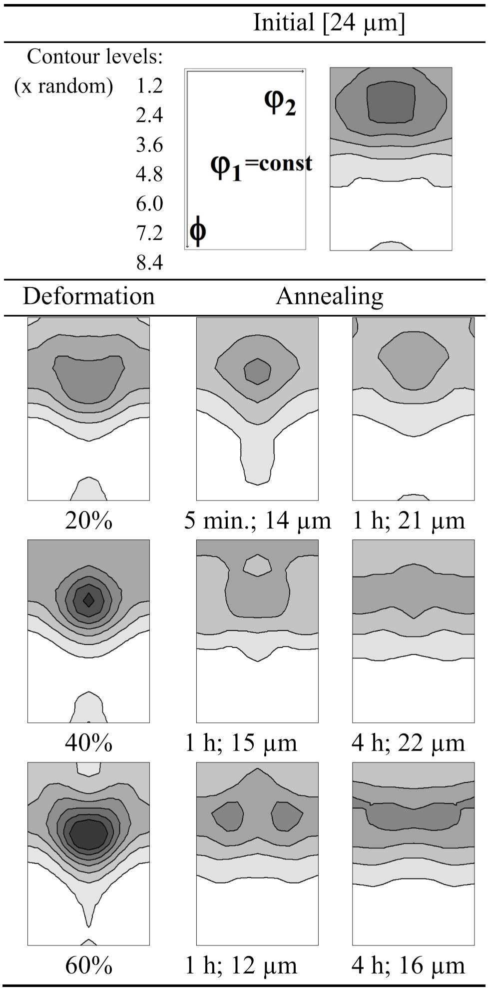

FIGURE 5: Texture evolution of Ti during annealing in 715°C.

main texture components are stable even after significant grain growth (21 μm). At the same time, in the sample deformed by 40% and annealed to obtain comparable grain size (22 μm), it is seen that the main deformation component (0°, 30°, 30°) is transformed into fiber (0°, 30°, 0° – 60°). Finally, in the sample deformed by 60% and annealed 1 h, the deformation component (0°, 35°, 30°) is split without significant grain growth (12 μm).

This work focus on the investigation of texture and microstructure evolution of commercially pure HCP-Ti caused by cold rolling and subsequent annealing. It is confirmed that compressive and tensile twins play significant role during deformation. Appropriate heat treatment leads to equiaxed microstructures. It is shown that parameters important from the viewpoint of final properties, such as: grain size and texture are strongly related with the level of deformation: the size of recrystallized grains clearly depends on the prior rolling reduction degree, which is consistent with the conclusion that highly fragmented areas obtained by higher deformations are preferable places for nucleation, whereas the analysis of ODF's cross-sections reveals that apart from the grain growth mechanisms, deformation degree strongly influences annealing textures.

Mariusz Jędrychowski has been partly supported by the EU Human Capital Operation Program, Polish Project No. POKL.04.01.01-00-434/08-02.

⋆ ⋆ ⋆

[1] F. J. Humphreys, M. Hatherly, Recrystallization and Related Annealing Phenomena, 2nd edition (Pergamon, 2004).

[2] O. Engler, V. Randle, Introduction to Texture Analysis; Macrotexture, Microtexture, and Orientation Mapping, 2nd edition (CRC PressINC, 2009).

[3] Y. B. Chun, S. H. Yu, S. L. Semiatin, S. K. Hwang, *Mater. Sci. Eng. A* **398**, 209 (2005).

[4] H. J. Bunge, Texture analysis in materials science — mathematical methods (London: Butterworths, 1982).

[5] N. Bozzolo, N. Dewobroto, T. Grosdidier, F. Wagner, *Mater. Sci. Eng. A* **397**, 346 (2005).

Magnetostriction in magnetite single crystals and the concept of the Verwey transition

Tomasz Kołodziej

Faculty of Physics and Applied Computer Science, AGH University of Science and Technology, Mickiewicza 30, 30-059 Kraków, Poland

Supervisor: Andrzej Kozłowski

The influence of external magnetic field (up to 8 T) and temperature (in the range 10 – 300 K) on the dimensions of zinc doped magnetite single crystalline samples $Fe_{3-x}Zn_xO_4$ *exhibiting the Verwey phase transition of first- (x=0,008) and second- (x=0,022) order was studied by the strain gauge (SG) method. Natural tendency to shrinking while cooling and the jump in size at the transition temperature was observed for monoclinic c direction parallel to strain gauge axis for both samples, however for c direction perpendicular to SG the behavior was different and reverse. These results (combined with previous experimental results of elastic constants measurements and recent refinement of the crystal structure in low temperatures) brought the new concept of the Verwey transition (VT), in which coexistence of two kinds of interaction (one natural „forces" binding the crystal and the other one, associated with orbital order) determines the transition at the certain point.*

Magnetite was always one of the most fascinating materials for the mankind. In the past, its magnetic properties were used to orient in the world: in nanoform it is present in the migrant species, and in macro scale it was used to build the compasses. Nowadays, the prospective usage of the material will be in spintronics, which is associated with the fact that on the Fermi level it has the electrons with one spin direction only. In T_V = 124 K (for ideal composition Fe_3O_4) magnetite undergoes the spectacular phase transition, called the Verwey transition after the name of the discoverer.[1] The transition is reflected in the discontinuity in all physical properties (e.g. 2 orders of magnitude jump in resistivity) including the change of symmetry from cubic *Fd-3m* above T_V to monoclinic below this temperature. In fact, the low temperature structure of magnetite was solved very recently.[2] The basic model described by Verwey and followed by other authors[1,3] explaining this phenomenon, assumes that the major interaction responsible for the transition is the Coulomb repulsion of the electrons from the octahedral iron atoms, what causes the localization of the charges moving freely above T_V (resulting in the jump in resistivity). Newer theoretical simulations[4] show that key interactions causing the transition (besides those mentioned above) is the electron-phonon coupling.

One of the still open questions is the existence of the two different orders of the transition. Depending on the level of doping in $Fe_{3-x}(Zn, Ti)_xO_4$ or nonstoichiometry in $Fe_{3(1-\delta)}O_4$, VT can be sharp (I-order) or continuous (II). Transition temperature lowers linearly with doping level x or nostoichiometry parameter 3δ, despite the fact that nonstoichiometry and Zn doping removes and Ti doping adds octahedral electrons from the system. The trend has a characteristic break in the point $x = 3\delta = 0{,}012$, in which the character of transition changes. So far, there is no microscopic explanation of this fact. Another phenomenon is the magnetic easy axis switching process (AS), in which the orientation of the magnetic easy direction, as well as the monoclinic c axis, can be forced to switch to another $\langle 100 \rangle$ direction by the application of the magnetic field below T_V.

In the experiment described below, both phenomena were observed by the examination of the size changes in magnetic field and in various temperatures in magnetite samples of 1st and 2nd order. This experiment was meant to complement our previous studies on the easy axis switching influence on magnetic [5,6] and charge transport [7] properties as well as on the atomic arrangement. [8]

Magnetostriction and thermal expansion measurements were already performed before. For example, clear anomalies in the vicinity of the Verwey transition were reported in literature. [9] The authors associate these anomalies with the field dependent Fe^{2+} orbital ordering below T_V, i.e. the effects that are also present in AS. The verification of those interesting conclusions is needed since the studies were performed on polycrystalline samples.

The samples we used were Zn doped magnetite single crystals ($x = 0{,}008$, with $T_V = 113$ K — a 1st order sample, and $x = 0{,}022$, $T_V = 92$ K), cut to expose (001) crystal plane. Size dependence on temperature (in T range 10 – 300 K) and on magnetic field (up to $B_{max} = 8$ T) was measured by the strain gauge glued along [010] direction.

The experiment was conducted in the PPMS working in the horizontal rotator option, which allows to apply the field in perpendicular [100] and [010] directions. To account for the strain gauge temperature and field characteristics, the same tensometer was glued to quartz single crystal sample and measured simultaneously. Consequently, the relative size change was calculated from the formula

$$\mu_{st} = \Delta L_{Fe_3O_4}/L0_{Fe_3O_4} - \Delta L_{quartz}/L0_{quartz},$$

where $\Delta L_{Fe_3O_4}$, ΔL_{quartz}, $L0_{Fe_3O_4}$, $L0_{quartz}$, are sample and quartz contractions from their initial lengths $L0$ at 300 K.

The results of a temperature dependence of samples dimensions along the c axis is shown on the Fig. 1; the orientation of c-axis was forced by cooling in an external magnetic field $B = 2$ T applied in [010], i.e. strain gauge direction). No changes were observed when small field ($B = 0{,}01$ T) was applied, indicating that the only significant parameter is the c axis direction. According to [10] we expect that FC sample shrinks at T_V on cooling in c direction (from 8,3939 Å at 130 K to 8,3858 Å at 90 K). This is, qualitatively, what we have found, however, in contradiction to previous experiences of author of this work, sample shrinking of c axis is more pronounced for the 2nd order sample.

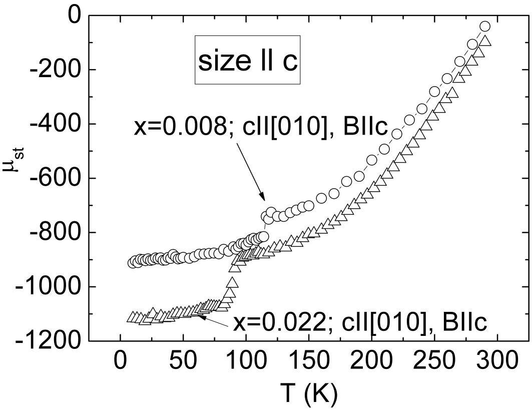

FIGURE 1: Temperature dependence of relative size μ_{st} in c direction and under magnetic field $B = 2$ T along c (parallel to [010]) for both samples.

The a-b plane size behaves at the VT in a completely different way (see Fig. 2, closed symbols; here the sample was field cooled with B along [100] to establish the c axis in the di-

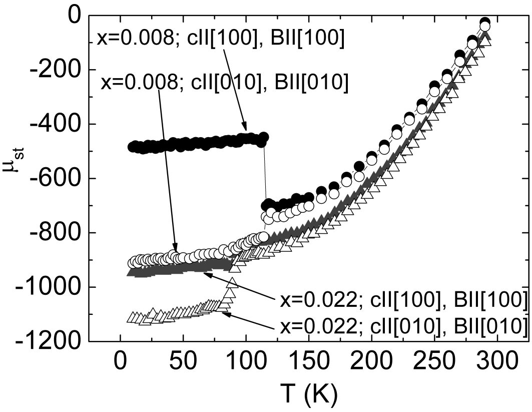

FIGURE 2: Temperature dependence of μ_{st} in a-b plane (perpendicular to c direction forced by FC along [100]). Open symbols denote data from Fig. 1 for comparison.

rection perpendicular to SG direction). In this case, the 1st order sample expands, opposite to the 2nd order, furthermore its expansion is much more pronounced than the 2nd order sample shrinking. In[11], where the results of powder diffraction experiment are presented, the same kind of an increase in *a*-*b* plane was observed. On the other hand, the $P2/c$ monoclinic lattice parameters are[10] $a_{\mathrm{M}} = 5{,}944$ Å and $b_{\mathrm{M}} = 5{,}925$ Å at 90 K for stoichiometric Fe_3O_4 that is $(a_{\mathrm{M}}^2 + b_{\mathrm{M}}^2)^{1/2} = 8{,}3927$ Å, what exactly corresponds to the cubic c axis at 130 K. This is rather equal to either 8,3939 Å, or 8,390 Å depending on the experiment.[10] Nevertheless, these values are very close to each other and do not suggest any significant *a*-*b* plane elongation, contrary to our observations.

These results might be understood if we assume that there is a sudden factor causing an expansion of the lattice, that is superimposed on a natural tendency to contraction of the crystal lattice in c direction for both kinds of material on cooling, with a large step in T_{V} (slightly larger than the one observed for $x = 0{,}022$). In this meaning, the ideal transition would take place without this additional factor. From previous observations of elastic constants[12] rather similar explanation might be deduced. Irrespective of a transition order, there is a common tendency of lattice behaviour when material is cooled down. Actually, the thermal evolution of the specific elastic constant c_{44} is very well described by the Landau theory of continuous phase transition, $c_{44} = c_{44}^0(T - T_{\mathrm{c}})/(T - \theta)$ with two parameters, θ (= 56 K), the temperature of transition predicted by the Landau theory, and T_{c} (= 66 K) — a critical temperature resulting from the linear coupling of order parameter to the strain. Thus not only the system prepares itself to some low temperature (θ) transition (irrespective to its order), but also the coupling to the elastic degrees of freedom is the same (represented by T_{c}). Apparently, high temperature properties are not so susceptible to departures from stoichiometry or doping and do not differentiate between I and II order type materials. In fact, they signal the Verwey transition of continuous order, and those correlations that ultimately trigger the Verwey transition set in just above T_{V}. Those correlations are, in our opinion, connected to the low temperature orbital order (OO). Orbital ordering, proved to be present in magnetite[2] in low temperatures builds rather complicated and rigid structure of three-atom chains (so called trimerons) (see reference[2] for further details). In our opinion this order might be interrupted by changing the number in the *d*-states electrons, which is caused by doping or introducing the iron vacancies; this would make the structure less rigid, i.e. the energy of these interactions is smaller and the temperature necessary to pull it apart is lower. Thus, the VT, in its natural character, does not depend on OO and would undergo at much lower temperatures (ca. 56 K), if not the orbital ordering that stabilizes the low T phase up to higher temperatures.

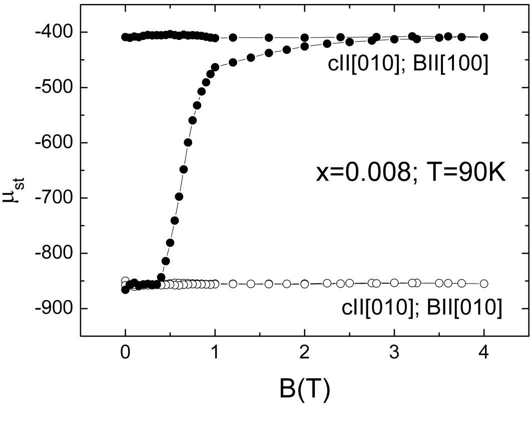

FIGURE 3: Relative size μ_{st} changes after the field was set along [010] (open circles) and, later, along [100] that caused AS (closed). Initially, c was along [010]. $x = 0{,}008$, $T = 90$ K.

After establishing of the c axis in the field cooling procedure and the application of the field in another cubic ⟨100⟩ direction, the transfer of an easy magnetization and crystallographic c axes to this field orientation takes place, provided the temperature is above 50 K. This phenomenon was proved to be accompanied with the rapid changes of transport properties,[7] as well as with the changes in microscopic properties.[8] The

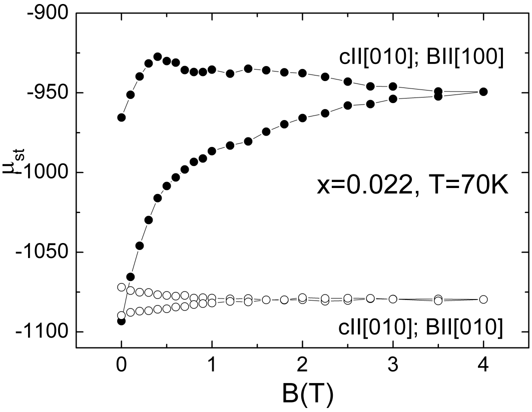

FIGURE 4: Same as Fig. 3, but for $x = 0{,}022$. Note that the AS starts already from lowest fields and is not completed by 4 T, in contrast to $x = 0{,}008$ sample.

main goal of the presented studies was also to find, if the influence of magnetic field on the dimensions can account for the AS phenomenon. The results of both samples are shown on the Figs. 3 and 4. The samples were first cooled with the field along strain gauge axis to define the c axis in this direction. With scanning field applied in this direction, the sample size changes were negligible (as already mentioned above). The field was then applied in [100] direction. While B exceeded 0,5 T a ca. 50% change of a 1st order sample deformation took place that was completed for $B = 2$ T and the subsequent field lowering resulted in no further change of size (see Fig. 3). For the 2nd order sample (see Fig. 4), the axis switching started in much lower fields than for 1st order, but practically was never completed. In accord with our previous magnetization studies,[6] the switching field in this case is an ill-defined parameter. Also, in this case a deformation change at AS does not exceed 10% of the total deformation ΔL at this temperature.

Concluding, we have performed magnetostricton measurements on two $Fe_{3-x}Zn_xO_4$ samples with different order of VT. We have found that both kinds of material contracts along crystallographic c direction while cooling across T_V. However, in the direction perpendicular to c (in a-b plane), there is large expansion for the 1st order, in contradiction to the material from 2nd order regime, where much less pronounced shrinking is observed. The influence of magnetic field on dimensions is rather weak and limited to the values saturating material magnetically. However, at temperatures close to the Verwey transition temperature, the switching of magnetic easy axis may occur, reflected here by a pronounced expansion of size in a-b plane and a respective c direction contraction. We suggest that these effects are caused by d-orbitals ordering changing in the field direction and that they are not linked intimately to those electronic interactions that are already present at high temperatures and drive the Verwey transition.

⋆ ⋆ ⋆

[1] E. J. Verwey, *Nature* (London) **144**, 327 (1939).
[2] M. S. Senn, J. P. Wright, J. P. Attfield, *Nature* **481**, 173 (2012).
[3] P. W. Anderson, *Phys. Rev.* **102**, 1008 (1956).
[4] P. Piekarz, K. Parliński, A. M. Oleś, *Phys. Rev. B* **76**, 165124 (2007).
[5] G. Król et al., *J. Alloy. Compd.* **442**, 83 (2007).
[6] Z. Kąkol et al., *Journal of Physics: Conference Series* **303**, 012106 (2011).
[7] G. Król et al., *J. Alloy. Compd.* **480**, 128 (2009).
[8] V. Chlan et al., *J. Appl. Phys.* **108**, 083914 (2010).
[9] E. Y. Aksienova et al., *Fizika Twerdolo Tela* **29**, 860 (1987).
[10] J. P. Wright, J. P. Attfield, P. G. Radealli, *Phys. Rev. B* **66**, 214422 (2002).
[11] Z. Kąkol, D. Owoc et al., *J. Solid State Chem.* **192**, 120 (2012).
[12] H. Schwenk et al., *Eur. Phys. J. B* **13**, 491 (2000).

Magnetic properties of 3D molecular magnet $\{[\mathrm{Fe}^{\mathrm{II}}(\mathrm{pyrazole})_4]_2[\mathrm{Nb}^{\mathrm{IV}}(\mathrm{CN})_8]\cdot 4\mathrm{H}_2\mathrm{O}_n\}$

Piotr Konieczny

The Henryk Niewodniczański Institute of Nuclear Physics Polish Academy of Sciences, Radzikowskiego 152, 31-342 Kraków, Poland

Supervisor: Tadeusz Wasiutyński

In this paper we present magnetic properties of a 3D molecular magnet $\{[\mathrm{Fe}^{\mathrm{II}}(\mathrm{pyrazole})_4]_2[\mathrm{Nb}^{\mathrm{IV}}(\mathrm{CN})_8]\cdot 4\mathrm{H}_2\mathrm{O}_\mathrm{n}\}$*. AC/DC magnetometry and Muon Spin Rotation (μSR) measurements were performed to characterise the sample. Special attention was put on critical behaviour around the phase transition* $T_\mathrm{C}\approx 7{,}8$ *K. The analysis of experimental results allowed to determine static exponents* β, γ *and a dynamic exponent* w*, which points to the 3D Heisenberg system with a noncollinear ferromagnetic arrangement.*

Molecular magnets are of great interest while they combine complex structure characteristic for organic compounds and physical properties common for inorganic ones. Those features rise with new properties like photoinduced magnetism,[1] magnetic sponge behaviour[2] or magnetic photoconductivity,[3] not possible to be achieved in classical magnetic materials.

The presented sample is a three dimensional hybrid cyanide-bridged organic-inorganic compound with the full chemical formula of $\{[\mathrm{Fe}^{\mathrm{II}}(\mathrm{pyrazole})_4]_2[\mathrm{Nb}^{\mathrm{IV}}(\mathrm{CN})_8]\cdot\cdot 4\mathrm{H}_2\mathrm{O}_n\}$ with the mole mass 1029,49 g/mol (pyrazole=$\mathrm{C}_3\mathrm{N}_2\mathrm{H}_4$). It crystallizes in tetragonal $\mathrm{I}4_1/\mathrm{a}$ space group.[4] The detailed synthetic procedure of the sample was reported in Pinkowicz et al.[4] In this structure the $\mathrm{Nb}^{\mathrm{IV}}$ and $\mathrm{Fe}^{\mathrm{II}}$ ions are coordinated to each order trough the cyanide bridges decorated with pyrazole molecules with only one type of linkage $\mathrm{Nb}^{\mathrm{IV}}$-CN-$\mathrm{Fe}^{\mathrm{II}}$ (Fig. 1). This arrangement makes both magnetic ions well localized with spins and g factors: $S_\mathrm{Fe}=2$, $g_\mathrm{Fe}=2{,}16$, $S_\mathrm{Nb}=1/2$, $g_\mathrm{Nb}=2$ respectively for $\mathrm{Nb}^{\mathrm{IV}}$ and $\mathrm{Fe}^{\mathrm{II}}$, which give the opportunity to test the predictions of existing spin models. Moreover, the structure makes the interaction between the same type ions negligible. Only the magnetic ions which are the nearest neighbours are coupled through CN bridges ($\mathrm{Nb}^{\mathrm{IV}}$–CN–$\mathrm{Fe}^{\mathrm{II}}$).

The structural character of the sample was checked using X-ray diffraction with the use of Pananalytical X'PERT PRO diffractometer. The magnetic properties of $\{[\mathrm{Fe}^{\mathrm{II}}(\mathrm{pyrazole})_4]_2[\mathrm{Nb}^{\mathrm{IV}}(\mathrm{CN})_8]\cdot 4\mathrm{H}_2\mathrm{O}_n\}$ were investigated using a Lake Shore 7000 magnetometer and the Cahn RG electrobalance. Fig. 2a presents the inverse susceptibility measured in applied 1000 Oe magnetic field. For temperatures above 10 K, a Curie-Weiss law was fitted in the form:

$$\chi=\frac{C}{T-\Theta}+\chi_0. \tag{1}$$

The obtained values are C=6,42 K cm^3/mol, $\mu_\mathrm{eff}=7{,}17\ \mu_\mathrm{B}$/f.u., $\chi_0=1{,}62\times 10^{-5}$ cm^3/g and Θ=13,4 K; where C is the Curie

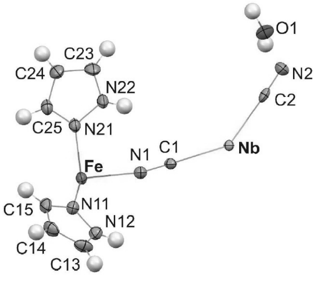

FIGURE 1: Asymmetric units of the sample, showing the position of ions connected throw CN bridges (adapted with the permission from[4]).

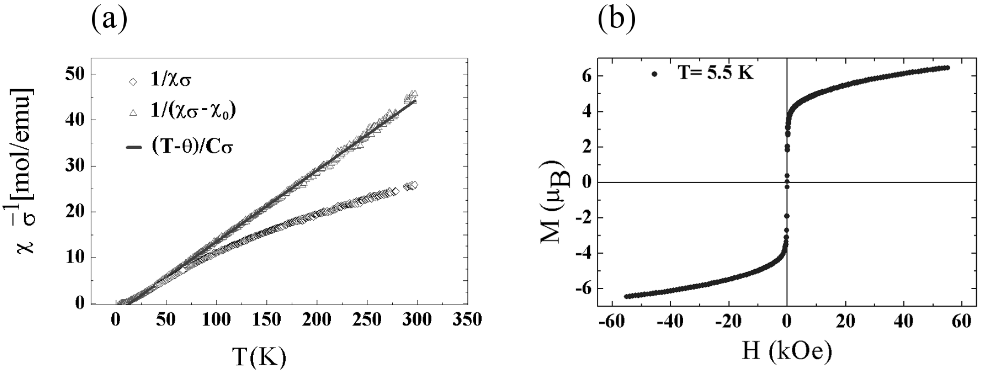

FIGURE 2: (a) Inverse DC susceptibility in applied 1 kOe without (circles) and with χ_0 correction (empty triangles). The line presents the fitted Curie-Weiss law. (b) Magnetization as a function of applied field in $T = 5{,}5$ K.

constant, μ_{eff} is an effective magnetic moment, χ_0 is a constant due to diamagnetic and device corrections, Θ is the Weiss constant. Positive value of Θ points to ferromagnetic coupling, however the extrapolated value of magnetization saturation (Fig. 2b), is around ~8,0 μ_{B}/f.u., which is lower than expected value of ~9,6 μ_{B}/f.u. for parallel ordered magnetic moments, and higher than value of ~7,6 μ_{B}/f.u. expected for antiparallel ordered magnetic moments. This inconsistency can be explain with an noncollinear arrangement due to local anisotropy of iron ions.

To exclude a spin glass state, the AC susceptibility χ_{ac} measurements were performed in different frequencies. No frequency dependence of temperature position of χ'_{ac} peak was observed, which precludes a spin glass transition. The AC susceptibility data was also used to obtained the γ critical exponent with the use of classical scaling relation of the form:

$$\chi = C\left(\frac{T}{T_{\mathrm{C}}} - 1\right)^{-\gamma}. \qquad (2)$$

Obtained value of $\gamma = 1{,}42 \pm 0{,}07$ for $T_{\mathrm{C}} = 7{,}8$ K (Fig. 3) fits well to the 3D Heisenberg model ($\gamma_{\mathrm{H}} \approx 1{,}4$).

The next part of our study was performed with the use of muon spin rotation measurements. μSR is a unique technique because it allows to measure local magnetic field with absence of external field. This feature is possible due to spin-polarized positive muons implanted in the sample, which mainly stops an interstitial position in the crystal. The muon spin is precessing in the presence of a local magnetic field, which is produced by the magnetic moments. The frequency of this precession (ω_μ) is proportional to the local field $\omega_\mu = \gamma_\mu B_\mu$, where γ_μ is a muon gyromagnetic ratio and B_μ is a local magnetic field on muon position. The muon itself is an unstable particle with the lifetime of $\tau_\mu \approx 2{,}2$ μs and decays to a positron and two neutrinos. The positron is emitted preferentially in the spin direction of the muon. This property is used to describe the muon precession inside the sample and is realized by asymmetry function:

$$A(t) = \frac{N_{\mathrm{B}}(t) - N_{\mathrm{F}}(t)}{N_{\mathrm{B}}(t) + N_{\mathrm{F}}(t)}, \qquad (3)$$

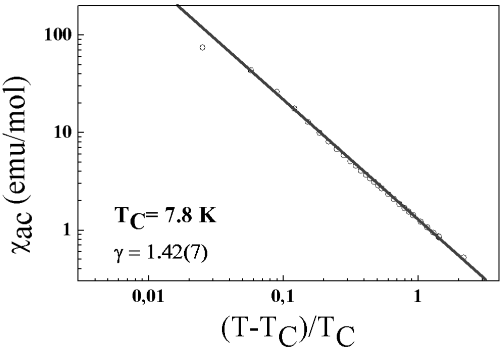

FIGURE 3: Result of classical scaling of the AC susceptibility where $T_{\mathrm{C}} = 7{,}8$ K.

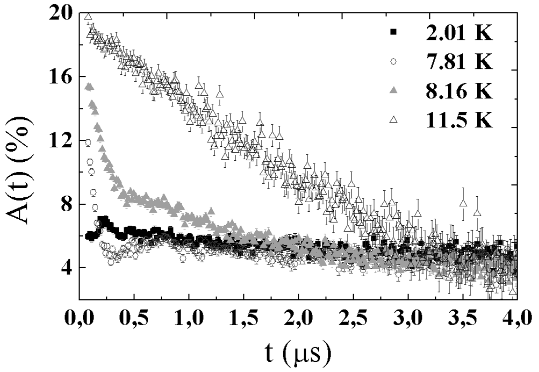

FIGURE 4: Four examples of measured asymmetry in zero applied field (ZF μSR) for temperatures 2,01; 7,81; 8,16 and 11,5 K.

where $N_{\mathrm{B}}(t)$ and $N_{\mathrm{F}}(t)$ denote the numbers of positrons detected by counters standing in the backward and forward of the sample. The output data of our μSR experiments were analysed with the WIMDA software.[5]

Fig. 4 presents examples of the measured time evolution of the asymmetry in the absence of external magnetic field (ZF μSR — zero-field measurements). Oscillations in asymmetry which indicates the precession of muon in local field from a long range magnetic ordered state, is observed for times below 1 μs and temperatures $T < 8$ K. It was found from the Fourier analysis of the asymmetry data that there is only one dominant frequency for temperatures below T_{C}. This indicates one muon stopping site. To access information about the local field, a function for polycrystalline sample with one frequency was fitted of the form:

$$A(t) = A_{\mathrm{bg}} + \frac{1}{3}A_{\mathrm{rel}}\exp\left(-\lambda_1 t\right) + \frac{2}{3}A_{\mathrm{rel}}\exp(-\lambda_2 t)\cos(\gamma_\mu B_\mu t + \varphi), \tag{4}$$

where A_{bg} is a constant related to contribution from the background, A_{rel} is the signal amplitude from the sample. The term $1/3\exp\left(-\lambda_1 t\right)$ stands for muons lying parallel to the local magnetic field and do not give oscillations signal. The temperature evolution of the local field extracted with the use of Eq. (4) from measured data, is presented in Fig. 5. To determine the β exponent those B_μ values were fitted with the phenomenological form:

$$B_\mu(T) = B_\mu(0)\left[1 - \left(\frac{T}{T_{\mathrm{C}}}\right)^{\sigma}\right]^{\beta}, \tag{5}$$

yielding $T_{\mathrm{C}} = 7{,}84 \pm 0{,}04$ K, $B_\mu(0) = 33{,}1 \pm 0{,}7$ mT, $\sigma = 1{,}12$ and $\beta = 0{,}38$. The obtained β agrees well with the value expected for the 3D Heisenberg model ($\beta_{\mathrm{H}} = 0{,}369$), which is consistent with the γ critical exponent from AC susceptibility measurements. Also the temperature of phase transition from those two techniques is similar. The obtained value of σ which is related to spin waves in temperatures well below T_{C}, is closer to the value for a 3D ferromagnetic system ($\sigma_{\mathrm{FM}} = 3/2$) than to an antiferromagnetic one ($\sigma_{\mathrm{AF}} = 3$).

Above the T_{C} the asymmetry have only the relaxing component and those data were fitted with a function of the form:

$$A(t) = A_{\mathrm{bg}} + A_{\mathrm{rel}}\exp(-\lambda_3 t), \tag{6}$$

where λ_3 is a relaxation rate and A_{rel} is a constant. The temperature evolution of λ_1, λ_3 is shown in Fig. 6. The exponential character of the asymmetry function above the phase transition points to dynamical fluctuation in the local field at the muon site[6] and can be written as $\lambda_3 \sim (\Delta B)^2\tau$, where ΔB is a variance of

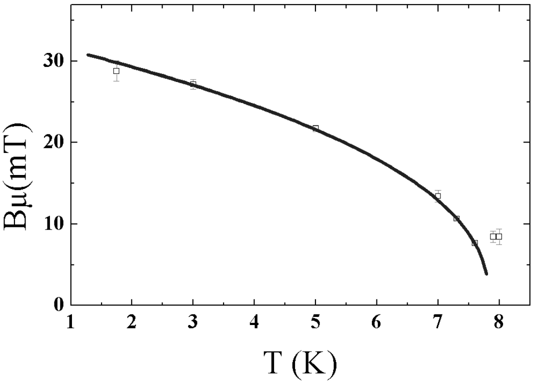

FIGURE 5: The local magnetic field at muon stopping position as a function of temperature. Solid line represents the result of fitting Eq. (5).

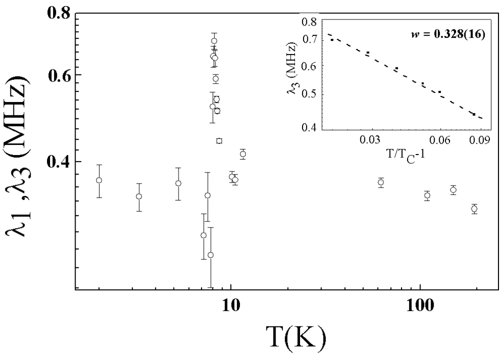

FIGURE 6: The relaxation rate of λ_1 and λ_3 as a function of temperature. Insert: The log-log plot of λ_3 as a function of reduce temperature $(T/T_C - 1)$. Dashed line represent the fit for critical exponent w.

the local magnetic field and τ is a correlation time.[7] The relaxation rate has a sharp peak near the T_C due to fluctuation related to the phase transition. The points on right side of the peak are the λ_3 values and they are mainly related to the correlation time, because the ΔB do not have strong temperature dependence in the absence of magnetic or structural transition. It can be noticed that there are two regions for λ_3, one on the right slope of the peak associated with slow dynamics (high τ) and second one with fast dynamics (low τ) for higher temperatures.[7] The critical temperature T_{CR} which separates these two regions was roughly estimated to 9 K. Values of λ_3 related to slow dynamics were used to fit the value of a dynamical critical exponent w (Fig. 6. insert), which describes a critical evolution of the diverging spin correlation time $\tau = |T - T_C|^{-w}$. The obtained value $w = 0{,}33 \pm 0{,}02$ agrees with the 3D Heisenberg model ($w_H = 0{,}328$).[8]

Magnetic and μSR measurements have been carried out for studying magnetic properties of the molecular magnet $\{[\mathrm{Fe}^{\mathrm{II}}(\mathrm{pyrazole})_4]_2[\mathrm{Nb}^{\mathrm{IV}}(\mathrm{CN})_8]\cdot 4\mathrm{H_2O}_n\}$, which allowed to obtain values of critical exponents: $\gamma = 1{,}42 \pm 0{,}07$, $\beta = 0{,}38$ and $w = 0{,}33 \pm 0{,}02$. The analysis of the muon spin rotation measurements have confirmed conclusions from the classical scaling of AC susceptibility data that the behaviour of presented compound is close to the 3D Heisenberg model. The compound orders to a ferromagnetic state below $T_C \approx 7{,}8$ K, however the magnetic character of the arrangement has to be confirmed by other type of measurements.

Authors would like to thank F. L. Pratt and P. M. Zieliński for help with the muon spin rotation measurements, D. Pinkowicz and B. Sieklucka for preparing the sample, R. Pełka for valuable discussion. This work has been partly supported by the EU Human Capital Operation Program, Polish Project No. POKL.04.01.01-00-434/08-02.

⋆ ⋆ ⋆

[1] S. I. Ohkoshi, H. Tokoro, T. Hozumi, Y. Zhang, K. Hashimoto, C. Mathoni'ere, I. Bord, G. Rombaut, M. Verelst, C. C. dit Moulin, F. Villain, *J. Am. Chem. Soc.* **128**, 270 (2006).

[2] M. Fitta, R. Pełka, M. Bałanda, M. Czapla, M. Mihalik, D. Pinkowicz, B. Sieklucka, T. Wasiutyński, M. Zentkova, *Eur. J. Inorg. Chem.* **24**, 3830 (2012).

[3] T. Naito, T. Karasudani, S. Mori, K. Konishi, T. Takano, Y. Takahashi, T. Inabe, S. Nishihara, K. Inoue, *J. Am. Chem. Soc.* **134**, 18656 (2012).

[4] D. Pinkowicz, R. Pełka, O. Drath, W. Nitek, M. Bałanda, A. M. Majcher, G. Poneti, B. Sieklucka, *Inorg. Chem.* **49**, 7565 (2010).

[5] F. L. Pratt, *Physica B* **289** – **290**, 710 (2000).

[6] R. S. Hayano, Y. J. Uemura, J. Imazato, N. Nishida, T. Yamazaki, R. Kubo, *Phys. Rev. B* **20**, 850 (1979).

[7] T. Lancaster, S. J. Blundell, P. J. Baker, F. L. Pratt, W. Hayes, I. Yamada, M. Azuma, M. Takano, *J. Phys. Condens. Matter* **19**, 376203 (2007).

[8] F. L. Pratt, T. Lancaster, P. Baker, S. Blundell, W. Kaneko, M. Ohba, S. Kitagawa, S. Ohira-Kawamura, S. Takagi, *Physica B* **404**, 585 (2009).

The structure of basic Ni-rich Al-Ni-Co decagonal quasicrystal

Paweł Kuczera

Faculty of Physics and Applied Computer Science, AGH University of Science and Technology, Mickiewicza 30, 30-059 Kraków, Poland

Supervisor: Janusz Wolny

Structure refinement of the basic Ni-rich Al-Ni-Co decagonal phase was performed in physical space. Statistical approach was used to derive the structure factor. Rhombic Penrose tiling with an edge length of 10,28 Å was chosen as a reference lattice. The best-fit structure model with 106 parameters and 2767 reflections gives R=12,3% and wR=6,2%. The observations-to-parameters ratio is high — 26,1, density and chemical composition of the resulting structure are very close to experimental values.

There are 8 different decagonal phases reported in the Al-Ni-Co system (reference[1] and references therein). The only phase, for which a qualitative structure refinement was performed, is the so called basic Ni-rich phase. In the majority of published papers a higher-dimensional approach i.e. the atomic surface modeling method is used for the optimization.[2,3] In this paper the results of a physical space structure refinement against single-crystal X-ray diffraction data of the basic Ni-rich decagonal phase is presented, without referring to the higher-dimensional properties of decagonal quasicrystals.

Structure factor, which was used for the modelling process, was calculated on the basis of the statistical method described in literature.[4,5] Rhombic Penrose tiling was used as a reference lattice. Initial atomic positions were set in the vertices of rhombuses divided four times with obedience to the inflation rules. Additionally atoms were divided into 24 groups. For each group occupation probability, TM (transition metal) concentration, a shift from initial position and two components of ADP (atomic displacement parameter) were optimized. Two components are necessary because of the clear anisotropy of the structure. One component is associated with xy plane, i.e. quasiperiodic plane, the other component with z direction, i.e. periodic direction. All together 106 parameters were refined. The optimization was performed on a set of 2767 symmetrically independent reflections (merged in $10/m$ Laue class) taken by a four-circle diffractometer at beamline D3, HASYLAB. The chemical composition of the sample was checked to be $Al_{70,6}Ni_{22,7}Co_{6,7}$.[2]

Structure of the basic Ni-rich decagonal Al-Ni-Co phase is known to consist of a periodic set of quasiperiodic planes stacked along the z direction. There are two planes within one period of the z axis. These planes are related by a 10_5 screw axis. The shortest interatomic distances in the structure of the basic Ni-rich decagonal Al-Ni-Co can be determined using a Patterson map.[2] These distances scale in exactly the same way as distances between vertices of Penrose tiling, providing that proper z coordinate is chosen for these vertices. Thus, it is assumed that the projection of the structure along z axis results in the Penrose tiling. The structure units are thick and thin rhombuses of Penrose tiling divided three times with obedience to the inflation rules. All positions from the 0-th, 1-th, 2-nd, and 3-rd division are occupied in the initial model. Some atoms, however, are also put in several positions of the fourth division to fulfil the density restriction. All 70 atoms decorating the structure units were divided into 24 groups. This division was made according to the matching rules for rhombuses,[4,5] overlapping rules for kite-clusters,[6] and an

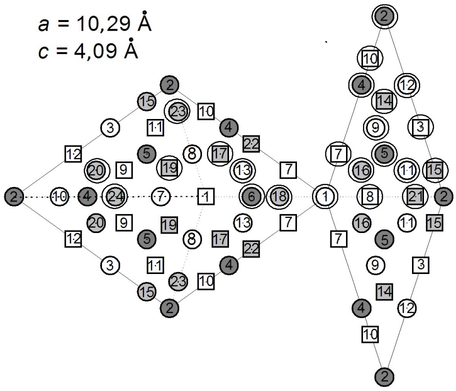

FIGURE 1: The division of atoms into 24 groups.

assumption that the decoration is symmetric with respect to the longer diagonal of thick rhombus and shorter of the thin one. The matching rules were used for all decorating atoms since they are essential for the correctness of the structure factor calculation. Also the assumption of a symmetric decoration was strictly obeyed. The overlapping rules for clusters were used solely for atoms from the 0-th, 1-th, 2-nd, and 3-rd division, which form a skeleton of the structure. The division of atoms into groups is illustrated in Fig. 1.

The edge length of the structure units (a) is 10,29 Å and the period along the z axis (c) 4,09 Å. Circles and squares distinguish the layers at $z = 0{,}25c$ and $z = -0{,}25c$ respectively. Dark grey symbol color denotes TM atoms light grey Al/TM atoms and white Al atoms. Some positions are marked by an additional circle. The results of structure refinement are given for these positions. In the initial model all occupation probabilities are equal to 1. Atoms from 0-th, 1-th, 2-nd, and 3-rd division are either Al or TM (white or dark grey symbols, groups 1 – 13). The initial concentration of TM atom at the positions of 4-th division was 0,25 (light grey symbols, groups 14 – 24). Atoms in the group 22 are slightly moved out of the edge, inside the thick rhombus. This is why there is no atom from the group 22 in the thin rhombus. A detailed explanation of this assumption is given further in the text.

The structure factor was calculated in the physical space on the basis of statistical approach. The concept of average unit cell for Penrose tiling and a detailed derivation of the structure factor for any decoration is extensively studied.[5] Here only the resulting formula is shown:

$$F(\vec{k}) = \sum_t \sum_\alpha \Bigg[F_t^\alpha(\vec{k}) \times \\ \times \sum_{j=1}^{n_t} p_j^t f_j^t D_j^t(\vec{k}) \exp\left(i\vec{k} \cdot \vec{r}_j^{\,t,\alpha} \right) \Bigg].$$

$F_t^\alpha(\vec{k})$ is the Fourier transform of a triangular probability distribution associated with a given structural unit in a given orientation. In the chosen rhomb Penrose tiling there are two basic structural units — a thick and a thin rhomb (sum over t) in 10 possible orientations (sum over α). The position of an atom j in a given structural unit t for orientation α is represented by $\vec{r}_j^{\,t,\alpha}$, p_j^t is the weight of a given atom in a structural unit (calculated as a fraction of the atom, which is inside a given rhomb), n_t is the number of atoms decorating a structural unit, $\vec{k}$ is a scattering vector and f_j^t is the average atomic form factor. A formula for f_j^t reads:

$$f_j^t = p_{\text{calc}}^{j,t} \left[p_{\text{TM1}}^{j,t} f_{\text{TM}} + \left(1 - p_{\text{TM1}}^{j,t} \right) f_{\text{Al}} \right].$$

p_{calc} is the occupation probability of an atom in a given position, p_{TM} is the concentration of TM atoms at a given position, f_{TM} is the atomic form factor for TM atoms, f_{Al} the one for Al atoms. $D_j^t(\vec{k})$ is the atomic displacement factor:

$$D_j^t(\vec{k}) = \exp\left\{ -\frac{1}{16\pi^2} \left[(k_x^2 + k_y^2) b_{xy} - k_z^2 b_z \right] \right\}.$$

b_{xy} is the average atomic displacement parameter (ADP) in the quasiperiodic plane, b_z is the ADP in the z-direction (periodic direction).

A conjugated gradient minimization algorithm was used for the refinement. Final values of the refined parameters are given in[7]. Here we shall only comment on the general results.

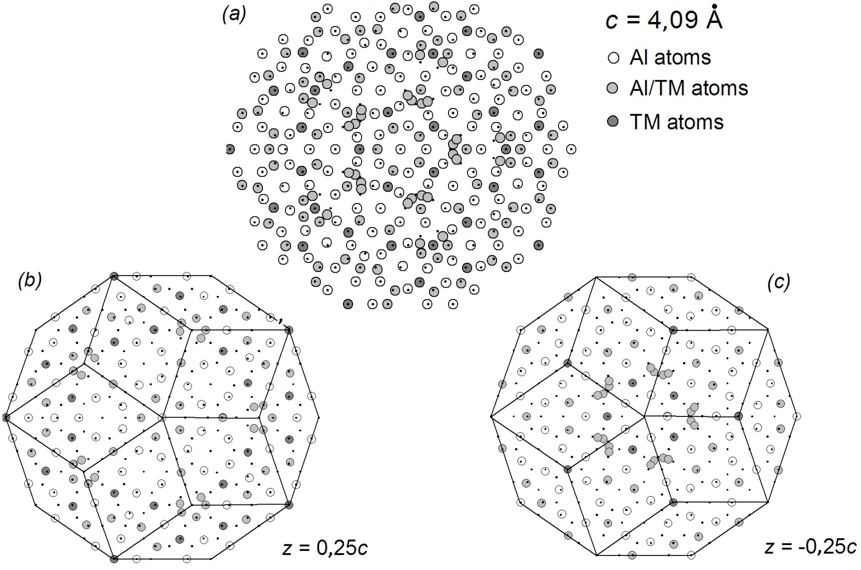

FIGURE 2: Refined structure.

A part of the refined structure is shown in Fig. 2. Dark grey circles denote TM atoms, light grey Al/TM atoms and white Al atoms. Black dots indicate ideal Penrose tiling positions. Fig. 2a shows a projection of the structure along the z axis. Figs. 2b and 2c show the layers at $z = 0{,}25c$ and $z = -0{,}25c$ respectively. The edge length (black lines in the Figs. 2b and 2c) was refined to be 10,29 Å and the period c along the z axis 4,09 Å. Shifts from ideal Penrose tiling positions are rather small and not greater than 8% of the edge length of rhombuses (and in most cases not greater than 4%). Generally shifts for atoms from first three inflation divisions (groups $1-13$), which form a „skeleton" of the structure are much smaller than for atoms from fourth division (groups $14-24$). Occupation probabilities for these skeleton atoms are 1 in most cases and always greater than 0,75. For other groups partial occupation is common. Similarly TM concentration is also well defined for skeleton atoms. Only for one group its value is not equal to 0 or 1. For other groups mixed occupation is possible. A sum of occupancy probabilities for pairs of atoms indicated by pairs of light grey circles, which touch each other or overlap in Figs. 2b and 2c, is lower than one. These are flip positions. In each tile atoms occupy either first or second position. If there are any distances shorter than 2,43 Å then a sum of occupation probabilities of atom pairs revealing to short interatomic distance is lower than 1. In the resulting structure there is a certain degree of disorder within the structure units — thin and thick rhombuses. This could be called a local or short-range disorder. On the other hand, these rhombuses form the rhombic Penrose tiling, thus, in this approach, the structure is also perfectly long-range ordered. Debye-Waller coefficients (b_{xy} and b_z) for most groups are smaller than 3 Å^2, which is an acceptable value for inorganic materials. Greater values may indicate a certain degree of static disorder in the structure. Some b_z i.e. the component associated with z direction exceed the value of 3 Å^2. This could mean that the atomic layers of the structure are puckered rather than flat. In[1] even an 8 Å superstructure was assumed. This means that the period along z axis is doubled. However, there are no half-integer reflections in the diffraction pattern, thus in experiment only an average 4 Å structure is observed. In this approach larger b_z values result from overlap-

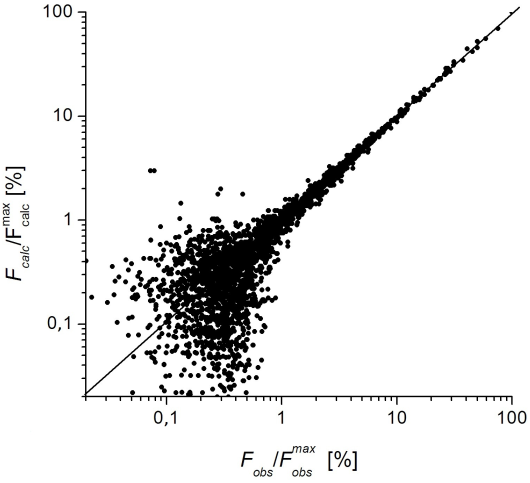

FIGURE 3: $F_{\mathrm{obs}}/F_{\mathrm{calc}}$ plot in logarithmic scale.

ping layers of the superstructure having opposite z displacements. In this paper only the average 4 Å structure is investigated. An extinction parameter g and scale factor between the calculated and measured diffraction pattern were the global parameters optimized. A total number of 106 parameters were refined, the observations-to-parameters ratio is high and equal 26,1. The final disagreement factors $R = 12{,}3\%$ and the $wR = 6{,}2\%$. Global parameters, R and wR values calculated for different numbers of strongest reflections are listed in Table 1. The refined structure has the exact chemical composition $\mathrm{Al}_{70,7}\mathrm{TM}_{29,3}$ (chemical composition of the sample was measured to be $\mathrm{Al}_{70,6}\mathrm{TM}_{29,4}$[1]). The point density of the structure is 0,0656 Å^{-3} and overall density 3,94 $\mathrm{g\,cm^{-3}}$. Experimental values are 0,0661 Å^{-3} and 3,94 $\mathrm{g\,cm^{-3}}$ respectively. The $F_{\mathrm{obs}}/F_{\mathrm{calc}}$ plot for the final structure in the logarithmic scale is shown in Fig. 3.

TABLE 1: Refinement parameters.

g	$2{,}(9)\cdot 10^{-5}$
R [%] all 2767 reflections	12,3
wR [%] all 2767 r.	6,2
R [%] $I > 3\sigma_I$ 1194 r.	4,3
wR [%] $I > 3\sigma_I$ 1194 r.	5,7
R [%] $I > 10^{-4}\, I_{\max}$ 837 r.	4,1
wR [%] $I > 10^{-4}\, I_{\max}$ 837 r.	5,4

In this paper the results of the structure analysis of a decagonal basic Ni-rich Al-Ni-Co quasicrystal were described. The refinement was conducted with only real space parameters. A decorated rhombic Penrose tiling was used as an initial structure for the refinement process. Within the statistical approach the structure factor unrelated to the perpendicular space could be derived. The resulting disagreement factors are low and comparable to other quasicrystal structure refinement present in the literature. The final model gives density values very close to the measured ones.

⋆ ⋆ ⋆

[1] S. Katrych, W. Steurer, *Z. Kristallogr.* **219**, 606 (2004).

[2] A. Cervellino, T. Haibach, W. Steurer, *Acta Crystallogr. B* **58**, 8 (2002).

[3] H. Takakura, A. Yamamoto, A. P. Tsai, *Acta Crystallogr. A* **57**, 576 (2001).

[4] B. Kozakowski, J. Wolny, *Phil. Mag.* **86**, 549 (2006).

[5] B. Kozakowski, J. Wolny, *Acta Crystallogr. A* **66**, 489 (2010).

[6] M. Duda, B. Kozakowski, J. Wolny, *J. Non-Cryst. Solids* **353**, 2500 (2007).

[7] P. Kuczera, B. Kozakowski, J. Wolny, W. Steurer, *J. Phys. Conf. Ser.* **226**, 012001 (2010).

Symmetry relations between different structural representations of magnesium borohydride

Arkadiusz Kupczak

Faculty of Physics and Applied Computer Science, AGH University of Science and Technology, Mickiewicza 30, 30-059 Kraków, Poland

Supervisor: Wiesława Sikora

Magnesium borohydride $Mg(BH_4)_2$ is a promising candidate for hydrogen storage material. Even thought it was synthesized over 60 years ago still discloses many features worth of further investigation. In particular its ground state crystal structure remains a mystery and is a source of discrepancies between theoretically and experimentally proposed structures. In an attempt to tackle this problem Symmetry Analysis (SA) turned out to be very useful. With its aid all space groups describing different structures of $Mg(BH_4)_2$ were connected to each other via group-subgroup relation. A common subgroup $C222_1$ (IT 20) has been found which bounds them all together. Furthermore SA was used to model new structures so far unreachable by theoretical simulations, that is orthorhombic Fddd (IT 70), hexagonal $P6_122$ (IT 178) and cubic $Fd\bar{3}m$ (IT 227).

Magnesium borohydride $\mathrm{Mg(BH_4)_2}$ due to its complex structure still evades from determining its crystal structure both by experimentalists and theoreticians. In first experimental work focusing on clarifying the crystal structure of $\mathrm{Mg(BH_4)_2}$ dated back to 70'[1] authors identified two phases, namely low temperature (LT) tetragonal and high temperature (HT) cubic, but without specifying the space group for them. After decades Her et al.[2] determined the LT phase with symmetry $P6_1$ (IT 169) and HT phase with the orthorhombic $Fddd$ symmetry. Later on Filinchuk et al.[3] with more precise single crystal measurements revise LT $P6_1$ structure into hexagonal $P6_122$ one. Simultaneously to these investigations many theoretical structure predictions were carried on[4–6] giving $I4_1/amd$ (IT 141), $I\bar{4}m2$ (IT 119), $I4_122$ (IT 98), $F222$ (IT 22) structures, but up to the present day all of them differs completely from the experimental ones, they never match to each other.

And here on the stage comes the SA revealing its power and relevance in dealing with crystal structures described by various space groups. It was used to find whether there is a possibility of linking together all structures of $\mathrm{Mg(BH_4)_2}$ found so far by connecting the space groups describing them via group-subgroup relation. The result of this analysis, the Birkhäuser tree of space groups, can be seen in Fig. 1. The k-vector describes the relations between lattices and an irreducible representation leads from high-symmetry space group to one of its subgroup. There are several fresh insights into the structure of magnesium borohydride that comes out from symmetry tree.

First of all the space group with lowest symmetry, which is a root binding all others was found, that is $C222_1$. Three different group-subgroup transition pathways meet at this point. First $I4_1/amd \Rightarrow I\bar{4}m2 \Rightarrow F222 \Rightarrow C222_1$, second $I4_1/amd \Rightarrow Fddd \Rightarrow F222 \Rightarrow C222_1$ and the third $I4_1/amd \Rightarrow I4_122 \Rightarrow F222 \Rightarrow C222_1$. Additionally the experimental LT $P6_122$ structure has as its direct subgroup the $C222_1$. The fact that finding all these group-subgroup connections was possible, brings us to a certain conclusion about all structures reported so far. They cannot be treated as separate structures, but only as different structural representation (described in different space groups) of magnesium borohydride with constraints throw on stoichiometry

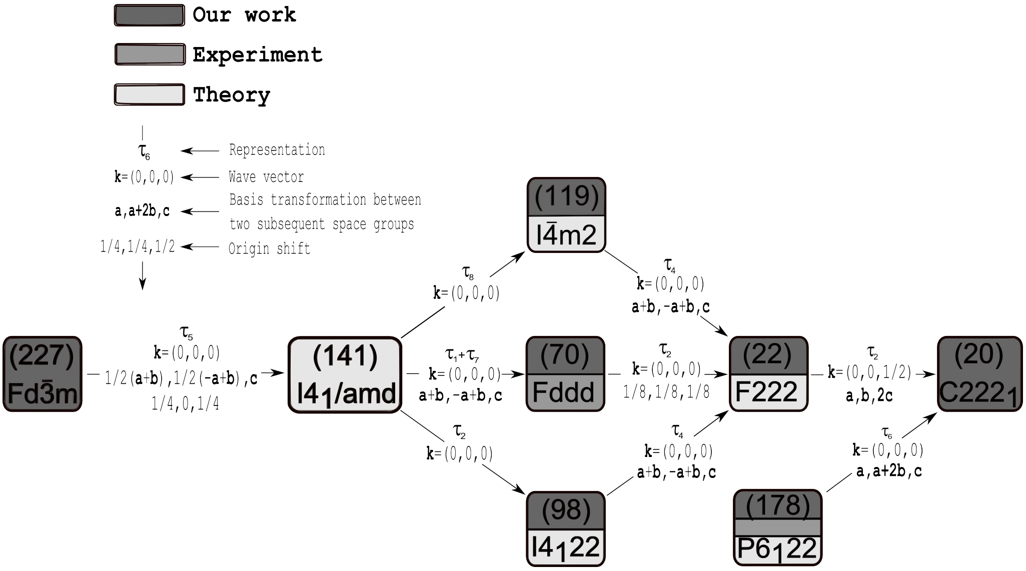

FIGURE 1: The Birkhäuser tree of the symmetry-related space groups of the optimized structures. Structures in a group-subgroup relations determined using SA analysis are connected with an arrow.

and coordination of particular atoms (magnesium is tetrahedrally surrounded by four boron to each of which four hydrogen atoms are bounded again creating tetrahedron). A simple example of that can be seen in the first step of the first pathway of analysis $I4_1/amd \Rightarrow I\bar{4}m2$. The $I4_1/amd$ transforms into its subgroup $I\bar{4}m2$ by splitting into two separate inter-penetrating substructures and one of them turns out to be nothing more than structure found previously by other authors.[7]

The SA can also be used as a tool for modeling new structures starting from already known ones. For a particular group-subgroup transition from SA we are able to find possible symmetry-allowed displacements of atoms breaking the symmetry of higher space group. In that way, starting from $I4_1/amd$ and imposing on atoms small symmetry-allowed movement, the experimental HT structure with $Fddd$ space group was theoretically modeled. The orthorhombic Fddd structure proposed by Her et al.[2] with lattice constants $a = 37,07$ Å, $b = 18,65$ Å, $c = 10,91$ Å containing 64 formula units (fu) was reduced by SA modelling to a unit cell with $a = 11,67$ Å, $b = 11,67$ Å, $c = 10,47$ Å and only 16 fu tremendously simplifying it. Magnesium atoms occupies *8a* and *8b* sites whereas all borons and hydroges are in *32h* Wyckoff positions. This structure differs from the experimental one both in sites occupied by atoms as well as in lattice constants.

The SA can not only be employ to search for relation between high symmetry space groups and their subgroups, but in a more wider way, to seek for any possible „inverse" correspondence, namely moving from a subgroup to another group with higher symmetry. This can be reached by reversing the displacement vector connecting positions of atoms in two space groups related by group-subgroup structural transition. Applying the inverse correspondence two structures were modelled: cubic $Fd\bar{3}m$ and hexagonal $P6_122$. Searching for the cubic as a starting point we took $I4_1/amd$ which is a subgroup of the desired one. To obtain appropriate atomic positions in $Fd\bar{3}m$ SA is needed because simple transformation of atomic coordinates from $I4_1/amd$ to $Fd\bar{3}m$ do not keep the correct stoichiometry and atomic coordination mentioned formerly. During inverse transition the

Mg atoms are not allowed to move, thus they can be transformed straightforwardly to cubic structure. When we do the same with boron atoms they occupy *96g* Wyckoff position, which is three times more than necessary number keeping the correct stoichiometry of $Mg(BH_4)_2$ (two magnesium atoms in $Fd\bar{3}m$ are set in *8a* and *8b*). Although, in contrary to Mg atoms, they are allowed by symmetry to move. The right Wyckoff position which ensures the correct stoichiometry and coordination of Mg atoms is *32e* and from SA we can get the appropriate displacements leading to this site. The atomic positions of hydrogen were chosen to yield tetrahedral environment around boron and to sustain correct stoichiometry, they occupy *32e* and *96g* sites. This new found structure is our answer to the experimentally determined cubic one done by Konoplev et al. in[1], but without providing any information about space group or atomic positions, only lattice constants and crystallographic system. In the same way, using inverse correspondence, the hexagonal $P6_122$ was modelled. Based on SA the $C222_1$ can be used to derive the atomic positions in hexagonal structure. The number of symmetry elements in the $P6_122$ space group is three times larger than in $C222_1$ space group, but the unit cell is two times smaller, because it involves the transformation from a C-face centered cell to a hexagonal one. Therefore, the number of atoms in elementary cell has to be multiplied by 3 and divided by 2. The result is that the SA structure is built from 24 fu whereas the experimental from 30 fu. Once again SA led to simpler model of $Mg(BH_4)_2$. The Mg atoms occupy the *12c*, *6a* and *6b* sites, while all boron and hydrogen are in *12c* and the positions of atoms are not the same as in experimental structure.

To conclude the symmetry analysis has shown to be extremely suitable to deal with structures described by different space groups as well as in modelling new ones. Applying its methodology to magnesium borohydride helped to connect all structures via group-subgroups relation making clear that they are not distinguish structures, but only a different structural representation of parent one. Furthermore three structures were modeled, namely orthorhombic $Fddd$, hexagonal $P6_122$ and cubic $Fd\bar{3}m$ and can be confront with experiment. A question why from SA we have structures which are inconsistent with the experimental still remains an open one.

⋆ ⋆ ⋆

[1] V. N. Konoplev, V. M. Bakulina, *Russian Chemical Bulletin* **20**, 136, (1971).

[2] J. Her, P. Stephens, Yan Gao, G. Soloveichik, J. Rijssenbeek, M. Andrus, J. Zhao, *Acta. Cryst. B* **63**, 561 (2007).

[3] Y. Filinchuk, R. Cerny, H. Hagemann, *Chem. Mater.* **21**, 925 (2009).

[4] B. Dai, D. S. Sholl, J. K. Johnsoon, *I. Phys. Chem. C* **112**, 4391 (2008).

[5] J. Voss, J. S. Hummelshoj, Z. Lodziana, T. Vegge, *J. Phys. Condens. Matter* **21**, 012203 (2009).

[6] A. Bil, B. Kolb, R. Atkinson, D. G. Pettifor, T. Thonhauser, A. N. Kolmogorov, *Phys. Rev. B* **83**, 224103 (2011).

[7] V. Ozolins, E. H. Majzoub, C. Wolverton, *Phys. Rev. Lett.* **100**, 135501 (2008).

Multireflection grazing incidence method for residual stress determination

Marianna Marciszko

Faculty of Physics and Applied Computer Science, AGH University of Science and Technology, Mickiewicza 30, 30-059 Kraków, Poland

Supervisor: Andrzej Baczmański

Multireflection Grazing Incidence X-Ray Diffraction (MGIXD) allows to perform a non-destructive analysis of the heterogeneous stress state below the surface of the sample. The average values of stresses weighted by absorption of X-ray radiation are measured. In this work the stress profiles as a function of penetration depth were determined for mechanically polished Al2017 alloy. Measurements were performed using classical X-ray diffractometer.

Residual stresses can be determined using diffraction methods from the displacement and broadening of the diffraction peak measured for different orientation of scattering vector with respect to the sample. One of this method is standard X-ray $\sin^2\Psi$ method,[1] however it is not advised for the analysis of heterogeneous stress states because the penetration depth of X-ray radiation varies significantly during measurement when the orientation of the scattering vector is changing.

The geometry based on the Grazing Incidence X-Ray diffraction, called the MGIXD-$\sin^2\Psi$ method[2–4] allows for non-destructive analysis of the heterogeneous stresses for different volumes below the surface of the sample. What is more stresses can be measured at very shallow depths of a few μm.

Grazing incidence geometry is characterized by a small and constant incidence angle (α in Fig. 1) and by different lengths and orientations of the scattering vector. In standard $\sin^2\Psi$ method,[1] the measurements are performed for one {hkl} plane whereas in MGIXD for different sets of {hkl} planes. It is possible by using appropriate values of $2\theta_{\{\mathrm{hkl}\}}$ scattering angles (Fig. 1). The interplanar spacing $\langle d(\varphi,\Psi)\rangle_{\{\mathrm{hkl}\}}$, average for the reflecting grains volume, can be obtained from the measured diffraction peak position ($2\theta_{\{\mathrm{hkl}\}}$) using Bragg law. Further the interplanar spacing measured in the direction of scattering can be related to residual stresses.[1]

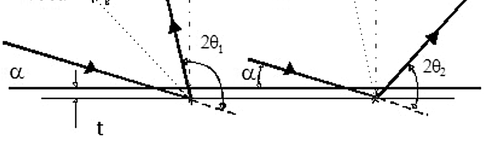

FIGURE 1: Geometry of MGIXD-$\sin^2\Psi$ method.

In standard methods, the orientation of the scattering vector can be chosen freely by proper selection of angles φ and Ψ,[1] which can be changed independently. In contrary in the MGIXD-$\sin^2\Psi$ geometry, only the φ angle (rotation around normal to the sample surface) can be chosen arbitrarily, but the Ψ angle (defined in Fig. 1) depends on the (hkl) reflections and the constant incidence angle α, i.e.:

$$\Psi_{\{\mathrm{hkl}\}} = \theta_{\{\mathrm{hkl}\}} - \alpha. \tag{1}$$

Consequently, the possible values of $\Psi_{\{\mathrm{hkl}\}}$ angles are limited to the number of (hkl) reflections used in the experiment.

The penetration depth (t) of X-ray radiation, defined as the distance from the sample surface for which $1 - 1/e$ of total intensity of the incident beam is absorbed

$$t = \left(\frac{\mu}{\sin(\alpha)} + \frac{\mu}{\sin\left(2\theta_{\{\mathrm{hkl}\}} - \alpha\right)} \right)^{-1}. \tag{2}$$

In the case of the MGIXD-$\sin^2\Psi$ method, the penetration depth is almost constant for

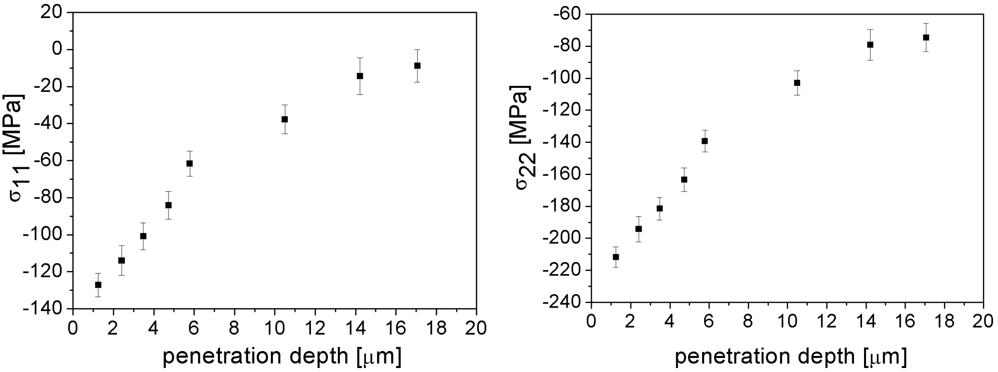

FIGURE 2: In-depth evolution of stresses in polished Al2017 alloy.

a fixed small α angle and for large range of the Ψ angle. Moreover, the stresses can be measured for different layers under the sample surface by setting different values of the α angle.

The grazing incidence measurements were performed on the PANalytical X'Pert diffractometer using Cu radiation for polished Al2017 alloy. The experiment was performed for various incidence angles α in order to find the in-depth evolution of the stresses in the sample.

TABLE 1: Single crystal elastic constants for aluminium.[7,8]

Single crystal elastic constants [GPa]		
C_{11}	C_{22}	C_{44}
106,8	60,4	28,3

In stress analysis the free-surface self-consistent method[1] was used to calculate diffraction elastic constants from single crystal elastic constants given in Table 1.

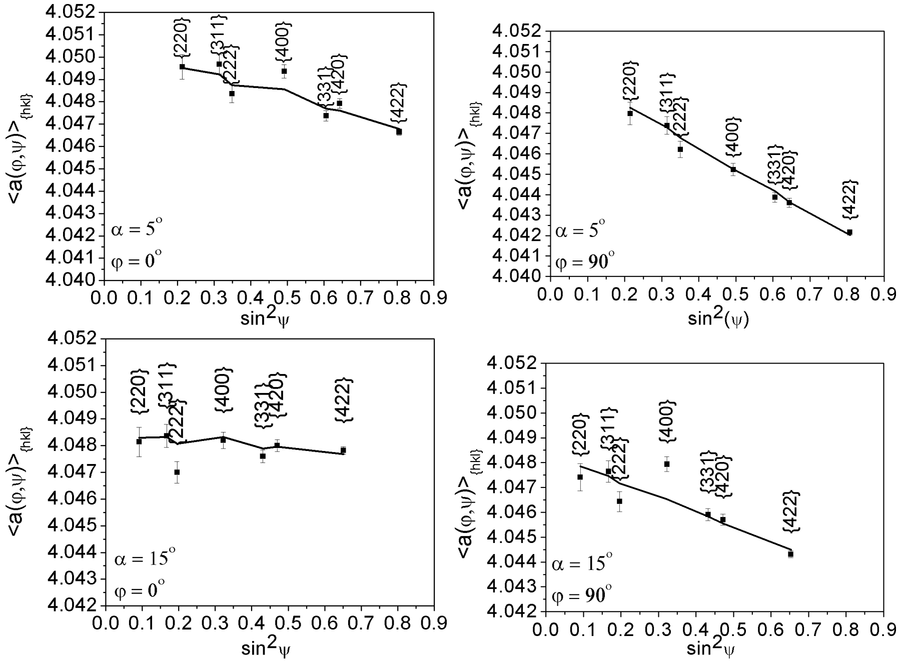

FIGURE 3: Measured lattice parameters (points) and theoretical results of fitting (continuous lines) vs. $\sin^2\Psi$ for Al 2017 alloy. Results of grazing incidence method for two angles α.

Results of stress analysis in polished Al2017 alloy and $\sin^2\Psi$ plots for grazing incidence method are shown in Figs. 2 and 3 respectively.

Concluding the results of stress measurement with MGIXD method showed that mechanical polishing introduced compressive stresses to Al2017 alloy. The highest compressive stresses are present near the surface of the sample and they are decreasing with the depth in the sample.

⋆ ⋆ ⋆

[1] A. Baczmański, P. Lipinski, A. Tidu, K. Wierzbanowski, B. Pathiraj, *J. Appl. Cryst.* **41**, 854 (2008).

[2] K. Van Acker, L. De Bayser, J. P. Celis, P. Von Houtte, *J. Apll. Cryst.* **27**, 56 (1994).

[3] C. Quaeyhaegens, G. Knuyt, *Surface and Coat. Technology* **74/75**, 104 (1995).

[4] S. J. Skrzypek, A. Baczmański, W. Ratuszek, E. Kusior, *J. Appl. Cryst.* **34**, 427 (2001).

[5] M. Schuster, H. Göbel, *J. Phys. D* **28**, A270 (1995).

[6] J. Bonarski, J. Smolik, L. Tarkowski, M. Biel, *Arch. Met. & Mat.* **53**, 49 (2008).

[7] M. Birkholz, Thin Film Analysis by X-ray Scattering (WILEY-VCH, 2006).

[8] G. Simmons, H. Wang, Crystal Elastic Constants and Calculated Aggregate Properties: A Handbook (The MIT Press, MA/London, Cambridge).

Examination of self-assembled monolayers influence on polymer/metal interfaces by KPFM and SIMS

Mateusz Marzec

Faculty of Physics and Applied Computer Science, AGH University of Science and Technology, Mickiewicza 30, 30-059 Kraków, Poland

Supervisor: Andrzej Bernasik

Buried interfaces between polystyrene (PS) or poly(methyl methacrylate) (PMMA) thin film and the gold surface patterned with CH_3- and $COOH-$ terminated alkanethiols self-assembled monolayers (SAM) were examined with Kelvin Probe Force Microscopy (KPFM) and Secondary Ion Mass Spectrometry (SIMS). Chemical composition of the interface was proved by SIMS. The contact potential difference (CPD) maps measured by KPFM on the PS and the PMMA films showed inverted contrast. This observation is discussed in term of reorientations of the COOH−SAM net dipole moments induced by interactions with PMMA.

Charge transport through the interface between an organic layer and an electrode plays a key role in designing of organic electronic devices such as light-emitting diodes, solar cells, transistors or chemical sensors. Electrical impedance of the interface has strong influence on the performance of these devices. Although this problem has been studied since conjugated polymers were discovered and employed to organic electronics, it is intensively investigated till now. Mechanism of energy level alignment at the interface is the main issue under consideration. [1,2]

To improve the efficiency of organic electronic devices, a self-assembled monolayer (SAM) is often placed at the interface. [3] The SAM can control not only dipole moment across the junction, but also modify morphology of the deposited organic layer. Both aspects are intensively studied. In the electronic devices mostly carboxylic acid molecules are employed. [4] Terminal groups of the molecules can induce different dipole moments. Also hydrophobic or hydrophilic terminal groups of alkylthioles molecules induce a dipole moment. The SAM deposited on substrate alters surface tension and changes wettability which influences morphology of the deposited organic layer and, in case of organic blends, affects phase separation. [5]

In this study buried interfaces formed between thin polymer layer and metal, modified by self-assembled monolayer, were investigated. The aim of this study is to characterize electric dipoles created at the buried interfaces and to determine shift of electronic levels. Two methods were employed. Kelvin Probe Force Microscopy allowed to reveal electronic properties of the polymer/metal interfaces with up to a nanometer scale resolution in addition with sample surface topography. Time-of-Flight Secondary Ion Mass Spectrometry was used to characterize chemical composition of the constituents of the surface and the buried interfaces with very high sensitivity and chemical specificity in nanometer scale lateral and depth resolution.

The gold surfaces (obtained by thermal evaporation of Au onto silicon wafers) were patterned with self-assembled monolayers (SAMs) of CH_3-terminated (16-hexadecanethiol) and/or COOH-terminated (16-mercaptohexadecanoic acid) thiols. The SAM patterns were micro-contact printed on gold surfaces with PDMS (poly[dimethylsiloxane]) stamp, consisting of brick-like structures with ~ 20 μm periodicity. Two types of SAM patterns were prepared: (i) COOH−SAM/CH_3−SAM obtained with one-step micro-contact print-

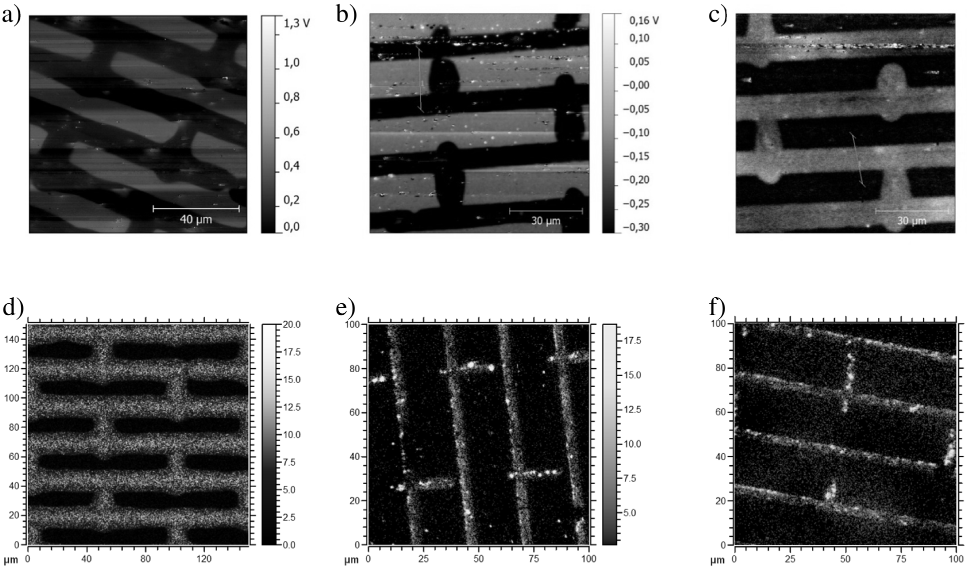

FIGURE 1: Upper part: CPD signals obtained using KPFM: a) COOH−SAM/CH_3−SAM patterned Au substrate, b) thin film (ca 100 nm) of PS on COOH−SAM/CH_3−SAM patterned Au substrate, c) thin film of PMMA on COOH−SAM/CH_3−SAM patterned Au substrate. Lower part: SIMS maps of intensity of negatively charged oxygen ions obtained during sputtering: d) COOH−SAM/CH_3−SAM patterned Au substrate, e) PS on COOH−SAM/CH_3−SAM patterned Au substrate, f) thin film of PMMA on COOH−SAM/CH_3−SAM patterned Au substrate.

ing (μCP) of COOH−SAM followed by immersion in the solution of CH_3−SAM and (ii) CH_3−SAM/COOH−SAM pattern resulting from μCP of CH_3−SAM regions and subsequent COOH − SAM formation in empty areas. In the next step polystyrene (PS) or poly(methyl methacrylate) (PMMA) chloroform solutions were spin-casted on the patterned substrates, forming a films with thickness of about 100 nm. All samples were prepared in glove-box working under argon atmosphere with the amounts of oxygen and water maintained under 0,1 ppm.

Kelvin Probe Force Microscopy (KPFM) is based on Atomic Force Microscopy (AFM) technique and is used to measure the contact potential difference (CPD) between an AFM tip and a sample. In amplitude modulation mode (AM-KPFM) the oscillating tip in mechanical resonance frequency and with applied voltages (DC and AC) is approached to the sample surface. The applied voltages induce electrostatic force between the tip and the sample surface which cause a tip deflections that are detected and enable simultaneous determination of topography and CPD. Measurements with KPFM, working in AM and non-contact modes, were performed with Agilent 5500 apparatus yielding surface topography simultaneously with the maps of CPD. All measurements were performed in air at room temperature.

Time-of-Flight Secondary Ion Mass Spectrometry (SIMS) is a powerful tool used in material science to characterize chemical composition of the constituents of the surface and thin films with high sensitivity and chemical specificity.[6] This technique is based on the mass spectroscopic analysis of secondary ions, which are generated by the interaction of a primary ion beam with a sample. The samples were analyzed by dual beam depth profiling carried in negative mode (negatively charged ions measured) using IONTOF ToF-SIMS.5 instrument: one gun was responsible for sputtering the surface and the other for the com-

TABLE 1: Hansen Solubility Parameters $[\mathrm{MPa}]^{1/2}$.

	δ_{total}	δ_{hb}	δ_{p}
PS	19,3	2,9	4,5
PMMA	21,5	5,1	10,5

position analysis. Instrument was equipped with Bi^+ liquid metal ion gun (Bi LMIG) and Cs^+ beam sputtering gun. Analysis were taken using 30 keV Bi^{3+} clusters (current of 0,1 pA) from an areas of 100×100 μm^2 in order to identify the species present at various depths and sputtering was taken using 1 keV Cs^+ ion gun in areas of 400×400 μm^2 (current of 37 nA).

The CPD signals (Fig. 1, upper part) indicate local dipole moment orientation induced by SAMs placed on the gold surface (Fig. 1a), at the interface between gold substrate and non-polar PS film (Fig. 1b) and gold substrate and polar PMMA film (Fig. 1c). The difference of CPD signal between SAM$-$COOH and SAM$-CH_3$ regions placed on gold (without coverage) and covered with non-polar PS thin layer is about 300 mV. The difference in CPD signal for PMMA covered patterned Au substrate is about 60 mV. SIMS maps of intensity of negatively charged oxygen ions (Fig. 1, lower part) indicate localizations of SAMs patterned substrate. In Fig. 1d it can be observed that O^- signal revealed COOH$-$SAM/CH_3-SAM pattern on gold, the first monolayer was analyzed. In the Fig. 1e and Fig. 1f the same signal was also used to reveal the localization of SAMs at the buried interface covered by PS and PMMA, respectively. It is noteworthy that for polar PMMA film the CPD signal is inverted as compared to that for non-polar PS film and bare SAM patterns on gold (as confirmed by SIMS O^- maps). The inversion of the CPD signals can be explained by inter-association and depolarization effects[7,8] between PMMA and COOH$-$SAM monolayer caused by hydrogen bonds. Net dipole moment of the SAMs deposited on the gold surface can be divided into two dipoles. The first one is attributed to the head (thiol) group, which is the same for the both molecular layers and directed out of the gold surface. The second dipole is related to the tail group and it is oriented in the same or in the opposite direction for the CH_3- or the COOH-group, respectively (Fig. 2). Possibility of polymer interactions with the substrate can be predicted from Hansen solubility parameters (Table 1). High values of the pa-

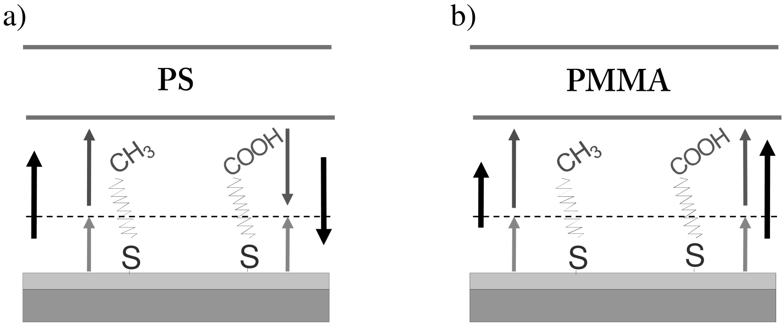

FIGURE 2: Schematic illustrations of dipole moments orientation of tail and head groups of SAMs and resulting net dipole moments (outer black arrows) between gold substrate and a) non-polar PS film or b) polar PMMA film. For polar PMMA film COOH$-$SAM tail group dipole moment is inverted compared to PS layer because of hydrogen bonds interactions causing depolarization effect and finally net dipole moment of the molecules became oppositely directed.

rameters indicate that permanent dipole and hydrogen bonding interactions are preferred for PMMA. Especially two types of hydrogen bonds interactions are expected. The first type may appear between carbonyl group of PMMA and hydroxyl group of COOH−SAM or second type between hydroxyl group of PMMA and carbonyl group of COOH−SAM. In turn, hydrogen bond interactions changed the direction and total net dipole moment of the COOH−SAM layer which becomes slightly smaller but accordingly directed with CH_3−tailed monolayers. This explains the much smaller difference (60 mV) between the bright and the dark regions on the CPD map for the PMMA film as against to the PS one (280 mV). Significant depolarization effect cannot be expected for the PS film because of the nonpolar character of polystyrene.

⋆ ⋆ ⋆

[1] H. Ishii, K. Sugiyama, E. Ito, K. Sei, *Adv. Mater.* **1**, 605 (1999).

[2] S. Braun, W. R. Salaneck, M. Fahlman, *Adv. Mater* **1**, 1450 (2009).

[3] H. L. Yip, S. K. Hau, N. S. Baek, H. Ma, A. K. Y. Jen, *Adv. Mater.* **20**, 2376 (2008).

[4] C. Goh, S. S. Scully, M. D. McGehee, *J. Appl. Phys.* **101**, 114503 (2007).

[5] P. Cyganik, A. Bernasik, A. Budkowski, B. Bergues, K. Kowalski, J. Rysz, J. Lekka, M. Lekki, Z. Postawa, *Vacuum* **633**, 307 (2001).

[6] H. Nygren, B. Hagenhoff, P. Malmberg, M. Nillson, K. Richter, *Microsc. Res. Techniq.* **70**, 970 (2007).

[7] M. L. Sushko, A. L. Shluger, *Adv. Funct. Mater.* **18**, 2228 (2008).

[8] M. M. Coleman, P. C. Painter, *Prog. Polym. Sci.* **20**, 1 (1995).

X-ray diffraction and polarizing microscope studies of phase transitions of *n*BBAA

Natalia Osiecka

The Henryk Niewodniczański Institute of Nuclear Physics Polish Academy of Sciences, Radzikowskiego 152, 31-342 Kraków, Poland

Supervisor: Maria Massalska-Arodź

Several derivatives of the homologues series of the bromobenzylidene alkoxyaniline, abbreviated as nBBAA ($n = 4 - 12$), exhibit liquid crystal polymorphism in a wide temperature range. In all of the substances the smectic B phase characterized by the hexagonal arrangement of molecules which are orthogonal to the planes of the smectic layers was found. In order to know which of the smectic B phase, hexatic or crystal, appearred in the subsequent nBBAA substances the X-ray diffraction and the polarizing microscope studies were performed.

In many organic materials with anisotropic shape of molecules thermodynamically stable liquid crystalline phases, liquid-like and/or crystalline-like, occur on cooling between isotropic liquid and crystalline solid phases. They may flow like a liquid and exhibit also some features typical for crystals like birefringence and X-ray diffraction pattern. Usually, the ratio of the length and the diameter of the molecules is larger than five.[1] The liquid crystal molecules are built of rigid core and flexible tails as for fully flexible molecules no orientational order appears and for rigid molecules direct transformation from the isotropic liquid to the crystalline solid phase occurs.[2] Liquid crystals can be deviated into two types: thermotropic and lyotropic. The thermotropic liquid crystals are pure substances, which change their properties with the temperature and pressure. The lyotropic liquid crystals, being mixtures of the organic substance and inorganic solvent, change properties with the temperature, pressure and concentration.[3]

Thermotropic liquid crystal are deviated in three categories: nematics, smectics and columnar phases. In the columnar phase the disc-shape molecules assemble into cylindrical structures. Long axes of molecules in nematic phase are aligned parallel to each other, but their centers of mass are arranged at random. In smectic phase molecules assemble in layers.[4]

This paper is focused on the homologous series of n–4–bromobenzylidene–4'–alkoxyanlines (nBBAA), exhibiting only smectic B (SmB), or a sequence of smectic A (SmA) and smectic B phases (in case of n larger than 5).[5] In the SmA phase, the long axes of molecules are oriented orthogonaly to the layer planes. In the SmB phase, the molecules in smectic layer have hexagonal arrangement. There are two types of SmB phase, crystalline and hexatic ones. The hexatic smectic B phase is characterized by the existence of a short range positional ordering of the molecules within the layers. In the crystal SmB phase there are correlations of molecular positions within and between the layers.[6]

Usually, type of liquid crystal phase is determined by one of three methods: X-ray diffraction, the polarizing microscope texture observations and miscibility studies. Two types of SmB phase are co-miscible so a miscibility study are not appropriate to determine which of SmB types are present in the nBBAA substances.[7]

Using the polarizing microscope we observed the textures of SmA and SmB phases of nBBAA. For 4BBAA and 5BBAA the mosaic textures of SmB occured. That observation suggests these substances exhibit crystal SmB phases.[8] For 6BBAA – 12BBAA observations are different. First of all, for SmA and SmB phases similar focal-conic fan textures

TABLE 1: The FWHM values for the (001) and (110) peaks.

nBBAA	FWHM (001) [°]	FWHM (110) [°]
4BBAA	0,1948	0,1624
5BBAA	0,1299	0,1299
6BBAA	0,1948	0,1624
7BBAA	0,1299	0,1624
8BBAA	0,1299	0,1948
9BBAA	0,1299	0,1624
10BBAA	0,1299	0,1948
11BBAA	0,1299	0,1299
12BBAA	0,1299	0,1624

were observed. At the point of phase transition usually transition bars appear, which give information what type of SmB phase appears. No change of texture in phase transition between SmA and SmB is a feature characteristic for hexatic type of the smectic B phase. In case of nBBAA ($n = 6 - 12$) substances only faint transient lines occurred at the point of transition and then quickly disappeared. As the transition proceeds the lines become wider until they meet and disappear what is a characteristic phenomenon observed for crystal SmB.[9]

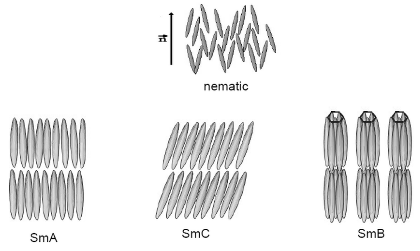

FIGURE 1: Various types of thermotropic liquid crystals.

X-ray diffraction pattern of SmB phase exhibits three peaks labeled as (001), (002) and (110). One can observe the bordering of the peaks due to the molecular dynamics. In case of crystal SmB phase full width at half maximum (FWHM) of (001) peak has similar value as that of the peak (110).[10,11] That phenomenon results from positional correlations, which are three dimensional and of long range. In case of hexatic SmB phase the FWHM value of (110) peak is two or three times broader than the (001) peak. Table 1 shows the FWHM values of (110) peak to (001) peaks in homologous series of nBBAA which occurred to be similar.

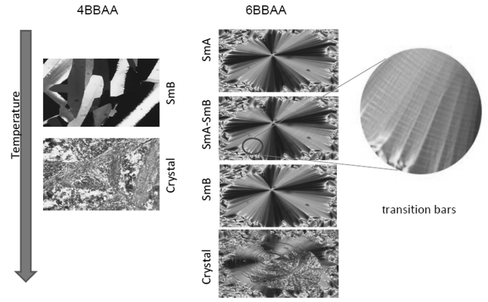

FIGURE 2: Phase polymorphism of 4BBAA and 6BBAA.

We tried to select those features of X-ray diffraction and polarizing microscope observations which may be helpful for identification of the types of SmB phase in the substances studied. The results suggest the appearance of the crystal SmB phase for all substances. For 6BBAA – 12BBAA the transition bars widen and disappear only after they met. Also the FWHM values of (001) peak and of (110) peak are similar.

⋆ ⋆ ⋆

[1] P. G. de Gennes, J. Prst, The physics of liquid crystals (Oxford University Press, New York, 1993).

[2] S. Chadrasekhar, Liquid crystals, 2nd edition (Cambrige University Press, New York, 1997).

[3] L. M. Blinov, V. G. Chigrinov, Electrooptical effects in liquid crystal materials (Springer-Verlag, New York, 1994).

[4] M. Barón, *Pure Appl. Chem.* **73**, 845 (2001).

[5] N. Osiecka, A. Budziak, Z. Galewski, M. Massalska-Arodź, *Phase Trans.* **85**, 314 (2012).

[6] A. J. Jin, M. Venum, T. Stoebe, C. F. Chou, J. T. Ho, S. W. Hui, V. Surendranath, C. C. Huang, *Phys. Rev. Lett.* **74**, 4863 (1995).

[7] D. S. Mitchell, W. J. Leigh, *Liq. Cryst.* **4**, 39 (1989).

[8] B. Bahadur, *J. Chem. Phys.* **67**, 3272 (1977).

[9] J. W. Goodby, R. Pindak, *Mol. Cryst. Liq. Cryst.* **75**, 233 (1981).

[10] A. J. Leadebetter, J. C. Frost, M. A. Mazid, *J. de Phys.* **40**, L-325 (1979).

[11] R. Pindak, D. E. Moncton, S. C. Davey, J. W. Goodby, *Phys. Rev. Lett.* **46**, 1135 (1981).

Basic concepts of mechanical alloying

Dariusz Rusinek

Faculty of Physics and Applied Computer Science, AGH University of Science and Technology, Mickiewicza 30, 30-059 Kraków, Poland

Supervisor: Łukasz Gondek

The mechanical alloying process is technique for synthesis materials at ambient temperature (not in elevated temperature). The driving force of the reactions are mechanical force originating from movement of balls in high energy mills. Plastic deformations, cold welding, introducing of various defects, which increase diffusivity and homogeneity of synthesised material take place upon milling process. By this method it is possible to produce amorphous, nanocrystalline and highly non-equilibrium material, which indicate new interesting properties and related applications. In this work it was shown the principle of mechanical alloying, models and different type of materials which can be produced by this method.

Scientist permanently endeavours to improve materials properties. Through by using the standard thermochemical processes many properties might be improved. New space, sport, industry technologies need new materials with advanced properties. These materials can be produced by a strict control of all processes in fabrication to obtain compositions, designed to specific application, due to its structure, microstructure, phases, texturing and stresses. Such properties can be also obtained in highly non-equilibrium conditions. One of the main methods for production highly-energized, metastable, non-equilibrium materials is mechanical alloying. This process is conducted in high energy ball mill like shakers, planetary ball mills, attritor mills. In this type of synthesis method it is possible to obtain glassy alloys, amorphous materials, nanocrystaline materials. Also by high-energy milling it is possible to carry out the chemical reaction it is on field of mechanochemistry. Mechanical milling has huge opportunities to obtain alloys, hydrates, semiconductors, ceramic materials and composites.[1–3]

All mills have a vials and parts, which work and transfer energy (e.g. balls) to the initial powder. As a consequence of colliding balls into powder, plastic deformations of powder were obtained. If in collision participates more than one particle of powder it cause aggregation and get a composite. After plenty of repetition of this collision powders are mixing chemically by diffusion or reaction. Mechanical alloying processes can be described by few models based on Smoluchowski's coagulation–fragmentation equations. Models describe process of mechanical milling from two points of view. The first describe milling design, mechanics of apparatus and the second is focused on powder charge evolution. Otherwise there are models which combine two of previous models. Models analysing mechanics of milling can predict characteristic of collision and demand for energy. From the other hand there are models, which use only basic information about equipment, like average collision and after repetition of this process. They can predict changes in powder properties.[4]

To control mechanical alloying process it is very important thing to understand the mechanism. There are main factors that control creation new materials like activation energy of induced defects, temperature and crystalline size. Diffusion of constituents to form a new alloy has been controlled by mechanical and thermal energy. Diffusivity may be controlled and decreased by temperature increasing and decreasing of particle size. On the first part of mechanical milling particles in high energy collisions may be cold welded together, flattened, fractured, new clean surfaces are produced and improve the contacts and aggregate. At the second stage, particles forms layered structure and are crumbling and fracturing. Materials are then mixed and dissolved, but homogeneous structure is still not obtained. Plastic deformations make particles harder, next particle size is decreasing by fatigue failure mechanism. At the last part, lamellae disappear and new homogenous alloy is produced. Unfortunately, decreasing of particle size has very low efficiency like 0,1%, in high energy ball mill it is less than 1%. The majority of supplied energy is wasted on heat, plastic and elastic deformations of grains. This waste heat cause warming of milling vial, balls and powder, hence it has huge influence on structure and microstructure of final powder. As a result of heating, higher diffusivity and recrystallization processes could be expected. To obtain nanocrystalline or amorphous alloys, diffusion should be lower, which implies lower temperature of process to be maintained.[1,5] The temperature of balls may exceed 600°C as was shown in work.[6] Therefore, the milling methodology must be well-suited to materials that should be synthesized. Namely, the milling cycles are usually followed by rest-time, to avoid overheating of the powder. For enhancing homogeneity, that is crucial in mechanical alloying, each cycle can be reversed. At last, for some cases suspensions or catalysers are introduced into the milling vial in order to achieve optimum milling conditions.

The group of metallic alloys and intermetallic compounds is the largest group of materials produced by mechanical synthesis. This method is widely used for hydrogen storage materials, e.g. compounds based on magnesium or titanium.[7,8] Mechanical alloying is a competition method for widely used rapid quenching for glassy alloys producing.[9] Also catalysers can be produced as in work,[10] where Cu_3Pt for direct methanol fuel cell (DMFC) were synthesised. This electro-oxidation catalyst material is cheaper than convectional Pt-based. One of the most important methods for producing iron-based magnetic alloys is mechanical alloying. This alloys are used in soft magnetic composite materials.[11]

Mechanical alloying is also used for production of advanced high temperature ceramics like carbides, borides, nitrides of metals in IV Group of transition metal (titanium, zirconium), and thallium and others. These compounds are commonly produced in high-temperature procedures, but mechanical alloying shows some beneficial like low cost and simplicity. Moreover this method is simple way to obtain nanosize materials in room temperature which after consolidation by hot pressing exhibit needed mechanical properties in elevated temperature. These materials ZrC ZrB, TiC, TiN TaC in relation to their properties high melting point high hardness, high elastic modulus, shock resistance, high strength has many possible applications like thermal protection, crucibles, in re-entry rocket technology, thermocouple, in machinery applications (cutting tools, wear parts, nozzles) and others.[12–14]

Also for semiconductors, mechanical alloying is simple and suitable method of production. Moreover it is possible to synthesis elements for spin electronic applications which have semiconductor and ferromagnetic properties e.g. Fe-doped ZnO.[15]

Except one-phase solid materials like metallic alloys and ceramics, the mechanical alloying may be also used to produce composites materials. Usually such composites have ductile metallic or intermetallic matrix and discontinuous second phase or second ductile. As a discontinuous phase used for reinforcement occur particles whiskers and chopped fibers, materials which are made are usually hard metalloid and ceramic compound (TiB_2, SiC). Second ductile phase of solid solutions is used for toughening of matrix ductile phase. Dispersed phase impede growing of grains in heightened temperature during consolidation. In consequence strength and hardness is achieved in lower temperature, which is known as Hall-Petch and Orowan hardening. Growing of grain size in elevated temperature results in softening of materials.[16] As an example $MoSi_2$ can be given, which is used in high temperature applications as heating element and also in electronics and engine construction. But this material has the low ductility and fracture toughness, what limits potential application. To prevent this properties particulates Si_3N_4 has been added to molybdenum silicide matrix. This addition increase fracture toughness and decrease creep rates in high temperatures, but unfortunately fracture toughness in room temperature remains still low.[17] Synthesised by high-energy mill and annealed in 600°C composite of copper and cementite was done to stabilize nano-size copper matrix. Recrystallization of nanoalloy conducts in 90°C. In composite Cu-Fe-C diffusivity coefficient are low and by pinning of grain boundaries and solute drag effects Fe_3C stabilise structure.[18]

Amorphous structure after mechanical alloying may be investigated by reverse Monte Carlo simulations. As an example $Si_{24}Nb_{76}$ can be given, that has interesting properties like high melting point and hardness, resistance oxidation. From conventional technics is possibly to obtain only Nb_3Si, a-Nb_5Si_3, b-Nb_5Si_3 and $NbSi_2$, but by mechanical alloying can be produced other stoichiometries. Properties of amorphous alloys are dependent on configuration of the nearest neighbours. Extracted from the experiment data and Monte Carlo simulations the structural parameters of Nb_3Si compound were obtained.[19] Similar research were investigated for $Cr_{25}Nb_{75}$, where experiment appeared to be in agreement with the predicted thermodynamic approach. The coordination numbers for the first neighbours and interatomic distances were obtained. The calculated chemical short-range order show similarity the atomic structure of the amorphous $Cr_{25}Nb_{75}$ with the additive hard sphere (AHS) model for same chemical composition alloy.[20] Not only single materials may be simulated, but also complex composites. Nano-composite powder of Al/SiC produced by mechanical alloying has been modelled by statistical approach. As process variables are time, speed of milling, weight of balls and weight of powders, as a result different composites with respect to crystallite and particle size or lattice strains can be obtained.[21]

Mechanical alloying is a simply, useful and powerful method to synthesise wide variety of materials: glassy, micro, nano and quasicrystaline of superalloys, intermetallic compounds, semiconductors, ceramics and composites. Non-equilibrium materials reveal great new properties and may find plenty of advanced applications. By mechanical alloying materials, impossible to obtain by traditional methods, can be produced. Mechanism of mechanical alloying is very complex and has a lot of variables, for this reason modelling is very difficult. In mechanical milling there are broad fields, which are still not discovered and developed. Therefore, a still growing interest focused on this method is observed.

⋆ ⋆ ⋆

[1] C. Suryanarayana, *Prog, Mater. Sci.* **46**, 1 (2001).

[2] B. S. Murty, S. Ranganathan, *Int. Mater. Rev.* **43-3**, 101 (1998).

[3] C. C. Koch, J. D. Whittenberger, *Intermetallics* **4**, 339 (1996).

[4] J. R. Harris, J. A. D. Wattis, J. V. Wood, *Acta Mater.* **49**, 3991 (2001).

[5] L. Lu, M. O. Lai, *Mater. Design* **16.1**, 33 (1995).

[6] Y.-S. Kwon, K. B. Gerasimov, S-K. Yoon, *J. Alloy. Compd.* **346**, 276 (2002).

[7] J. Huot, G. Liang, R. Schulz, *Appl. Phys. A* **72**, 187 (2001).

[8] M. Lucaci, Al. R. Biris, R. L. Orban, G. B. Sbarcea, V. Tsakiris, *J. Alloy. Compd.* **488**, 163 (2009).

[9] J. Eckert, *Mater. Sci. Eng. A* **364**, 226 (1997).

[10] Y.-F. Hsieh, Y.-C. Hsieh, Y.-C. Tseng, P.-W. Wu, C. G. Chao, P. Lin, J.-F. Lee, *J. Alloy. Compd.* **552**, 329 (2013).

[11] H. Shokrollahi, *Mater. Design,* **30**, 3374 (2009).

[12] H. Abderrazak, F. Schoenstein, M. Abdellaoui, N. Jouini, *Int. J. Refract. Met. H.* **29**, 170 (2011).

[13] D. Ağaoğulları, H. Gökçe, İ. Duman, M. L. Öveçoğlu, *J. Eur. Ceram. Soc.* **32**, 1447 (2012).
[14] M. Naidoo, O. Johnson, I. Sigalas, M. Herrmann, *Int. J. Refract. Met. H.* **37**, 67 (2013).
[15] Y. Lin, D. Jiang, F. Lin, W. Shi, X. Ma, *J. Alloy. Compd.* **436**, 30 (2007).
[16] C. C. Koch, *Mater. Sci. Eng. A* **244**, 39 (1998).
[17] C. Suryanarayana, *Mater. Sci. Eng. A* **479**, 23 (2008).
[18] P. A. Carvalho, I. Fonseca, M. T. Marques, J. B. Correia, A. Almeida, R. Vilar, *Acta Mater.* **53**, 967 (2005).
[19] J. C. de Lima, A. R. Jerônimo, A. Gomez, S. M. Souza, D. M. Trichês, C. E. M. Campos, T. A. Grandi, S. Kycia, *J. Non.-Cryst. Solids* **354**, 4598 (2008).
[20] J. C. de Lima, T. O. Almeida, A. R. Jerônimo, S. M. Souza, C. E. M. Campos, T. A. Grandi, *J. Non.-Cryst. Solids* **352**, 109 (2006).
[21] M. R. Dashtbayazi, A. Shokuhfar, *Comp. Mater. Sci.* **40**, 466 (2007).

The Average Unit Cell concept for icosahedral quasicrystals based on Ammann tiling

Radosław Strzałka

Faculty of Physics and Applied Computer Science, AGH University of Science and Technology, Mickiewicza 30, 30-059 Kraków, Poland

Supervisor: Janusz Wolny

The paper describes the application of the statistical approach based on Average Unit Cell concept for modeling of icosahedral quasicrystals. As a model structure the Ammann tiling is used. The derivation of structure factor for non-decorated structure within the Average Unit Cell approach is presented and the analytical diffraction pattern is calculated. There is also the perfect agreement between statistical approach and higher-dimensional analysis shown. Finally, the first attempts to find a decoration scheme for Ammann tiling are done and some results are shown in the paper.

Icosahedral quasicrystals (*i*-QCs) are 3D structures with no translational symmetry and fully aperiodic arrangement of atoms in space. The diffraction pattern represents the symmetry elements of an icosahedron (Platonian solid with 20 equilateral triangular faces, Fig. 1a), in particular it has 5-fold rotational symmetry. The non-crystallographical Laue class of icosahedral quasicrystals is $m\bar{3}\bar{5}$.

It is worth mentioning that first quasicrystalline structures, discovered by Shechtman in 1982,[1] were the icosahedral aperiodic Al-Mn alloys. The spots on electron diffraction pattern showed 5-fold icosahedral symmetry.

The modeling of icosahedral structures is done by using the Ammann tiling. This is a set of points in 3D space which exhibits the icosahedral symmetry. Ammann tiling is the 3D extension of Penrose tiling used for modeling the 2D decagonal quasicrystals. The building units are oblate and prolate rhombohedra. Here we consider the model Ammann structure without decorative atoms (so called „empty lattice").

The Average Unit Cell (AUC) concept[2,3] obtained by statistical approach can describe the diffraction pattern of quasicrystals. As a starting model in case of icosahedral quasicrystals the Ammann tiling is used. The AUC method was successfully applied to decagonal phases by Kozakowski and Kuczera[4–7] and to other aperiodic structures.[8]

The diffraction pattern of Ammann tiling can be indexed in the reciprocal space basis $V^\star$ by parallel components $\hat{x}_1 - \hat{x}_6$ of the basis vectors Fig. 1a, which reflect the icosahedral symmetry.[9] The peak position is then characterized by 6 indices and is the following:

$$\vec{k} = h_1\hat{x}_1 + h_2\hat{x}_2 + h_3\hat{x}_3 + h_4\hat{x}_4 + h_5\hat{x}_5 + h_6\hat{x}_6, \quad (1)$$

where $h_1 - h_6$ are the integer Miller indices of a diffraction peak.

The direct space vectors are formed by the orthogonality condition against $\hat{x}_1 - \hat{x}_6$ and have the similar spatial orientation.

The AUC is the distribution of the projections of the atomic positions onto the so called reference grid, which is periodic. The lattice parameters of the grid can be defined by the reciprocal space vectors. However, instead of using the oblique basis $\hat{x}_1 - \hat{x}_6$, the Cartesian one can be used (Fig. 1b). Six basis vectors $\hat{x}_1 - \hat{x}_6$ are then replaced by pairs of vectors $\vec{q}_i, \vec{k}_i$, $i = \{1,2,3\}$, which are the linear combinations of $\hat{x}_1 - \hat{x}_6$. The peak position is now:

$$\vec{k} = h\vec{q}_1 + h'\vec{k}_1 + h\vec{q}_2 + h'\vec{k}_2 + l\vec{q}_3 + l'\vec{k}_3\ , \quad (2)$$

where indices h/h', k/k', l/l' are the linear combination of $h_1 - h_6$. What is crucial, the lengths of vectors $\vec{q}_i$ is τ-times smaller than the lengths of $\vec{k}_i$ ($\tau \approx 1{,}618$ is called the golden mean ratio).

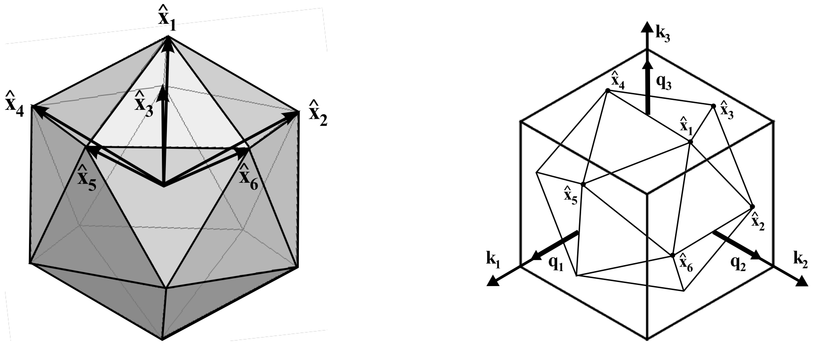

(a) (b)

FIGURE 1: (a) The definition of reciprocal space vector basis. Vectors of the so called „icosahedral” basis span the icosahedron. (b) The Cartesian basis of reciprocal space and its relation with the „icosahedral” basis.

The reference grid constants are related to $\vec{q}_i, \vec{k}_i,\ i=\{1,2,3\}$ as follows:

$$\lambda_{ki}=\frac{2\pi}{k_i};\qquad \lambda_{qi}=\frac{2\pi}{q_i};\qquad i=\{1,2,3\}, \tag{3}$$

where k_i, q_i are the lengths of vectors $\vec{q}_i, \vec{k}_i$, $i=\{1,2,3\}$.

The need of use the two reference grids is well-known for quasicrystals and discussed in [2–4]. Every position of points in Ammann tiling can be projected on the reference lattices. As a result we get the distribution $P(u_\mathrm{i}, v_\mathrm{i})$ of new positions u_i,v_i, $i=\{1,2,3\}$:

$$\begin{aligned} x_i &= N\lambda_{ki}+u_i, &\quad N\in\mathbf{Z}\\ x_i &= M\lambda_{qi}+v_i, &\quad M\in\mathbf{Z} \end{aligned} \tag{4}$$

The positions u_i belong to the the reference grid of lattice parameter λ_{ki} and v_i–λ_qi. One of the properties of the AUC is that the distribution $P(u_i, v_i)$ is only non-zero along lines $v_i = -\tau^2 u_i$ what is called the TAU2-scaling for quasicrystals. [10] This relation reduces the size of the distribution to $P(u_i)$ what we call the AUC. This distribution is uniform and continuous.

From the formulas (3) and (4) it is clear that the shape of the AUC is dependent on the choice of reciprocal space vectors $\vec{q}_i, \vec{k}_i,\ i=\{1,2,3\}$. With the choice of reciprocal space vectors $\vec{q}_i$,$\vec{k}_i$, $i=\{1,2,3\}$ like in the Fig. 1b, i.e. spanning the Cartesian reciprocal space basis, the shape of the distribution $P(u_i)$ is regular rhombic triacontahedron — solid dual to icosahedron with the same symmetry elements Fig. 2. This is important in terms of analytical calculations. The lengths of vectors $\vec{q}_i$,$\vec{k}_i$, $i=\{1,2,3\}$ are: $k_i=2\tau/\sqrt{2+\tau}\approx 1{,}70$; $q_i=2/\sqrt{2+\tau}\approx 1{,}05$.

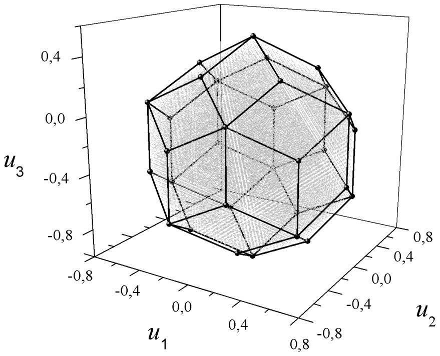

FIGURE 2: The points of AUC generated numerically for reciprocal space vectors $k_i\approx 1{,}70$; $q_i\approx 1{,}05$; $i=\{1,2,3\}$. The shape of the AUC is the rhombic triacontahedron (skeleton marked in the plot).

The structure factor for empty Ammann lattice can be calculated fully in real space by using the statistical approach. The formula is the following:

$$F(\vec{k})=\iiint_{\mathrm{AUC}}\exp[i\,(\kappa_1u_1+\kappa_2u_2+\kappa_3u_3)]\,du_1du_2du_3, \tag{5}$$

where the components κ_1, κ_2, κ_3 are $k_1(h'-\tau h)$, $k_2(k'-\tau k)$, $k_3(l'-\tau l)$. The

Fourier transform in the formula (5) runs over the shape of the AUC. Considering the uniformity and the finite size of the distribution, one can rewrite the formula (6) to:

$$F(\overrightarrow{k})=\int_0^{\lambda_{k1}}\int_0^{\lambda_{k2}}\int_0^{\lambda_{k3}}P(u_1,u_2,u_3)$$
$$\exp[i(\kappa_1u_1+\kappa_2u_2+\kappa_3u_3)]\,du_1du_2du_3. \qquad (6)$$

The intensity of diffraction pattern is calculated as a square of modulus of the structure factor. In the Fig. 3 the comparison of diffraction pattern calculated analytically over the shape of the AUC and in the higher-dimensional approach (the analytical volume integral over rhombic triacontahedron) and numerically as the Fourier transform of AUC is shown. The direction $\vec{k}_2$ has been chosen for the plot (Fig. 3).

The higher-dimensional approach has been not discussed in this paper. However the Fig. 3 shows the perfect agreement in terms of analytical calculations for the statistical approach and higher-dimensional analysis. The only difference is that calculation in statistical approach is carried out in physical space only without 6D modeling. The numerical integral over the distribution $P(u_i)$ gives the same result with some deviations occurring for small peaks only (numerical reason).

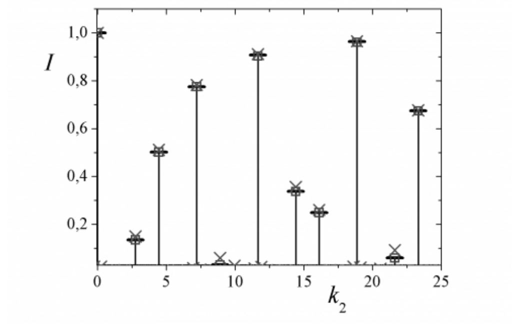

FIGURE 3: The plot of diffraction pattern for empty Ammann lattice in direction $\vec{k}_2$: horizontal dashes — analytical calculation in statistical approach; squares — analytical calculation in higher-dimensional approach; crosses — the numerical integral over AUC points (see Fig. 2). The agreement of first two plots is perfect, the numerical results have little deviations for small peaks.

The last part of this paper is dedicated to decoration scheme of Ammann rhombohedra. First important thing is to find the possible orientations of rhombohedra in real space and corresponding positions in AUC. In the AUC one need to find regions belonging to the atoms of a certain kind (the structure composition can be binary or ternary) and of certain orientation of rhombohedron. There are five 6-fold axes, but it can be shown that only two orientations of pair: prolate-oblate rhombohedron divide the AUC in the separate regions. Every rhombohedron consists of eight vertices, so the total possible orientations of regions in AUC is 960. In the Fig. 4 the distribution of rhombohedra with „z-orientation" is shown. The prolate and oblate rhombohe-

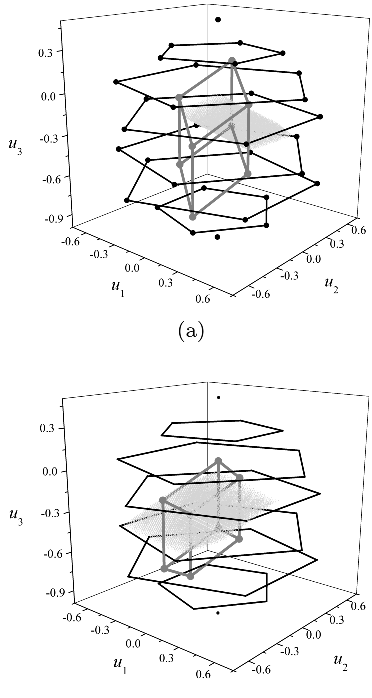

(a)

(b)

FIGURE 4: The possible distribution of oblate (a) and prolate (b) rhombohedra in AUC for „z-orientation". The rhombohedra built by basis vectors as discussed in the text.

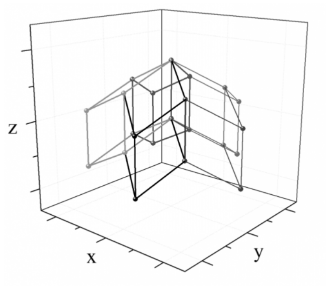

(a)

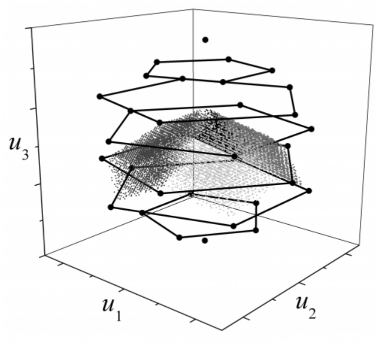

(b)

FIGURE 5: (a) Five orientations of prolate rhombohedron in real space (rotation over 5-fold axis „z"). (b) Corresponding five distributions of possible orientations for prolate rhombohedra along „z-axis". The rotation over an angle 72° corresponds to the rotation over an angle 144° in the AUC. Some covering of the distributions is observable.

dra are built by three of six direct space basis vectors. The distributions for different orientations can overlap in the AUC. Such regions suggests that the nodes of rhombohedra with certain orientation in real space must be decorated with atom of the same kind. Using all these rules will result in decoration scheme for Ammann tiling. The whole description of the decoration scheme is not complete yet, however the problem with possible orientations is already solved. In the Fig. 5 one can see all orientations of the prolate rhombohedra along „z-axis" and corresponding distributions in the AUC.

The results presented in this paper show that the statistical approach can successfully describe the diffraction pattern of i-QCs modelled with Ammann tiling. The obtained in this approach diffraction pattern for empty lattice agrees with the one obtained by commonly used higher-dimensional analysis. The outlook of the author's work is to find the complete decoration scheme and to derivate the formula for structure factor for freely decorated Ammann tiling. This will enable the diffraction data refinement for different i-QCs.

⋆ ⋆ ⋆

[1] D. Shechtman, I. Blech, D. Gratias, J. W. Cahn, *Phys. Rev. Lett.* **53**, 1951 (1984).

[2] J. Wolny, *Philos. Mag. A* **77**, 395 (1998).

[3] J. Wolny, *Acta Crystallogr. A* **54**, 1014 (1998).

[4] B. Kozakowski, J. Wolny, *Acta Crystallogr. A* **66**, 489 (2010).

[5] P. Kuczera, B. Kozakowski, J. Wolny, W. Steurer, *J. Phys. Conf. Ser.* **226**, 012001 (2010).

[6] P. Kuczera, J. Wolny, F. Fleischer, W. Steurer, *Philos. Mag.* **91**, 2500 (2011).

[7] P. Kuczera, J. Wolny, W. Steurer, *Acta Crystallogr. B* **68**, 578 (2012).

[8] J. Wolny, B. Kozakowski, P. Kuczera, R. Strzałka, A. Wnęk, *Isr. J. Chem.* **51**, 1275 (2011).

[9] W. Steurer, S. Deloudi, Crystallography of Quasicrystals, (Springer-Verlag, 2009)

[10] J. Wolny, B. Kozakowski, P. Kuczera, L. Pytlik, R. Strzałka, *Aperiodic 2012 conference proceedings*, Springer, *in print.*

Magnetostriction measurements of polycrystalline intermetallics using electrical resistance strain gauge method

Barbara Winiarska

Faculty of Physics and Applied Computer Science, AGH University of Science and Technology, Mickiewicza 30, 30-059 Kraków, Poland

Supervisor: Jarosław Pszczoła, Piotr Guzdek

Intermetallics of $Tb_{0,27}Dy_{0,73}(Fe_{1-x}Al_x)_2$ series, prepared by arc melting technique, are reported. Structural characteristic curves were carried out on powders by taking X-ray diffraction pattern. The Al-substitution of 3d-sublattice of $Tb_{0,27}Dy_{0,73}Fe_2$ compound was studied. This work demonstrated that partial substitution of Fe by addition of Al atoms reduces magnetostriction values.

Magnetostrictive materials, a class of smart materials, are drawing much attention due to their practical applications. Magnetostriction has been defined as an elastic strain causing a change in shape of material during magnetization. In the magnetic field magnetostrictive material reorientates its magnetic domains, so it causes physical length change in the material. Magnetostriction is reversible and keeps volume of sample unchanged. Quantitatively we can write magnetostriction as:

$$\lambda = \frac{\Delta l}{l}, \qquad (1)$$

where λ — magnetostriction, Δl — change of length, l — initial length of sample.

Most ferro- and ferrimagnets exhibit magnetostrictive properties.[1–3] Usually relative change in length is on the order of 10^{-5} – 10^{-3}. During 1960's A. E. Clark and others discovered giant ($> 10^{-3}$) magnetostriction in rare earth elements (Tb, Dy) at cryogenic temperature. In 1971 they got huge values of magnetostriction for $TbFe_2$ and $DyFe_2$, intermettalics of C15 Laves phase structure at room temperature. Unfortunately these compounds have big magnetocrystalline anisotropy, what means that they need high values of magnetic field to magnetize. Few years later they had found specially formulated alloy of Terbium, Dysprosium and Iron (Terfenol-D) which exhibits giant magnetostriction, also at room temperature. Terfenol-D overcame both temperature and anisotropy difficulties by balancing the ratio of Terbium and Dysprosium (0,27/0,73), two elements with oppositely signed magnetocrystalline anisotropy. Effective anisotropy of that compound was zero at room temperature. Since then Terfenol-D has become main magnetostrictive material commonly used in engineering. Researchers continue studies to find new magnetostrictive materials. That's why I took the trouble to investigate new descent from Terfenol-D compounds.

The way of magnetostriction description could be following. If the direction of magnetostriction measurement is parallel to the magnetic field direction we say about a longitudinal magnetostriction $\lambda_{\parallel}$. If the direction of measurement is perpendicular to the field — it is called transverse magnetostriction $\lambda_{\perp}$. Saturation magnetostriction λ_s is defined as such a value of magnetostriction that further increasing field causes no increase of magnetostriction value any more. For monocrystals we know λ_{hkl} constants which describe relative change of length measured along hkl crystallographic directions. For polycrystals of cubic structure we got such a formula:

$$\lambda_{pc} = \frac{2}{5}\lambda_{100} + \lambda_{111}, \qquad (2)$$

where: λ_{100}, λ_{111} — magnetostriction constants measured along the main crystallographic directions 100 and 111 accordingly. For Terfenol-D: $\lambda_{pc} = 1020 \times 10^{-6}$.

Intermetallic compound $Tb_{0,27}Dy_{0,73}Fe_2$ (Terfenol-D) exhibits strong magnetostrictive properties.[4] Magnetostriction of Terfenol-

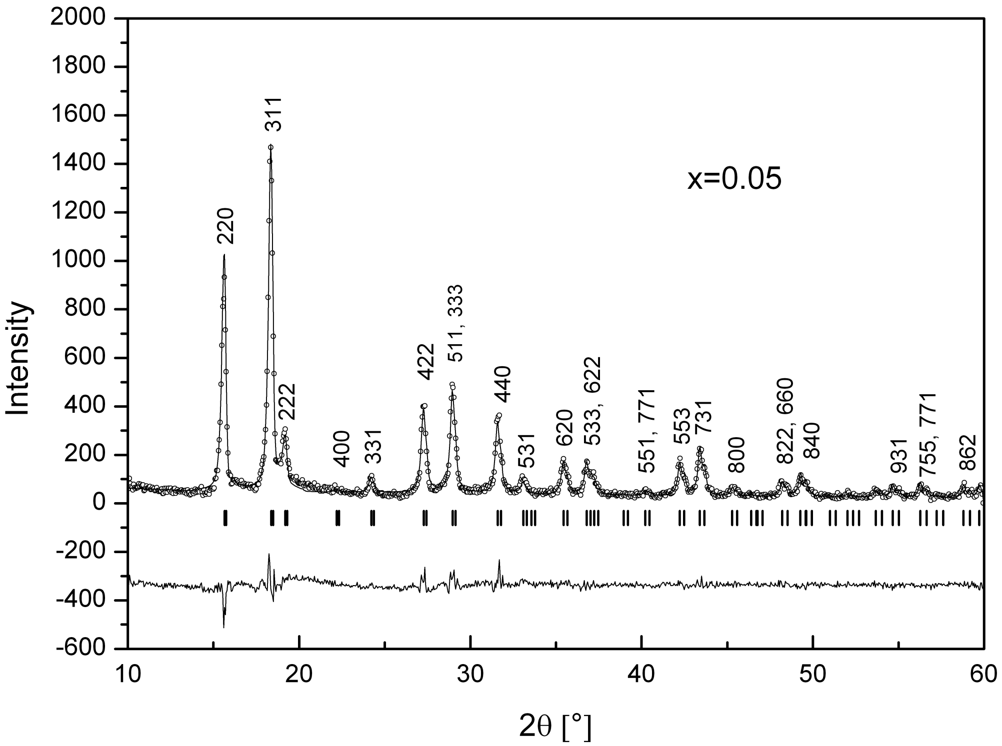

FIGURE 1: Exemplary diffraction pattern for $Tb_{0,27}Dy_{0,73}Fe_2$ intermetallic.

D monocrystal is highly anisotropic, i.e. $\lambda_{111} \gg \lambda_{100}$. It has many practical applications in the technics. It is a good material for actuators and sensors. Also, it is used for controlling noise level and construction vibrations, micropositioning devices, surgical tools, line motors, and so on. This material has some limitation in its technical adoption. First issue is eddy current losses due to high frequency operation, the second one is poor durability. These issues could be eliminated by forming polymer matrix composites of magnetostrictive material and the polymer (or other piezoelectric material). All investigated samples of series $Tb_{0,27}Dy_{0,73}Fe_2$ were prepared using arc melting method in a high purity argon atmosphere from the appropriate amounts of the Tb, Dy (99,9% purity), Fe and Al (all 99,99% purity) starting materials. Then the samples were annealed in vacuum at 850°C for one hour.

A standard X-ray powder diffraction pattern was obtained for each sample using Mo K_α radiation at room temperature (Fig. 1). For all obtained compounds ($x = 0$; 0,05; 0,1; 0,15; 0,2) the clean X-ray patterns corresponding to the cubic, $Fd3m$, $MgCu_2$-type (C15) Laves phase (Fig. 2) were registered.

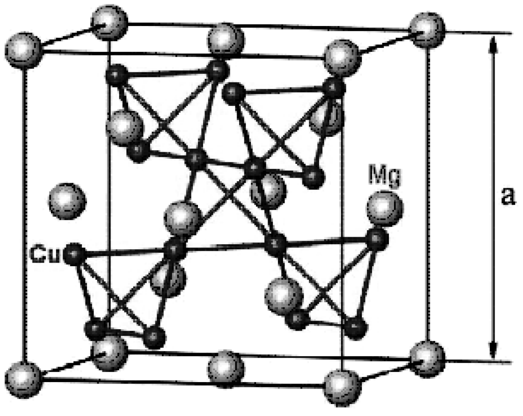

FIGURE 2: Laves phase called C15 type ($MgCu_2$) structure.

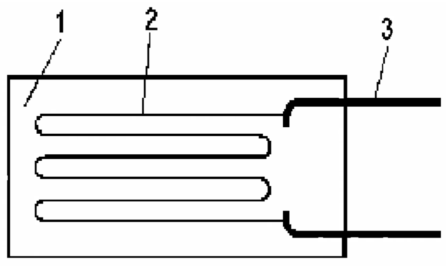

FIGURE 3: Metal-foil strain gage. 1 — foil backing, 2 — resistance wire grid, 3 — leads.

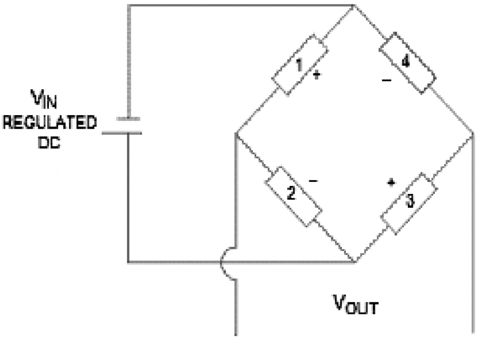

FIGURE 4: Wheatstone Bridge.

Unit cell parameters were obtained from the numerical analysis of the experimental X-ray patterns: a — for the $MgCu_2$-type of crystallographic structure. Lattice parameter increases from 7,3389 Å for $x=0$ to 7,4400 Å for $x = 0{,}2$; due to a larger atomic radius of Al (1,43 Å) compared with Fe (1,24 Å). Also the unit cell volume increases starting from the value $V\,(x=0)=395{,}2691$ Å^3.

During my work, magnetostriction measurements were carried out using Strain Gauge Technique. This method consists in strain monitoring using strain gauges. In this work I tried to describe axial strains in the magnetic field. A strain gage is the active electrical resistant element that senses the change in length to the initial length and converts it into en electrical signal. Each strain gage, as an electric conductor, changes its geometric dimensions (length l and cross-section A) when it is treated by external forces. It causes the change in its resistance. Before selecting a strain gage type and strain gage configuration you have to consider some important factors, like the direction, type and resolution of strain you need to measure. Ideal strain gage should be small enough, inexpensive, accurate, repeatable, easily attached, highly sensitive to strain. I have chosen metal-foil strain gages for my purpose (Fig. 3). We want to measure relative small length changes so we need a suitable method. I used the Wheatstone Bridge configuration, shown in Fig. 4, which is capable of measuring these small resistance changes. We have to remember that total strain is always the sum of the four strains and represented by output voltage V_{OUT}.

I met some measurement issues. First of all, using this method you have to take into account the strain gage sensitivity for ambient conditions (humidity, temperature). Fortunately using Wheatstone Bridge configuration compensates this effect. Secondly you need to apply suitable adhesive for bonding strain gages with the samples (I used cyanoacrylic glue). Assembly of strain gage should be carried out precisely according to the producer prescription. You should also remember about the positioning of strain gage, as it should be accurately aimed parallel to the field direction. Otherwise you can get potential errors of measurements.

Results of magnetostriction measurements demonstrate that longitudinal magnetostriction for Terfenol-D sample $(x=0)$ saturates near 800 ppm (Fig. 5). Saturation magnetostriction values for next samples $(x=0{,}05;\ 0{,}1;\ 0{,}15)$ reduce. And longitudinal magnetostriction for $Tb_{0,27}Dy_{0,73}(Fe_{0,85}Al_{0,15})_2$ saturates near 380 ppm. As regards transverse magnetostriction, obtained values are negative what means that samples shrink in the direction perpendicular to the field. And absolute values of saturation magnetostriction reduce, starting from 560 ppm for $x=0$ up to 210 ppm for $x=0{,}15$.

As we see, Al substitution in the $Tb_{0,27}Dy_{0,73}(Fe_{1-x}Al_x)_2$ series introduces some changes in structural and magnetostrictive properties of such compounds. It increases the lattice parameter with x, increases the average distance between the

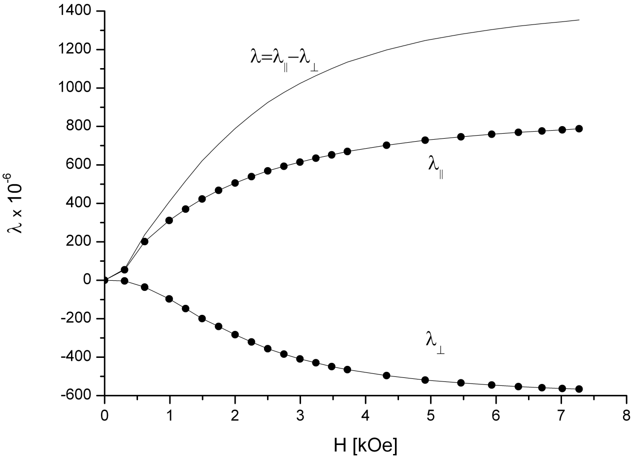

FIGURE 5: Magnetostriction plot for Terfenol-D sample.

nearest neighbours of transition metal atoms and consequently changes magnetostrictive properties. Saturation magnetostriction decreases with Al content. These results seem to be useful for further study to find the best compounds for construction composites exhibiting giant magnetoelectric effect.

⋆ ⋆ ⋆

[1] K. H. J. Buschow, *Rep. Prog. Phys.* **40**, 1179 (1977).

[2] A. E. Clark H. S. Belson, *Phys. Rev.* **B5**, 3642 (1972).

[3] A. E. Clark, Ferromagnetic Materials, vol 1, ed. Wolfhart, E. P. (Amsterdam: North-Holland 1980).

[4] M. J. Dapino, A. B. Flatau, F. T. Calkins, *Proceedings of SPIE Smart Structures and Materials* **3041**, 256 (1997).


Serializer
Serial output
Parallel input (10 bit)
sample
PLL
x10
Sample CLK (fs)
10 x fs
DOS(E) (arb. units)
E (eV)
Ef
{3}
X
L
x [nm]